THE UNIVERSITY *of* EDINBURGH

Theoretical modelling of ultrasound contrast agents

Pádraig Looney

A thesis submitted for the degree of Doctor of Philosophy.
The University of Edinburgh.
April 2, 2011

Abstract

This thesis compares theoretical models of ultrasound contrast agents to the acoustic response from single Microbubbles(MBs). The acoustic response was compared using a range of driving parameters. A rigid shelled contrast agent and a lipid shelled contrast agent were used in the comparison.

While attempts to model the behaviour of some contrast agents at low mechanical index (MI) have been successful at higher MI the behaviour of MBs is still not well understood. Understanding and predicting the response of MBs to medical ultrasound can lead to improvements in the clinical use of MBs through improved contrast agent design or improved signal processing.

Numerical models were developed to compare to three specific cases; 1) Rigid shelled contrast agents 2) Lipid shelled contrast agents 3) Responses from lipid shelled contrast agents that are hit by subsequent driving pulses. Three models were used to compare to the responses from single rigid shelled contrast agents. Two of these models have been used before and the third was developed based on the optical observations of the responses of these rigid shelled agents at these MI. Two shelled models were used to compare to the response of single lipid shelled MBs. Using statistical methods the parameters defining the shell properties were found. The parameters that gave best agreement with the lipid shelled data was then used with a model to account for the molecular diffusion of gas from a MB and a new model to account for the optically observed shedding of the shell from a MB to compare to the multiple response from single MBs.

While the theoretical prediction of an acoustic response of a suspension of MBs or the radial oscillation of single MBs has been compared before to experimental data, the successful comparison of the acoustic response of single MBs to the theoretical prediction is the first of it's kind known to the author. The new theoretical model of the rigid shelled MB that was developed in this thesis gave better agreement with the experimental data than the other previously used models. The shell parameters of the lipid shelled MB were determined for the lowest driving amplitude and were in agreement with those measured previously from optical observations. Finally, the model for the shedding of the shell was shown to give quantitative agreement with the multiple acoustic responses from single MBs. When shedding of the shell was included the

choice of constitutive equation for the shell was shown to strongly affect subsequent responses from the MB.

Declaration of originality

I hereby declare that the research recorded in this thesis and the thesis itself was composed and originated entirely by myself, except where otherwise stated, in the Department of Medical Physics and Medical Engineering at The University of Edinburgh.

Pádraig Looney

Acknowledgements

I would like to thank the Engineering and Physical Sciences Research Council for funding my PhD as part of the Biologically Inspired Acoustics Systems collaborative grant.

I would also like to thank my supervisor Vassilis Sboros for his help throughout my PhD. Thanks also to Norman McDicken and Tom Anderson for their help. Nikos Pelekasis, Robin Steel and David Thomas all provided fruitful discussion on various topics in this PhD.

The experimental data used in this thesis for the comparison with the theoretical models was measured by David Thomas. The theoretical models used for this comparison were developed in previous work by Kostas Tsiglifis.

Many thanks also to my colleagues in the Royal Infirmary for all their help and in particular to Irene Craig.

Contents

List of figures

List of tables

Chapter 1
Ultrasound contrast agents

1.1 Introduction

Ultrasound imaging is a safe and low cost imaging technique compared to other imaging modalities such as MRI and CT. In clinical usage MRI and CT function typically provide much greater image resolution compared to ultrasound imaging. Ultrasound contrast agents improve the quality of ultrasound images and also provide other clinical applications. Ultrasound contrast agents are gas filled microbubbles(MBs) that have a diameter of a few microns. The size of the MB allow the MB to pass safely through the vascular system. The acoustic properties of the MB results in a large acoustic scattering cross-section so that when tissue is insonified by ultrasound the scattered echo is increased by the presence of the MBs.

1.2 Uses of UCAs

Perfusion imaging involves the visualisation and the measurement of the amount of blood flowing in and out of an organ. It has been shown that UCAs can be used to measure perfusion in the heart, liver and kidney[51].

UCAs can be used for the delivery of drugs and genes to specific locations in the body[97]. If a drug or gene is present in an UCA the drug or gene may be delivered locally by driving the MBs at high amplitudes using ultrasound. The disruption of the shell due to the high amplitude oscillation releases the drug or gene. By attaching markers to the UCA shell the UCA can bind in specific locations and can show where disease may be present[145].

High intensity focused ultrasound is used therapeutically to destroy tissue. Pathogenic tissue is destroyed by the localised heating caused by the high intensity focused ultrasound. When contrast agents are used the amplitude of the pressure required to destroy tissue is lowered[134].

Name	Shell type	Thickness	Stiffness	Gas type	Manufacturer
Echovist	N/A	N/A	N/A	Air	Schering AG
Levovist	Palmitic acid	N/A	N/A	Air	Schering AG
Echogen	N/A	N/A	N/A	Dodecafluoropentane	Sonus pharmaceuticals
Albunex	Albumin	15nm	8N/m	Air	Mallinckrodt Inc
Optison	Albumin	15nm	8N/m	Octafluoropropane	GE Heathcare
biSphere	Polymer/Albumin	15nm	1-6N/m	Air	POINT Biomedical Corp
Sonovue	Phospholipid	1nm	0-4N/m	Sulfurhexafluoride	Bracco
Definity	Phospholipid	1nm	0-2N/m	Octafluoropropane	Lantheus Medical Imaging, Inc.
MP1950	Phospholipid	1nm	0-2N/m	Decafluorobutane	Mallinckrodt Inc
Sonazoid	Phospholipid	1nm	4-9N/m	Perfluorobutane	Amersham Limited

Table 1.1: *Selected UCAs, their properties and developer.*

1.3 Origin of UCAs

When agitated saline was injected into the venous blood supply during an ultrasound scan an increased echo from the blood relative to the tissue was found[48]. Agitated saline contains tiny air bubbles. These bubbles dissolve quickly compared to encapsulated MBs. Since they are removed by the lungs and the blood returning in the pulmonary artery would have a much lower echo than that in the right side of the heart. The presence of MBs in the left side of the heart suggests the movement of blood through the septum of the heart (a right to left shunt).

In the fetus there is a channel connecting the left and right atria directly. This channel closes after birth but in a fraction of the population it can remain and give rise to what is know as a patent foramen ovale and as a result a right to left shunt. Left to right shunts give an increased risk of decompression illness in divers since the formation of bubbles due to dissolved gas can last longer in the blood system by bypassing the lungs via the shunt[42]. Patent foramen ovales have also been seen to be more common in patients with stroke[73]. Agitated saline is still used today to detect a patent foramen ovale and a right to left shunt noninvasively.

1.4 Encapsulated MBs

To allow imaging of UCAs over a longer period of time MBs that can pass through the lungs and that do not dissolve as quickly as free gas bubbles are required. In 1991 the contrast agent Echovist® (Schering, Berlin, Germany) was approved for medical use by the German health care authorities. In 1994 Albunex® ((Molecular Biosystems Inc (MBI), San Diego, USA and Nycomed Imaging AS, Oslo, Norway)) was approved for use in the USA. Albunex® is a gas

MB surrounded by a shell made of human serum albumin. In 1996 the UCA Levovist® (Schering, Berlin, Germany) was approved for use. Both Echovist® and Levovist® have air bubbles that form on the irregularities of sugar crystals. In the case of Levovist® palmitic acid is used to stabilise the MB.

In subsequent years many contrast agents have been developed. Most of these contrast agents are similar to Albunex® in that they consist of a gas core surrounded by a stabilising shell. UCAs that consist of a gas MB with an encapsulating shell can be classified as rigid or soft shelled MBs. Rigid shelled MBs have a shell that is composed of albumen or a polymer or in the case of biSphere^{TM} (Point Biomedical Corp., San Carlos, CA, USA) both albumen and a polymer. Soft shelled MBs have a shell that is composed of a phospholipid. Other types of UCA include phase shift colloids. Phase shift colloids (e.g Echogen® (Sonus Pharmaceuticals, Bothell, Washington, USA)) have a boiling point below the body temperature of the animal on which they are used. When an emulsion of these phase shift colloids are injected they vaporise to form MBs.

1.5 Imaging techniques

Rigid shelled MBs are activated by using a high amplitude pulse to disrupt the MBs. The disrupted MBs then give an increased echo. The shell stiffness and shell thicknesses of rigid shelled UCAs are shown in table 1.1. Soft shelled MBs give a large echo without the use of the high amplitude driving pulse. The shell stiffness and shell thickness are much lower than those for the rigid shelled UCAs.

UCAs can be injected intravenously as a bolus or at a slow infusion rate of approximately 2.5 mL/min. Infusion has been shown to be more suited to measuring the blood flow in and out of the heart[144].

Tissue can behave as a nonlinear scatterer when the ultrasound propagates a large distance through tissue. Infinitesmal generation of higher harmonics occurs when tissue is compressed and relaxed since the elastic properties vary slighty. When the pulse travels a distance though tissue this effect is magnified and can produce nonlinear distortion of the beam. The response of MBs to the ultrasound is also nonlinear. This results in increased scatter of harmonics, subharmonics and ultraharmonics. Since the tissue is a linear scatterer the harmonic response from MBs is higher. Harmonic imaging can be used to distinguish the vascular system from the

tissue[135].

When the driving pulse is inverted a linear scatterer has an inverted response while a nonlinear scatterer generally does not. Hence by using suitable pulse sequences where the phase is inverted the nonlinear response of UCAs can be distinguished from the linear response of tissue [52].

1.6 Understanding MBs

A complete explanation of the response of UCAs to medical ultrasound does not exist. Understanding and predicting the response of UCAs will help further to improve their use. Contrast agent design, signal processing of MB's responses and optimisation of the driving parameters will be improved by a deeper understanding of MB behaviour.

Using experimental and theoretical methods the knowledge of UCAs and their behaviour can be furthered. This thesis aims to improve the understanding of rigid and soft shelled MBs by improving upon the theoretical models for them. Theoretical models were developed in this thesis for both rigid and lipid shelled contrast agents and these models were compared to the experimental responses from single MBs. The thesis is structured as follows;

Chapter 1. Chapter 1 has given an introduction to UCAs, their uses, the development of UCAs, the types of contrast agents, how they are imaged and the research into UCAs.

Chapter 2. Chapter 2 gives a greater description of the research on UCAs and in particular those results that are relevant to the work in this thesis.

Chapter 3. Chapter 3 introduces the theoretical models of shell encapsulated MBs that are used in this thesis. The dependence of the models on the driving parameters and the relevance of these results to clinical use is discussed.

The linear model is investigated and the relationship between important features such as resonance, the phase shift and the shell properties are discussed.

The predictions of the theoretical models that are important clinically and the dependence of the response on the shell properties is found.

Previously experimentally observed phenomenon such as compression dominated behaviour is shown to be predicted by the theoretical models for some shell parameters.

Chapter 4. Chapter 4 uses three theoretical models, two of which have been used previously to model rigid shelled contrast agents and one new model developed in this thesis, to compare to the experimental response of single rigid shelled biSphere^{TM} MBs.

A method of comparison of the distribution of responses measured experimentally to the theoretical models is developed.

The method of comparison is then applied to three separate models.

A new theoretical model that is developed in this thesis is shown to give a better prediction than any existing models.

Chapter 5. Chapter 5 takes two shell models and compares them statistically to the acoustic response from single MBs. Using statistical methods the shell parameters are obtained.

Hence, the shell parameters can be determined for the Skalak model and the Mooney-Rivlin models.

Chapter 6. Chapter 6 compares the response of theoretical models for the multiple responses from MBs using two shell models. A molecular diffusion model and a model that accounts for the loss of shell material were used.

The molecular diffusion of gas is used to estimate the change in acoustic response of MBs to subsequent responses but is shown to be inadequate in predicting the decrease in acoustic response.

A new model, the lipid shedding model, is developed to account for changes in the shell and it is shown that using the shell parameters found in chapter 5 the Skalak model predicts a much greater decrease than the Mooney-Rivlin model.

The lipid shedding model together with the Skalak model is shown to predict the previously experimentally observed phenomenon of increasing compression only behaviour of MBs.

Chapter 7. The results of the previous chapters are summarised and future work on each of these topics is suggested.

Chapter 2
Previous work

2.1 Introduction

MBs in a large volume of water will respond differently than MBs in the body since the properties of water are much different those of blood. The signal can be attenuated by tissue in the body and the MBs can interact with other MBs and the surrounding tissue. To understand the behaviour of MBs in the body the simplest case of a MB in a large volume of fluid that is assumed throughout the later chapters of this thesis must first be understood. The experimental and theoretical investigation of MBs has progressed from considering single isolated MBs to considering MBs in tubes and also the interaction of MBs. We begin by discussing the theoretical modelling of single MBs and then discuss the experimental observations of MBs and the comparison of the theoretical models to the experimental data. The subharmonic response of MBs and the transition to chaotic behaviour is reviewed. The work done on the disappearance of MBs due to diffusion or fragmentation is discussed and is considered in further detail in chapter 6 where theoretical models are compared to the multiple responses of MBs. The effects of boundaries on MBs is also discussed because the presence of boundaries can effect the response of MBs in experiments involving constrained MBs. Reviews on the physics of unshelled MBs can be found by Plesset and Prosperetti; Prosperetti[91;100] and reviews for shelled MBs can be found by Stride and Saffari; Sboros[125;111].

2.2 Single MBs

2.2.1 Shell-free bubbles

Theoretical models for the response of single shell-free MBs in an infinite fluid began long before the invention of UCAs and medical ultrasonography. The study of the oscillation of a cavity in a fluid began with the analysis of Rayleigh[103]. Rayleigh derived an equation for a spherical gaseous cavity in an infinite fluid assuming that the fluid was incompressible and neglecting viscosity of the fluid. The response of a bubble to a driving pulse including the

surface tension was formulated by Plesset[90]. Noltingk and Neppiras developed an equation of motion for a bubble in an oscillating pressure field[86;85]. The model for an oscillating bubble in a fluid was extended to a viscous fluid by Poritsky[92]. Cavitation is the generation of vapor bubbles in a fluid when the pressure in the fluid drops below a threshold pressure. From the numerical solutions the threshold for cavitation in liquids and the dependence of this threshold on the driving frequency, driving amplitude and bubble radius distribution was found. From this work the Rayleigh, Plesset, Noltingk, Neppiras and Poritsky (RPNNP) equation was developed. This equation modelled the response of a free bubble oscillating in a viscous fluid due to some pressure wave and assumed the fluid to be incompressible.

When the speed of sound in the fluid is taken to have a finite value the equations of motion of the MB must be modified. Many seemingly different models taking into account the finite speed of sound in the fluid have been formulated. A model for a bubble where the fluid is compressible was first formulated by Herring[53]. By considering the collapse of a gas bubble in a liquid the equation found by Herring[53] was reproduced by Trilling[136]. Another similar equation for a bubble taking into account the finite velocity of sound was derived by Keller and Miksis[63]. Gilmore[43] used the enthalpy of the liquid instead of assuming the density of the liquid to be constant to formulate another model for a bubble in a slightly compressible fluid.

The equations of Keller-Miksis, Herring-Trilling and Gilmore all reduce to the RPNNP equation if the velocity of sound is taken to be infinite. Knowing which of these equations is most accurate when terms inversely proportional to the velocity of sound are included is important since each of these models were formulated to incorporate these terms. These equations are all shown to have the same level of accuracy by Prosperetti and Lezzi[101]. By comparing these equations with numerical results to the exact equations of the fluid it was shown that the Keller-Miksis equation using the enthalpy of the liquid is most accurate. An equation for the bubble motion of second order in the compressibility was derived by Lezzi and Prosperetti[75]. By comparing these models with the exact equations of fluid dynamics the different equations of second order were compared with each other. The reduction of the second order equations to the Keller-Miksis type equations was also discussed. The Keller-Miksis equation is used throughout this thesis since it has a high level of accuracy.

These models for a shell-free MB have been solved numerically to study the behaviour of MBs and have also been modified to include other effects. Large wall velocities of MBs were studied by Angelsen et al.[2]. A new model was developed and the results were compared to

that of the Trilling model and Rayleigh-Plesset model. Tomita and Shima[133] compared the model of a bubble in a compressible liquid and an incompressible liquid. Vokurka[143] compared the numerical results from the models of Herring, Gilmore and Rayleigh for different bubble radii and driving pressure amplitude. An equation of motion for a bubble taking into account the vaporisation of the fluid surrounding the bubble was derived by Fujikawa and Akamatsu [39]. The theoretical results were compared with experimental results from a centimetre sized bubble subjected to a shock wave with amplitude of the order of 10^4 atm. The experimental results supported the theoretical finding that MBs can produce a strong acoustic response during the phase just proceeding the minimum radius (rebound) of the MB. The condensation of water vapour and the amount of gas in the MB was found to greatly affect the results of the theoretical model. Oscillations of shell free MBs have been found numerically and are compared to the experimental response of UCAs in this thesis.

2.2.2 Shell encapsulated MBs

The first model of a shell was developed by de Jong et al.[26]. Using the RPNNP model in combination with an ad hoc model for the shell elasticity and damping the response of Albunex® was modeled. The variation of the scattering cross-section of the fundamental and second harmonic was calculated for a free bubble and for a shelled bubble. The predicted values of the fundamental and second harmonic from the linear model are compared with those of the non-linear model for both the shell-free and shelled bubble. A large difference between the acoustic response was found between the non-linear response of the shell-free and shelled MB.

An improved approach to modeling contrast agents was made by Church[21]. Using the Navier-Stokes equations and assuming that the stress tensor of the shell satisfies certain conditions an equation for the motion of a shelled MB was derived. Using the linearised version of this equation analytic results for the scattering cross sections were found. The dependence of the resonance frequency and scattering cross section on shell elasticity was considered and it was shown that bubbles with a shell elasticity of 85 MPa and a shell thickness 15 nm are better scatterers at lower biomedical frequencies.

A number of constitutive equations to model shell have been since proposed. Doinikov and Dayton[28] used a linear Maxwell constitutive equation to model the shell, a Newtonian model for the shell was used to study Optison^{TM}(Mallinckrodt, Inc., St. Louis, MO and Molecular Biosystems, San Diego, CA) by Chatterjee and Sarkar[16]. Using the viscoelastic model of

Church[21] and assuming an exponential stress-strain relation a new model for the shell was developed by Hoff[58]. A strain hardening model and a strain softening model of the MB shell have been developed by Tsilglifis[138]. Most of these models have been compared to the experimental response of UCAs. In this thesis the model developed by Hoff[58] has been used to model rigid shelled MBs and the models developed by Tsilglifis[138] are used to model the response of a lipid shelled MB.

The viscoelastic effects of blood and tissue alter the dynamics of MBs. Encapsulated MBs in a viscoelastic liquid were modelled by Khismatullin and Nadim[66]. The Kelvin-Voight model was used to model the shell and the 4-constant Oldroyd model was used to model the surrounding fluid.

2.2.3 Comparison of theory with experiment

The theoretical models have been compared to experimental responses from many different contrast agents. The comparison has used two experimental methods; 1) acoustical data from suspensions of MBs, 2) optical measurement of the radial oscillation of MBs. By comparing the theoretical models to the experimental responses the unknown parameters used in the theoretical models can be found. The parameters describing the shell of Albunex®, the shell stiffness and shell friction, were found by matching the experimentally measured transmission coefficients to the numerically calculated first harmonic by de Jong et al.[25] and de Jong and Hoff[24].

The experimental response of Nycomed has been compared with simulations using a model for an encapsulated MB with a thin shell by Hoff et al.[60]. The shell parameters in the model were calculated by fitting the theoretically predicted attenuation frequency curves against the experimental results. Simulations assuming the ratio of the shell thickness to MB radius was constant and simulations assuming that the shell thickness was constant were compared to experimental data. The simulations using a variable shell thickness gave better agreement with the experimental data.

The radial response of two contrast agents were measured optically by Morgan et al.[83]. The shell parameters were determined by fitting curves from theoretical models to the measured radial response. The contrast agents used were Optison^{TM} and MP1950. The lipid shelled MB MP1950 was found to give a more predictable response than the albumin coated MB

Optison^{TM}. The shelled model used was found to give poor prediction of the radial response of Optison^{TM} but for MP1950 good agreement was found.

The shell parameters of the lipid shelled UCA Sonovue^{TM}(Bracco, Milan, Italy) was measured using the attenuation spectrum by Gorce et al.[46]. van der Meer et al.[140] used simulations incorporating the shell to compare to optically measured radius response curves from Sonovue^{TM}. From the resonance response curves the shell parameters were determined by fitting the theoretical curves to the experimental curves. The shell parameters determined this way were in close agreement with those measured from the attenuation spectrum by Gorce et al.[46].

By fitting the equations of motion of the MB to the radial response values for the shell parameters can be obtained. The shell elasticity of the contrast agent Definity®(Lantheus Medical Imaging, N Belarica, MA) was measured to be negligible by Morgan et al.[82]. Yang et al.[146] performed optical measurements of Definity® MBs using high frequency driving pulses. The ringdown of a MB is the oscillation of the MB when the driving pulse has stopped. The shell viscosity was calculated from the observed ringdown of the MB.

2.2.4 Optical observations

Optical observations of rigid shelled MBs have shown that in some cases the shell does not oscillate when MBs are insonified. In other cases gas has been observed to leak out of the MB and return during the compression phase or to be ejected away from the shell and form free MBs. Optical and acoustical observation were performed on Optison^{TM}, Albunex® and MP1950 by Dayton et al.[23]. The escape of the gas was not observed for the phospholipid shelled MP1950 but was observed for Optison^{TM} and Albunex®. The assumptions of the shell models may not be correct when applied to rigid shelled contrast agents since the shell may not retain it's integrity at higher driving amplitudes.

Using driving pulses in the MPa range the behaviour of polymer and lipid shelled MBs have been studied optically by Bloch et al.[7]. The polymer shelled MB was seen to have higher stability since fragmentation of the lipid shelled MBs occured at a lower driving amplitude compared to the polymer shelled MB. The gas bubbles ejected from the polymer shelled MB were seen to move up to several diameters away from the shell. The radial response of the rigid shelled UCA biSphere^{TM} was investigated optically by Bouakaz et al.[10]. Driving pulses with mechanical indices (MI) ranging from 0.3 to 1.52 were used. The mechanical index is the peak

negative of the ultrasound pressure divided by the square root of the driving frequency. It was seen that for a MI of 0.3 that there was little to no oscillation from the MBs. At a MI of 0.6 (depending on initial size) leaking of gas from the MBs was observed. A strong dependence of the leaking of gas from the MBs was observed with smaller MBs being more stable than larger MBs. Jetting of gas from Quantison^{TM} MBs, which also have an albumin shell, has also been observed Postema et al.[96]. No theoretical model exists that take account of this behaviour. In chapter 4 a theoretical model is developed that uses the leaking of gas from a MB to find the acoustic response of rigid shelled MBs.

Soft shelled MBs behave very differently to rigid shelled when insonified. The effect of varying the driving amplitude on the oscillation of a phospholipid MB was studied by Emmer et al.[34]. Optical measurements were taken of MBs using different values for the driving pulse amplitude. The response was seen to increase linearly with driving amplitude. A threshold at 30 kPa was proposed below which no MB oscillation occurs. A MB oscillation is defined as compression dominated if the deviation of the MB from the equilibrium radius is greatest at the minimum MB radius. Similarly the MB oscillation is defined as expansion dominated if the deviation of the MB from the equilibrium radius is greatest at the maximum MB radius. A comparison of the experimental data to theoretical models found that while the experimental data had compression dominated responses the theoretical responses were expansion dominated. The theoretical model used a linear model for the shell. In addition to the optical observations of Definity® MBs mentioned in the previous section optical observations on Definity® were performed by Kudo and Yamamoto[71]. Fragmentation of the Definity® MBs was observed above 270 kPa.

Diameter time curves of lipid shelled MBs obtained using optical methods were found by de Jong et al.[27]. "Compression-only" behaviour was observed for MBs with radii below 4 μm when driven by a 1 MHz pulse. The standard equations, similar to the RPNNP equation, used to model the MBs did not agree with the experimental data. A model which takes into account the buckling and breaking of the shell was proposed by Marmottant et al.[78]. The "compression-only" behaviour found experimentally was observed when the radius was close to the buckling radius used in the thesis. The direct comparison of the radius time curves from the theoretical models to the experimental radius time curve found good agreement for suitable choices of model parameters. The fragmentation and subsequent coalesence of a lipid shelled MB was observed by Postema et al.[94]. The aspherical oscillation of MBs can be expanded in terms of Laplace's spherical harmonics. The MB was seen to fragment into eight MBs suggesting a

second spherical harmonic mode. The formation of a jet in the MB was also observed.

2.2.5 Subharmonic and non-periodic oscillations

Nonlinear equations of motion can predict a transition from a periodic response to an aperiodic response. A common route for this transition is the period doubling route[45]. In this case the response goes from a periodic response to a response with one half the driving frequency as a parameter of the equation is varied. As the parameter is varied further the period splits again and so on until an aperiodic response is found. As discussed in chapter 1 the subharmonic, ultraharmonic and second harmonic components in the scattered wave can be used to improve the contrast of ultrasound images. Understanding how the subharmonic and other non-linear responses vary with driving amplitude, MB radius and other driving and MB parameters can help to fully exploit these non-linear responses to improve imaging.

As discussed previously subharmonic, ultraharmonic and second harmonic components in the scattered wave can be used to improve the contrast. Subharmonic components in the response of free MBs was predicted from theory[84]. By studying the stability of the solution to the RPNNP equation the conditions under which a free MB will have a subharmonic response of order one half has been investigated by Eller and Flynn[31]. The amplitude of the driving pulse at which the subharmonic component appears in the response was looked at by Safar[105]. Analytical solutions to the RPNNP equation for the fundamental, second harmonic and subharmonic modes of the steady state solution are found using the asymptotic method by Prosperetti[98]. The subharmonics of order one half and one third were considered. Analytic solutions for the dependence of the phase of these subharmonics on the parameters of the driving pulse were found. The analytic results were compared to numerical calculations. The approach was extended to the transient solutions by Prosperetti[99]. A numerical study on the response of submicron MBs has been performed by Zheng et al.[148]. The subharmonic, ultraharmonic and second harmonic component is compared for different bubble sizes. Some parameters for the bubbles produced a larger subharmonic component and other parameters produced a larger second harmonic component.

An oscillator is defined to have a chaotic response when the solution to the equation of motion of the oscillator is not periodic even though the driving force is periodic. The minimum requirements that an equation will have a chaotic response are met by the RPNNP model for a free MB[45]. Hence, under certain conditions the steady state response of a free MB can be non-

periodic. This chaotic behaviour depends on the driving amplitude, radius and other parameters in the RPNNP equation. The general methods of chaos physics and the use of these methods in studying the behaviour of free MBs has been presented by Lauterborn and Parlitz[72] and Parlitz et al.[89]. These methods can be applied to understand how the response from a MB can change from a periodic response to an aperiodic response. A bifurcation diagram can be used to show the long term behaviour of an observable of a system as a parameter of the system is varied. Typically the observable at time points separated by one period is plotted against the parameter of the system. A linear response would be single valued, a subharmonic response would be double valued and a chaotic response would be many valued at a given value of the parameter of the system. Bifurcation diagrams can show how the different harmonics, subharmonics and ultraharmonics, appear when a particular parameter of the equation of motion of the MB is varied. Using different numerical techniques the bifurcation structure of a free MB was studied by Kamath and Prosperetti[62]. Thermal conduction between the gas and the surrounding liquid was included in the model. The bifurcation structure of a cluster of bubbles was studied by Takahira et al.[126] and the bifurcation structure of a shelled MB was studied by Macdonald and Gomatam [77]. The period doubling route to chaos was observed by both Takahira et al. and Macdonald and Gomatam.

The subharmonic response from a suspension of Albunex® MBs was studied by Lotsberg et al. [76]. No threshold for the subharmonic response was observed and the subharmonic response varied as the cube of the driving amplitude. The amplitude of the subharmonic and ultraharmonic response from a suspension of Optison^{TM} MBs was measured by Shi and Forsberg[119]. The subharmonic and ultraharmonic response observed by by Shi and Forsberg increased faster than the fundamental and second harmonic response at intermediate driving pressures. The subharmonic and ultraharmonic response of the soft shelled contrast agent ST68-PFC were studied by Basude and Wheatley[3]. The ultraharmonic response was seen to provide better contrast than the second harmonic.

A Newtonian model for the shell was used by Chatterjee and Sarkar[16] to study the subharmonic response of Optison^{TM}. The parameters describing the shell were determined in the linear regime. These values were then used to study the subharmonic emission from contrast agents undergoing nonlinear oscillations. The subharmonic response of Optison^{TM} was also studied by Shankar et al.[118]. A peak in the subharmonic response was found when the driving frequency was equal to one half the resonance frequency since the pressure threshold was found to be

minimum at this frequency. Subharmonic generation was observed at low driving amplitudes. Using viscoelastic shell models the shell parameters for Sonazoid^{TM} (GE Healthcare, Oslo, Norway) were calculated by Sarkar et al.[106]. The values for the elasticity and viscosity were calculated from the experimental attenuation spectra at different concentrations of Sonazoid^{TM}. Using these values of the shell parameters the theoretically predicted subharmonic response and fundamental amplitude was compared with the experimental results and good agreement was found.

The majority of work on the subharmonic response of MBs has used suspensions of MBs. The subharmonic response of single MBs has also been observed optically and acoustically. Yang et al.[146] performed optical measurements of the contrast agent Definity® using a 10 MHz transmitting transducer and a 5 MHz receiving transducer to look at the subharmonic component of the scattered signal. Subharmonic radial oscillations were observed as well as a subharmonic acoustical response. Using the acoustic response from single MBs the threshold driving pressure for subharmonic emission from Sonovue^{TM} was examined by Biagi et al.[6]. Stable and transient subharmonic emissions from the contrast agent were observed. Prior to the disappearance of the MB a subharmonic response from the MB was observed.

The ambient pressure is another parameter in the model for a MB that can affect the response. In all of the above work the ambient pressure is constant. The dependence of the subharmonic response of Optison^{TM} on the ambient pressure was studied theoretically and experimentally by Ganor et al.[41]. An in vitro study of the subharmonic emission from the contrast agents Optison^{TM} and Levovist® was performed by Forsberg et al.[36]. A strong dependence of the subharmonic response on the ambient pressure and amplitude of the driving pulse was found.

The subharmonic response of MBs and the aperidic response of MBs has been well studied experimentally and theoretically. It has been shown that the parameters of MBs can affect the subharmonic generation from contrast agents. Hence, an accurate knowledge of the shell properties must be known in order to fully exploit the subharmonic and other non-linear responses of MBs. The effect of the ambient pressure on the response of a MB is especially relevant to clinical imaging since the ambient pressure varies over the cardiac cycle. Further work on the dependence of the response of a MB on the ambient pressure may help to further exploit the nonlinear response of MBs.

2.3 Decay of MBs

Two mechanisms that can be responsible for the reduction in the response and the disappearance of MBs are diffusion and fragmentation. Fragmentation can occur instantly or can develop over time from an irregularity in the spherical shape. The diffusion of gas from a MB is a gradual process and even for free MBs the diffusion time can be long compared to the length of a driving pulse[74].

2.3.1 Instability

Instability of a bubble can be due to a Rayleigh-Taylor instability[130] or due to a parametric instability[12]. The Rayleigh-Taylor instability occurs at the interface of fluids with different densities and is on a much shorter timescale than the parametric instability. These two mechanisms have been compared by Leighton[74].

Near the minimum radius of the MB small fluctuations in the sphericity of the MB can grow rapidly leading to instability of the MB. These fluctuations can give rise to the fragmentation and rapid destruction of the MB. The stability of spherical harmonic oscillations has been considered by Brennen[11]. The fission process that occurs when the MB contracts is examined in detail. The damping effects as well as the formations of jets were also discussed. Using the theory developed by Brennen[11] a threshold for the fragmentation of a MB was found by Postema et al.[96]. The dependence of fragmentation of MBs on the radius and shell parameters was looked at by Postema and Schmitz[93]. The pressure amplitude at which fragmentation is expected for free and lipid shelled MBs was compared. Using the approach developed by Brennen[11] a threshold for the fragmentation of a MB was found. The threshold for fragmentation was shown to be well below that predicted from the Blake threshold that is used to find the onset of explosive growth of a MB and is valid for small MBs[74]. The onset of the transient growth of shelled MBs has been examined in the work by Stride and Saffari[124]. Assuming that the shell model used was correct the stress on the shell were found to be so large that destruction of the MB would be expected at these driving pressures of a few hundred kPa[124].

The experimental responses from three phospholipid shelled contrast agents containing different gases has been compared to theoretical responses including diffusion effects by Bevan et al.[5]. This was done with and without including fragmentation. Bubbles were assumed to fragment provided they met the criteria found by Postema et al.[96]. Simulations including the fragmen-

tation gave better agreement with the experimental data at high driving amplitudes. Optical measurements of the contrast agent MP1950 were studied by Chomas et al.[19]. Fragmentation of the MBs due to the Rayleigh-Taylor instability was observed as well as another mechanism that was related to the pulse length. The latter may have resulted from a perturbation in the spherical shape growing over time. The resulting maximum expansion was compared with the theoretical prediction.

In the majority of the models described above the assumption of spherical symmetry is a basic assumption. During the oscillation however small perturbations in the MB shape from a spherical shape can increase over time. If the MB shape is sufficiently distorted the MB can fragment forming new MBs. This mechanism is related to pulse length similar to the observations of Chomas et al.[19]. Using a multiple scale expansion the non spherical motion of bubbles was studied analytically by Hall and Seminara[50]. The analytic solutions obtained were valid away from resonance. The stability of the MB was analysed for the case of a synchronous oscillation and a subharmonic oscillation. At a driving frequency of 3MHz the spherical stability of free microbubbles has been studied by Grossmann et al.[49]. By varying the amplitude of the driving pulse it was found that modes of oscillations of bubbles of certain radii are unstable with bubbles of smaller radii generally being more stable. It was also seen that the viscosity of the surrounding fluid increased the stability of the MB. The experimentally observed threshold for instability in the motion of free bubbles in a standing wave and the theoretically predicted parametric instability has been discussed by Eller and Crum[33]. The threshold for the parametric instability of the MBs for three different theories of different accuracy was compared. The onset of the erratic dancing motion of MBs observed experimentally was found to coincide with the threshold for shape oscillations measured by Strasberg[123].

The dependence of the surface modes of the phospholipid shelled contrast agent BR-14 on radius and amplitude of the driving pulse were studied experimentally and theoretically by Versluis et al.[141]. Surface modes were observed at pressures of 100 kPa. A model for the spherical harmonics of a shelled bubble was developed. A critical radius below which surface modes would not be expected was found from theory. The surface modes of a phospholipid contrast agent was studied by Dollet et al.[29]. This was done for a range of bubble radii and driving amplitudes. The effect of a boundary on the MBs was studied. The contribution of these surface modes to the scattered wave is then discussed. Fragmentation of MBs due to surface instabilities have been observed by Chomas et al.[19].

Fragmentation can arise from a rapid formation of an instability in a MB or from a gradual change in the MB shape. Fragmention is important when comparing theoretical models to the acoustic response of single MBs since high driving amplitudes or long driving pulses could cause the MB to fragment and this would affect the acoustic response. This will be taken into account when comparing the acoustic response of single MBs to the theoretical models in this thesis.

2.3.2 Diffusion

The pressure gradient across a MB and the concentration of gas in the surrounding liquid can result in the movement of gas molecules from the liquid into the MB or from the MB into the liquid. An unshelled MB in a fluid will dissolve due to the pressure gradient from the surface tension in unsaturated water. The oscillation of the MB and the presence of a shell alter the rate at which MBs dissolve and can under certain conditions result in the growth of the MBs.

The simplest non-trivial case we can consider of a MB experiencing diffusion of gas is a static MB. The diffusion of gas in a static bubble due to surface tension was studied by Epstein and Plesset[35]. Numerical solutions for the diffusion of gas out of a bubble in an undersaturated solution and the growth of a bubble in an oversaturated solution were found. The theory of diffusion of gas into or out of oscillating bubbles has been studied by Eller and Flynn[30]. Using time averages from the RPNNP equation and assuming that the dissolution of gas can be decoupled from the motion of the bubble an equation for the diffusion was derived. The growth of bubbles has been considered by Skinner[122]. An equation to model the growth was derived but a double boundary layer was used as opposed to the single boundary layer used by Eller and Flynn[30]. Church[20] used the theory developed by Eller and Flynn[30] to model the behaviour of micron sized bubbles at biomedical frequencies. The threshold for transient cavitation and rectified diffusion were compared. An analytic solution for the threshold for rectified diffusion was derived. Other models that have less restrictive assumptions than those assumed by Eller and Flynn[30] about diffusion have been developed. A formulation for the dissolution of an oscillating bubble which takes account of the varying gas concentration field outside the bubble was developed by Fyrillas and Szeri[40]. Meidani and Hasan[79] modelled the motion of a bubble taking into account the temperature field and the gas concentration field surrounding the bubble.

The theory developed by Eller and Flynn[30] has been used to compare to the experimentally observed growth of bubbles[32]. The experimental and theoretical thresholds were in rough agree-

ment. Above the threshold for rectified diffusion some of the observed growth rates were 20 times greater than the numerical prediction. It was suggested that acoustic streaming may be responsible for this discrepancy. The origin of the discrepancy in these results was also discussed by Church[20]. The influence of acoustic streaming on the diffusion of gas from a bubble was studied by Gould[47]. Acoustic streaming can have a large effect on the diffusion rate. Acoustic streaming near a boundary has been studied theoretically by Nyborg[87] and Kolb and Nyborg [68]. Experimental results on the growth of MBs were compared with theoretical predictions by Crum[22]. The same model developed by Eller and Flynn[30] was used to compare to the experimental data. Provided no surface waves were present the theory and experimental data agreed well. The effect of varying the surface tension on the diffusion rate was measured and compared with the theoretical prediction.

The shell was introduced to stabilise the MBs and increase their lifespan in the body so it is expected that the shell slows down diffusion. The diffusion of gas out of a MB and the resulting effect on the stability of the shell has been considered by Krasovitski and Kimmel[70]. Using shell parameters of the contrast agent Optison^{TM} the critical radius at which the shell of the MB becomes unstable was determined. The effect of a varying hydrostatic pressure on the dissolution time of bubbles containing different gases was simulated by Michiel Postema and de Jong[80]. The subharmonic and fundamental components in the response from a MB were compared for a dissolving MB in different hydrostatic pressures. The response from bubbles containing different gases was simulated to determine which gas would be most sensitive to changes in the hydrostatic pressure. The disappearance of Quantison^{TM} MBs has been studied by Frinking et al.[38]. A solution of the MBs was insonified with high amplitude pulses. The resulting free bubbles were then observed using low amplitude pulses. The lifespan of the ruptured bubbles was in the millisecond range suggesting diffusion of gas from free MBs. The response of Sonazoid^{TM} MBs was measured by Shi et al.[120]. Multiple pulses were used to investigate the decay of the MBs over a few milliseconds. It was proposed that diffusion was the process responsible for the destruction of Sonazoid^{TM} with pulses having a MI between 0.4 to 1.0. The experimental responses from three phospholipid shelled contrast agents containing different gases has been compared by Bevan et al.[5] to theoretical responses including diffusion effects. High amplitude pulses were used to disrupt the shell of the MBs. At low driving amplitudes above the threshold for disruption the shrinking of the MBs was consistent with the free diffusion of gas from a MB.

The effect of the shell on the dissolution of gas from a MB has been studied by Borden and Longo[8]. The structure of the shell was varied to investigate the effect on the dissolution time. A model was developed for the dissolution of a shelled MB. The affect of the shell permeability on the diffusion rate was included in the theoretical model. Optical images were taken of MBs indicating a process where the MB radius decreases due to dissolution and the shell deforms until it eventually sheds some of it's shell material to restore equilibrium. Takahira et al.[127] compared optical observations of dissolving MBs with numerical simulations. Free and shelled MBs were studied. For the shelled MB good agreement between the experimental data and numerical data was found provided the shell was taken into account. Optical observations on Levovist® and Definity® were performed by Kudo and Yamamoto[71]. In the case of Levovist a strong non-linear relationship between the driving amplitude and oscillation amplitude was found. The fragments from Levovist® were seen to dissolve faster than the fragments from Definity®. The diffusion of the gas in Levovist® was 16 times faster than the gas used in Definity®. The diffusion time of the Levovist® fragments were still well below that expected from theory.

The model of Eller and Flynn[30] will be used in chapter 6 to compare the response of MBs to multiple driving pulses. The loss of shell material similar to the mechanism observed by Borden and Longo[8] will also be considered and compared to the multiple responses from MBs.

2.4 Boundaries

The presence of a boundary in the vicinity of a MB destroys the spherical symmetry assumed in the free MB models above and can significantly alter the dynamics of a bubble. The oscillation of free bubbles close to a boundary and the formation of jets in bubbles has been observed by Benjamin and Ellis[4]. The oscillation of MBs in vessels is important since MBs are injected into the blood system and are contained in blood vessels. Optical experiments also frequently use small tubes to image the MBs and often the MBs are in close proximity to the tube wall. It is uncertain how this affects the results as, to our knowledge, no studies are available that test the effect of the wall and the tube. Since a MB in a vessel responds differently to a free MB care must be taken when comparing theoretical models for free MBs to experimental data from MBs in tubes.

Theoretical models have included the effect of the vessel on the response of MBs. The simplest

approach to including the presence of a boundary in the theoretical models is to treat it as a linear perturbation of the spherically symmetric model. Models for a bubble in open and closed vessels has been considered by Oguz and Prosperetti[88]. The resonance frequency calculated using the boundary integral method was compared to the linear approximations and gave good agreement. A model for a bubble in a vessel was also developed by Sassaroli and Hynynen[108]. It was found that the resonance frequency is lower in a vessel than in an unbounded liquid. As in the free case it decreases with bubble radius and it also decreases as the bubble approaches the centre of the vessel. The effect of varying the length of the vessel on the resonance frequency was calculated in the subsequent work Sassaroli and Hynynen[109]. The resonance frequency of a MB was lowest in the centre of the vessel. Depending on the vessel and MB parameters the unconstrained resonance was recovered for vessels between 200-300 μm.

Another method to include the effects of the vessel is to use the boundary integral method. The boundary integral method is used to solve the partial differential equations numerically. The motion of a bubble close to a rigid boundary was studied by Sato et al.[110] using the boundary integral method and the method of images. The method of images can be used to replace a single MB and boundary with multiple unconstrained MBs. The method of images is commonly used in electromagnetism to replace charges and boundaries with charges and hence simplifies the problem. The formation of jets in the bubble during the oscillation was studied. The effect of the boundary on the frequency response curves was found and the resonance frequency was seen to be lowered by the presence of the vessel. It was found that jets formed in the bubble during the expansion phase of the MB as well as during the collapse phase. The expansion phase is the time period between the minimum radius and the maximum radius and the collapse phase is the time period between the maximum radius and the minimum radius. The formation of jets during the collapse of the bubbles were shown also to depend on the geometry of the vessel and the driving frequency[69].

A lumped parameter model was developed by Qin and Ferrara[102] to describe MBs in elastic vessels. The required driving amplitude to induce MB fragmentation in vessels of varying size was predicted. The circumferential stress and hence the chance of vessel rupture was found to increase when the radius of the vessel is decreased. A model of a bubble in a vessel that is large compared to the size of the MB and takes into account non-spherical oscillations was developed by Hu et al.[61]. The predictions of the model for an unconstrained MB were compared with the asymmetric model. Higher stresses on the vessel wall were found using the asymmetric model.

The acoustic response of MBs in tubes was studied experimentally by Zhao et al.[147]. Adhered MBs and free MBs were distinguished optically and their acoustic responses were measured. The echo from adhered MBs was seen to give a larger response at the fundamental when compared to the freely flowing MBs. Above a threshold for the driving amplitude jets were formed and were directed towards the boundary. The amplitude of oscillation was less than that for unconstrained MBs. Experimental work on the response of Albunex® MBs in a vessel to shock wave lithotripsy was performed by Zhong et al.[149]. Asymmetric oscillations of the MBs were observed in the vessel. The effect of vessel diameter on the oscillation of the MB was investigated. The MB oscillation was observed to become increasingly constrained as the vessel diameter decreased. Optical measurements on the oscillation of MBs in tubes of varying diameter were performed by Caskey et al.[14]. Translation of the MB due to the driving pulse was observed. At a driving amplitude of 1.4 MPa the observed expansion of the MBs was greater than that predicted by the RPNNP equation. The predicted expansion ratio for unconstrained MBs exceeded the observed expansion ratios of the MBs.

Tubes are used in many experiments to measure the response of MBs. As has been shown the tubes can alter the response of the MB. Hence, comparison of theoretical models for unconstrained MBs to the experimental response of MBs in tubes may not be valid. The experimental data used for comparison in this thesis is from single unconstrained MBs. This allows the use of theoretical models for unconstrained MBs to be used for comparison. Advances in the understanding of unconstrained MBs and the extension of the theoretical models to MBs in tubes may help improve the clinical applications of MBs. Shifts in resonance due to the vessels and the affect on the non-linear response of MBs could be utilized to improve the quality of ultrasound scans.

2.5 Bubbly Fluids and Bubble bubble interaction

The models described above focus on simulating the response of a single isolated MB. When MBs are in a suspension interaction of the individual MBs can be important and can affect their behaviour.

The theory on a suspension of MBs has been produced by Chin and Burns[17]. Extending the single bubble models to a suspension and using the measured radial distribution of Optison and the measured transducer simualtions were performed. The model did not include the shell of the

contrast agent. Theoretical models of interacting MBs has shown that small MBs experience a size dependant interaction with smaller MBs experiencing a larger shift in response[1].

The focusing of the Ultrasound and other effects on the beam profile in a bubbly weakly compressible fluid has been predicted in[65]. Assuming that nonlinear propagation is negligible a model for the formation of an US image in the presence of a suspension of MBs has been constructed by Uhlendorf[139]. The effect of the nonlinear propagation of the US beam through a suspension of MBs has been studied experimentally and numerically by Tang and Eckersley [128]. It was shown how the suspension of MBs can lead to a linear scatterer being interpereted by an US scanner as a nonlinear scatterer due to the nonlinear propagation of the beam.

The complexity of a suspension of MBs interaction with ultrasound provides difficulty in investigating the behaviour of single MBs. The experimental data used in this thesis is obtained from a dilute stream of MBs where each MB can be considered a single isolated MB.

2.6 Conclusion

Theoretical models and experimental interrogation of UCAs have proven useful in explaining the behaviour of some UCAs at some driving amplitudes. Better theoretical understanding of UCAs can help to improve their use by improving contrast agent design and methods of imaging them. Further advances in the modelling of UCAs in vessels may help in the imaging of small blood vessels. The established theoretical models used in this thesis have been verified by comparison to the numerical results found by Leighton; Hoff[74;57].

A wide variety of responses from contrast agents has been observed experimentally. The response of rigid-shelled contrast agents are very different to soft shelled MBs. Defects in the shell are suspected to allow gas to leak and thereby interact with the ultrasound and scatter the ultrasound driving beam. No model taking into account the leaking of the gas exists. This is a complicated phenomena and the size of the defect would determine the leaking of the gas so it is of no surprise that it is a difficult phenomena to model theoretically. A model that takes into account the leaking of the gas is proposed in chapter 4.

All of the comparisons of theoretical models to experimental models have used either optical observations of single MBs or the acoustic behaviour of suspensions of MBs. This thesis uses a new method of comparison. The acoustic response of single MBs is compared to the theoret-

ically predicted echo from single MBs. This method has the advantage that the responses are from single MBs and that the MB oscillates unconstrained in a relatively large volume of water. Using this method the shell parameters of the UCA Definity® are found in chapter 5.

There still does not exist a theoretical model for the decrease in radial oscillation and scattered pressure upon subsequent insonation from MBs. While many authors have included the effects of molecular diffusion to explain this phenomenon the predictions using molecular diffusion still do not agree with the observed experiment data. In chapter 6 the response of single MBs is compared to experimental response using the molecular diffusion and a new model that takes account of the loss of shell material similar to that observed by Borden and Longo[8].

Boundaries and multiple MB interactions can change the response of MBs when compared to single MBs without a boundary. The experimental method to obtain the echo from MBs that is compared to theory in this thesis allows both the effects of boundaries and multiple MB interactions to be minimized. This justifies the asssumptions of the theoretical models used throughout this thesis where interactions of MBs with boundaries and with other MBs are neglected.

Chapter 3
Theoretical introduction to MBs

3.1 Introduction

This chapter introduces the theory that is used in subsequent chapters to compare the responses from a rigid shelled contrast agents and from a lipid shelled contrast agents. The low amplitude linear approximation of these models is discussed and the importance of the parameters in determining the response from the MB is investigated. The nonlinear oscillation of MBs using different models and with different shell parameters for a range of driving frequencies are then investigated.

3.2 Previous work

A prerequisite for the development of a theoretical model for a shell encapsulated gas MB is a theoretical model of an oscillating free gas bubble. As discussed in the previous chapter, a model for a free bubble in an incompressible fluid under an external pressure wave was developed from work done by Rayleigh[103], Plesset[90], Noltingk and Neppiras[86;85] and Poritsky [92]. This model was extended to a compressible fluid by Herring[53], Trilling[136], Gilmore[43] and Keller and Miksis[63]. Although the equations found by Herring[53], Trilling[136], Gilmore[43] and Keller and Miksis[63] have a different form they were shown to have the same level of approximation by Prosperetti[101]. The equation of Keller and Miksis[63] is used throughout this thesis.

By including the pressure due to the shell a model for contrast agents was developed[26;21]. Since then a number of constitutive equations to model the shell have been used. Doinikov and Dayton[28] used a linear Maxwell constitutive equation for the shell, a Newtonian model for the shell was used to study the contrast agent Optison by Chatterjee and Sarkar[16], using the viscoelastic model of Church[21] and assuming an exponential stress-strain relation a new model for the shell was developed by Hoff[58]. A strain hardening Skalak model and strain softening Mooney-Rivlin model have been used by Tsilglifis[138]. Four different shell models have been

used in this thesis, the Hoff model, the Mooney-Rivlin model, the Skalak model and the Kelvin-Voigt model. The Skalak model, Mooney-Rivlin model and Kelvin Voigt model are compared in this chapter. The Hoff model has been used previously to model the behaviour of a rigid shelled MB[58] and is used in the next chapter to model the response from biSphere MBs. The behaviour of the shell of soft shelled MBs is not well understood. The Skalak strain hardening [121] model and Mooney-Rivlin strain softening model are used to model the soft shelled UCA Definity® in later chapters. The Skalak model has been previously proposed as a model for the membrane of a cell. For comparison a strain softening model is also used.

The predictions of the theoretical models are investigated. Many of the features found experimentally are found from the theoretical models for certain parameters. Experimental observations on the response of single MBs can be measured using optical and acoustical methods. The features from these observations that are of particular significance include the ratio of expansion to compression of the radial oscillation, the magnitude of the radial oscillation and its dependence on equilibrium radius and the magnitude of the fundamental, harmonic, subharmonic and ultraharmonic component of the scattered pressure wave.

A model for the buckling and breaking of the shell has been developed[78] to explain the diameter time curves of lipid shelled MBs obtained using optical methods where compression only behaviour was observed for MBs with radii below 4 μm when driven by a 1 MHz pulse[27]. The expansion to compression ratio of each of two theoretical models for a shelled MB is compared for a range of driving amplitudes and shell parameters below.

As discussed in the previous chapter, from the equations of motion of a free MB one would expect that under certain conditions that the steady state response would be aperiodic. This chaotic behaviour depends on the driving amplitude, radius and other parameters in the RPNNP equation. The general methods of chaos physics and the use of these methods in studying the behaviour of free MBs has been presented by Lauterborn and Parlitz[72] and Parlitz et al.[89]. These methods can be applied to understand how the response from a MB can change from a periodic response to an aperiodic response. As mentioned in the previous chapter Sarkar et al. [106] used viscoelastic shell models to caculate the shell parameters for Sonazoid and to determine the resonance frequency. The peak in the subharmonic response was found at a driving frequency of one twice the resonance frequency. The fundamental, harmonic, subharmonic and ultraharmonic component of the scattered pressure wave of two theoretical models for a shelled MB for a range of driving amplitudes and shell parameters are investigated in this chapter.

3.3 Theory

3.3.1 Free bubble

For the free bubble model the Keller-Miksis equation[63]

$$-\left(\frac{3}{2}-\frac{\dot{R}}{2c}\right)\dot{R}^2+\left(1+\frac{\dot{R}}{c}\right)\left(\frac{P}{\rho}\right)+R\left(\frac{\dot{P}}{\rho c}\right)=\left(R\left(1-\frac{\dot{R}}{c}\right)+\right)\ddot{R}, \tag{3.1}$$

was used. R, c, $\dot{R}$, P and $\ddot{R}$ are the radius, velocity of sound in the fluid, velocity of bubble wall, pressure on bubble wall and bubble wall acceleration. P is the pressure on the gas

$$P=\left(P_\infty+\frac{2\sigma}{R_0}+P_{SH}(R_0)\right)\left(\frac{R_0}{R}\right)^{3\gamma}-4\eta_S\left(\frac{\dot{R}}{R_0}\right)-\frac{2\sigma}{R(t)}-P_{Sh}(R)-P_{ex}, \tag{3.2}$$

here P_∞, σ, R_0, P_{SH}, P_{ex} and γ is the hydrostatic pressure, surface tension, equilibrium radius, pressure due to the shell, driving pressure and ratio of specific heats of the gas respectively. The transfer of heat between the gas and the surrounding fluid was neglected and hence the expansion of the gas was assumed adiabatic so γ is set to 1.4. In the free model the shell term P_{SH} is zero. The value for the surface tension is that for a air-water interface 0.0728 N/m.

3.3.2 Shell model

In this thesis viscoelastic models for the shell have been used to model contrast agents. The simplest and one of the first viscoelastic models used to model the shell of a MB is the linear Kelvin-Voigt model[21]. In the linear Kelvin-Voigt model the pressure P_{Shell} is

$$P_{Sh}=12\frac{d_{Se}G_S}{R_0}\left(\frac{R-R_0}{R_0}\right)+\eta_S 12\frac{d_{Se}}{R_0}\left(\frac{\dot{R}}{R_0}\right). \tag{3.3}$$

where d_{Se}, G_S, R_0, R and η_S are the shell thickness, shell stiffness, equilibrium radius, radius, and shell viscosity respectively. The model of a red blood cell membrane was developed by Skalak et al.[121] and this energy functional was used to model the shell of a contrast agent by Tsilglifis[138]. The constitutive equation used in the Skalak model is

$$P_{Sh}=\frac{2d_{Se}G_S}{R}\left(\left(\frac{R}{R_0}\right)^2(1-C)+C\left(\frac{R}{R_0}\right)^6-1\right)+\frac{12\dot{R}\eta_S d_{Se}}{R_0^2}. \tag{3.4}$$

C in this equation is a measure of the hardening of the shell and is set to 1 throughout this thesis. The Mooney-Rivlin model was developed to describe the behaviour of rubber Rivlin[104], Mooney[81], and was used to model the shell of a contrast agent by Tsilglifis[138]. The constitutive equation used in the Mooney-Rivlin model is

$$P_{Sh} = \frac{2d_{Se}G_S}{R}\left(1-\left(\frac{R_0}{R}\right)^6\right)\left(1+B\left(\left(\frac{R}{R_0}\right)^2-1\right)\right)+\frac{12\dot{R}\eta_S d_{Se}}{R_0^2}. \tag{3.5}$$

B in this equation is a measure of the shell softening and is set to 0 throughout.

The parameters C and B appearing above can be varied to produce different amounts of strain softening or strain hardening and effectively produce different constitutive equations for the shell. In this thesis they are set to the values of 0 and 1 since at these values both models have similar behaviour at low amplitudes for the same shell elasticity. With these choices of shell parameters the equations differ by a minus sign and also the numerator R_0 and R are switched. This gives rise to the similar behaviour at low amplitude and the divergence of the models at larger amplitudes of oscillation. If the radius of the MB, R, is written as

$$R = R_0(1+\epsilon), \tag{3.6}$$

where ϵ is small , $B = 0$ and when $C = 1$, equation (3.4) and equation (3.5) reduce to the form of the linear Kelvin-Voigt model shown in equation (3.3)

$$P_{Sh} = 12\frac{d_{Se}G_S}{R_0}\epsilon + \eta_S 12\frac{d_{Se}}{R_0}\dot{\epsilon}. \tag{3.7}$$

A comparison of the Skalak, Mooney-Rivlin and Kelvin-Voigt stress strain relationships are shown in figure 3.1. Provided C is set to 1, B is set to 0 and the shell stiffness is the same then when the MB shell expands beyond its equilibrium point the magnitude of the stress of the Skalak model is greater than the magnitude of the stress of the Kelvin-Voigt model but for the Mooney-Rivlin model the magnitude of the stress is less than the magnitude of the stress of Kelvin-Voigt model (figure 3.1). When the shell contracts below its equilibrium the magnitude of the stress of the Skalak model is greater than the magnitude of the stress of the Kelvin-Voigt model but for the Mooney-Rivlin model the magnitude of the stress is greater than the magnitude of the stress of the Kelvin-Voigt model (figure 3.1). Close to the equilibrium the three models are equivalent, which is the domain of small ϵ as mentioned above (figure 3.1).

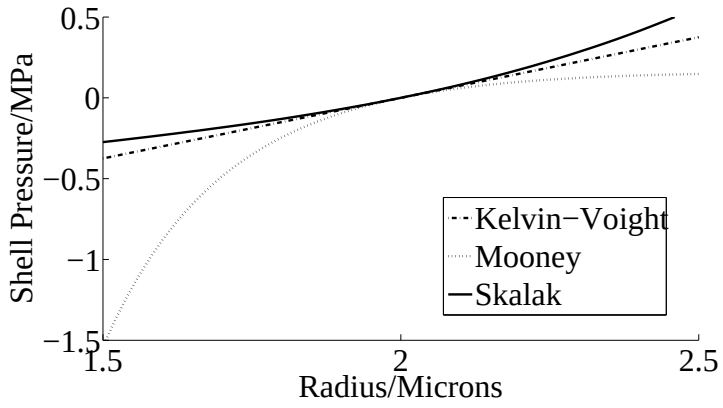

Figure 3.1: *The pressure on the gas in a MB due to the shell for the Skalak, Mooney-Rivlin and Kelvin-Voigt models. The equilibrium radius, shell thickness and shell stiffness of the MB are 2 μm, 5 nm and 50 MPa respectively. The constants C and B are set to 1 and 0 respectively.*

Materials do not generally behave according to the simple linear Kelvin-Voigt model. Instead they tend to have complicated behaviour like that modelled by the Skalak and Mooney-Rivlin models. The behaviour of the Kelvin-Voigt, Mooney-Rivlin and Skalak models have been compared previously by Tsiglifis and Pelekasis[137]. Tsiglifis and Pelekasis showed how the resonance behaviour varies with driving amplitude for each of the models. The acoustic response of Skalak and Mooney-Rivlin MBs is examined below for a range of shell parameters that are relevant to the contrast agents considered in this thesis. The Mooney-Rivlin and Skalak models are important since the shell pressures of these models span a range of shell behaviour within which the linear Kelvin-Voigt model is contained (figure 3.1). Therefore, since any viscoelastic model can be linearised the Mooney-Rivlin and Skalak models provide an insight into the effect of constitutive law when a theoretical model is compared to experimental data.

3.3.3 Linear model

Although the equation of motion equation (3.1) is nonlinear, at low amplitudes of driving pressure it can be linearised. The linear approximation can give insight into the variation of response of MBs due to driving frequency, equilibrium radius and shell parameters. If the radius of the MB R is written as

$$R = R_0(1 + \epsilon), \tag{3.8}$$

where ϵ is small then

$$P_{Shell} = 12\frac{d_{Se}G_S}{R_0}\epsilon + \eta_S 12\frac{d_{Se}}{R_0}\dot{\epsilon}. \tag{3.9}$$

Substituting this into equation (3.1) we find an equation of the form

$$\ddot{\epsilon} + \delta\dot{\epsilon} + \omega_0^2\epsilon = P_0 sin(\omega t), \tag{3.10}$$

where

$$\delta = \frac{\left(\left(12G_S d_{Se}\frac{\sigma}{R_0} + 3\gamma(\frac{2\sigma}{R_0} + P_\infty) - \frac{2\sigma}{R_0}\right)\frac{1}{\rho R_0 c} + \left(\frac{4\eta_L}{\rho R_0^2}\right) + \left(\frac{4\eta_S d_{Se}}{\rho R_0^3}\right)\right)}{\left(1 + \frac{4\eta_L}{\rho R_0^2} + \frac{4\eta_S d_{Se}}{\rho R_0^3}\right)}. \tag{3.11}$$

and

$$\omega_0 = \sqrt{\frac{(3\gamma(\frac{2\sigma}{R_0} + P_\infty) - \frac{2\sigma}{R_0} + 12G_S)}{\left(1 + \left(\frac{4\eta_L}{\rho R_0^2}\right) + \left(\frac{4\eta_S d_{Se}}{\rho R_0^3}\right)\right)}}. \tag{3.12}$$

The resonance frequency f_{res} is defined as the frequency that gives a local maximum in the radial response

$$f_{res} = \frac{1}{2\pi}\sqrt{\omega_0^2 - \delta^2}. \tag{3.13}$$

It has been suggested that the phase response of MBs could be used as a means of determining their resonance frequency[140]. The linear model model shows how this could be possible. When the driving frequency is well below the resonance frequency of a MB the radial response of a free MB is in phase with the driving pulse. This is intuitive since when the pressure is varied slowly the radius of the MB would be minimum when the driving pressure is maximum and visa versa.

From the radius the scattered pressure at a distance r from the MB can be found using Bernoulli's equation[142]

$$P_{Sc} = \frac{\rho R}{r}\left(R\ddot{R} + 2\dot{R}^2\right). \tag{3.14}$$

At low amplitudes a similar expansion as that used in equation 3.8 can be used again to show that the scattered pressure can be approximated by

$$P_{Sc} = \frac{\rho R_0^2\ddot{R}}{r}. \tag{3.15}$$

The scattered pressure is proportional to the second derivative of the radius (equation (3.15)).

Hence, the scattered pulse is π radians out of phase with the radial response since $\ddot{R}$ and R differ by a minus sign. If the MBs resonance frequency is well above the driving frequency the radius will be at its minimum when the pressure is at its maximum. Hence the radial response will be π radians out of phase with the driving pulse. Hence the scattered pressure is in phase with the driving pulse since the scattered pulse is π out of phase with the radial response. As the radius increases the resonance frequency decreases and the MBs do not respond as rapidly so that for driving frequencies well above the undamped resonance $\frac{1}{2\pi}\omega_0$ a phase shift of the scattered pressure to the driving pressure of π radians occurs[74].

3.4 Methodology

3.4.1 Numerical Methods

Equation (3.1) was solved using MATLAB(R2007b,Mathworks) to give the radial motion of the MB. Driving pulses with MIs of 0.025 0.05 0.1 and 0.2 were used to examine the amplitude dependant response of the models. These values of mechanical index (MI) were chosen since when these models are compared to the response of single MBs in chapter 5 the lowest MI used to insonify was 0.13 and the highest was 0.44. The mechanical index was used since as the frequency is increased a driving pulse would decrease in energy if the acoustic pressure remained constant but if the MI remains constant it does not. This allows the nonlinear behaviour at higher frequency to be investigated. The driving pulses were 10 cycle pulses with driving frequencies of 1 MHz, 2 MHz and 4 MHz. Values of 5 MPa, 50 MPa and 200 MPa for the shell stiffness and for the shell viscosity values of 0.1 Pas, 1 Pas and 10 Pas were used in equation (3.4) and equation (3.5). The response of MBs with equilibrium radii up to 10 μm was found. These values were chosen since it was found that the values of shell parameters of the lipid shelled contrast agent Definity® lie in this range. Once the radial motion is known the scattered pressure can be found using Bernoulli's law. The scattered pressure was calculated at a distance of 7.5 cm from the MB, as is the case in the experimental method used to measure the acoustic response from single MBs that is used for comparison in this thesis[131]. The scattered wave was then filtered as described by Thomas[132] to find the fundamental, harmonic, subharmonic with a frequency of $\frac{1}{2}$ times driving frequency and ultraharmonic with a frequency of $\frac{3}{2}$ times the driving frequency. The root mean squared value of these filtered scattered pulses was used as a quantitaive measure of the pulse since it is directly related to the energy of the pulse.

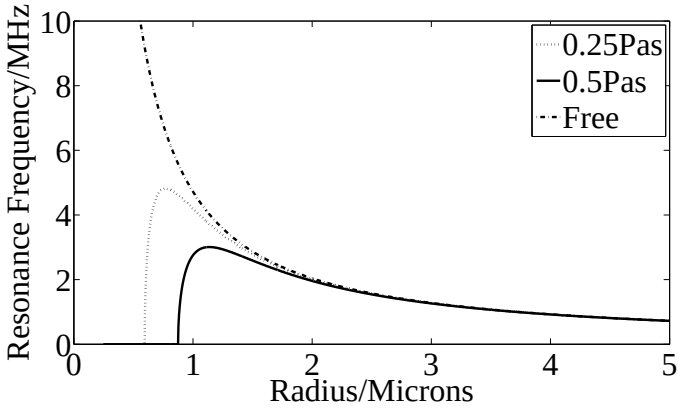

(a) The stiffness is zero.

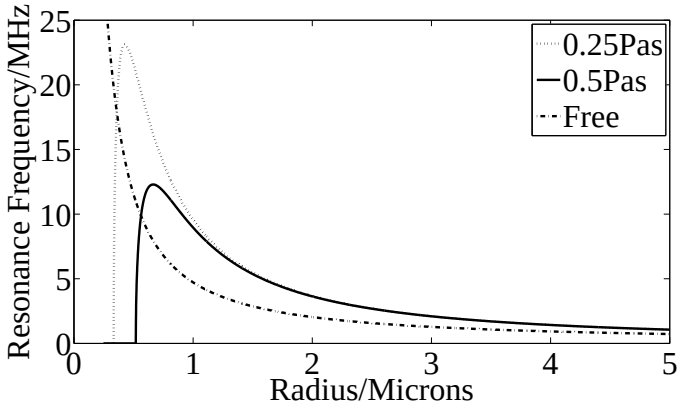

(b) The stiffness is set at 50 MPa in the models except for the free model.

Figure 3.2: *The resonance frequency of MBs for a shell stiffness of 0 MPa and a shell stiffness of 50 MPa is shown for shell viscosities of 0, 0.25 and 0.5 Pas. As the stiffness increases the resonance frequency of a MB increases.*

3.5 Results

3.5.1 Linear Model

The radius at which maximum relative oscillation occurs (resonance radius) can be calculated from the linear model. A graph of driving frequency against resonance radius is shown in figure 3.2. The resonance radius decreases as the driving frequency is increased. Depending on the shell viscosity there may be a cutoff in driving frequency above which there is no resonance radius. The cutoff decreases as the shell viscosity is increased. When the shell stiffness is increased the resonance radius at a given driving frequency decreases (figure 3.2).

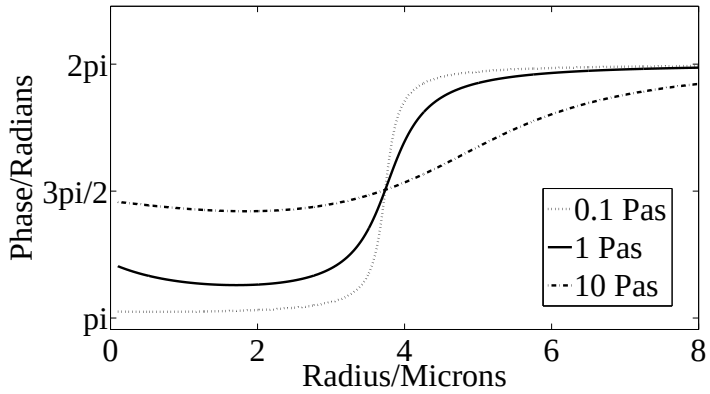

(a) The phase of the scattered pressure.

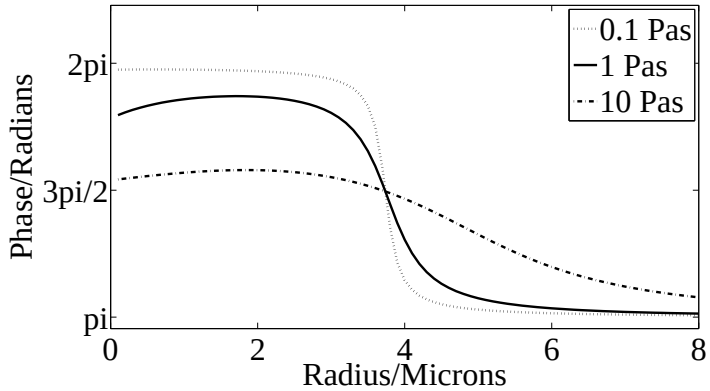

(b) The phase of the radial response.

Figure 3.3: *The phase response of MBs relative to the driving pulse using a driving frequency of 1 MHz. A shell stiffness of 0 MPa and shell viscosities of 0.1 Pas, 1 Pas and 10 Pas are used. The resonance radius of the MBs is at below 4 μm.*

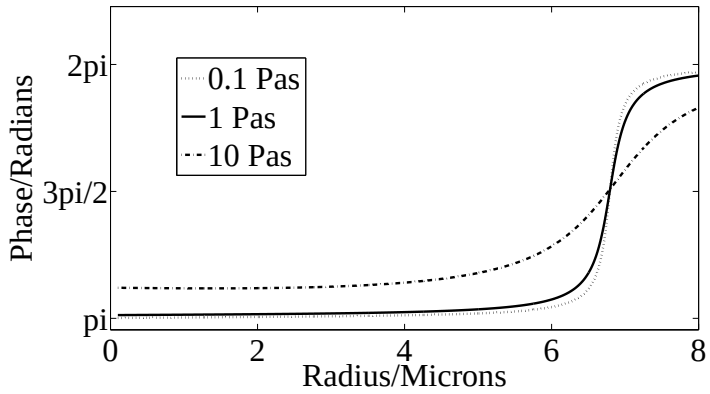

(a) The phase of the scattered pressure.

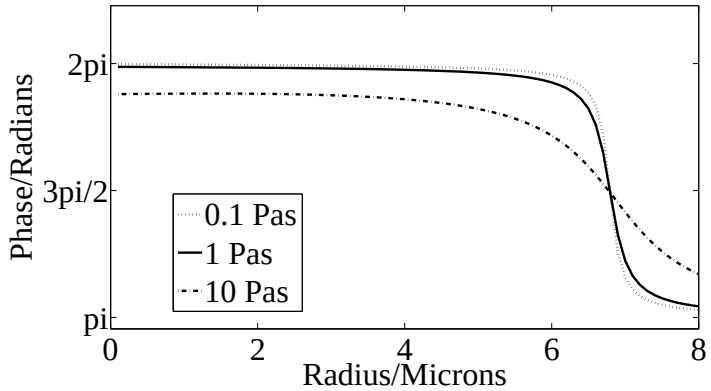

(b) The phase of the radial response.

Figure 3.4: *The phase response of MBs relative to the driving pulse using a driving frequency of 1 MHz. A shell stiffness of 50 MPa is used. The resonance radius of the MBs is at above 6 μm.*

The phase response of MBs relative to the driving pulse is shown in figure 3.3 and figure 3.4. The undamped resonance is at the point of intersection of each of the phase curves for different viscosities, 4 μm and 7 μm, for shell stiffnesses of 0 MPa (figure 3.3) and 50 MPa (figure 3.4) respectively. For a shell stiffness of 0 MPa and with a shell viscosity of 0.1 Pas there is a phase shift of the scattered pressure relative to the driving pulse below resonance close to 2π radians (figure 3.3(a)). If the shell viscosity is increased to 1 Pas the phase shift of the scattered pressure relative to the driving pulse below resonance is less than 2π radians (figure 3.3). At the highest shell viscosity tested, 10 Pas, the phase shift of the scattered pressure relative to the driving pulse is reduced to under 5 radians (figure 3.3).

For a shell stiffness of 50 MPa and with a shell viscosity of 0.1 Pas the phase shift below resonance is close to 2π radians (figure 3.3(a)). If the shell viscosity is increased to 1 Pas there is a phase shift close to 2π radians (figure 3.4(a)). At the highest shell viscosity tested, 10 Pas, the phase shift is reduced to under 6 radians (figure 3.4(a)). Higher shell viscosities result in an increased phase shift away from resonance. Hence the phase shift could be used to measure the shell viscosity.

The linear model gives an insight into the phenomena that occur around resonance and how the resonance depends on the shell parameters. The results above of phase of a MB assumes a steady state linear response for the MB. When using contrast agents the MB is generally not driven for more than a few cycles and the MB response is nonlinear. Under these conditions the assumption of the steady state response is not valid since the transient response can not be neglected. The linear model assumes a radial oscillation that has an equal expansion and compression and is not valid at high amplitudes of oscillation. Nonlinear models can predict driving amplitude dependent responses such as subharmonic responses, compression or expansion dominated radial responses and shifts in the resonance peak and are discussed in the following section.

3.5.2 Free model

The resonance frequency of a 3 μm MB as shown in figure 3.2 is approximately 1MHz. In figure 3.5(c) a peak can be seen in the expansion and compression at 1MHz. At a MI of 0.2 the difference between the maximum expansion and compression is greater than the difference between the maximum expansion and compression at lower MI and is expansion dominated. An expansion dominated behaviour is expected at higher MI since there is no bound on the maximum radius unlike the minimum radius which must clearly be above zero for to make physical sense. The effects due to surface tension decrease as the radius increases further reducing the pressure on the MB. The MB response is almost symmetrical in expansion and compression for MIs of 0.025, 0.05 and 0.1. The subharmonic peak is not visible for a MI of 0.1 0.05 and 0.025 (figure 3.5(b)). The subharmonic peak is visible at a MI of 0.2 and is at a driving frequency of 1 MHz. The linear model predicts that the resonance frequency will be at 1MHz (figure 3.2). At larger amplitudes the fundamental and harmonic peaks shift to lower frequency (figure 3.5(a)).

The dependence of response of MBs with radii up to 10 μm are shown in figure 3.6. Driving pulses with frequencies of 1 MHz, 2 MHz and 4 MHz and MIs of 0.025 0.05 0.1 and 0.2 were used. The peak in the radial displacement is shifted to lower radii as the driving frequency is increased (figure 3.6(c), figure 3.6(f) and figure 3.6(i)). The response of the MBs to the highest MI is highly nonlinear as can be seen from figure 3.6(c) where the resonant MBs expand to three times their initial radii. These MBs also have a violent collapse and hence produce a pressure wave that is also nonlinear. This pressure wave contains many higher harmonics and as a result the curves in figure 3.6 corresponding to the highest MI are not as smooth as those at a lower MI where the response is not as violent. With a MI of 0.1 and at a driving frequency of 1MHz the free MBs had a peak subharmonic response at a radius of 6 μm and had a subharmonic RMS of 20 Pa at this radius. The peak subharmonic response decreased to a magnitude of 8 Pa at a driving frequency of 4 MHz. From equation (3.2) the resonance frequency of a 6 μm MB is 0.5 MHz (figure 3.2). This is similar to previous observations of the subharmonic resonance occurring at twice the fundamental resonance[106]. The same can be seen at driving frequencies of 1 MHz and 2 MHz. At a MI of 0.2 the peak of the subharmonic response shifts to a lower radius (figure 3.6(c), figure 3.6(f) and figure 3.6(i)). The radial response predicted by the free model is expansion dominated at all MI. At the highest MI of 0.2 the resonant MBs had an expansion of three times the initial radius (figure 3.6(c), figure 3.6(f) and figure 3.6(i)).

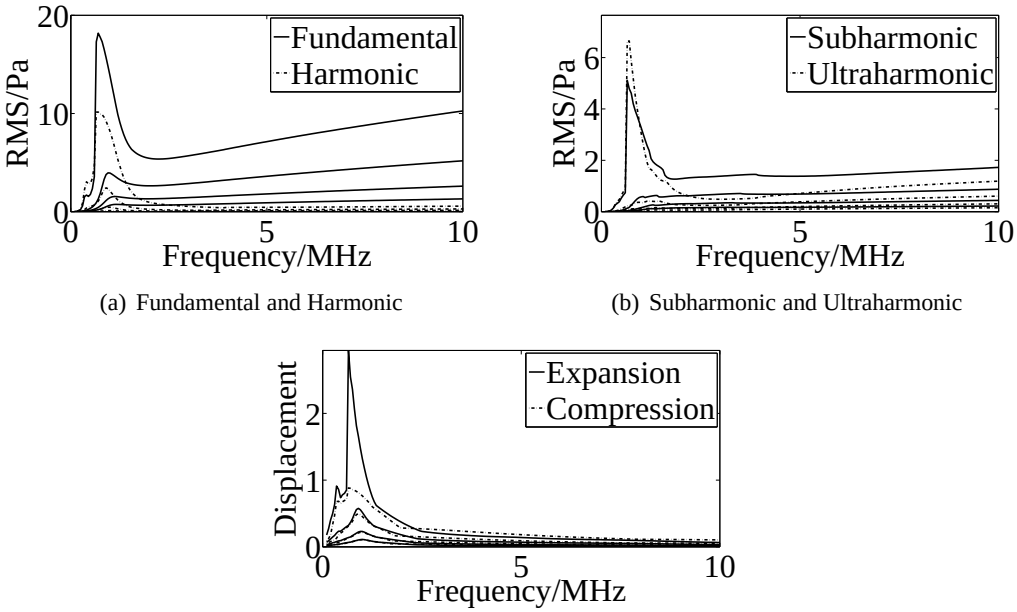

(a) Fundamental and Harmonic

(b) Subharmonic and Ultraharmonic

(c) Expansion to Compression Ratio

Figure 3.5: *The response of a 3 μm free MB at increasing MI for a range of driving frequencies with MI of 0.025 to 0.2. The resonance frequency of a 3 μm free MB is near 1 MHz (figure 3.5(c)). The resonance of the subharmonic and ultraharmonic responses increase much faster between a MI of 0.1 and 0.2 compared to the resonances in the fundamental, harmonic, expansion and compression. The radius oscillation and RMS (root mean squared) pressure of the scattered pulse generally increase as the MI is increased and this is assumed throughout the figures in this chapter.*

While the maximum radial expansion does not vary greatly as the driving frequency increases from 1 MHz to 4 MHz the absolute expansion will decrease since the absolute expansion is the product of the equilibrium radius and the radial expansion shown in figure 3.6(c), figure 3.6(f) and figure 3.6(i). The scattered pressure decreases as the driving frequency increases because the resonance is shifted to lower MBs that undergo smaller oscillations.

The modelling of UCAs uses the shell-free model together with a term that includes the elasticity and viscosity of the shell as detailed in section 3.3.2. It has already been shown that the shell elasticity increases the resonance frequency and that the shell viscosity can alter the phase shift. The effects of the shell will be examined in the next section at higher driving amplitudes where nonlinear responses are present for the Skalak and Mooney-Rivlin models.

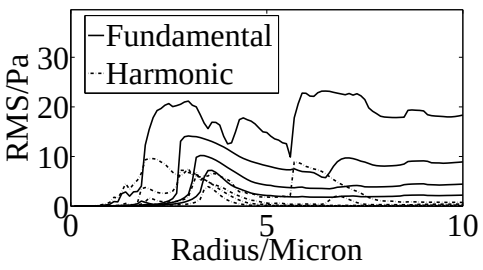

(a) Fundamental and Harmonic

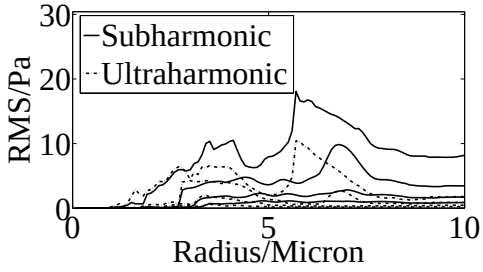

(b) Subharmonic and Ultraharmonic

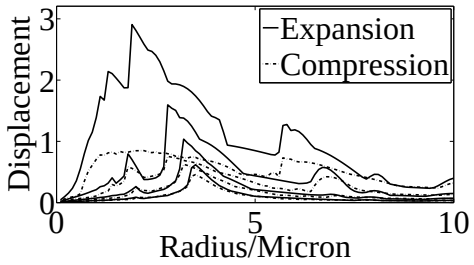

(c) Expansion and compression

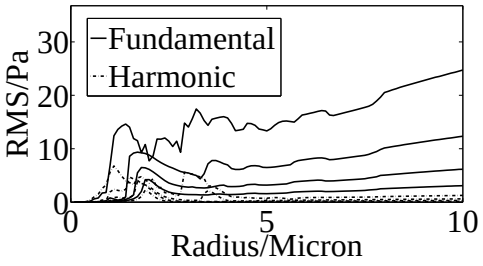

(d) Fundamental and Harmonic

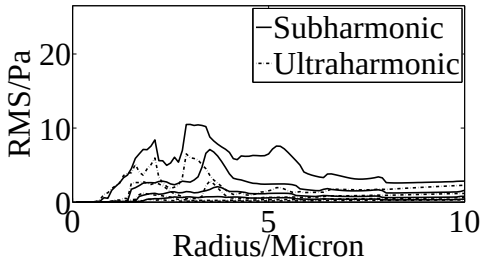

(e) Subharmonic and Ultraharmonic

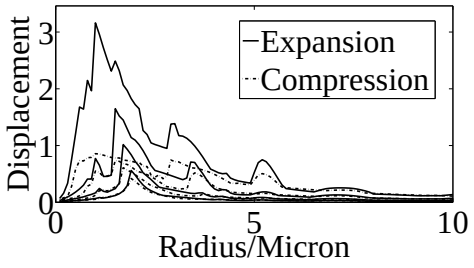

(f) Expansion and compression

Figure 3.6: *continued overleaf*

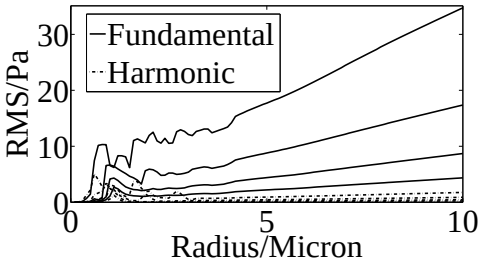

(g) Fundamental and Harmonic

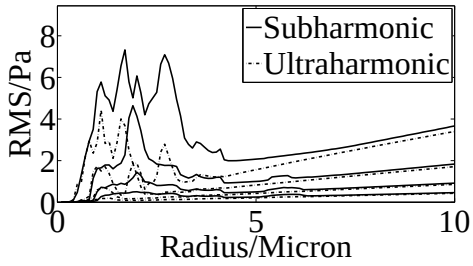

(h) Subharmonic and Ultraharmonic

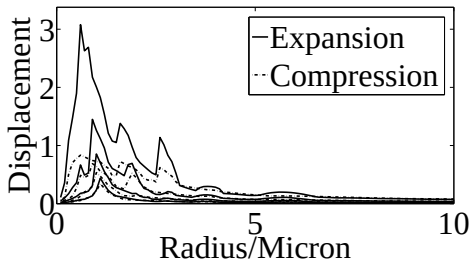

(i) Expansion and compression

Figure 3.6: *The dependence of response of free MBs on equilibrium radius at a driving frequency of 1 MHz(figures 3.6(a)-3.6(c)), 2 MHz(figures 3.6(d)-3.6(f)) and 4 MHz(figures 3.6(g)-3.6(i)) using driving pulses with MIs of 0.025 to 0.2. The peak radial response at a MI of 0.2 is shifted to lower radii as the driving frequency is increased(figures 3.6(c),3.6(f),3.6(i)).*

3.5.3 Shell model

3.5.3.1 Dependence of response on driving frequency

The linear model shows that if the shell stiffness of a MB increases then the resonance frequency also increases (figure 3.2(b)). The response of a 3 μm MB was calculated numerically for driving frequencies from 0.1 MHz to 10 MHz and MIs of 0.025, 0.05, 0.1 and 0.2 for the Skalak model (figures 3.7a-3.7c) and the Mooney-Rivlin model (figures 3.7d-3.7f). The shell parameters in these simulations were 50 MPa and 1 Pas for the stiffness and viscosity respectively. The shell thickness is set at 5 nm. The resonance peak at the lowest MI is at 2 MHz in both of the models (figure 3.7(c) and figure 3.7(f)). This is 1 MHz greater than the resonance frequency of a similar free MB. As the driving amplitude is increased the resonance peaks shifts to higher frequencies for the Skalak model and to lower frequencies for the Mooney-Rivlin model. There is no observable peak in the subharmonic response for the Skalak model. However, there is a peak in the subharmonic response for the Mooney-Rivlin model but only for the highest MI. This peak occurs at twice the resonance frequency 4 MHz. The Mooney-Rivlin model has an expansion dominated response around resonance while the Skalak model has a compression dominated response around resonance.

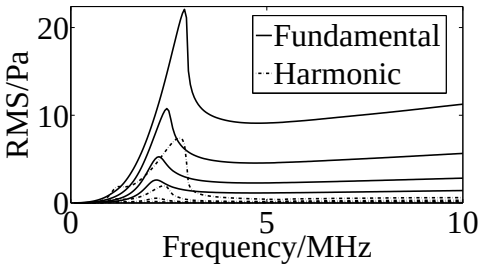

(a) Fundamental and Harmonic

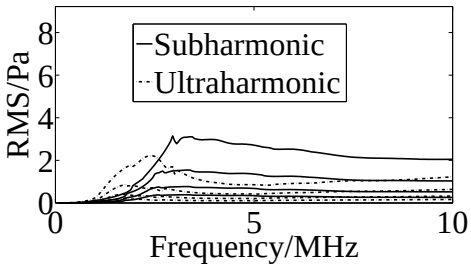

(b) Subharmonic and Ultraharmonic

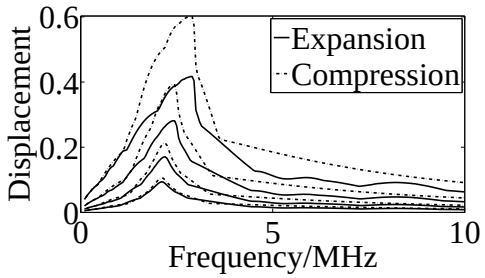

(c) Expansion to Compression Ratio

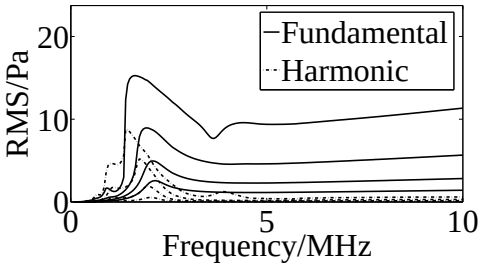

(d) Fundamental and Harmonic

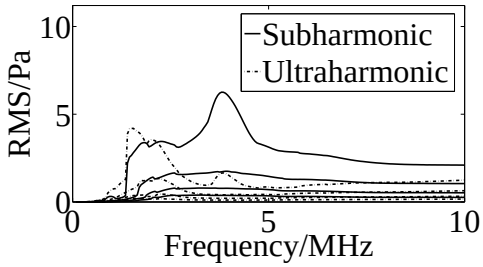

(e) Subharmonic and Ultraharmonic

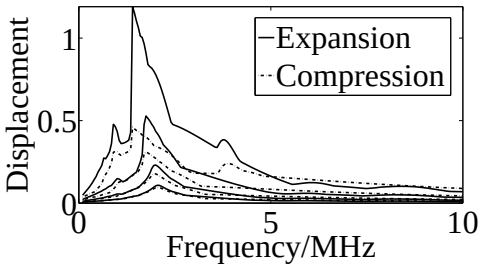

(f) Expansion to Compression Ratio

Figure 3.7: *The response of a $3\mu m$ shelled MB for a range of driving frequencies with MI of 0.025 to 0.2 for the Skalak (figures 3.7(a)-3.7(c)) and for the Mooney-Rivlin models (figures 3.7(d)-3.7(f)). The shell stiffness is 50 MPa and the shell viscosity is 1 Pas. Expansion dominated behaviour is observed for the Mooney-Rivlin model but not for the Skalak model. The subharmonic resonance is larger and more prominent in the Mooney-Rivlin model than in the Skalak model. As the MI increases the resonance peaks shift to lower frequencies in the Mooney-Rivlin model but to higher frequencies in the Skalak model.*

3.5.3.2 Dependence of response on radius at different driving frequencies

The response of MBs with radii ranging from 0.1 μm to 10 μm was calculated numerically for driving frequencies of 1 MHz, 2 MHz and 4 MHz and MIs of 0.025, 0.05, 0.1 and 0.2 for the Mooney-Rivlin model and the Skalak model (figure 3.8, figure 3.9 and figure 3.10). The shell parameters in these simulations were 5 MPa and 0.1 Pas for the stiffness and viscosity respectively. For a driving pulse of 1 MHz the resonance peak at the lowest MI is at 4 μm in both of the models (figure 3.8(c) and figure 3.8(f)). The linear model predicts a resonance at this peak for the MBs (figure 3.2). As the MI is increased the resonance peak shifts to higher radii for the Skalak model and to lower radii for the Mooney-Rivlin model. Both the Mooney-Rivlin model and the Skalak model have a greater maximum expansion than maximum compression at each driving frequency (figure 3.8(c), figure 3.8(f) figure 3.9(c), figure 3.9(f), figure 3.10(c) and figure 3.10(f)). However, the Mooney-Rivlin model has a higher expansion to compression ratio than the Skalak model. This is expected as the Skalak model restricts the expansion more than the compression while the opposite is true for the Mooney-Rivlin model (figure 3.1). The radius at which the peak in the maximum expansion occurs shifts to lower radii as the driving frequency is varied from 1 MHz to 4 MHz. This is expected from the linear model since MBs with lower radii have a higher resonance frequency so that the peak at higher driving frequencies occurs at lower radii (figure 3.2).

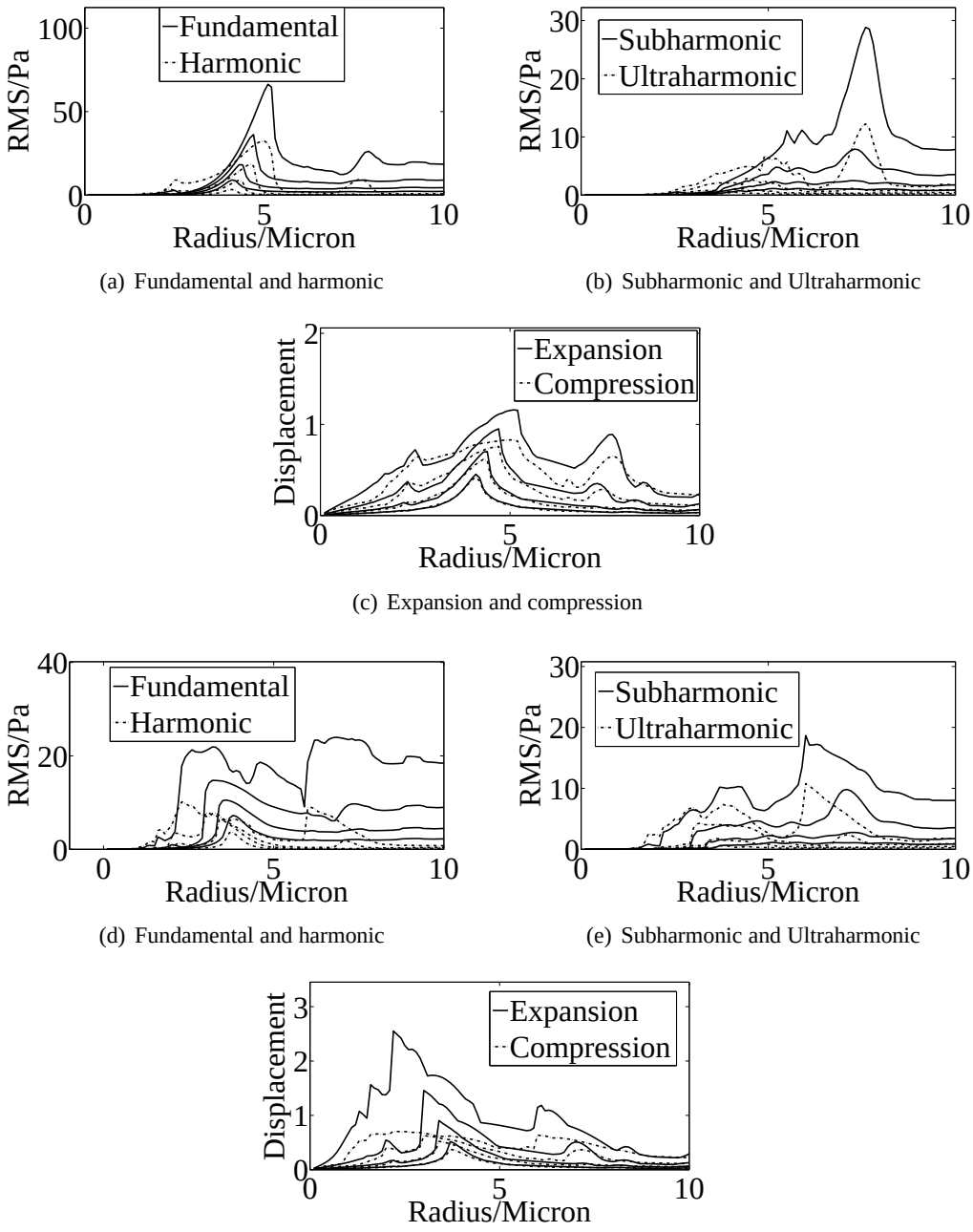

(a) Fundamental and harmonic

(b) Subharmonic and Ultraharmonic

(c) Expansion and compression

(d) Fundamental and harmonic

(e) Subharmonic and Ultraharmonic

(f) Expansion and compression

Figure 3.8: *The dependence of response of Skalak MBs (figures 3.8(a)-3.8(c)) and Mooney-Rivlin MBs (figures 3.8(d)-3.8(f)) on equilibrium radius at a driving frequency of 1 MHz using MIs of 0.025 to 0.2 for MBs with a shell stiffness of 5 MPa and a shell viscosity of 0.1 Pas.*

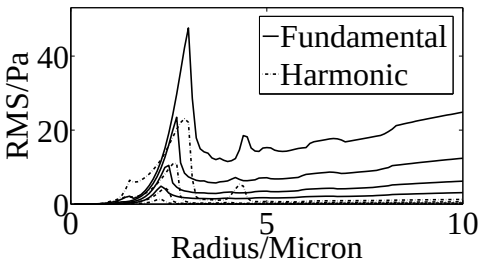

(a) Fundamental and harmonic

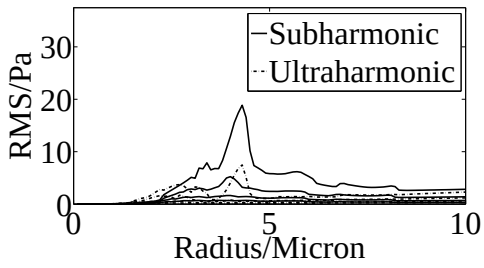

(b) Subharmonic and ultraharmonic

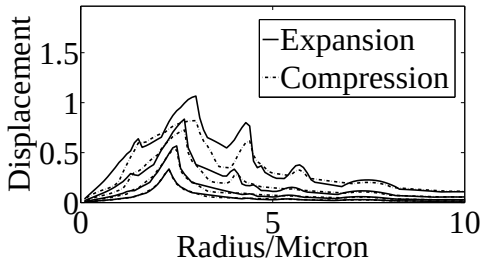

(c) Expansion and compression

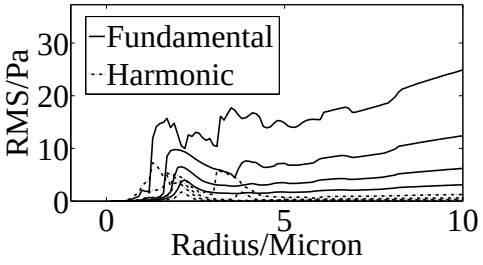

(d) Fundamental and harmonic

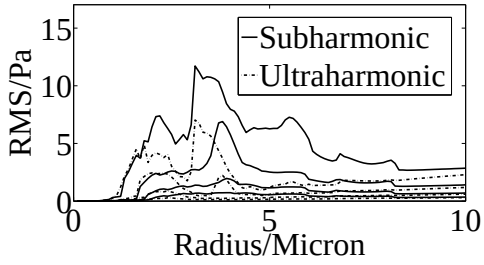

(e) Subharmonic and Ultraharmonic

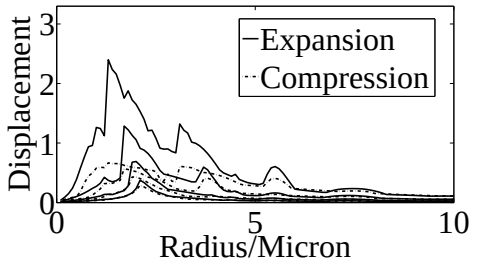

(f) Expansion and compression

Figure 3.9: *The dependence of response of Skalak MBs (figures 3.9(a)-3.9(c)) and Mooney-Rivlin MBs (figures 3.9(d)-3.9(f)) on equilibrium radius at a driving frequency of 2 MHz using MIs of 0.025 to 0.2 for MBs with a shell stiffness of 5 MPa and a shell viscosity of 0.1 Pas. The peak in the expansion and compression is at a lower radii for both the Mooney-Rivlin and Skalak models than at a driving frequency of 1MHz (figure 3.8).*

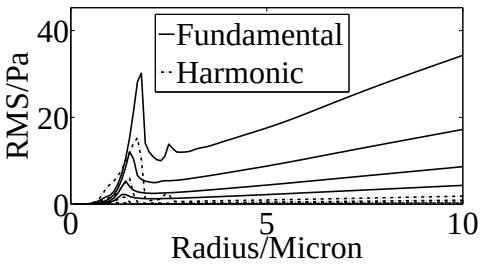

(a) Fundamental and harmonic

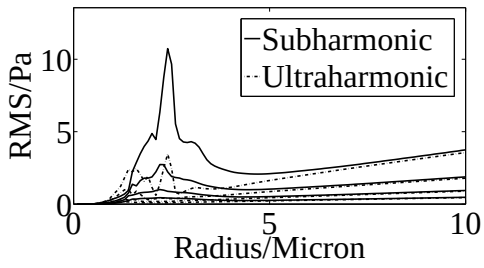

(b) Subharmonic and Ultraharmonic

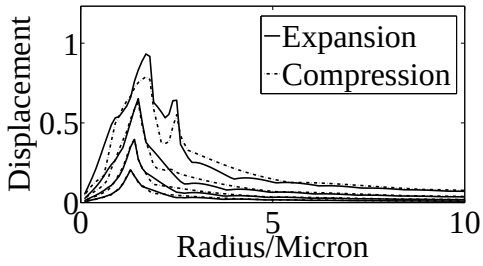

(c) Expansion and compression

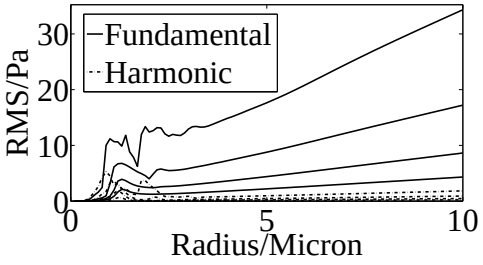

(d) Fundamental and harmonic

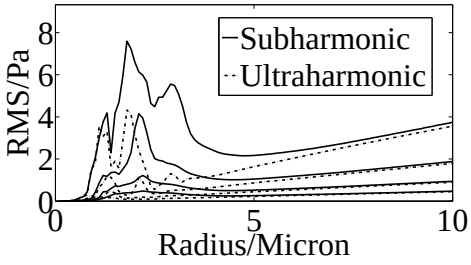

(e) Subharmonic and ultraharmonic

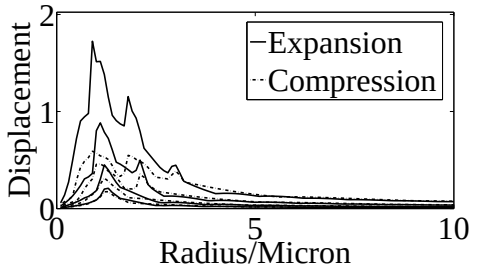

(f) Expansion and compression

Figure 3.10: *The dependence of response of Skalak MBs (figures 3.10(a)-3.10(c)) and Mooney-Rivlin MBs (figures 3.10(d)-3.10(f)) on equilibrium radius at a driving frequency of 4 MHz using MIs of 0.025 to 0.2 for MBs with a shell stiffness of 5 MPa and a shell viscosity of 0.1 Pas. The peak in the expansion and compression is at a lower radii for both the Mooney-Rivlin and Skalak models than at a driving frequency of 2 MHz (figures 3.9).*

3.5.3.3 Dependence of response on radius with different shell stiffnesses

Skalak and Mooney-Rivlin shelled MBs with radii ranging from 0.1 μm to 10 μm and with shell stiffnesses of 5 MPa, 50 MPa and 200 MPa are shown in figure 3.11 and figure 3.12 respectively. The shell viscosity is 1 Pas and the driving frequency is 1 MHz. The maximum relative expansion for MBs with a shell stiffness of 5 MPa is 1.326 for the Skalak model at the highest MI (figure 3.11(c)) and for MBs with a shell stiffness of 200 MPa the maximum expansion compression ratio is 0.549 for the Skalak model at the highest MI (figure 3.11(i)). The maximum relative expansion for MBs with a shell stiffness of 5 MPa is 2.470 for the Mooney-Rivlin model at the highest MI (figure 3.12(c)) and for MBs with a shell stiffness of 200 MPa the maximum expansion compression ratio is 2.465 for the Mooney-Rivlin model at the highest MI (figure 3.12(i)). As the shell stiffness is increased the Skalak MBs have a much greater decrease in the maximum compression expansion ratio compared to the Mooney-Rivlin MBs. This is expected since the shell will restrict the expansion further in the Skalak model (figure 3.1).

At the lowest MI the relative expansion and compression of Skalak MBs with shell stiffness of 5 MPa, 50 MPa and 200 MPa has a maximum at 4.5 μm, 5.5 μm and 7 μm respectively (figure 3.11(c), figure 3.11(f) and figure 3.11(i)). As the MI increases the peak shifts to higher radii for Skalak MBs. For Mooney-Rivlin MBs the relative expansion and compression of MBs with shell stiffness of 5 MPa, 50 MPa and 200 MPa has a maximum at 4.5 μm 5.5 μm and 7 μm respectively (figure 3.12(c), figure 3.12(f) and figure 3.12(i)). As the MI increases the peak shifts to lower radii for Mooney-Rivlin MBs. At the lowest MI both models have peaks at similar locations that are also predicted from the linear model (figure 3.2) but as the amplitude increases the peaks shift to different radii.

The fundamental and harmonic RMS predicted by the Skalak model and Mooney-Rivlin model with shell stiffness of 5 MPa, 50 MPa and 200 MPa have a local maximum at 4.5 μm 5.5 μm and 7 μm respectively similar at the lowest MI (figure 3.11(a), figure 3.11(d), figure 3.11(g), figure 3.12(a), figure 3.12(d) and figure 3.12(g)). At the highest MI the subharmonic local maximum has a value close to 20 Pa at the lowest stiffness of 5MPa and at the highest MI of 0.2 for both the Skalak and Mooney-Rivlin models (figure 3.11(c) and figure 3.12(c)). At a shell stiffness 50 MPa the Skalak model subharmonic resonance is no longer visible (figure 3.11(e)) but the subharmonic resonance of the Mooney-Rivlin model is shifted to higher radii than at a shell stiffness of 5 MPa and has a magnitude of close to 20 Pa (figure 3.12(e)). As predicted

from figure 3.2 the resonances of the MB increase when the shell stiffness is increased in either model. The maximum magnitude of the radial oscillation decreases but the since the scattered pressure at resonance increases because the size of the MB at resonance is increased.

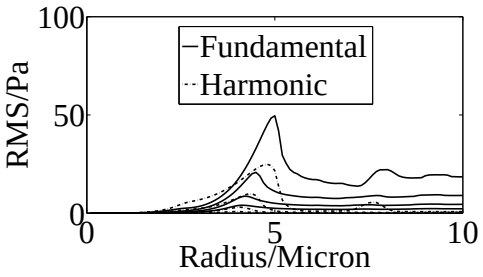

(a) Fundamental and harmonic

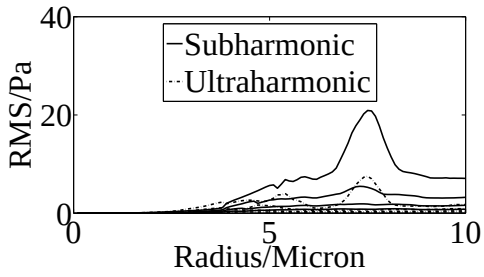

(b) Subharmonic and ultraharmonic

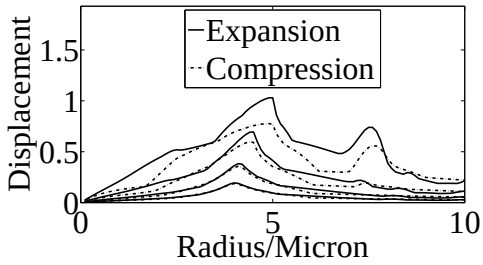

(c) Expansion compression

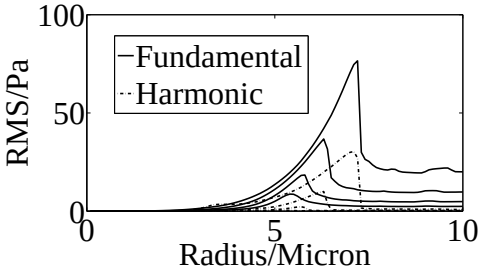

(d) Fundamental and harmonic

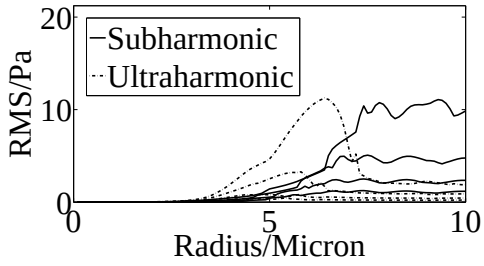

(e) Subharmonic and ultraharmonic

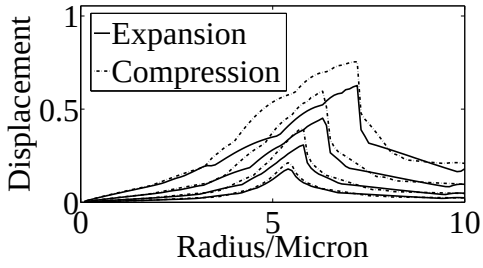

(f) Expansion and compression

Figure 3.11: *continued overleaf*

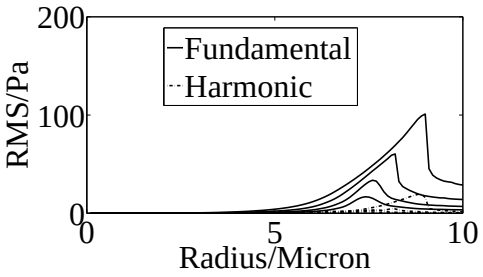

(g) Fundamental and harmonic

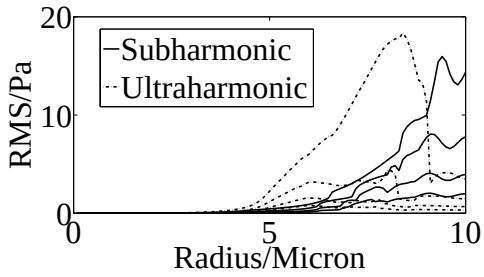

(h) Subharmonic and ultraharmonic

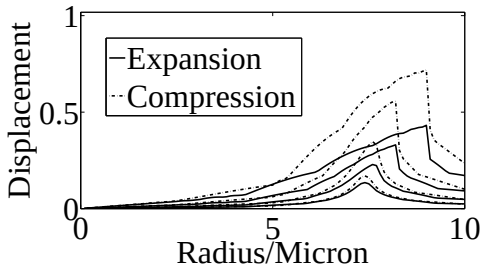

(i) Expansion and compression

Figure 3.11: *The dependence of response of Skalak MBs on equilibrium radius at a driving frequency of 1MHz using MIs of 0.025 to 0.2 for MBs with shell stiffnesses of 5 MPa (figures 3.11(a)-3.11(c)), 50 MPa (figures 3.11(d)-3.11(f)) and 200 MPa (figures 3.11(g)-3.11(i)) and a shell viscosity of 1 Pas. The resonance peaks are shifted to greater radii as the shell stiffness increases.*

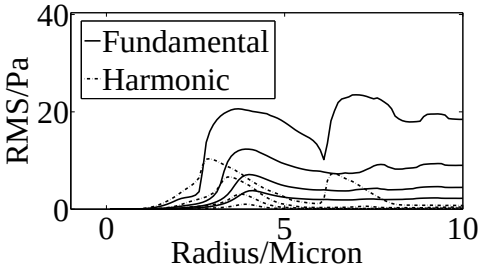

(a) Fundamental and harmonic

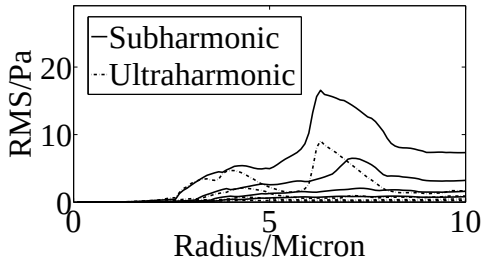

(b) Subharmonic and ultraharmonic

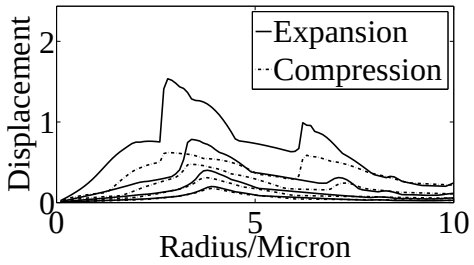

(c) Expansion and compression

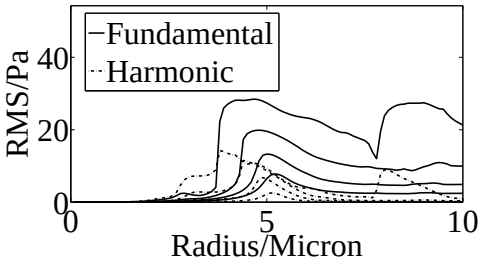

(d) Fundamental and harmonic

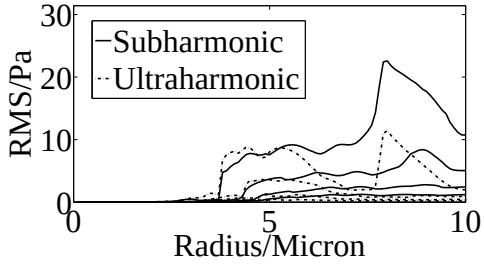

(e) Subharmonic and ultraharmonic

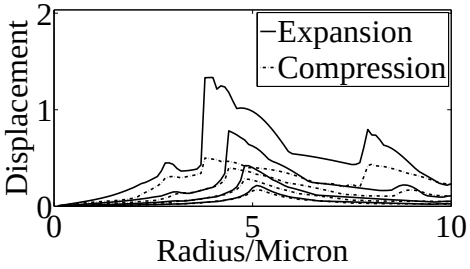

(f) Expansion and compression

Figure 3.12: *continued overleaf*

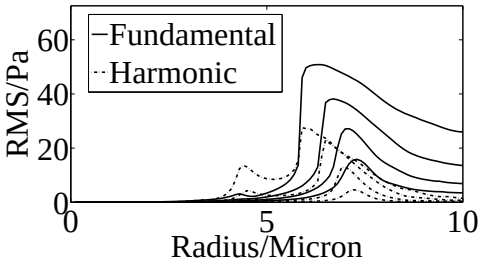

(g) Fundamental and harmonic

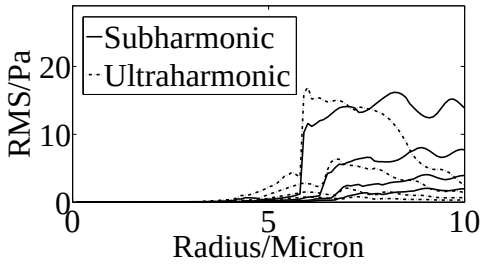

(h) Subharmonic and ultraharmonic

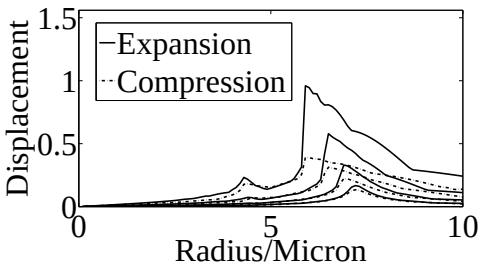

(i) Expansion and compression

Figure 3.12: *The dependence of response of Mooney-Rivlin MBs on equilibrium radius at a driving frequency of 1MHz using MIs of 0.025 to 0.2 for MBs with shell stiffnesses of 5 MPa (figures 3.12(a)-3.12(c)), 50 MPa (figures 3.12(d)-3.12(f)) and 200 MPa (figures 3.12(g)-3.12(i)) and a shell viscosity of 1 Pas. The resonance peaks are shifted to greater radii as the shell stiffness increases.*

3.5.3.4 Dependence of response on radius with different shell viscosities

Skalak and Mooney-Rivlin MBs with radii ranging from 0.1 μm to 10 μm and with shell viscosities of 0.1 Pas, 1 Pas and 10 Pas are shown in figure 3.13 and figure 3.14 respectively. The shell stiffness is 5 MPa and the driving frequency is 1 MHz. At a shell viscosity of 0.1 Pas the Skalak MBs have a fundamental peak at over 60 Pa (figure 3.13(a)), at 1 Pas this is reduced to below 60 Pa (figure 3.13(d)) and at 10 Pas the peak is no longer observable (figure 3.13(g)). At a shell viscosity of 0.1 Pas the Mooney-Rivlin MBs have a fundamental peak at over 20 Pa (figure 3.14(a)), at 1 Pas this is reduced to below 20 Pa (figure 3.14(d)) and at 10 Pas the peak is no longer observable (figure 3.14(g)).

At the highest driving amplitude and for Skalak MBs a subharmonic response of 30 Pa was found for a shell viscosity of 0.1 Pas (figure 3.13(b)). The shell viscosity was increased to 1 Pas and the peak in the subharmonic was reduced to 22 Pa (figure 3.13(e)). At a shell viscosity of 10 Pas no peak in subharmonic was observed (figure 3.13(h)).At the highest driving amplitude and for Mooney-Rivlin MBs a subharmonic response near 20 Pa was found for a shell viscosity of 0.1 Pas (figure 3.14(b)). The shell viscosity was increased to 1 Pas and the peak in the subharmonic was reduced to below 20 Pa (figure 3.14(e)). At a shell viscosity of 10 Pas no peak in subharmonic was observed (figure 3.14(h)). The increase of the shell viscosity also makes the response curves smoother. The effect of increasing the shell viscosity is to reduce the oscillation and hence it reduces the nonlinear oscillations that are the origin of the jagged response curves seen from the Mooney-Rivlin MBs (figures 3.14a,3.14(c)).

For Skalak MBs the maximum relative expansion of 1 for shell viscosities of 0.1 Pas and 1 Pas and was reduced to 0.3 for a shell viscosity of 10 Pas (figure 3.13(c), figure 3.13(f) and figure 3.13(i)). The damping of the MB motion due to the increased shell viscosity decreases the MB oscillation compared to MBs with lower shell viscosity. The maximum relative expansion was 2.5, 1.6 and 0.3 for shell viscosities of 0.1 Pas, 1 Pas and 10 Pas respectively (figure 3.14(c), figure 3.14(f) and figure 3.14(i)). The radius at which these peaks occurred was largely unaffected by the change in viscosity and for a shell viscosity of 10 Pas the two models are identical (figures 3.13(h),3.14(h)).

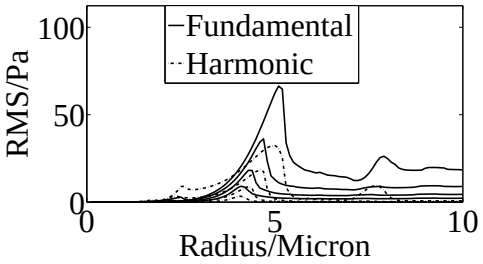

(a) Fundamental and harmonic

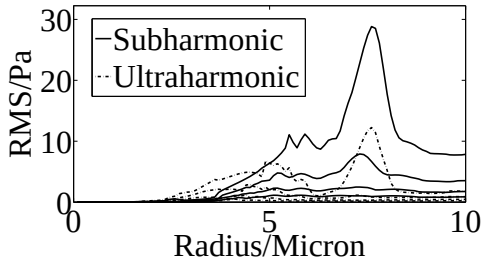

(b) Subharmonic and ultraharmonic

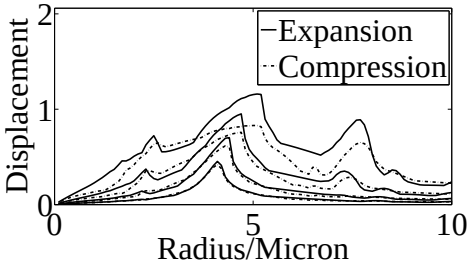

(c) Expansion and compression

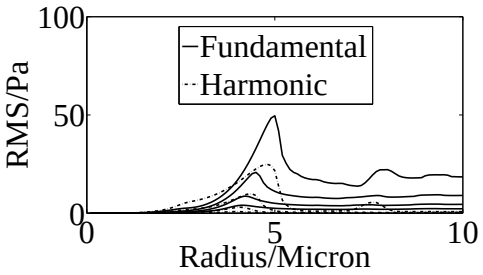

(d) Fundamental and harmonic

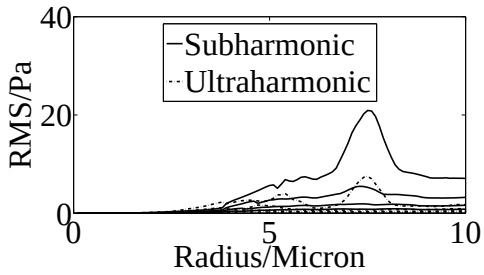

(e) Subharmonic and ultraharmonic

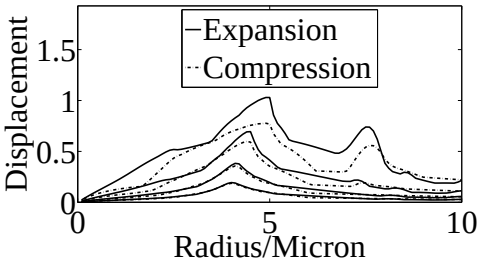

(f) Expansion and compression

Figure 3.13: *continued overleaf*

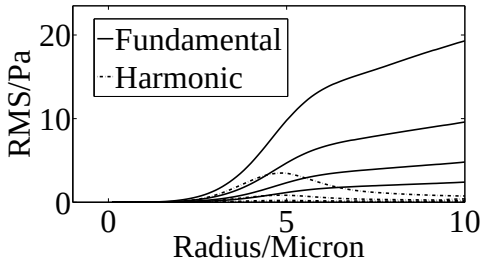

(g) Fundamental and harmonic

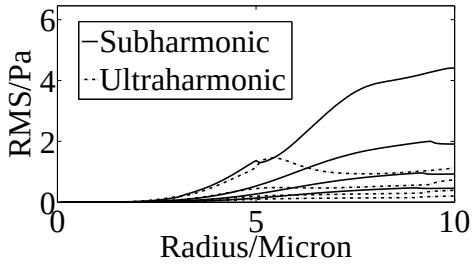

(h) Subharmonic and ultraharmonic

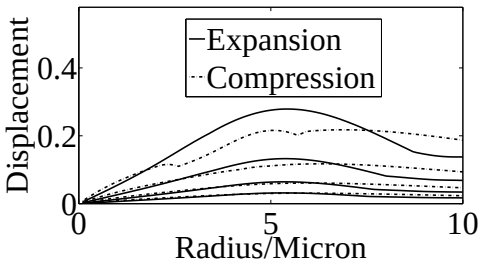

(i) Expansion and compression

Figure 3.13: *The dependence of response from a Skalak MB on MB equilibrium radius at a driving frequency of 1 MHz using MIs of 0.025 to 0.2 for MBs with a shell stiffness of 5 MPa and shell viscosities of 0.1 Pas (figures 3.13(a)-3.13(c)), 1 Pas (figures 3.13(d)-3.13(f)) and 10 Pas (figures 3.13(g)-3.13(i)). The resonance peaks decrease in magnitude as the shell viscosity is increased.*

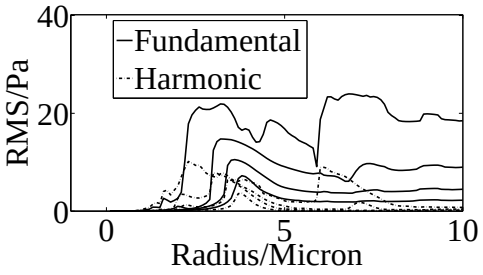

(a) Fundamental and harmonic

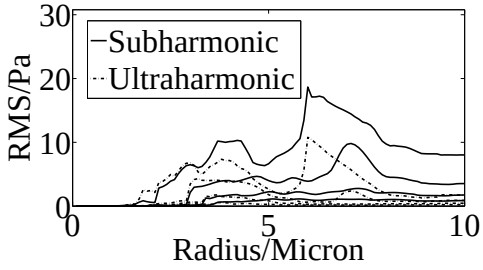

(b) Subharmonic and ultraharmonic

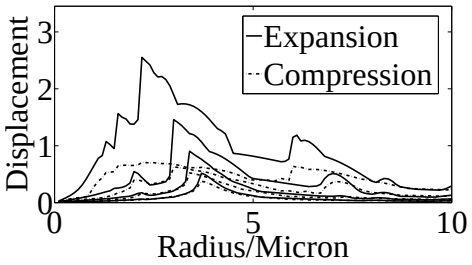

(c) Expansion and compression

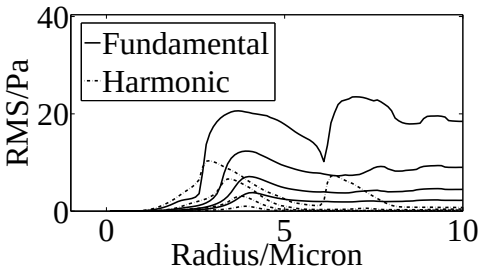

(d) Fundamental and harmonic

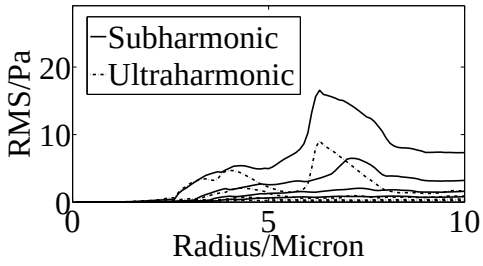

(e) Subharmonic and ultraharmonic

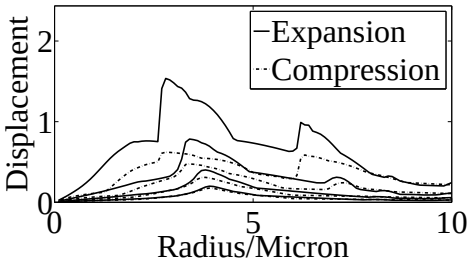

(f) Expansion and compression

Figure 3.14: *continued overleaf*

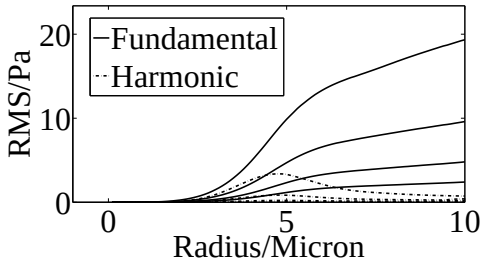

(g) Fundamental and harmonic

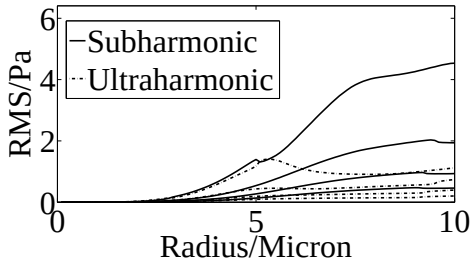

(h) Subharmonic and ultraharmonic

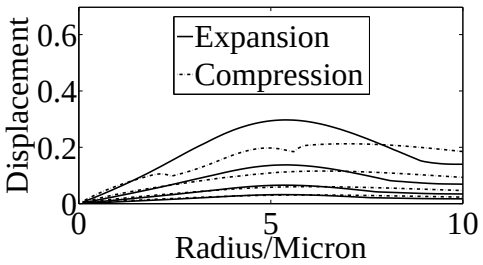

(i) Expansion and compression

Figure 3.14: *The dependence of response of a Mooney-Rivlin MB on equilibrium radius at a driving frequency of 1 MHz using MIs of 0.025 to 0.2 for MBs with a shell stiffness of 5 MPa shell viscosities of 0.1 Pas (figures 3.14(a)-3.14(c)), 1 Pas (figures 3.14(d)-3.14(f)) and 10 Pas (figures 3.14(g)-3.14(i)). The resonance peaks decrease in magnitude as the shell viscosity is increased.*

3.6 Discussion

The development of a theoretical model for an UCA using the spherically symmetric viscoelastic approach requires the parameters of the shell to be established and the choice of a constitutive model for the shell such as the Skalak or Mooney-Rivlin model. Assuming that a constitutive model is correct the parameters of the shell can be found for this model by comparison with either the fundamental, harmonic, subharmonic, ultraharmonic, or radial response. For the theoretical models discussed here the theoretical models have similar responses at low amplitudes but at higher driving amplitudes and with larger shell elasticity the difference in the prediction of the models begin to diverge. These theoretical models have been compared previously in the work by Tsiglifis and Pelekasis[137].

The response of equation (3.1) has been shown to have a strong dependence on the shell parameters, driving amplitude, driving frequency and equilibrium radius. At larger driving amplitudes the response was also seen to depend on the choice of constitutive equation of the shell.

The linear model shows how the response from a MB depends on the equilibrium radius, shell parameters and driving frequency and can predict the resonance frequency of MBs for low driving amplitudes. The steady state response of MBs has a phase shift of π radians across the undamped resonance. Undamped MBs with radii below the resonance radius are in phase with the driving pulse while MBs above the resonance radius are π out of phase. The steady state response of MBs with radii below the resonance radius has an increased phase shift relative to the driving pulse as the shell viscosity is increased. The phase of a damped MB relative to an undamped MB increases as the shell viscosity is increased. The dependence of the phase shift in the response on the radius and shell parameters has been considered in previous work [93;140]. The phase shift close to resonance could be exploited to distinguish between the scatter from MBs to the scatter from tissue. An accurate understanding of the properties of the shell is vital to predicting the expected phase shift of the scattered signal from a MB. Since the phase shift is also related to the resonance frequency the phase has also been proposed as a means to determine the resonance frequency of a MB[140]. In theory the measurement of the phase could allow the shell elasticity to be measured from the undamped resonance that is given by the radius at which there is a $\frac{\pi}{2}$ phase shift. The viscosity could also be established by measuring the phase shift of MBs above and below resonance. In practice however, this is difficult since the accurate measurement of phase is difficult[140] and the linear model is not valid at higher driving amplitudes.

The linear model of the free MB and shelled MB predicts that the resonance of the MBs will shift to lower radii at higher driving frequencies (figure 3.2). The predictions of the resonance peaks from the linear model are close to those found numerically at the lowest MI in the non-linear model. However at the highest MI of 0.2 the resonance peaks are significantly shifted relative to the prediction of the linear model. There is clearly a lower bound on the linear model since the radial response must be positive in order to have physical meaning. A negative radius is not an acceptable solution. As a result the nonlinear model must be used to consider the response at higher MI. At all the MI tested here for the nonlinear model the linear model produces solutions that are not physical.

The subharmonic resonance peak from a MB, if one was found, was generally at a radius whose resonance frequency is half the driving frequency (figure 3.6) or with a driving frequency that is half the resonance frequency (figure 3.5). For the free MB model a peak was found in the subharmonic at a driving frequency close to the same frequency at which the fundamental peak occurs. This is due to the highly nonlinear response of the MB at this frequency that results in a broadband response. The subharmonic response can be used to determine the resonance frequency and hence the shell parameters can be found or if the shell parameters are known the subharmonic prediction can be tested[106]. The linear model predicts that the relative expansion and compression would be equal and does not predict the presence of a subharmonic or ultraharmonic response. As stated previously, increasing the driving amplitude in the linear model produces unphysical results for the MI tested here. As a result the nonlinear model is required at higher MI. Increasing the MI of the driving pulse increases the difference between the expansion and compression, and the amplitude of the subharmonic and ultraharmonic responses (figure 3.8(b) and figure 3.8(c)). The maximum expansion of the Skalak model is less than the maximum expansion of the Mooney-Rivlin model with similar shell parameters in all cases. The stress-strain relationship (figure 3.1) shows that the Skalak model has a stronger stress during the expansion phase than in the compression phase and hence restricts the expansion more than the compression while the Mooney-Rivlin model has a stronger stress during the compression phase than in the expansion and hence restricts the compression more than the expansion.

The radii and frequencies at which the resonance peaks occur are also shifted relative to those predicted by the linear model. The linear model can give a good insight into the response of MBs at low driving amplitudes however the nonlinear equation is required to describe phe-

nomena at higher driving amplitudes such as shifts of resonance, appearance of subharmonics, ultraharmonics. As the driving amplitude is increased the resonance peak in the Skalak model shifts to higher radii while for the Mooney-Rivlin and free model the resonance shifts to lower radii at higher driving amplitude. The magnitude of the subharmonic and ultraharmonic response depends strongly on the incident driving amplitude and a threshold of MI below which the subharmonic and ultraharmonic response is much lower than above was observed (figure 3.7(e)). This threshold effect is expected from theoretical considerations[106]. Figure 3.8(b) and figure 3.8(e) show how the subharmonic response decreases much faster than the fundamental or harmonic response (figure 3.8(a) and figure 3.8(d)) below a MI of 0.1 for both the Skalak model and the Mooney-Rivlin model as has been seen in previous work[106]. This behaviour is dependent on the shell parameters and shell model and could be used to test the validity of a theoretical model in addition to comparing the fundamental or harmonic response of a theoretical model to the experimental response.

Increasing the shell stiffness in both the Skalak models and Mooney-Rivlin models increases the resonance frequency and hence reduces the radius at which the resonance peak occurs. At a shell stiffness of 5 MPa both models are compression dominated at resonance (figure 3.11(c) and figure 3.12(c)). The full width three quarters maximum is over twice the full width three quaters maximum in the Mooney-Rivlin model compared to the Skalak model (figure 3.11(a),figure 3.12(a)). As the shell stiffness increases to 50 MPa the Skalak model has an expansion dominated response at resonance with a driving pulse of MI 0.2 (figure 3.11(f)) while the Mooney-Rivlin model has a compression dominated response at resonance (figure 3.12(f)). Experimental observations of compression dominated behaviour has been reported previously[27]. Figure 3.11 and figure 3.12 show that the choice of shell model and shell parameters can effect the occurrence of compression only behaviour. The subharmonic response also depends on the shell model. At the highest driving amplitude the subharmonic resonance is visible for both models with a shell stiffness of 5 MPa but for only the Mooney-Rivlin model for a shell stiffness of 50 MPa (figure 3.12(e)).

As well as changing the phase response of a MB, the amplitude of oscillation is highly dependent on the shell viscosity while the resonance frequency is not largely affected. As the shell viscosity increases the magnitude of the resonance peaks for the fundamental, harmonic, subharmonic, ultraharmonic, expansion and compression decrease. If the shell viscosity is large enough there will be no resonance peak in the fundamental or harmonic response (figure 3.14)

[64]. Comparison of the phase, acoustic response or radial response can allow for the measurement of the shell viscosity of a MB assuming that a given theoretical model is suitable. The type of viscous behaviour of the shell considered here is standard in the literature. Other theoretical models for the shell viscosity do exist[54] but have not been considered when modelling UCAs.

3.7 Summary

The theoretical predictions of the free, Skalak and Mooney-Rivlin models for a MB have been compared for a range of driving amplitudes, shell parameters, driving frequencies and radii. Features such as resonance subharmonic response and expansion/compression dominated behaviour have been investigated numerically over a range of MI.

The linear model was thoroughly examined. The resonance behaviour was found and could be compared to that found from the nonlinear model and it was shown that the phase response has a high dependence on the shell viscosity and shell stiffness of the MBs.

The choice of model and shell parameters was shown to affect the occurrence of compression dominated behaviour. The shell stiffness and MI were shown to determine the resonance radius and resonance frequency. The shell models also gave different shifts in the resonances at higher MI. The threshold for subharmonic response that has been studied theoretically previously was observed in the numerical results.

Theoretical models like the ones studied here will be compared to experimental responses from the rigid shelled contrast agent biSphere and the lipid shelled contrast agent Definity® (Lantheus Medical Imaging,N Belarica, MA) in subsequent chapters.

Chapter 4
Comparison of theoretical models to the response from a rigid shelled contrast agent

4.1 Introduction

Rigid-shelled Optison^{TM}(Mallinckrodt, Inc., St. Louis, MO and Molecular Biosystems, San Diego, CA) MBs have been observed to decrease in size slowly when insonified with a low amplitude driving pulse[23]. At higher MI the gas from the Optison^{TM} MBs was seen to leak from the shell and form a free MB. The response of the rigid shelled contrast agent BG1135 (Bracco Research, Geneva, Switzerland) has been observed optically, while the oscillation of the shell was not evident[7]. In some cases the gas was observed to leak from the shell and form a free MB. The free MB often moved away from the shell to a few microns from a MB. In both cases, for Optison^{TM} and BG1135 a defect formed in the shell was suggested to be responsible for the leaking of gas.

Gas release was confirmed by optical observations of other rigid shelled MBs[10;95], and was shown to be dependent on the ultrasound driving frequency. The radius distribution of the leaked gas bubbles from Quantison^{TM} and biSphere^{TM} (also known as PB127) was measured for two different frequencies[95]. At the higher frequencies with the same mechanical index (MI) more MBs were observed to release gas from the shell. Acoustical observations have also shown that the attenuation spectra are dependent on the driving frequency. The attenuation spectra of a suspension of Optison^{TM} MBs before and after insonation by a high power pulse were compared by Bouakaz and Shung[9]. After insonifying the MBs with the high power pulse the magnitude of the attenuation decreased dramatically[9]. Filters of various sizes were applied to the suspension and it was shown that the rate of destruction of the filtered distributions was dependent on the applied frequency. It is evident that the driving frequency affects rigid shelled MB behaviour, although the mechanisms are not entirely clear.

A thorough examination of the effect of the MI on biSphere^{TM}(Point Biomedical Corp., San

Carlos, CA, USA) provided the optical observation of an array of responses from the agent [10]. It was seen that when insonating biSphere^{TM} MBs with a low MI driving pulse of 0.3 that there was little to no oscillation from the shelled MBs of any radius[10]. At a MI of 0.6 gas was observed to leak from the shell of a 4 μm MB during the ultrasound cycle. During the later ultrasound cycles the gas was observed to be drawn into the shell during the compression phase of the ultrasound and to be released from the shell during the expansion phase of the ultrasound. The response of two smaller MBs to the same driving pulse showed no gas release. At a high MI of 1.33 the larger MBs were observed to release the gas from the shell at the beginning of the ultrasound pulse while the smaller MBs released the gas from the shell at later times during the insonation or upon a second insonation. From this paper the gas release is shown to be dependent on both MI and size of MBs. It appears that a threshold size for gas release is actually dependent on MI, which suggests that the higher the driving amplitude the likelihood of cracking the shell, which is followed by gas release, is increased. It is also important to note that at low MIs these MBs have a very low oscillation due to the ultrasound, while at high MIs the effects are more violent and the gas may be ejected from the shell. Theoretical models of rigid shelled agents have been developed[25] for low driving ultrasound amplitudes where the shell is not disrupted, while at high MIs it may be difficult to achieve good mathematical agreement with the experiments as the reproducibility of the observed phenomena is low. At intermediate MIs the gas was shown to oscillate in and out of the shell in a reproducible manner. A model of this behaviour is not available in the literature and is the subject of the present communication.

BiSphere^{TM} MBs have a double polymer/Albumin shell encapsulating air. The inner shell of biodegradable polymer provides physical stability while the outer layer acts as a biological interface. Echoes from single biSphere^{TM} MBs have been previously measured[131] using a microacoustic system[117;114]. A model is proposed here to account for the observed leaking of gas out of a MB shell during the expansion phase and the return of the gas into the shell during the compression phase. This will be compared with the available experimental data. Previous theoretical models for rigid shell contrast agents include the shell-free bubble model and a form of shelled bubble model. The RPNNP equation for a free MB has been used to model the scattered pressure from the rigid shelled contrast agent Sonovist$^{®}$ (Bayer Schering Pharma AG, Berlin, Germany)[55]. Shelled models have been used to study the rigid shelled contrast agents Albunex$^{®}$ (Molecular Biosystems Inc (MBI), San Diego, USA and Nycomed Imaging AS, Oslo, Norway)[25], Sonazoid^{TM} (GE Healthcare, Oslo, Norway)[59] and a polymer shelled MB(Nycomed Imaging AS, Oslo, Norway)[60]. These shell models assume that the shell

remains intact and participates in the oscillation. Although, in the light of Bouakaz's findings [10], the shell-free model and shelled models do not accurately model biSphere^{TM} behaviour at intermediate MIs, we include the shell-free model and a shelled model here for comparison.

Echoes from single biSphereTM MBs have been previously measured[131] using a microacoustic system[117;114]. A large number of echoes was recorded for as low as 160 kPa (1.6 MHz, MI=0.13) and responding to the full duration of the transmit field, while partial echoes of cracked bubbles appeared at higher acoustic pressures. This suggested that shell destruction may not be the sole mechanism for gas release and that the defects on the shells of bubbles may provide leaking sites. These results are in agreement with atomic force microscopy data, where biSphere^{TM} topographies revealed shell defects[116]. In addition the shell's Young modulus increased with the decrease of diameter[44;115], which is suggestive of a correlation of the number of defects on the shell surface with the microbubble size. A model is proposed here to account for the observed leaking of the gas out of a MB shell during the expansion phase and the return of the gas into the shell during the compression phase. Experimental data with the duration of the transmit field will be considered for comparison with the model. Using the knowledge from the above discussion we assume that shorter pulses require energy transfer from the ultrasound beam to the bubble shell to induce cracking. Our model will not address the complexities of cracking and thus these data will be excluded from the comparison.

4.2 Methodology

The methodology of the experimental procedure that was used for the capture of the single biSphere^{TM} echoes is detailed by Thomas et al.[131] (D). Here this is briefly explained in order to elaborate on the simulation of the experimental conditions, that enable an accurate comparison between theory and experiment. The experimental setup used a focused flow to spatially isolate single MBs and enable the measurement of their acoustic response[117;114]. MBs were injected into the centre of a laminar flow using a micropipette. The flow was directed toward an ultrasound transducer, thus enabling MB alignment with the centre of the ultrasound beam. Using suitable dilutions the response from single MBs, separated several cm from each other, at a distance of around 7.5 cm from the transducer was measured. The system was calibrated with a membrane hydrophone on transmit Precision Acoustics Ltd., Dorchester, UK) and using linear scatterers as previously described[114] on receive. The absolute values (Pa) of the fundamental and harmonic components from single MBs could then be calculated.

R	bubble radius
$\dot{R}$	bubble wall velocity
$\ddot{R}$	bubble wall acceleration
R_0	equilibrium radius
c	velocity of sound in the fluid
P_∞	hydrostatic pressure
σ	surface tension
η_L	viscosity of water
γ	ratio of specific heats
G_S	shell stiffness
eta_S	shell viscosity
d_{Se}	shell thickness

Table 4.1: *Table of parameters used in the theoretical models.*

4.2.1 Theory

The model of a bubble, as found most often in the literature, consists of a spherically symmetric gas in an infinite fluid. For a shelled MB the gas is surrounded by a viscoelastic shell and it is assumed to maintain its spherical shape throughout the oscillation. From the radius time curve the scattered pressure at a distance r from the MB can be found using Bernoulli's equation (equation 3.14)[142]. The scattered pressure at a distance of 7.5 cm from the transducer was calculated here for all simulations. This pressure waveform was then filtered using an elliptic filter with 0.8 MHz bandwidth to find the fundamental and second harmonic response for a given radius. This was repeated over the radii of the MB distribution as measured by a particle sizer (Malvern Mastersizer, Malvern Instruments, Worcs.,UK). A size-weighted distribution for the fundamental RMS(root mean squared) pressure and second harmonic RMS pressure was generated, and was subsequently used for statistical comparison with the experimental data.

As mentioned in the introduction although optical observations have demonstrated that rigid MBs scatter by a means of gas leak, to date there is no theoretical model that can simulate this behaviour. The basic mathematical formalism for a MB oscillation in the presence of an ultrasound field as developed by Keller and Miksis[63] is adopted here, and three theoretical models that specifically address the contribution of the shell were considered for comparison;
A. the shell-free model (i.e. no shell). This model has been previously proposed as a good approximation for the gas escape from rigid shelled MBs and subsequent oscillation in the presence of an ultrasound field[55].

B. The fixed elasticity shell model. This model was used for two reasons: a. the biSphere^{TM} MBs are coated in a shell and at low MI the shell may remain intact and perform small oscillations[10] and b. it may be useful as a comparison with the other models and
C. The newly proposed model that allows gas-leaking (GL) and subsequent movement in and out of a rigid shell as observed by Bouakaz et al.[10] at intermediate MI. The parameters used in the theoretical models are shown in table 4.1.

4.2.1.1 Shell-free model

As described in chapter (3), the shell-free bubble model uses the Keller-Miksis equation[63],

$$-\left(\frac{3}{2}-\frac{\dot{R}}{2c}\right)\dot{R}^2+\left(1+\frac{\dot{R}}{c}\right)\left(\frac{P}{\rho}\right)+R\left(\frac{\dot{P}}{\rho c}\right)=\left(R\left(1-\frac{\dot{R}}{c}\right)+\right)\ddot{R}. \tag{4.1}$$

R, c, $\dot{R}$, P and $\ddot{R}$ are the radius, velocity of sound in the fluid, velocity of bubble radius, pressure on bubble wall and bubble wall acceleration. Where P is the pressure of the liquid on the gas

$$P=\left(P_\infty+\frac{2\sigma}{R_0}+P_{Sh}(R_0)\right)\left(\frac{R_0}{R}\right)^{3\gamma}-\frac{2\sigma}{R(t)}-P_{Sh}(R)-P_{ex}, \tag{4.2}$$

where P_∞, σ, R_0, P_{Sh}, P_{ex} and γ is the hydrostatic pressure, surface tension, equilibrium radius, pressure due to shell, driving pressure and ratio of specific heats of the gas respectively. The expansion of the gas was assumed adiabatic so γ is set to 1.4. An isothermal expansion was also tested, γ is equal to 1, but little difference was found. In the free model the shell term P_{Sh} is zero.

4.2.1.2 Fixed elasticity Shell model

In addition to the above Keller-Miksis equation (equation 3.1) here the Church-Hoff model is assumed and the pressure due to the shell P_{Sh} is given by[60]

$$P_{Sh}(R)=12\frac{d_{Se}}{R_0}\left(\frac{1}{8}G_S(1-e^{-8\frac{R-R_0}{R_0}})+\eta_S e^{-4\left(\frac{R-R_0}{R_0}\right)}\frac{\dot{R}}{R_0}\right). \tag{4.3}$$

Although the shell thickness for biSphere^{TM} is proportional to the equilibrium radius[44], the actual contribution to the shell oscillation as observed by optical experiments is difficult to calculate. In addition the optical data show little or no shell movement in the presence of

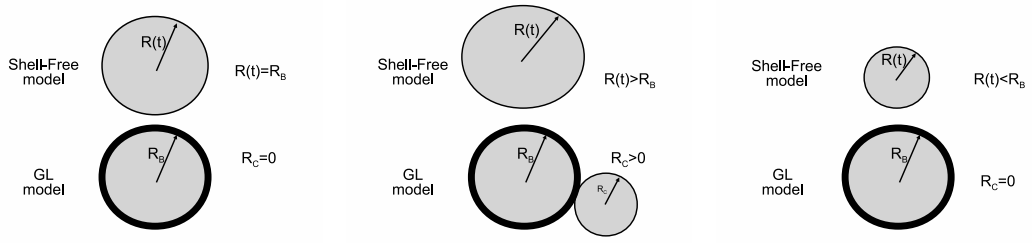

(a) Equilibrium (b) Expansion phase (c) Compression phase

Figure 4.1: *The shell-free model is used to determine the radius R_c of the leaked MB in the GL model. At equilibrium the radius of the leaked MB is zero. During the expansion phase of the shell-free MB the gas in the GL model gas leaks from the shell to form a new MB whose radius R_c is found from equation 4.6. During the compression phase of the shell-free MB the radius of the leaked MB is zero.*

an ultrasound field, which conceptually rules out the validity of this model. We use standard values for these parameters to enable the comparison with the other models. Parameter values are available in the literature for rigid shelled MBs. The shell stiffness, shell viscosity and shell thickness for Albunex® has been calculated as 120 MPa, 2.2 Pas 15 nm respectively[25], for Sonazoid^{TM} 50 MPa, 0.8 Pas 4 nm respectively[59]. A polymer shelled MB (Nycomed Imaging AS, Oslo, Norway) was found to have a shell stiffness and a shell viscosity of 11.5 MPa and 0.4 Pas respectively,with thickness proportional to the MB size[60]. The values of the stiffness G_S, viscosity η_S and thickness d_{Se} used here, similar to those found in the literature, were 50 MPa, 1 Pas and 15 nm respectively.

4.2.1.3 Gas-leaking (GL) model

Neither the shell-free or shell model account for the optically observed leaking of gas in and out of a MB[95]. To simulate the leaking of gas from a shell we propose a new model, the gas-leaking model or (GL model). The volume of gas emitted from the shell is approximated by that given by the shell-free MB model. It is assumed that the gas emitted outside the equilibrium radius forms a separate MB. The scattered pressure is then found from the radial motion of the emitted MB. The model assumes that the gas of the MB will consist of two portions, one portion that is surrounded by the shell and another portion that is outside the shell[10]. Gas can move between the two portions. The amount of gas outside the equilibrium radius in the shell free model is assumed to be equal to the amount of gas outside the shell in the GL model. In the case of the

GL model the gas does not expand radially outward from the centre of the MB as in the shell free model but forms another MB at a defect in the shell. Using the shell-free model to find the movement in gas over the time of the driving pulse the size of the formed MB in the GL model is found. The radiated pressure can then be found from the radius.

It is assumed that the rigid shell will have insignificant movement during ultrasound exposure. When the radius $R(t)$ calculated from the Keller-Miksis equation is greater than the equilibrium radius R_0 the volume of gas outside the MB, V_{ex}, is

$$V_{ex} = \frac{4\pi}{3}(R(t)^3 - R_0^3). \tag{4.4}$$

A schematic representation of the GL model and the shell-free model is shown in figure 4.1. If this volume of gas was to form a separate MB the volume of the new MB would decrease due to the increase of the surface tension. The expansion is isothermal since the temperature of the leaked volume of gas is assumed to be at the same temperature as the shell-free MB throughout the oscillation. The leaked MB is assumed spherically symmetric with radius R_c. Assuming the new MB is in equilibrium with the hydrostatic pressure then from the ideal gas law

$$\left(P_\infty + \frac{2\sigma}{R_c}\right)\left(\frac{4\pi R_c^3}{3}\right) = P_I V_{ex}, \tag{4.5}$$

where P_I is the internal pressure in the shell-free MB. The radius, $R_c(t)$ of the emitted MB is the solution to the polynomial

$$P_\infty R_c^3 + 2\sigma R_c^2 - \frac{3}{4\pi} P_I V_{ex} = 0. \tag{4.6}$$

When the radius $R(t)$ is less than or equal to the equilibrium radius R_0 the volume of gas outside the MB is zero. From this we can find the radial oscillation of the emitted MB and hence the scattered wave from the emitted MB.

4.2.2 Comparison of theory with experiment

Using the same driving pulses used in the experiments the scattered pressure predicted from the equations of motion of the models were compared with the experimental data for the radii in the radius distribution of biSphere (figure 4.2). A typical driving pulse used in the experiment and theory is shown in figure 4.3.

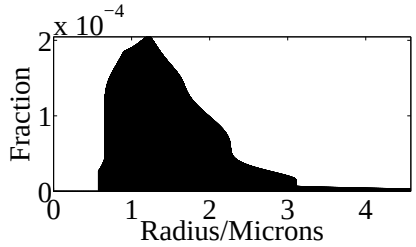

Figure 4.2: *The radial distribution of biSphere^{TM} MBs. A radius cutoff of 2 μm was used in the comparison with the experimental results.*

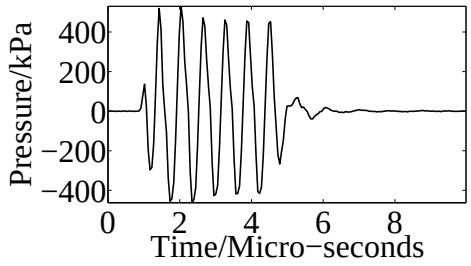

Figure 4.3: *A typical six cycle driving pulse used to insonate the MBs. The peak negative of this pulse is 500 kPa. The driving frequency is 1.6 MHz*

The response from a MB is short if its duration is less than that of the driving pulse. The leaking of gas has been observed to occur after the beginning of the driving pulse. It has been suggested that shorter acoustic responses could be due to shell disruption and leaking of the gas during the insonation[10;131]. Since the theoretical models do not account for this phenomenon only full length experimental responses were used in the comparison with the theoretical models.

4.2.3 Statistical analysis

The statistical analysis of the data was programmed in order to compare populations of theoretical and experimental MB echoes without assuming a specific distribution behaviour for these populations. From a theoretical standpoint the only known variable is the radius of the MB. Since the radius of the MBs that produce the echo is unknown and has a distribution of values the comparison of experimental and theoretical responses of MBs with a given radius is not possible. Instead comparisons of distributions of MBs can be made using the Komolgorov-Smirnov (KS) statistic. This method of comparison of theoretical models to experimental measurements on MBs has not been performed previously.

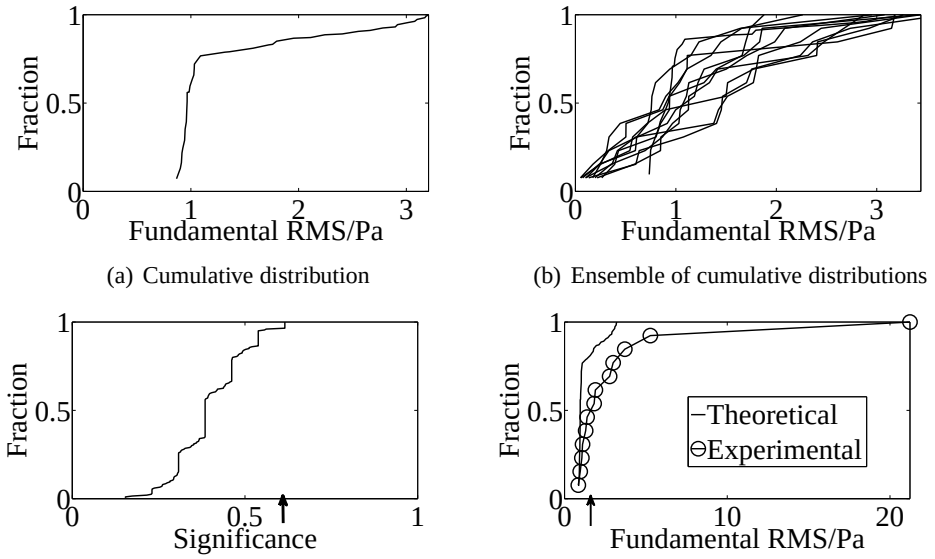

(a) Cumulative distribution

(b) Ensemble of cumulative distributions

(c) The significance curve.

(d) Numerical and Experimental cumulative distributions

Figure 4.4: *Cumulative distributions of the GL model fundamental RMS at a driving frequency of 1.5 MHz with peak negative pressure of 550 kPa. An error was added to each numerical value of RMS in figure 4.4(a) and a new cumulative distribution was found. Ten such curves are shown in figure 4.4(b). This was repeated two hundred times and the maximum difference in the new cumulative distributions was found. This produced the significance curve shown in figure 4.4(c). The arrow in figure 4.4(c) indicates the value of significance below which 95% of theoretical simulations lie. In this case the significance (maximum difference between the experimental and theoretical cumulative distributions found at the arrow in figure 4.4(d) is less than 0.6 and the theory and experimental fundamental distributions are not significantly different.*

The probability that a MB in the distribution has radius R_i is P_i (figure 4.2). The initial probability distribution is normalized i.e. the sum of the probabilities is one. For each radius there corresponds a fundamental RMS or harmonic RMS since the response depends on the equilibrium radius. Hence there is for each fundamental RMS $RMS_f(R_i)$ and harmonic RMS $RMS_h(R_i)$ a probability $P_i(RMS_i)$.

The fundamental and harmonic distributions that are predicted by the theoretical models were compared with the experimental data using the one dimensional Komolgorov-Smirnov (KS) statistic for both the RMS of the fundamental and the RMS of the harmonic[15]. As an example the KS statistical comparison is explained for the fundamental response of the GL model at a driving frequency of 1.5 MHz. The cumulative distribution is calculated by ordering the fundamental response with ascending magnitudes of fundamental RMS. From the optical data, for MI similar to those used here, a threshold radius of two microns was observed above which gas was released from the MBs[10]. This may be used as a cutoff value for MB response from theoretical models. Also, in the experimental data used here for comparison with the theory, there is a noise threshold below which no observations are possible. In practice, the minimum echoes from the MBs observed experimentally is an easier threshold to implement for comparison with theory, as the echoes with larger amplitude than this encompasses all the available experimental data. Thus the minimum MB fundamental RMS pressure was used as another cutoff value for theory. The probability distribution P_i below the cutoffs was not taken into account and renormalised by dividing it by the sum of all probabilities $\sum P_i$ in order for the probability distribution to sum up to one. The cumulative probability at a value of fundamental RMS RMS_i is defined as the integral of all the probabilities $P(RMS_i)$ corresponding to a fundamental less than or equal to RMS_i and above the cutoff.

$$P_{cu}(RMS_i) = \int_{cutoff}^{RMS_i} P(RMS_f) dRMS_f, \tag{4.7}$$

where $P(RMS_f)$ is the probability of a response with fundamental RMS RMS_f (figure 4.4(a)). The same statistical analysis was applied for the harmonic RMS cumulative probability.

The experimental cumulative distribution is defined as a step function increasing by $1/N$, where N is the number of MBs detected experimentally, at each detected value of fundamental (or harmonic). The maximum difference D between the theoretical and experimental cumulative distributions shown in figure 4.4(d) was found. The experimental and theoretical fundamental distributions are said not to be statistically different provided that this number is less than the

significance. The significance was calculated using a Monte Carlo approach as follows.

The experimental error, ϵ_{err}, was set at 18% of each value of fundamental (or harmonic) RMS as found previously[114]. From the original distribution P_i a new distribution was found by first adding an error to each entry. For each value RMS_i an error ϵ_{RMS_i}, within the sum of the experimental error ϵ_{err} and the minimum experimentally detected fundamental RMS_{min}, was found randomly and added

$$|\epsilon_{RMS_i}| \leq |\epsilon_{err} + RMS_{min}| \,. \tag{4.8}$$

This produced a new distribution P_i'. The cutoff was also varied randomly by adding an error less than or equal to 20% of RMS_{min}. The distribution P_i' was deleted below the cutoff and was renormalised by dividing it by the sum of all probabilities $\sum P_i'$. A large, greater than 1000000, population of MBs was created from the distribution P_i' such that the population had the same fraction of MBs with a given fundamental as in the distribution P_i'. From this population a sample of weighted random MBs with RMS pressure $RMS_j' \,|_{j=1}^{j=N}$ was chosen so that the number of MBs in the sample was equal to the number of MBs measured experimentally N. The new cumulative distribution P_{cu}' is defined as a step function increasing by $1/N$ at each value of fundamental RMS_j'. This process was repeated two hundreds times, to produce an ensemble of numerical cumulative distributions (figure 4.4(b)). The number of iterations was optimal to create a smooth significance curve at low runtimes. The maximum difference in cumulative probability, the significance, between each distribution was found.

$$Sig = \max_j \left(\left| P_{cu}(RMS) - P_{cu}'(RMS_j) \right| \right) . \tag{4.9}$$

This is repeated over the ensemble of numerical cumulative distributions. The significance curve is obtained by plotting the significance D against a step function that increases by 1/(200), i.e the number of iterations, at each value of significance (figure 4.4(c)).

From the significance curve (figure 4.4(c)) we can see that if this theoretical model is correct then in 95% of cases (95% of the numerical ensembles) the difference between the significance of the experimental and the numerical cumulative distributions will be less than 0.475 (figure 4.4(d)). This method of comparison was used for each driving pulse, theoretical model and for the fundamental and harmonic distribution. Two identical MBs distributions with identical responses for each radius will have fundamental and harmonic cumulative distributions that are identical. However, if the fundamental and harmonic cumulative distributions and the radius

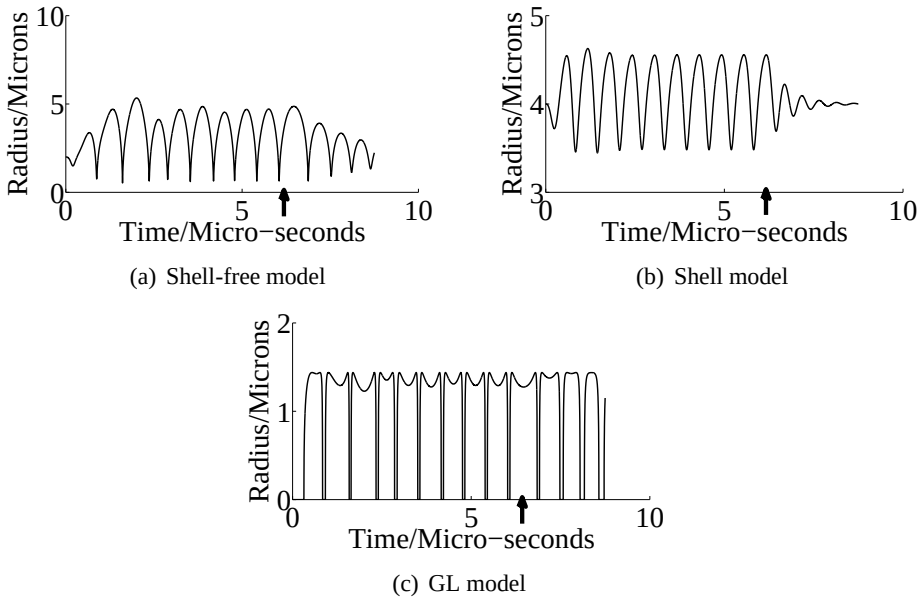

(a) Shell-free model

(b) Shell model

(c) GL model

Figure 4.5: *The radial response of a resonant MB using the shell-free, GL and shell model. A ten cycle driving pulse with driving frequency 1.6 MHz and peak negative pressure of 160 kPa was used. The end of the driving pulse is indicated by the arrow in each figure.*

distribution of the MBs are identical it does not imply that the MBs responses for each radius will be identical. To supplement the statistical comparison plots of the fundamental against harmonic response are used to compare the experimental and theoretical responses in this chapter and also in later chapters.

4.3 Results

The radial response of a resonant MB is shown in figures 4.5-4.6 at 1.6 MHz driving frequency and peak negative pressures 160 kPa and 550 kPa respectively. The 2 μm resonant shell-free MB at 550 kPa shows a distinct broadband non-linear behaviour, which provides rebounding events after the end of the transmitted pulse as evidence of cavitation. This behaviour is not observed in the 4 μm resonant shelled bubble, owing to the damping and elasticity of the shell. The shell-free model predicts radial excursions of over three times the equilibrium radius while the shell model radial excursion is less than twice the equilibrium radius. These effects are less pronounced at lower pressures where highly nonlinear events are not observed. The GL model predicts the expansion of gas during the expansion phase but during the compression phase the

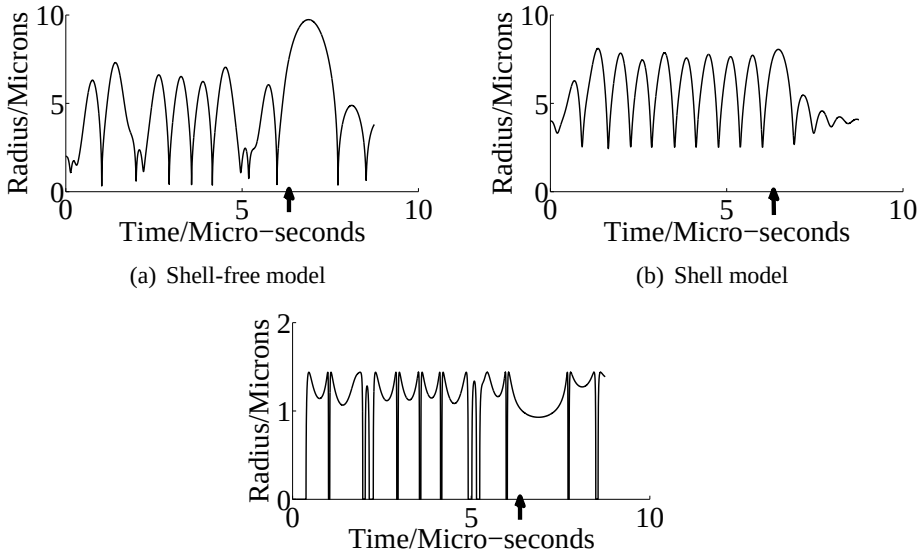

(a) Shell-free model

(b) Shell model

(c) GL model

Figure 4.6: *The radial response of a resonant MB using the shell-free, shell and GL model. A ten cycle driving pulse with driving frequency 1.6 MHz and peak negative pressure of 550 kPa was used. The end of the driving pulse is indicated by the arrow in each figure.*

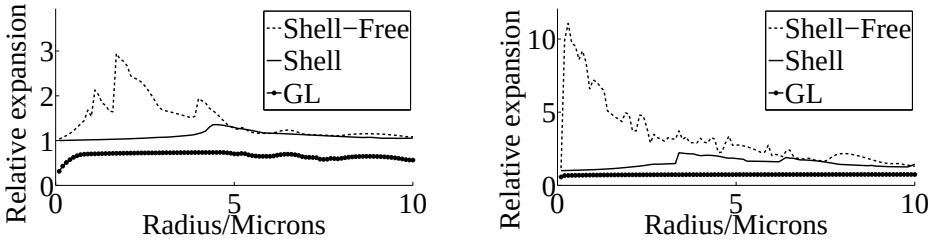

(a) 160kPa

(b) 550kPa

Figure 4.7: *The radial expansion for both the shell-free model and the GL model at a driving frequency of 1.6 MHz using a 10 cycle pulse. The expansion is reduced in the GL model and the resonance is diminished at this driving amplitude. At 160 kPa the response the shell-free model has a resonance at 2.5 μm and the shell model has a resonance just below 5 μm. At 550 kPa the shell model resonance is shifted to lower radii. At this driving amplitude the shell-free model predicts a radial expansion of up to 10 times the initial radius.*

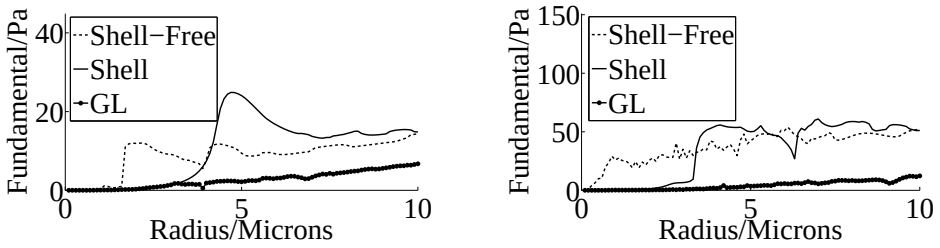

(a) 160kPa (b) 550kPa

Figure 4.8: *The fundamental RMS for both the shell-free model the GL model and the shell model at a driving frequency of 1.6 MHz using a 10 cycle pulse. The fundamental RMS is reduced in the GL model and the resonance is diminished at this driving amplitude. At 160 kPa the response the shell-free model has a resonance at 2.5 μm and the shell model has a resonance just below 5 μm. At 550 kPa the resonance of the shell-free model is not apparent due to the increased non-linear response.*

radius of the leaked MB is zero. It also does not show a distinct resonant behaviour and at both sizes and acoustic pressures it distinctly lies at lower amplitudes compared to the other two models.

The dependence of relative expansion and the fundamental root mean square (RMS) of the scattered pressure against radius for each model are shown in figure 4.7 and figure 4.8 respectively. The relative expansion is defined as the maximum radial expansion of the MB during the oscillation divided by the equilibrium radius of the MB. The shell-free model has a larger expansion than the other two models at almost all radii and both acoustic pressures. The lack of smoothness in the curve at 550 kPa is attributed to the high non-linearity of the MB response as explained above. Upon conversion of this radial movement to a pressure wave (i.e. equation 3.14), the shelled MB provides the largest fundamental response at around the resonant MB sizes compared to the other two models owing to the elastic property of the shell. The curves are also smoother in agreement with figure 4.6. The fundamental response of the free model is greater than the shell model fundamental response for MBs with radii below 4 μm at 1.21 MHz and for MBs with radii below 3 μm at 2 MHz. Since the radii in the biSphere^{TM} radius distribution are less than 4 μm one would expect that the scattered fundamental from the shell-free model will be greater than that predicted by the GL and shelled models for the driving pulses tested here. At radii above 1 μm the GL model predicts that the relative expansion is almost constant (figure 4.5). Hence the maximum radius of the emitted MB for MBs with equilibrium radii above 1 μm is proportional to the radius of the mother nucleus.

	Shell-free		Shell		Gas-Leaking	
Freq/MHz	Fun	Har	Fun	Har	Fun	Har
1.2	S	S	0.30	0.43	0.55	0.43
1.3	S	S	0.17	S	0.39	0.40
1.4	S	S	S	0.29	S	S
1.5	S	S	0.22	0.25	0.52	S
1.6	S	S	0.35	S	0.53	0.30
1.8	S	S	0.30	S	S	S
2.0	S	S	S	S	0.46	0.39
2.1	S	S	0.22	S	0.37	0.31
2.5	S	S	S	S	0.19	0.12
3.7	S	S	S	S	0.09	S
5.2	S	NA	S	NA	0.17	NA

Table 4.2: *The significance value is the maximum difference between the theoretical and numerical distributions (section 4.2.3). If this value is greater than that found in 95% of cases there is a statistically significant difference "'S"' between the theory and experiment. Fun denotes fundamental and Har denotes harmonic. "'NA"' denotes "'Not Applicable"' At a driving frequency of 5.2 MHz the bandwidth of the transducer does not allow the harmonic to be measured so no comparison was made at this frequency. The driving pulses have a peak negative pressure of 550 kPa.*

The resonance behaviour has been examined by using ten cycle sinusoidal pulses. The experimental responses from single MBs were measured using six cycle pulses. These pulses were not sinusoidal but had a range of frequency components. Overall 407 experimentally captured MB were used to compare to the theoretical models.

4.3.1 Variable frequency

Using the transmit 6-cycle pulses that were used for the experiments with a peak negative of 550 kPa and with frequencies ranging from 1.21 MHz to 5.2 MHz (corresponding to MIs of 0.48 to 0.32), the scattered pressure of MBs was computed for the free bubble model, the GL model and the shelled model. As explained in the methodology the radius distribution of the MBs used in the simulations was taken to be the experimentally measured radius distribution of the biSphere^{TM} MBs. Weighted random samples of MBs, found as described in section 4.2.3, from each of the models are plotted with the experimental data in figure 4.13 for 1.6 MHz. The GL-model is in statistical agreement with the experimental data, unlike the other two that overestimate the scatter pressure in both fundamental and harmonic components. The statistical comparison of the theoretical and the experimental results using the KS statistic are summarised

	Shell-free		Shell		Gas-Leaking	
Freq/MHz	Fun	Har	Fun	Har	Fun	Har
1.2	S	S	0.40	0.29	0.55	0.43
1.3	S	S	S	S	0.35	0.60
1.4	S	S	S	S	S	S
1.5	S	S	S	S	0.50	0.39
1.6	S	S	S	S	0.60	0.27
1.8	S	S	S	S	S	0.24
2.0	S	S	S	S	0.48	S
2.1	S	S	S	S	0.37	0.25
2.5	S	S	S	S	S	S
3.7	S	S	S	S	S	S
5.2	S	NA	S	NA	S	NA

Table 4.3: *The significance value is the maximum difference between the theoretical and numerical distributions (section 4.2.3). In this case the radial cutoff was used. If this value is greater than that found in 95% of cases there is a statistically significant difference "'S"' between the theory and experiment. The driving pulses have a peak negative pressure of 550 kPa.*

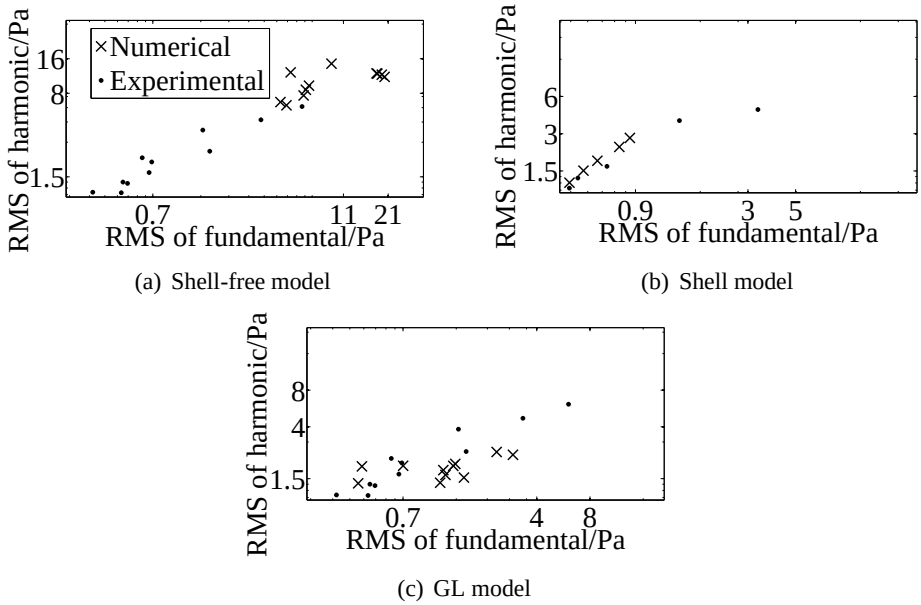

(a) Shell-free model

(b) Shell model

(c) GL model

Figure 4.9: *Experimental and sampled numerical responses of MBs at a driving frequency of 1.21 MHz with peak negative pressure of 550 kPa. The shell-free, shell and GL models all are not significantly different from the experimental data.*

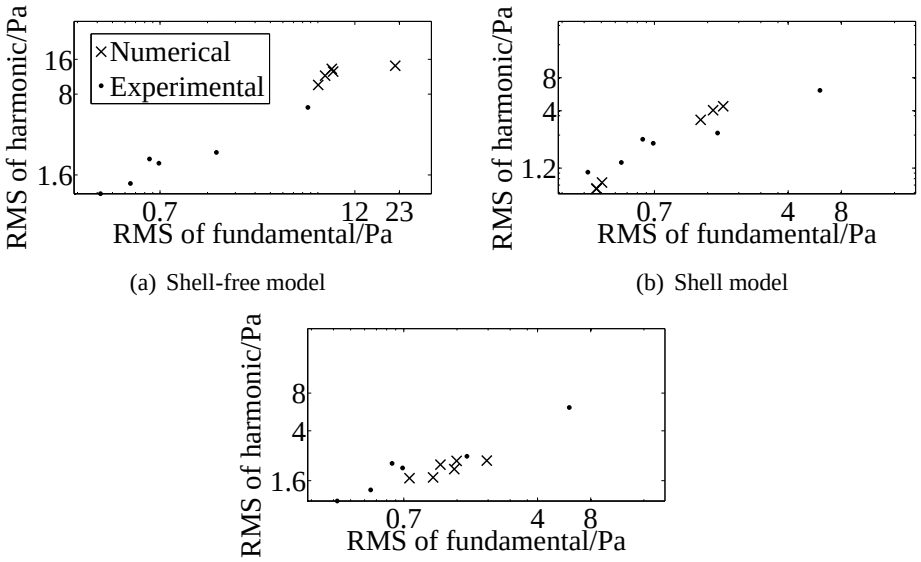

(a) Shell-free model (b) Shell model

(c) GL model

Figure 4.10: *Experimental and sampled numerical responses of MBs at a driving frequency of 1.30 MHz with peak negative pressure of 550 kPa. The shell-free model is significantly different. The shell model is not significantly different in the harmonic and the GL model is not significantly different in the fundamental or harmonic.*

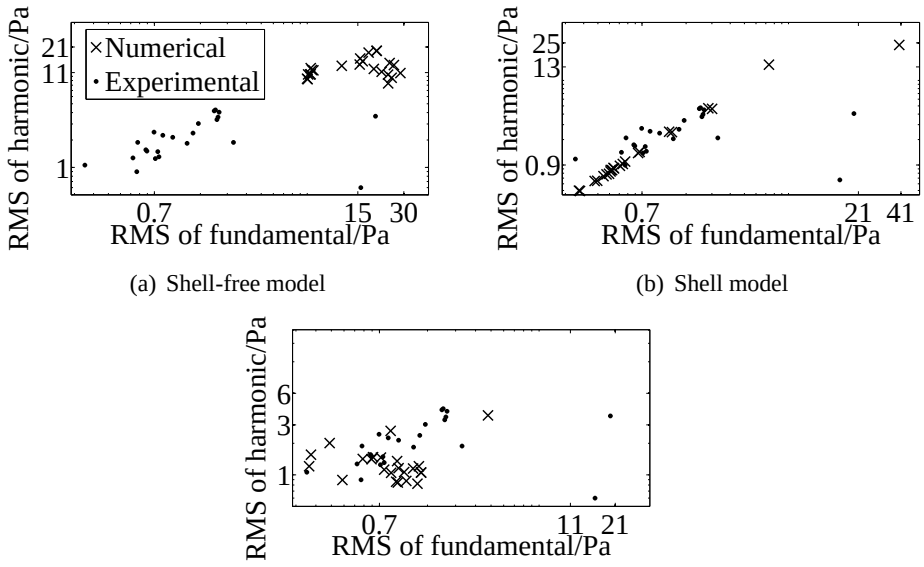

(a) Shell-free model (b) Shell model

(c) GL model

Figure 4.11: *Experimental and sampled numerical responses of MBs at a driving frequency of 1.42 MHz with peak negative pressure of 550 kPa. Only the harmonic distribution of the shell model is not significantly different to the experimental data.*

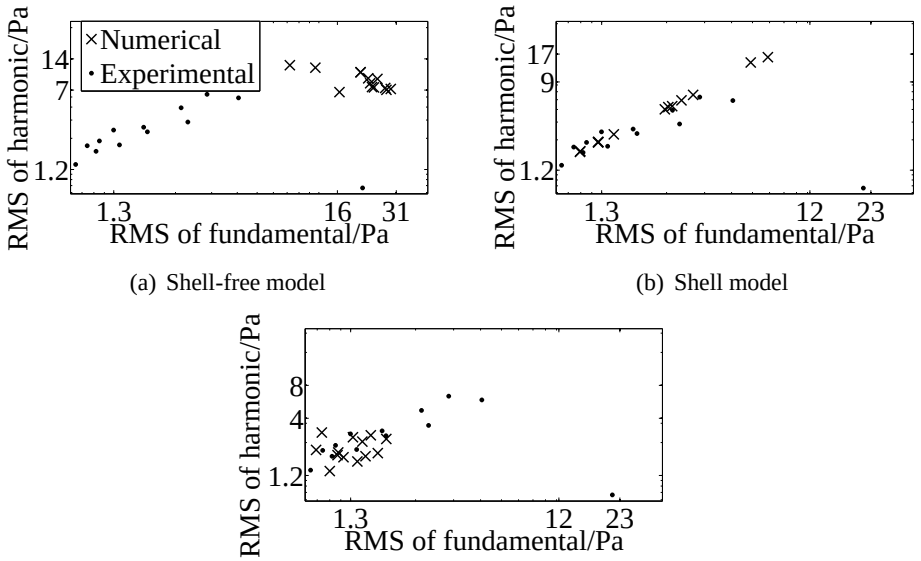

(a) Shell-free model

(b) Shell model

(c) GL model

Figure 4.12: *Experimental and sampled numerical responses of MBs at a driving frequency of 1.50 MHz with peak negative pressure of 550 kPa. The shell model fundamental and harmonic and the GL model fundamental distributions are not significantly different to the experimental data.*

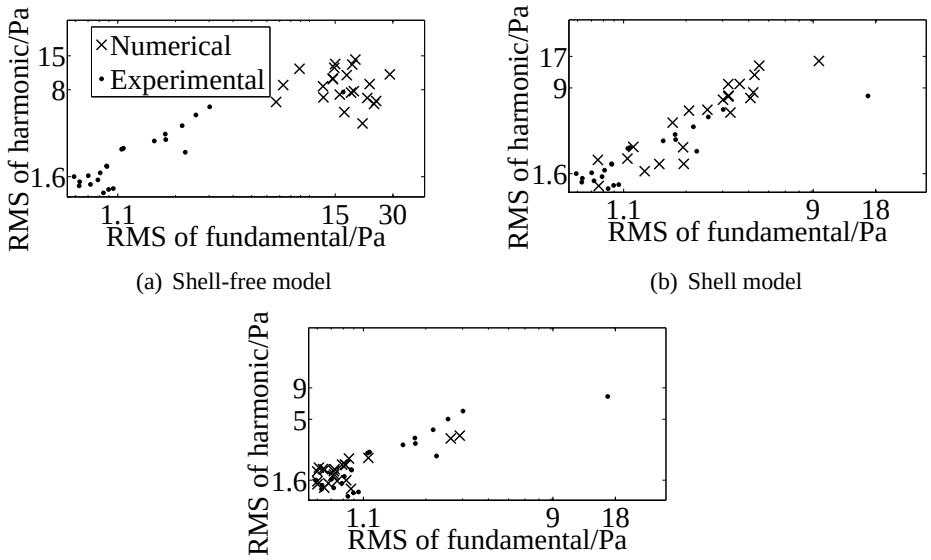

(a) Shell-free model

(b) Shell model

(c) GL model

Figure 4.13: *Numerical and experimental responses of MBs at a driving frequency of 1.6 MHz with peak negative pressure of 550 kPa. The shell model's fundamental and the GL model's fundamental and harmonic distributions are not significantly different to the experimental data.*

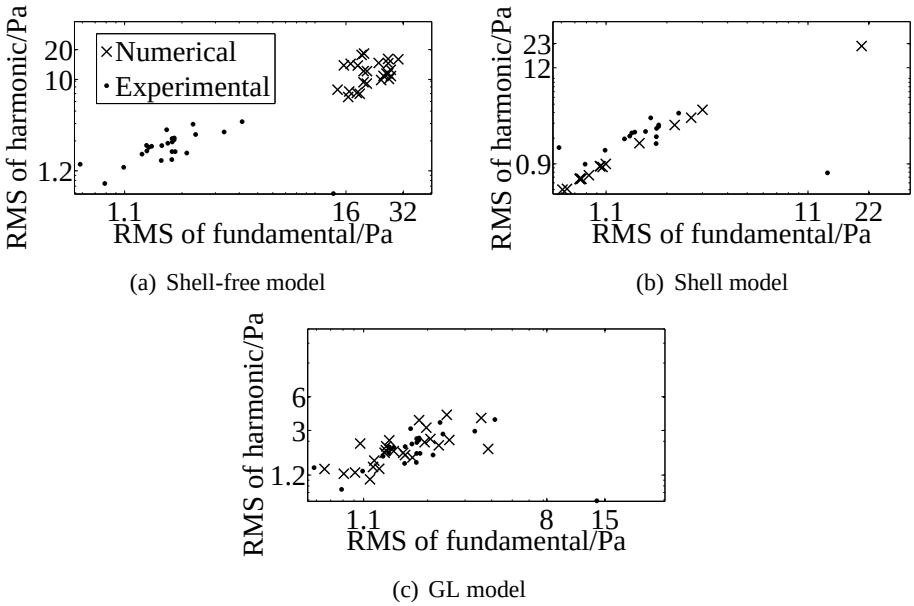

(a) Shell-free model

(b) Shell model

(c) GL model

Figure 4.14: *Numerical and experimental responses of MBs at a driving frequency of 1.8 MHz with peak negative pressure of 550 kPa. The shell-free model is significantly different with and without the radial cutoff. Only the fundamental distribution of the shell model is not significantly different to the experimental data.*

in table 4.2 using the minimum MB echo cutoff and table 4.3 using the additional radius cutoff as described above.

A similar outcome is shown for the rest of the frequencies. For all incident pulses the theoretical fundamental and harmonic distribution predicted by the shell-free model significantly overestimate the MB response compared to the experimental data (table 4.2). The introduction of a radius cutoff did not alter this significance (table 4.3).

As shown in table 4.2 agreement and disagreement between experimental and theoretical data can be both found in the range of used frequencies for the shelled model. When the radius cutoff was imposed the shell model fundamental and harmonic was significantly different for all frequencies apart for 1.21 MHz (table 4.3).

The predicted fundamental response from the GL model was in general agreement with the experimental data except for the frequencies 1.42 MHz and 1.83 MHz (table 4.2). The predicted harmonic response from the GL model was significantly different from the experimental data at 1.42 MHz, 1.50 MHz, 1.83 MHz and 3.71 MHz (table 4.2). When a radius cutoff was imposed both the harmonic and fundamental predictions of the GL model were significantly different

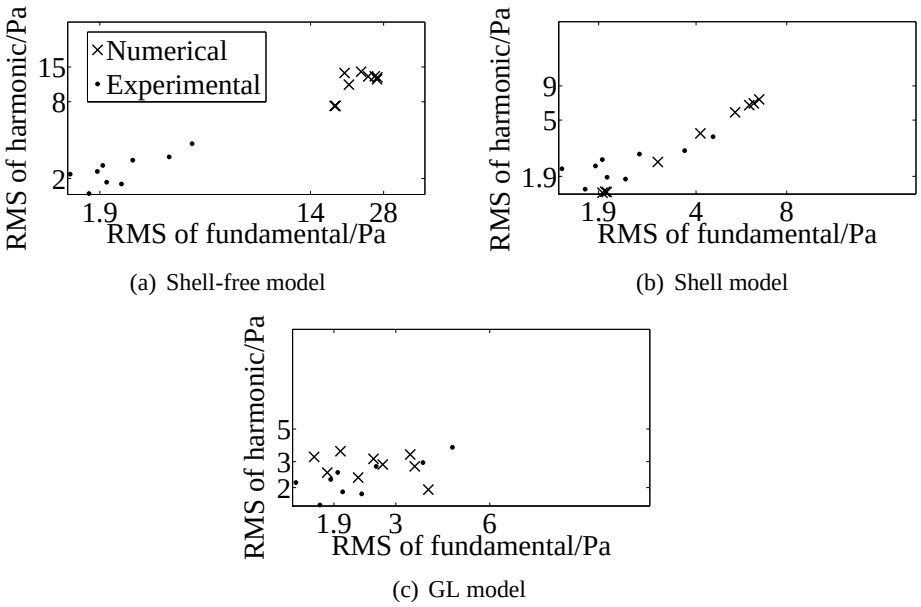

Figure 4.15: *Numerical and experimental responses of MBs at a driving frequency of 2.00 MHz with peak negative pressure of 550 kPa. The shell-free and shell models are significantly different with and without the radial cutoff. The GL model is not significantly different when both fundamental and harmonic are compared to the experimental data.*

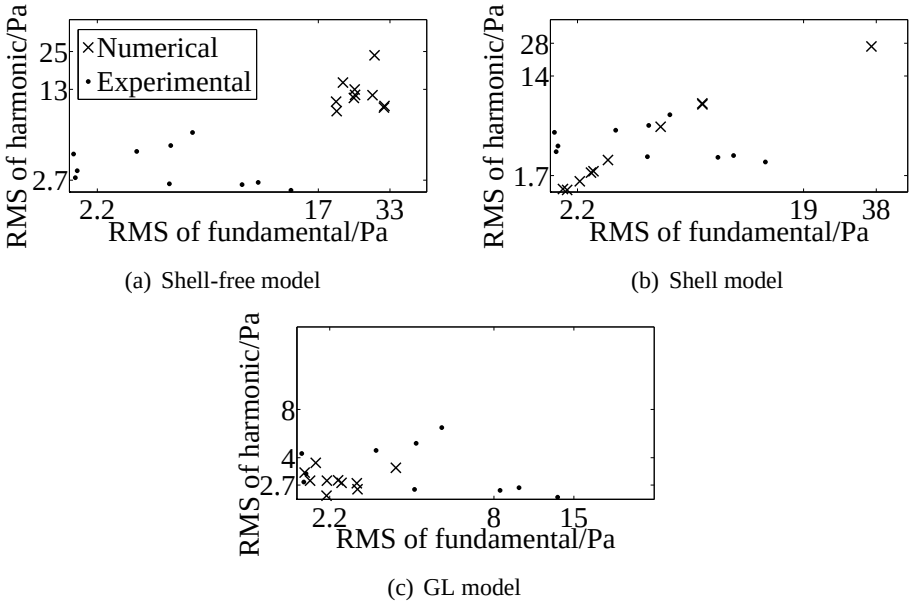

(a) Shell-free model

(b) Shell model

(c) GL model

Figure 4.16: *Numerical and experimental responses of MBs at a driving frequency of 2.11 MHz with peak negative pressure of 550 kPa. The GL model's fundamental and harmonic distributions and the shell model's fundamental distribution are not significantly different to the experimental data.*

for frequencies above 2.11 MHz, and in general agreement in that and below that frequency (table 4.3).

4.3.2 Variable pressure

A similar procedure was followed for the comparison at different acoustic pressures. An example of weighted random samples of MB responses from each of the models at peak negative amplitudes of 160 kPa and 1020 kPa (corresponding to MIs of 0.13 to 0.81), found as described in section 4.2.3, are plotted with the experimental MBs for driving pulse in figures 4.19-4.27. The 550 kPa data are seen in figure 4.13. The GL model agrees with the experiment at 550kPa and underestimates significantly in the other two pressures, while the shell-free and the shelled models generally overestimate the MB scatter.

A summary of the statistical comparison of the theoretical and the experimental results using the KS statistic are shown in table 4.4 using the minimum MB echo cutoff and table 4.5 using the additional radius cutoff as described above. The free theoretical fundamental distribution was significantly different to the experimental data for all driving amplitudes, and the harmonic

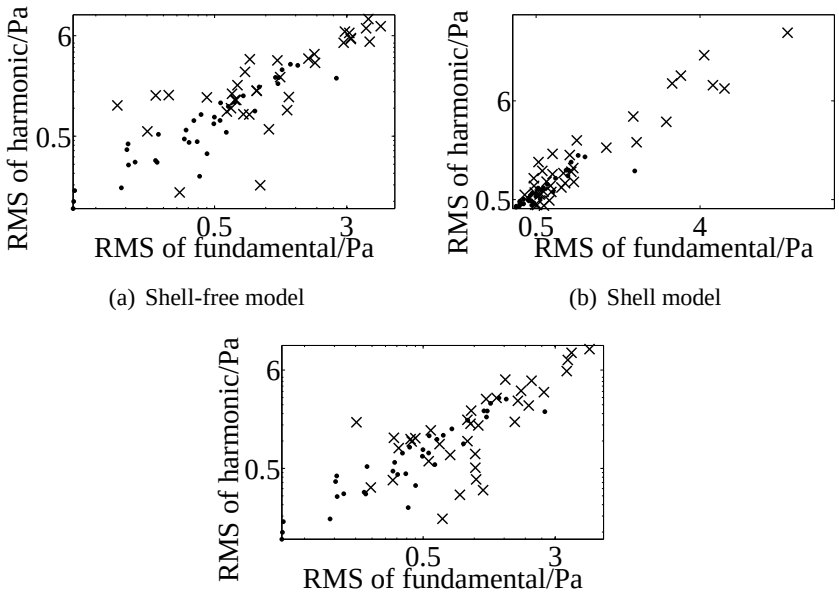

(a) Shell-free model

(b) Shell model

(c) GL model

Figure 4.17: *Numerical and experimental responses of MBs at a driving frequency of 2.52 MHz with peak negative pressure of 550 kPa. The shell-free and shell model's fundamental and harmonic distributions are significantly different and the GL model's fundamental and harmonic distributions are not significantly different.*

	Shell-free		Shell		Gas-Leaking	
Pres/kPA	Fun	Har	Fun	Har	Fun	Har
160	S	0.82	0.41	S	S	S
215	S	0.83	0.23	S	0.29	S
265	S	S	S	S	S	S
335	S	S	0.37	S	S	S
500	S	S	0.36	S	0.41	0.28
550	S	S	0.35	S	0.53	0.30
570	S	S	0.37	S	S	0.31
710	S	S	0.39	S	S	S
850	S	S	0.43	S	S	S
1020	S	S	S	S	S	S

Table 4.4: *The significance value is the maximum difference between the theoretical and numerical distributions (section 4.2.3). If this value is greater than that found in 95% of cases there is a statistically significant difference "'S"' between the theory and experiment.*

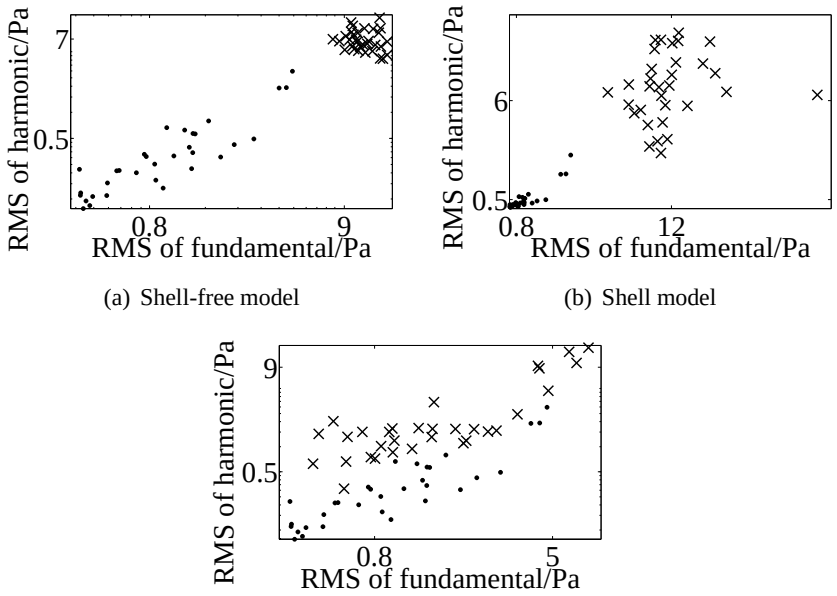

(a) Shell-free model

(b) Shell model

(c) GL model

Figure 4.18: *Numerical and experimental responses of MBs at a driving frequency of 3.71 MHz with peak negative pressure of 550 kPa. The shell-free and shell model's fundamental and harmonic distributions are significantly different and the GL model's fundamental distribution is not significantly different.*

	Shell-free		Shell		Gas-Leaking	
Pres/kPA	Fun	Har	Fun	Har	Fun	Har
160	S	S	0.33	S	S	S
215	S	0.76	0.14	S	0.29	S
265	S	0.74	S	S	S	S
335	S	S	0.14	S	S	S
500	S	S	S	S	0.41	0.28
550	S	S	S	S	0.60	0.27
570	S	S	S	S	S	0.31
710	S	S	S	S	S	S
850	S	S	S	S	S	S
1020	S	S	S	S	S	S

Table 4.5: *The significance value is the maximum difference between the theoretical and numerical distributions (section 4.2.3). In this case the radial cutoff was used. If this value is greater than that found in 95% of cases there is a statistically significant difference "'S"' between the theory and experiment.*

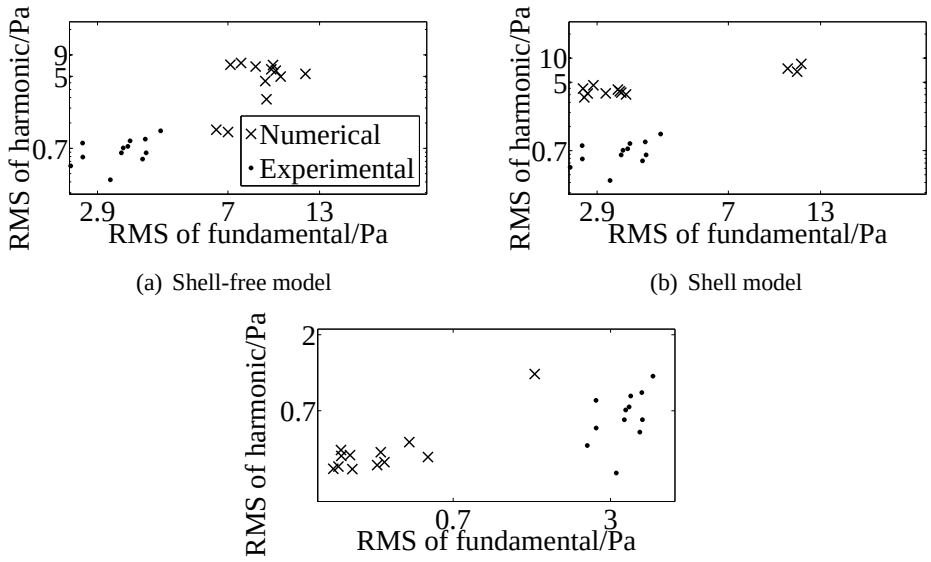

(a) Shell-free model

(b) Shell model

(c) GL model

Figure 4.19: *Numerical and experimental responses of MBs at a peak negative pressure of 160 kPa and with driving frequency of 1.6 MHz. No radial cutoff was used. The fundamental response of the shell model is not significantly different but the harmonic response is significantly different to the experimental response. Both the shell-free and GL models are significantly different. At this driving amplitude all the responses from the GL model are below noise.*

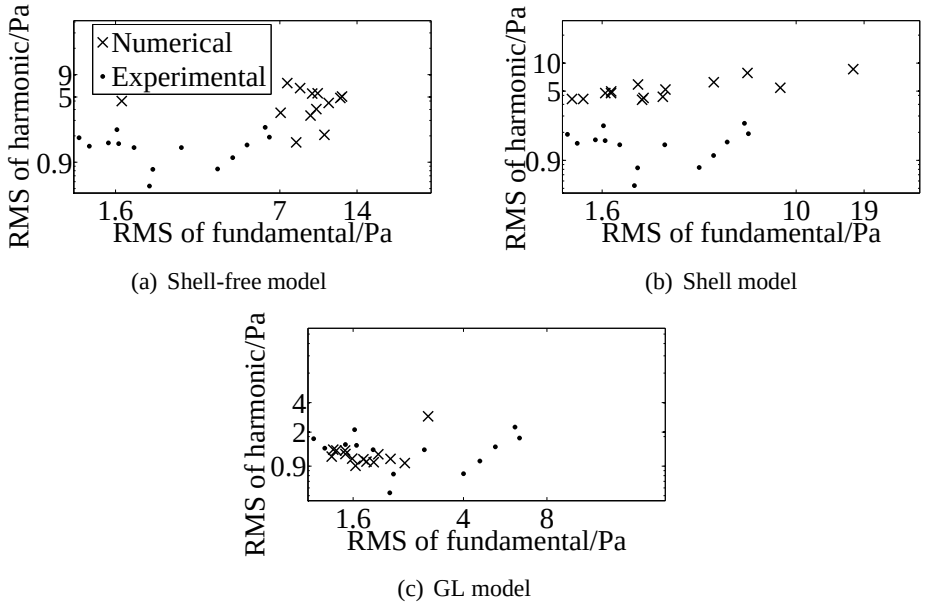

Figure 4.20: *Numerical and experimental responses of MBs at a peak negative pressure of 215 kPa and with driving frequency of 1.6 MHz. The shell-free model harmonic, the GL model fundamental and the shell model fundamental are not significantly different.*

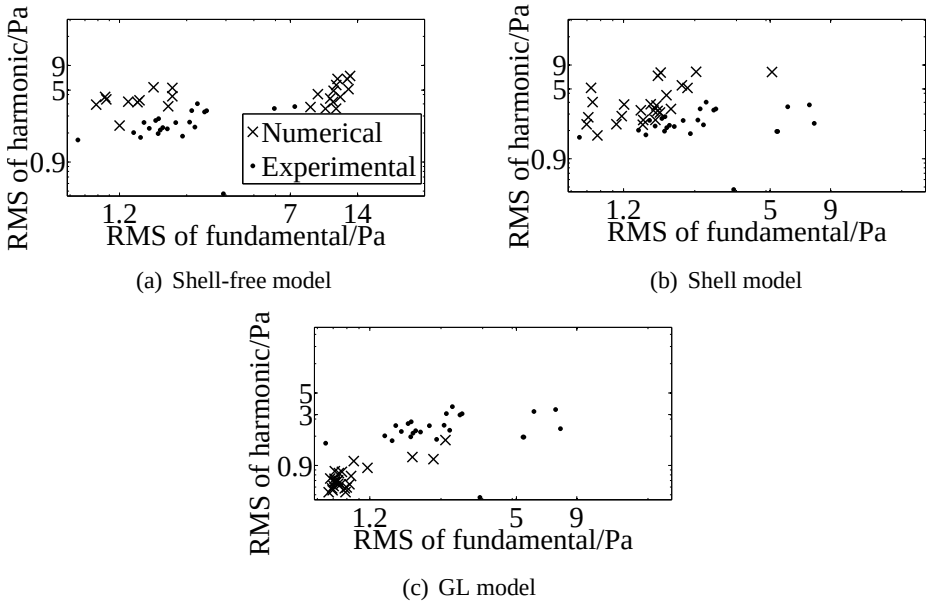

Figure 4.21: *Numerical and experimental responses of MBs at a peak negative pressure of 265 kPa and with driving frequency of 1.6 MHz. Both the fundamental and harmonic distributions of all three models are significantly different to the experimental data.*

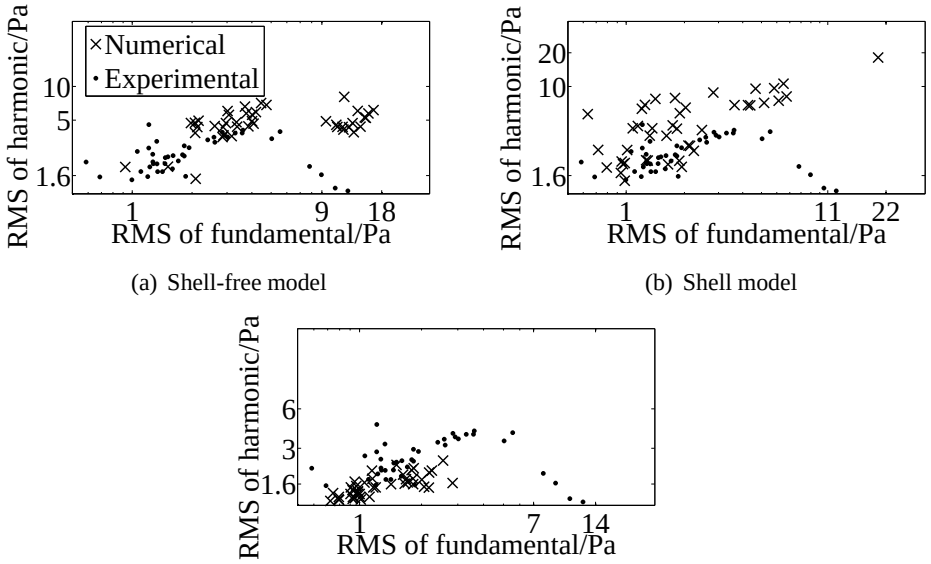

(a) Shell-free model (b) Shell model

(c) GL model

Figure 4.22: *Numerical and experimental responses of MBs at a peak negative pressure of 335 kPa and with driving frequency of 1.6 MHz. Only the shell model fundamental is not significantly different.*

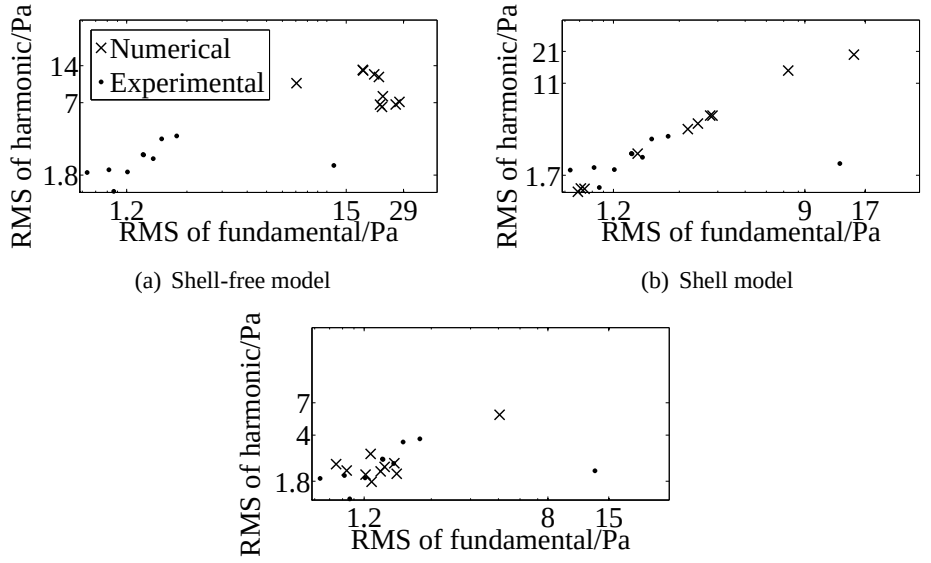

(a) Shell-free model (b) Shell model

(c) GL model

Figure 4.23: *Numerical and experimental responses of MBs at a peak negative pressure of 500 kPa and with driving frequency of 1.6 MHz. No radial cutoff was used. The shell-free model is significantly different. The shell model fundamental is not significantly different but the harmonic is significantly different. The GL model is not significantly different.*

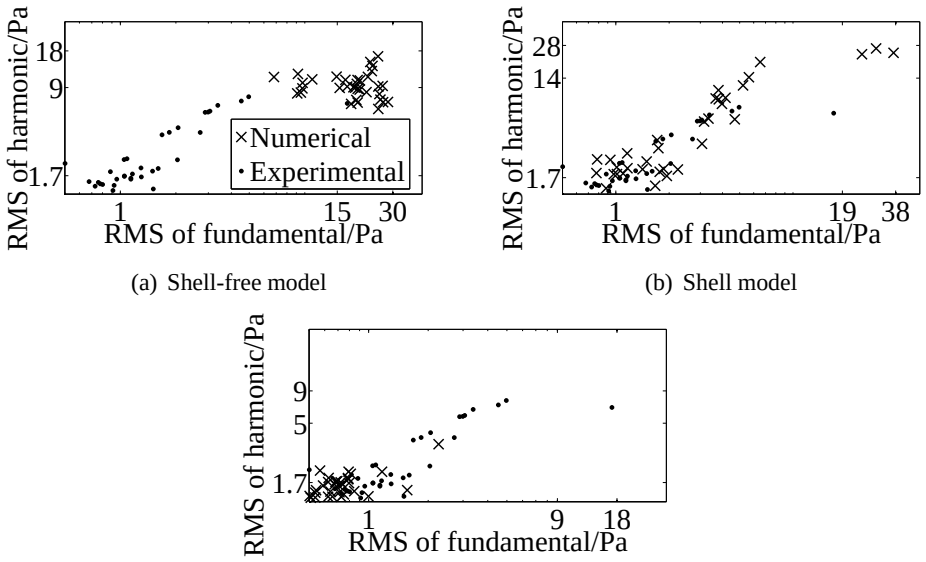

(a) Shell-free model

(b) Shell model

(c) GL model

Figure 4.24: *Numerical and experimental responses of MBs at a peak negative pressure of 570 kPa and with driving frequency of 1.6 MHz. No radial cutoff was used. The shell-free model is significantly different. The shell model fundamental is not significantly different but the harmonic is significantly different. The GL model harmonic distribution is not significantly different.*

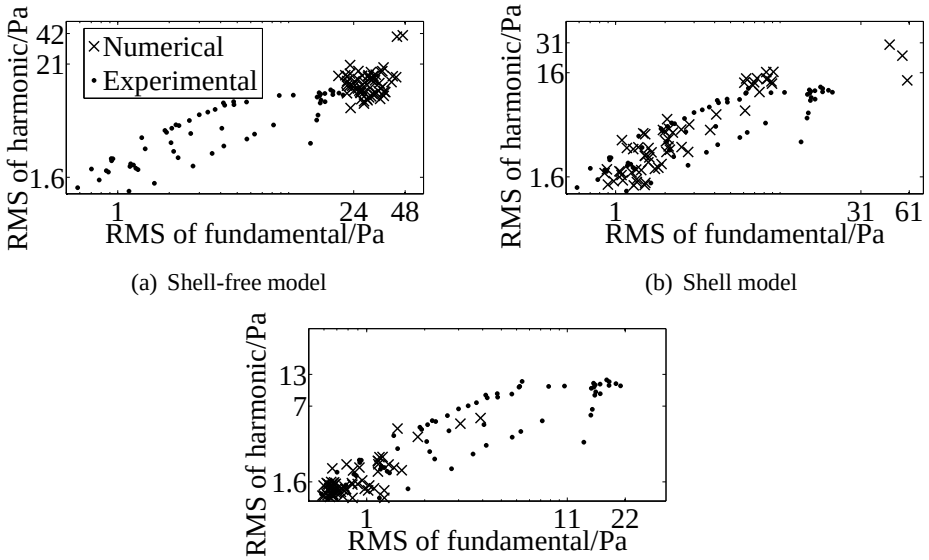

(a) Shell-free model

(b) Shell model

(c) GL model

Figure 4.25: *Numerical and experimental responses of MBs at a peak negative pressure of 710 kPa and with driving frequency of 1.6 MHz. No radial cutoff was used. The shell model fundamental is not significantly different but the harmonic is significantly different.*

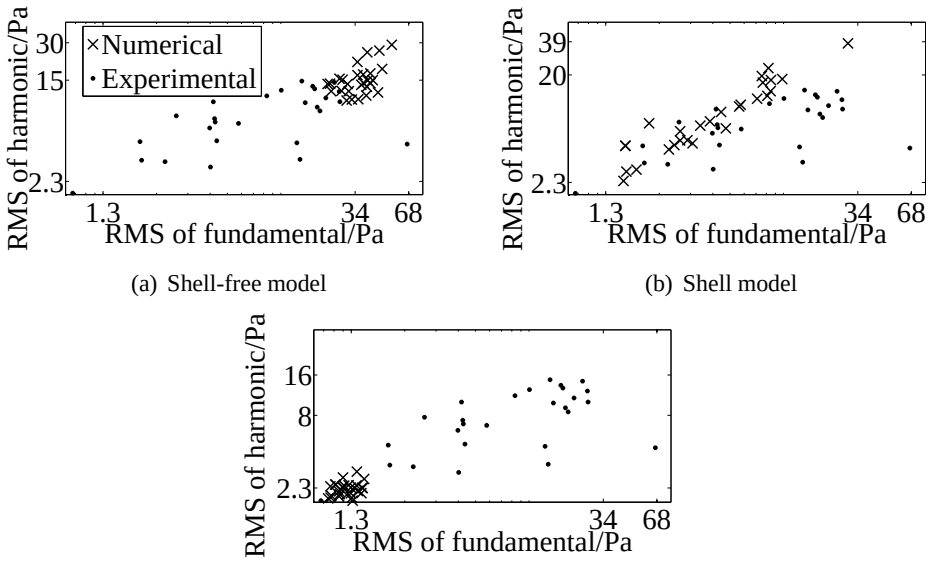

(a) Shell-free model

(b) Shell model

(c) GL model

Figure 4.26: *Numerical and experimental responses of MBs at a peak negative pressure of 850 kPa and with driving frequency of 1.6 MHz. No radial cutoff was used. The shell model fundamental is not significantly different but the harmonic is significantly different.*

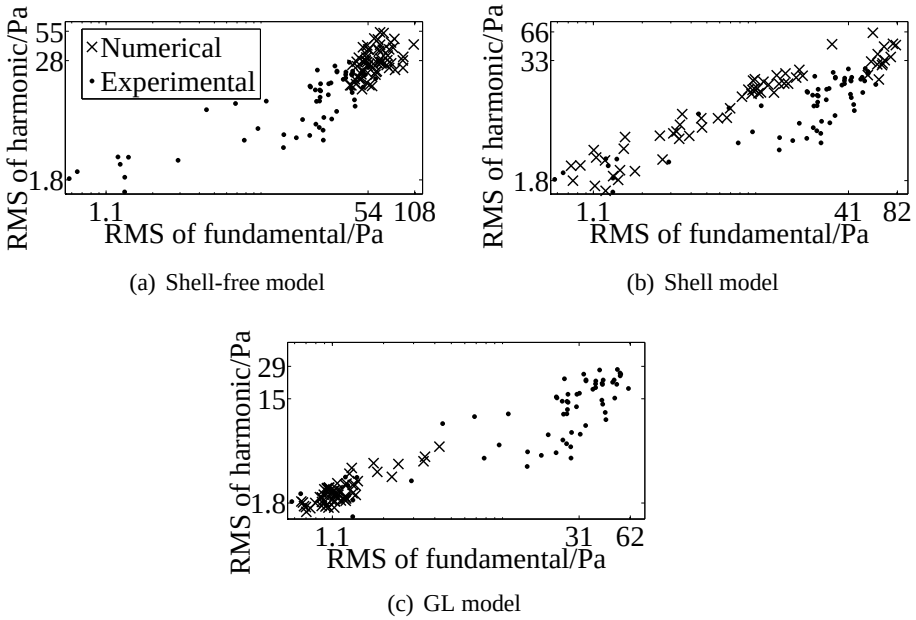

Figure 4.27: *Numerical and experimental responses of MBs at a peak negative pressure of 1020 kPa and with driving frequency of 1.6 MHz. No radial cutoff was used. The shell-free, GL and shell model are significantly different to the experimental distributions.*

was significantly different for all except 160 kPa and 215 kPa (table 4.4). When the radius cutoff was imposed the result remained unaltered (table 4.5).

The fundamental distributions of the shelled model were in general agreement to the experimental distributions (table 4.4). When the radius cutoff was used the fundamental distribution showed agreement only at 160 kPa, 215 kPa and 335 kPa (table 4.5). The harmonic was significantly different between the shelled model and the experimental data.

The GL model theoretical fundamental distribution showed agreement with the experimental data between 215 kPa and 550 kPa, while the harmonic between 500 kPa and 570 kPa (table 4.4). This behaviour was recorded when the radius cutoff was imposed (table 4.5), thus showing that the GL model was the only model that simulated successfully the experimental data in both spectral components between 500 kPa and 550 kPa.

4.4 Discussion

A new theoretical model was proposed here in order to explain some of the behaviour that has been observed optically for rigid spheres that leak gas and generate scatter in this way. The GL model assumes that the leaked MB is spherically symmetric and that the amount of gas that is in and out of the shell is equal to that in the free model. However, the GL model assumes that this gas is in equilibrium with the hydrostatic pressure and the surface tension increases because the radius is smaller than that of a free MB. As shown in figure 4.8 both of these effects result in a much lower acoustical response predicted by the GL model compared to a shell-free or a shelled MB. Resonance is concealed in figure 4.7 as the excess gas available to leak is related to the size of the MB and this is the dominant mechanism that relates acoustic response to bubble size. At low MI the assumptions of the formation of a spherical MB from the leaked gas may be incorrect leading to the discrepancy of the theoretical results with the experimental results. At high MI the gas may be ejected violently to form free MBs leading to the disagreement with the basic assumption of the model, which explains the discrepancy at high MI.

At intermediate MI (0.35-0.5) leaking of the gas in and out of the shell has been observed optically[95]. The shell-free and shelled models produce similar results overestimating the scatter from biSphere^{TM}. The GL model was developed to model this behaviour, as shown by optical microscopy data[10], and gave good agreement with the experimental data. At 550 kPa between 1.27 MHz to 5.2 MHz agreement was achieved before the radius cutoff was imposed. The shell model does give agreement at a driving frequency of 1.21 MHz but the assumption of shelled oscillation at this MI is contrary to optical observations[10]. It is difficult to directly compare our data with the optical observations. The GL-model MB with radius 2 μm gives a maximum leaked gas expansion at around 1.4 μm at a MI of 0.13 (figure 4.5), whereas at a MI of 0.43 this expansion has not changed significantly (figure 4.6). In optical observations for all leaked MBs up to a MI of 0.9 the maximum expansion remains in very similar values[10]. Note that, unlike the experimental data here that are from MBs in free space, the optical experiments are always performed inside narrow tubing, which may provide instabilities at lower MI or may increase the damping of MB oscillations[111]. More important however, is the fact that in both optical observations and the GL-model the expansion of the leaked gas does not increase with the increase of MI (within the above limits), but rather remains almost constant. This is an important feature of leaking MBs, and a further confirmation of the validity of the GL-model.

For low MI $\leq$ 0.35 the response from the free model was much larger than that measured

experimentally, which is compatible with optical evidence that suggests the lack of free MBs [10]. The GL model significantly underestimated the experimental data for MI less than 0.38. Theoretical shell models have agreed with experimental measurements on the contrast agent Quantison^{TM} for driving amplitudes below 200 kPa[37]. Suitable choices of shell parameters for the shelled model may give good agreement with the experimental results from single biSphere^{TM} MBs. However, optical observations on this contrast agent have shown that the oscillation of a biSphere^{TM} MB with an intact shell is small and that the release of gas is the mechanism responsible for the scatter. The maximum shell oscillation observed optically at a MI of 0.3 is less than 0.2 μm for a MB with a radius of 2 μm[10]. With the shell model used here, which simulates better softer shells, the oscillation of a similar MB at a MI of 0.3 is greater than 0.5 μm disagreeing with these optical observations[10]. It is possible with a different set of shell parameters that fit the elastic properties of the biSphere^{TM} to reach an agreement with the radial oscillation but the scattered pressure would be much lower than those measured from single MBs. However, there is an alternative explanation to the disagreement between models and experimental data. It is not certain that gas does not escape these MBs especially considering that the scattered pulses generated are not very far from the intermediate MIs. In other words it is possible that the MBs that have such behaviour are a very low number to be detectable in the sample size available to Bouakaz et al.[10]. It has been shown that several bubbles have structural defects such as big fragments of shell missing[116]. It is then possible for these MBs to perform oscillations similar to a free bubble attached to the rigid wall. This would provide scatter less than the free bubble. Moreover, the vicinity of a wall does not alter their behaviour [13], which strengthens the above argument. An attached MB model is not investigated here, but it is a suggestion for future research work in order to explain the behaviour of biSphere^{TM} at low MI.

At higher MI $\geq$0.6 the gas has been observed to be ejected from the shell and form a free MB [7]. At the highest driving amplitude, 1020 kPa figure 4.27(b), the GL model underestimates the maximum response in the fundamental by 50 Pa. At these driving amplitudes the gas in the MB is forced violently out of the shell and may be ejected far from the MB[95], which is contrary to the assumption of the GL model but also to the assumption of the shell model. The free model remains the only candidate to simulate such oscillations. At these driving amplitudes, however, large amplitude aspherical oscillations may be prominent and the assumptions of the spherically symmetric free model may be invalid[49]. The free model predicted a higher fundamental and harmonic response than the experimental MBs at high MI. It is known that surface instabilities

may cause significant reduction in scattered pressure, which is in agreement with the described discrepancy[74].

Improvements in the experimental technique would allow better comparison with theoretical models. Knowledge of the equilibrium radius would allow direct comparison of experimental MBs and theoretical MBs of the same radii. Further improvements in the modelling of rigid shelled MBs may include a more realistic model of the release of gas from a MB at intermediate MI. Since the GL model is based on the shell-free model the GL model predicts rebounds of the MB above some MI similar to the shell-free model. This behaviour is contrary to the behaviour that has been observed experimentally. The small gaps seen in the radial pulsation curves of the GL model is attributed to a reduction of the free bubble model to create a clipping effect. The gas in the GL expansion is assumed to be at the same temperature as the MB in the free bubble model. As a result of this assumption when the reduction in the volume of the gas due to the cooling effect of the expansion in the shell-free model is larger than the volume of gas outside the equilibrium radius the GL model can predict a reduction in the size of the MB. This is seen in figure 4.5 where the GL model has a local minimum while the shell free model has a local maximum. The acoustic response from experimental MBs some times provide a small number of large amplitude responses (figure 4.27 and figure 4.19). Dayton et al.[23] has observed gas to be ejected from the shell of a MB and to form free MBs. The equilibrium radius of leaked MBs can vary and some gas can remain in the shell while the rest is expelled[95]. The GL model does not predict such high amplitude responses as those observed in figure 4.27 and figure 4.19. The large amplitude acoustic responses from single MBs may be due to the formation of free MBs similar to that observed by Dayton et al.[23]. Although the comparison of the theoretical shell-free MBs to the leaked MBs is problematic since the equilibrium radius of the leaked MB may be less than the equilibrium radius of the initial encapsulated MB[95] the shell-free model does predict high amplitude responses similar to those observed experimentally (figure 4.27 and figure 4.19) suggesting that these high amplitude responses observed experimentally may be due to free MBs.

4.5 Conclusion

The scatter from single biSphere^{TM} MBs has been compared to the predicted scatter from theoretical models. Three models were used, namely the free bubble model, the GL model and a shelled bubble model. The GL model was developed to account for the flow of gas in and out

of a MB at intermediate MI and showed agreement with acoustical and optical experimental observations. The GL model does not account for the expansion of the gas when it is out of the shell. At higher MI the free bubble model theory does not accurately predict the response from these contrast agents, as MBs may not be spherically oscillating. At lower MIs the GL model may need to be improved to simulate the MB behaviour.

Chapter 5
Measuring the shell properties of lipid shelled microbbubbles

5.1 Introduction

Definity® (Lantheus Medical Imaging,N Belarica, MA) MBs consist of a lipid shell encapsulating the gas octafluoropropane. In this chapter the acoustic responses from single Definity® MBs are compared to the responses predicted by theoretical models. By comparing the predicted theoretical acoustic response of single MBs to the experimentally measured response from single MBs the parameters that characterise the MB shell can be determined.

5.2 Previous Work

In previous theoretical work the main focus was the shell property. To date there is no experimental technique that can provide an accurate measurement of this. As a result a number of assumptions on the shell property have been tested using data generated with available experimental tools. The comparisons of theoretical predictions were made to: A. The acoustical attenuation spectra of MB suspensions and B. The optically observed radial response of MBs [111]. In the current communication we introduce a third type of experimental data in this comparison, namely the acoustic response of single MBs. Attenuation spectra of the lipid shelled agent Sonovue^{TM} (Bracco, Milan, Italy) were compared to simulations to fit shell parameters [46]. The RPNNP equation and a linear shell model was used in the theoretical model. From the optically measured resonant response from Sonovue^{TM} the shell parameters were determined using the same model [140] and they were found to be in agreement with those calculated from attenuation spectra [46]. In another experiment that Sonovue^{TM} MBs was subjected to a range of driving amplitudes between 20 kPa to 250 kPa with a centre frequency of 1.7 MHz were compared to the theoretical prediction of the Church model [21] by Emmer et al. [34]. The results were in agreement with the previous work mentioned above.

Both approaches of measuring the shell parameters, using acoustical attenuation spectra and using optical radial response curves, have limitations. Attenuation measurements, similarly to all acoustic measurements that measure some acoustic parameter from a suspension of scatterers, use the response from a suspension volume that is subjected to acoustic pressures that range from zero to the peak value. As a result a single acoustic pressure cannot be assumed, and furthermore it is impossible in principle to simulate the acoustic pressure field that every MB is subjected to. This is because the beam profile is impossible to calculate accurately within the 3D space of a suspension of non-linear scatterers. The strong non-linear and MB behaviour unexplained by current theoretical models are the limiting factors, thus hindering such approaches from gaining true quantitative meaning. The optical experiments have a different problem. As MBs are in the vicinity of a microscope objective it is difficult to calibrate the transmitted beam very accurately. In addition, the MBs are very close or in contact to a tube wall, which has an unknown effect to their behaviour. The presence of a wall is theoretically claimed to affect their behaviour. The experiments mentioned above employ low acoustic pressures to enable small non-linear effects that are only attributed to the MB properties to be recorded, but to our knowledge this has not been verified. Nevertheless, optical experiments have provided unprecedented insight on MB behaviour and remains the most powerful tool in the effort to understand the shell contribution. Building on the evidence that single MB acoustic responses are possible to record[67;113], the first micro-acoustic system that provide absolute measurements of these responses was built[114;117].The additional advantage of this tool is that the MB generated pressure field is recorded instead of the radial oscillation, which is more related to MB wall velocity and acceleration[56], not available from optical techniques. Conveniently this information is useful for the development of signal processing approaches that may advance MB enhanced imaging. The comparison of the acoustic response from single MBs to theoretical models and extraction of shell parameters has, to our knowledge, not been performed previously and is proposed here as an alternative approach in an effort to provide an understanding of the shell property.

In this chapter the shell parameters are estimated by comparing the theoretical prediction of three theoretical models, the free model, Skalak model and Mooney-Rivlin model. The model of a red blood cell membrane was developed by Skalak et al.[121] and was used to model the shell of a contrast agent by Tsilglifis[138]. The Mooney-Rivlin model was developed to describe the behaviour of rubber Rivlin[104], Mooney[81]. The results of the theoretical models were compared to previous results for the shell parameters found optically from radial response curves[82].

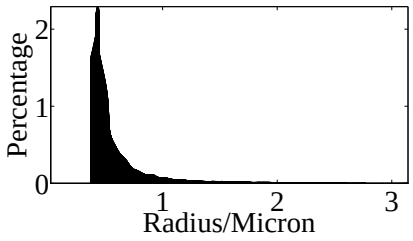

Figure 5.1: *The radius distribution of Definity® MBs as measured using a laser diffraction technique (Malvern Mastersizer)*[131].

5.3 Methodology

5.3.1 Theoretical Models

The Definity® MB distribution is shown in figure 5.1. Errors in the measurment of the size distribution have been included in the statistical analysis. An accurate measurement of the radius distribution is needed to allow the statistical analysis to discriminate between models and shell parameters. MATLAB(R2007b,Mathworks) ode23s equation solver was used to solve the nonlinear equation of motion for MBs with equilibrium radii from the size distribution of the Definity® MBs. The Keller-Miksis equation (equation 3.1) was used to find the radial motion of the MBs,

$$-\left(\frac{3}{2}-\frac{\dot{R}}{2c}\right)\dot{R}^2+\left(1+\frac{\dot{R}}{c}\right)\left(\frac{P}{\rho}\right)+R\left(\frac{\dot{P}}{\rho c}\right)=\left(R\left(1-\frac{\dot{R}}{c}\right)+\right)\ddot{R}. \tag{5.1}$$

R, c, $\dot{R}$, P and $\ddot{R}$ are the radius, velocity of sound in the fluid, velocity of bubble radius, pressure on bubble wall and bubble wall acceleration. P is the pressure of the liquid on the gas

$$P(R)=\left(p_\infty+\frac{2\sigma}{R_0}+P_{SH}(R_0)\right)\left(\frac{R_0}{R(t)}\right)^{3\gamma}-\frac{2\sigma}{R(t)}-P_{SH}(R(t))+P_{Lqvis}. \tag{5.2}$$

where P_∞, σ, R_0, P_{SH}, P_{ex}, γ and P_{Lqvis} are the hydrostatic pressure, surface tension, equilibrium radius, pressure due to shell, driving pressure, ratio of specific heats of the gas and viscosity respectively. The viscosity P_{Lqvis} is

$$P_{Lqvis}=\frac{4\dot{R}\eta_L}{R} \tag{5.3}$$

where η_L is the viscosity of water and has a value of 0.001 Pas. The expansion of the gas was assumed adiabatic. An isothermal expansion was also used but little difference was found. In the free model the shell term P_{SH} is zero. The surface tension was that of a air-water interface 0.0728 N/m. Two theoretical shell models were used to compare to the experimental data, the Skalak model and the Mooney-Rivlin model.

The simplest and one of the first viscoelastic models used to model the shell of a MB is the linear Kelvin-Voigt model[21]. In the linear Kelvin-Voigt model (equation 3.3) the pressure P_{Shell} is

$$P_{Shell} = 12\frac{d_{Se}G_S}{R_0}\left(\frac{R-R_0}{R_0}\right) + \eta_S 12\frac{d_{Se}}{R_0}\left(\frac{\dot{R}}{R_0}\right). \tag{5.4}$$

where d_{Se}, G_S, R_0, R and η_S are the shell thickness, shell stiffness, equilibrium radius, radius and shell viscosity respectively.

5.3.1.1 Skalak-Strain Hardening

The constitutive equation for the Skalak model is written as

$$P_{Shell} = \frac{2d_{Se}G_S}{R}\left(\left(\frac{(R)}{(R_0-U)}\right)^2(1-C) + C\left(\frac{(R}{(R_0-U)}\right)^6 - 1\right) + P_{Shvis} \tag{5.5}$$

where G_S and d_{Se} are the shell stiffness and shell thickness respectively. U is the initial displacement of the shell from equilibrium and is assumed to be 0. P_{Shvis} is the pressure due to viscosity of the shell. The constant C determines the amount of hardening and is set to 1.

5.3.1.2 Mooney-Rivlin-Strain Softening

The constitutive equation used in the Mooney-Rivlin model is

$$P_{Shell} = \frac{2d_{Se}G_S}{R}\left(1-\left(\frac{(R_0-U)}{R}\right)^6\right)\left(1+B\left(\left(\frac{R}{(R_0-U)}\right)^2-1\right)\right) + P_{Shvis}. \tag{5.6}$$

where G_S and d_{Se} are the shell stiffness and shell thickness respectively. U is the initial displacement of the shell from equilibrium and is assumed to be 0. P_{Shvis} is the pressure due to viscosity of the shell. The constant B determines the amount of softening of the shell and is set to 0.

For small oscillations, with the constants B and C set to 0 and 1 respectively, both of these models reduce to the linear Kelvin-Voigt model[138] (figure 3.1). In the simulations in this chapter it was assumed that the displacement of the shell from equilibrium when the MB is at rest, U, was zero. From figure 3.1 we see that during expansion the Skalak model experiences greater strain than the Mooney-Rivlin model for shells with the same elasticity. The choice of models, Mooney-Rivlin and Skalak provide a wider range of shell behaviour than the Kelvin-Voigt model allows us to examine the effect of constitutive model on the predicted response and dependence of the accuracy of the prediction of the acoustic response of single MBs using these theoretical models.

5.3.1.3 Shell Viscosity

In both the shell models The viscous term P_{Shvis} is

$$P_{Shvis} = \frac{12\dot{R}\eta_S d_{Se}}{R^2}, \tag{5.7}$$

where η_S, d_{Se} and R are the viscosity, thickness and radius. It was assumed that the shell viscosity did not vary with radius for all of the simulations except those using the empirical dependence on equilibrium radius found by Morgan et al.[82]. In that case the viscosity η_S was found to be given by the empirical formula

$$d_{Se}\eta_S = (10^{-9})1.49(R_0 - 0.86), \tag{5.8}$$

where R_0 is the equilibrium radius in microns. The shell thickness throughout this chapter is assumed to be 5 nm. In the equations of motion (equations 5.5-5.6), the shell thickness enters the equation of motion as a scaling factor so that doubling the thickness is equivalent to doubling the stiffness and viscosity. The values of the shell stiffness and viscosity used in this chapter to test the theoretical models were chosen since the previous results of Morgan et al.[82] found that the shell parameters lie in this range.

5.3.2 Statistical comparison

The radius distribution of Definity® [131] was used to find the fundamental and harmonic distribution predicted by the free and shelled models (section 4.2.3). For each driving pulse, model and choice of shell parameters the theoretical distribution was compared to the experimental

distribution. An experimental error of 10% was used to calculate the significance. The fundamental and harmonic distributions predicted by each of the theoretical models were compared statistically to the experimental fundamental and harmonic distributions using the one dimensional Komolgorov-Smirnov (section 4.2.3).

5.4 Results

5.4.1 Variable pressure

The responses from single Definity® MBs at a centre frequency of 1.6 MHz and with peak negative amplitudes of 160 kPa, 275 kPa, 375 kPa and 550 kPa were compared to the models. Shell stiffnesses of 0.5 MPa, 5 MPa, 15 MPa, 25 MPa, 50 MPa and 100 MPa and shell viscosities of 0 Pas, 0.5 Pas, 1 Pas, 2 Pas, 6 Pas and the empirical dependence of viscosity on radius (equation 5.8) found by Morgan et al.[82] were used. An iteration over the range of stiffnesses and viscosities was avoided as it is computationally expensive and prohibitive considering all the other analysis. As shown later in the results section this was not necessary for the current work. The statistical comparison of the shell free model with the experimental data are shown in table 5.1. The tables of the statistical comparison of the experimental and theoretical responses are abbreviated in table 5.2. If the theoretical model fundamental and harmonic distributions are significantly different then the theoretical model with the given parameters do not agree with the experimental data. By comparing the theoretical models over a range of parameters those parameters which do not disagree with the experimental data can be determined. In the following analysis the theoretical models will be said to ”not disagree with the experimental” data provided both the fundamental and harmonic distributions do not disagree and will be said to ”disagree with the experimental data” if either the fundamental or harmonic distributions disagree with the experimental data. Random samples of MBs from the theoretical distributions were found as described in section 4.2.3 and are plotted against the experimental responses from single MBs for each driving amplitude in figures 5.2-A.13.

Pas / kPa	0		Fer		0.5		1		2		6	
	F	H	F	H	F	H	F	H	F	H	F	H
160	0	1	0	0	1	1	1	1	1	1	0	0
275	1	1	1	0	1	1	1	1	1	1	1	0
375	1	1	1	1	0	1	0	1	0	1	1	0
550	0	0	0	0	1	1	0	1	1	1	1	0

Table 5.1: *The results of the KS statistic for the free model and the free model with shell viscosity for driving amplitudes of 160 kPa to 550 kPa at driving frequency of 1.6 MHz. "'Fer"' denotes the empirical dependence on the shell radius (equation 5.8). 1 denotes not significantly different and 0 denotes significantly different.*

kPa	Shell-Free		Skalak		Mooney-Rivlin	
	G_S/MPa	η_S/Pas	G_S/MPa	η_S/Pas	G_S/MPa	η_S/Pas
160	0	0.5-2	0.5	0.5-2	NA	NA
			0.5-5	0.5	0.5	0.5-1
					0.5-5	1
275	0	0-2	15-100	FER	0.5-5	Fer
			15-50	0	50-100	Fer
			100	1-2	0.5	0-0.5
			5-50	0.5-2	0.5-50	2
					25-50	0-1
375	NA	NA	15-25	FER	0-15	Fer
			0.5-25	0	0.5-5	0
			5-25	0.5	50	0.5-2
			15-25	1	25-50	2
			5-15	2		
550	NA	NA	5-15	FER	0.5-5	0.5
			5-15	0-1		
			0.5-5	2		

Table 5.2: *The regions of parameters where the theoretical models do not disagree with the experimental data are shown. Regions where the consecutive values of shell elasticity or shell viscosity used such that the theoretical models do not disagree with the experimental data are chosen and those where isolated values of parameters are discarded. Fer denotes the empirical dependence on shell radius.*

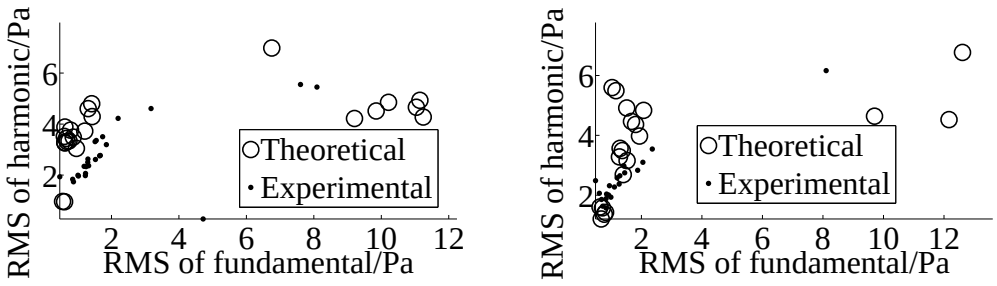

(a) 160kPa (b) 275kPa

Figure 5.2: *MBs chosen at random from the theoretical distribution of the free MBs are plotted with the experimental response from single MBs. The fundamental distribution is significantly different at a driving amplitude of 160 kPa and the fundamental and harmonic distributions are not significantly different at a driving amplitude of 275 kPa.*

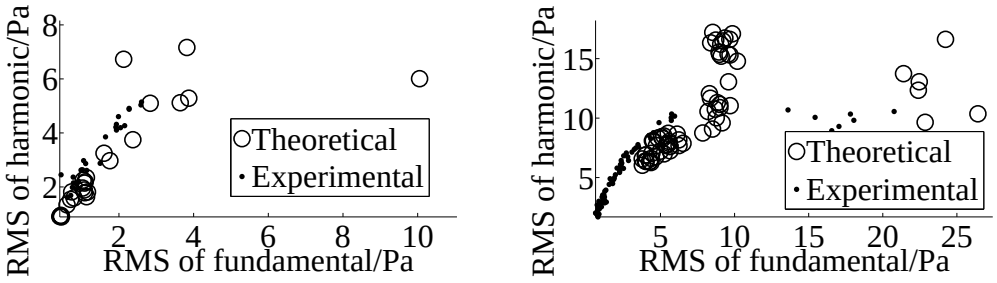

(a) 375kPa (b) 550kPa

Figure 5.3: *MBs chosen at random from the theoretical distribution of the free MBs are plotted with the experimental response from single MBs. The fundamental and harmonic distributions are not significantly different at a driving amplitude of 375 kPa and the fundamental and harmonic distributions are significantly different at a driving amplitude of 550 kPa.*

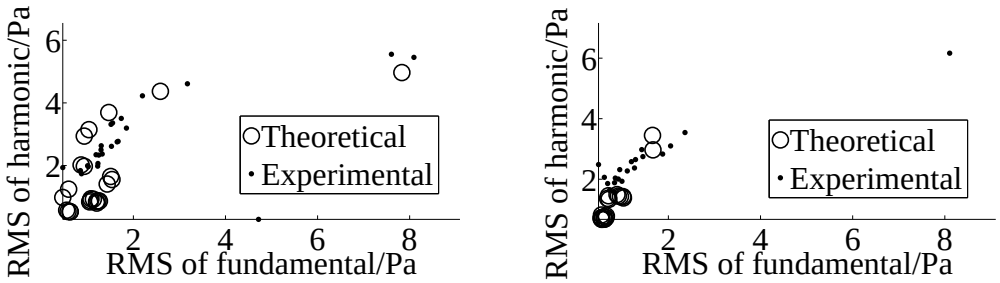

(a) 160kPa (b) 275kPa

Figure 5.4: *MBs chosen at random from the theoretical distribution of the free MBs with radially dependent shell viscosity are plotted with the experimental response from single MBs. The fundamental and harmonic distributions are significantly different at a driving amplitude of 160 kPa and the harmonic distribution is significantly different at a driving amplitude of 275 kPa.*

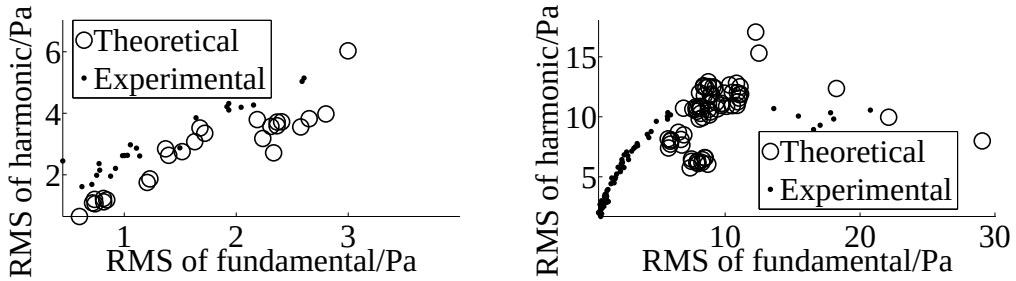

(a) 375kPa (b) 550kPa

Figure 5.5: *MBs chosen at random from the theoretical distribution of the free MBs with radially dependent shell viscosity are plotted with the experimental response from single MBs. The fundamental and harmonic distributions are not significantly different at a driving amplitude of 375 kPa and the fundamental and harmonic distributions are significantly different at a driving amplitude of 550 kPa.*

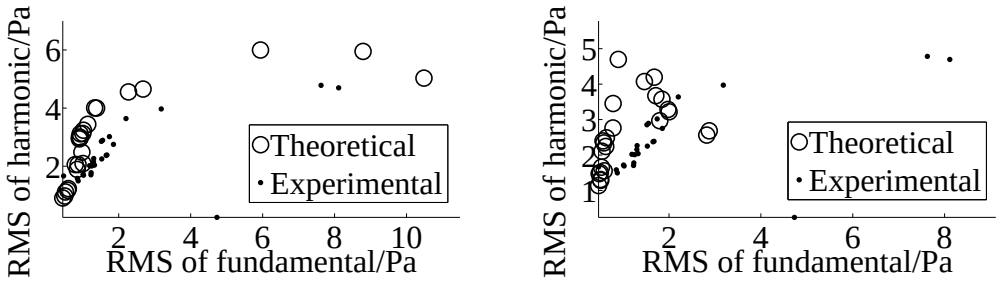

(a) Shell stiffness of 0.5 MPa (b) Shell stiffness of 50 MPa

Figure 5.6: *MBs chosen at random from the theoretical distribution of the Skalak MBs with radially dependent shell viscosity are plotted with the experimental response from single MBs for shell stiffnesses of 0.5 MPa and 50 MPa at a driving amplitude of 160 kPa. Within the experimental error both theoretical distributions are significantly different in the fundamental or harmonic.*

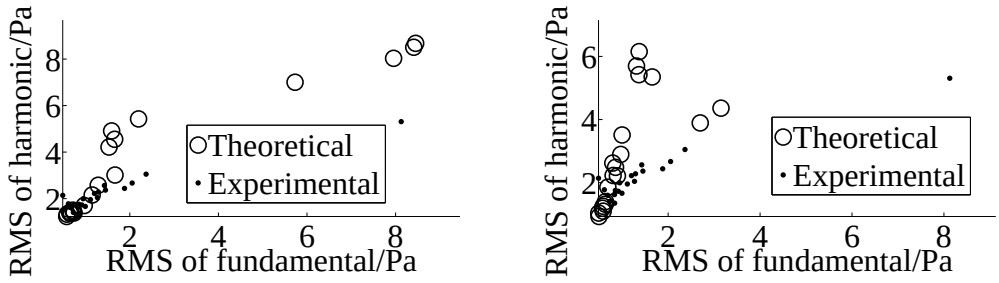

(a) Shell stiffness of 0.5 MPa (b) Shell stiffness of 50 MPa

Figure 5.7: *MBs chosen at random from the theoretical distribution of the Skalak MBs with radially dependent shell viscosity are plotted with the experimental response from single MBs for shell stiffnesses of 0.5 MPa and 50 MPa at a driving amplitude of 275 kPa. Within the experimental error both theoretical distributions are not significantly different in either fundamental or harmonic.*

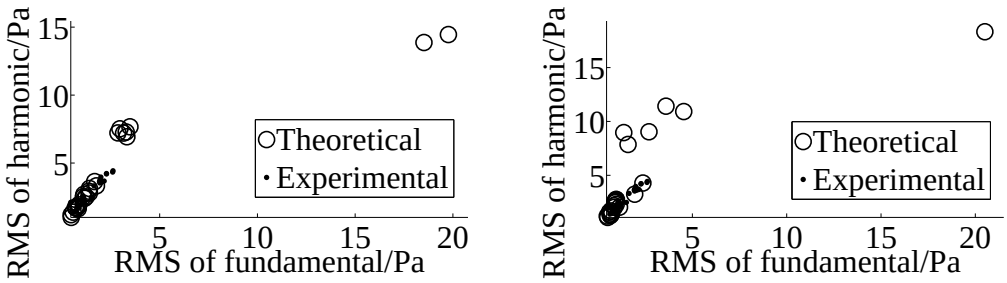

(a) Shell stiffness of 0.5 MPa (b) Shell stiffness of 50 MPa

Figure 5.8: *MBs chosen at random from the theoretical distribution of the Skalak MBs with radially dependent shell viscosity are plotted with the experimental response from single MBs for shell stiffnesses of 0.5 MPa and 50 MPa at a driving amplitude of 375 kPa. Within the experimental error the harmonic distribution is not significantly different for a shell stiffness of 0.5 MPa and the fundamental distribution is not significantly different for a shell stiffness of 50 MPa.*

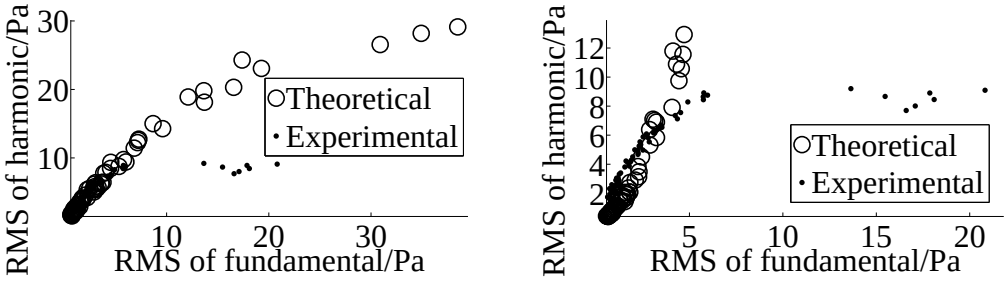

(a) Shell stiffness of 0.5 MPa (b) Shell stiffness of 50 MPa

Figure 5.9: *MBs chosen at random from the theoretical distribution of the Skalak MBs with radially dependent shell viscosity are plotted with the experimental response from single MBs for shell stiffnesses of 0.5 MPa and 50 MPa at a driving amplitude of 550 kPa. Within the experimental error both theoretical distributions are significantly different in either the fundamental or harmonic.*

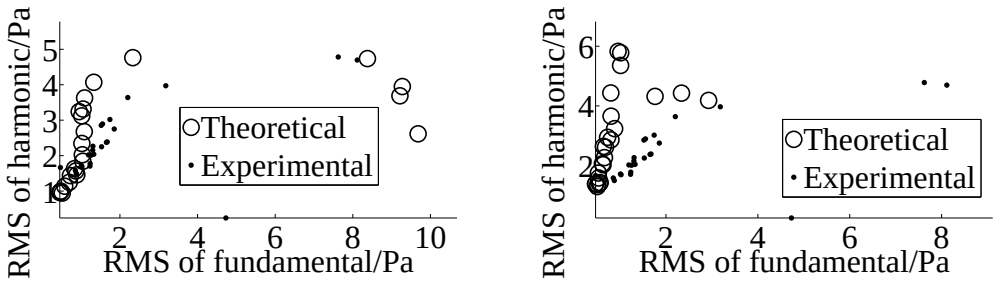

(a) Shell stiffness of 0.5 MPa

(b) Shell stiffness of 50 MPa

Figure 5.10: *MBs chosen at random from the theoretical distribution of the Mooney-Rivlin MBs with radially dependent shell viscosity are plotted with the experimental response from single MBs for shell stiffnesses of 0.5 MPa and 50 MPa at a driving amplitude of 160 kPa. Within the experimental error both theoretical distributions are significantly different in either fundamental or harmonic for a shell stiffness of 50 MPa.*

When the empirical radial dependence of the shell viscosity found by Morgan et al.[82] was used with both the Skalak and Mooney-Rivlin model for shell stiffnesses of 0.5 MPa, 5 MPa, 15 MPa, 25 MPa, 50 MPa and 100 MPa both the Skalak and Mooney-Rivlin models disagreed with the experimental data at a driving amplitude of 160 kPa (table 5.2). Both models did not disagree with the experimental data for some shell stiffnesses at higher driving amplitudes. A shell stiffness of 15 MPa for the Skalak model and a shell stiffness of 50 MPa for the Mooney-Rivlin model did not disagree with the experimental data for all driving amplitudes above 160 kPa (table 5.2).

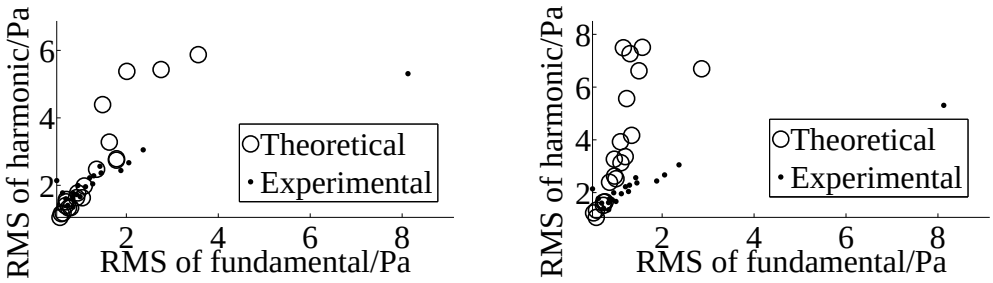

(a) Shell stiffness of 0.5 MPa (b) Shell stiffness of 50 MPa

Figure 5.11: *MBs chosen at random from the theoretical distribution of the Mooney-Rivlin MBs with radially dependent shell viscosity are plotted with the experimental response from single MBs for shell stiffnesses of 0.5 MPa and 50 MPa at a driving amplitude of 275 kPa. Within the experimental error both theoretical distributions are not significantly different in both fundamental and harmonic.*

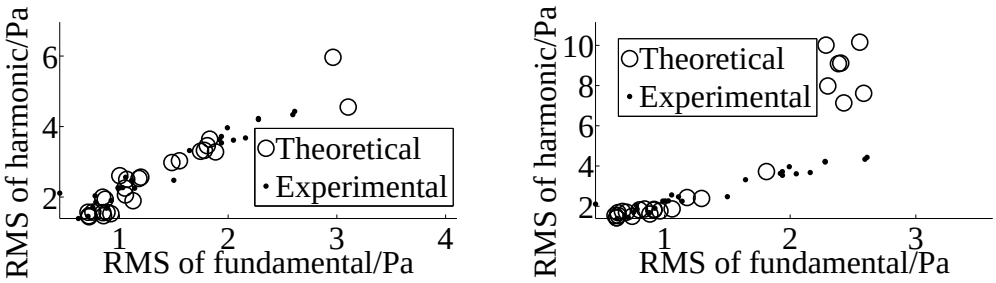

(a) Shell stiffness of 0.5 MPa (b) Shell stiffness of 50 MPa

Figure 5.12: *MBs chosen at random from the theoretical distribution of the Mooney-Rivlin MBs with radially dependent shell viscosity are plotted with the experimental response from single MBs for shell stiffnesses of 0.5 MPa and 50 MPa at a driving amplitude of 375 kPa. Within the experimental error both theoretical distributions are not significantly different in either fundamental or harmonic.*

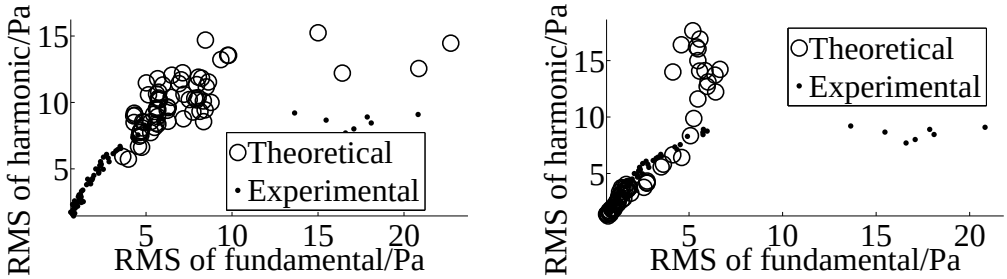

(a) Shell stiffness of 0.5 MPa

(b) Shell stiffness of 50 MPa

Figure 5.13: *MBs chosen at random from the theoretical distribution of the Mooney-Rivlin MBs with radially dependent shell viscosity are plotted with the experimental response from single MBs for shell stiffnesses of 0.5 MPa and 50 MPa at a driving amplitude of 550 kPa. Within the experimental error both theoretical distributions are significantly different in either fundamental or harmonic.*

The Skalak model with a shell stiffness of 0.5 MPa and shell viscosities of 0.5 Pas, 1 Pas and 2 Pas and a shell stiffness of 5 MPa and a shell viscosity of 0.5 Pas do not disagree with the experimental data. All other parameters disagree with the experimental data at a driving amplitude of 160 kPa (table 5.2). At 275 kPa and 375 kPa a shell stiffness of 0.5 MPa disagreed for all nonzero shell viscosities (table 5.2). Shell viscosities greater than 5 MPa did not disagree for some choices of shell viscosity for driving amplitudes above 160 kPa (table 5.2). The only choice of shell stiffness and shell viscosity that did not disagree for all of the driving amplitudes was 5 MPa and 0.5 Pas. The shell viscosity of 6 Pas disagreed with the experimental data for all shell elasticities and for all driving pulses (table 5.2).

At a driving amplitude of 160 kPa the Mooney-Rivlin model does not disagree with the experimental data for harmonic for shell stiffnesses of 0.5 MPa with a shell viscosities of 0.5 Pas and 1 Pas and for a shell stiffness of 5 MPa with a shell viscosity of 1 Pas (table 5.2). For driving amplitudes of 275 kPa and 375 kPa shell stiffnesses greater than 5 MPa did not disagree with the experimental data (table 5.2). Over all the driving amplitudes a shell stiffness of 0.5 MPa with a shell viscosity of 0.5 Pas gave the best agreement with the experimental data since it disagreed with the experimental data only for driving amplitudes of 375 kPa. The shell viscosity of 6 Pas disagreed with the experimental data for all shell elasticities and for all driving pulses (table 5.2).

5.4.2 Variable frequency

Using pulses with a peak negative of 550 kPa and with frequencies ranging from 1.21 MHz to 2.1 MHz the scattered pressure of MBs was computed for the free bubble model, free bubble model with viscosity, shelled models with empirical viscosity and for the shelled models with constant shell parameters.

The free model and free model with viscosity (table not shown) are significantly different for all driving frequencies. The shelled models with the empirical dependence of shell viscosity on the equilibrium radius were significantly different for all driving frequencies. Mooney-Rivlin model with shell parameters of 0.5 MPa and 0.5 Pas for shell stiffness and shell viscosity were not significantly different for a driving frequency of 2.1 MHz. For all other shell parameters and driving pulses the Mooney-Rivlin model was significantly different to the experimental data. The Skalak model was significantly different to the experimental data for all frequencies.

5.5 Discussion

At the lowest driving amplitude the free model, free model with viscous damping, and both shell models with the empirical viscous damping are significantly different to the experimental data. The statistical analysis found that when the shell viscosity was between 0.5 Pas-2 Pas and the shell stiffness was between 0 MPa-5 MPa some combinations of shell parameters are not significantly different to the experimental data. This shows that the shell parameters lie in this range assuming that the theoretical models are valid at this driving amplitude. At this driving amplitude and with such a low shell elasticity both shell models do not differ to the Kelvin-Voight model (figure (3.1)). This is the domain of low driving amplitude and subsequently low nonlinear behaviour. It is important to note that at this pressure lower numbers of MBs were available for comparison than at higher driving amplitudes. This was the lowest acoustic pressure where data collection was possible with this experimental setup. The calculated cutoff was 0.45 microns for a shell elasticity of 0.5 MPa and a shell viscosity of 0.5 Pas at a driving amplitude of 160 kPa and as expected, provided a small MB diameter range for comparison. The cutoff decreased to 0.41 microns at a driving amplitude of 550 kPa. Fragmentation of Definity® MBs was not observed at these MI[71] suggesting that the assumption of the spherically symmetric model with an intact shell at this MI is valid and hence, the models used for comparison may not be valid at higher driving amplitudes.

Some of the values for the shell viscosity between 0.5 Pas-2 Pas and the values for the shell stiffness between 0 MPa-5 MPa that gave agreement at 160 kPa no longer gave agreement at 275 kPa, 375 kPa and 550 kPa suggesting that the models may only be valid at lower driving amplitudes. This is consistent with the theoretical results found by Stride and Saffari[124] that showed that contrast agent destruction would be expected at a few hundred kPa due to the stresses on the shell of a MB. The range of values for the shell parameters that did not disagree with the experimental data increased as the driving amplitude was increased. The only values that gave any agreement with the driving pulses at 550 kPa with different frequencies were the same as those that gave agreement for both the Skalak model and Mooney-Rivlin model at the lowest driving amplitude. Also, the only frequency for which the theoretical models did not disagree was the highest frequency and hence the lowest MI. For a shell elasticity of 0.5 MPa would, neglecting the effects of resonance, give a lower amplitude oscillation where the theoretical models would be valid.

From figure 5.5 we see that the lowest response from the shell-free model is greater than the lowest response measured experimentally at a driving amplitude of 550 kPa because the lowest radii in the distribution has a fundamental response greater than that measured experimentally. The shell models with non-zero shell elasticity and non-zero viscosity have a minimum response over the distribution less than that measured experimentally (figure 5.6-5.10). These figures together with the statistical analysis show the failure of the free model in describing the response of the contrast agent and the necessity of including the effects of the shell on the motion of the MB.

The failure of the shell-free model implies that the influence of the shell cannot be neglected for the contrast agent Definity®. Of the 40 radial responses from Definity® MBs measured optically by Morgan et al.[82] the shell parameters that gave the best fit had a maximum value of shell stiffness and viscosity of 680 MPa and 1 Pas respectively. For a shell stiffness of 100 MPa the theoretical responses of both of the models tested here were significantly different to the experimental results at the lowest driving amplitude. The mean shell stiffness found by Morgan et al.[82] was close to zero. Overall the driving pulses tested the choice of shell parameters that gave the best agreement was for a shell stiffness and shell viscosity of 0 MPa-5 MPa and 0.5 Pas to 1 Pas respectively. These values are in agreement with those found by Morgan et al.[82] where 22 of the 40 MBs had a best fit with a shell stiffness of below 40 MPa.

The failure of any of the models to predict the response of Definity® at 550 kPa with frequen-

cies of 1.21 MHz to 2.21 MHz indicates that the assumptions of the models may be incorrect at these driving amplitudes. Possible mechanisms that have not been accounted for include fragmentation, variation in the shell properties[44], diffusion[30] and shedding of shell material[8].

At driving amplitudes above 0.27 MPa at a driving frequency of 1 MHz fragmentation of the contrast has been observed[71]. Fragmentation of Definity® MBs during insonation is not accounted for by the theoretical models and could be responsible for the failure of the models to consistently predict the experimental response at amplitudes of 275 kPa and above.

Optical observations of Sonovue^{TM} MBs has shown that MBs with the same equilibrium radius can respond differently to a driving pulse[34]. This implies that the shell properties may vary for each MB. Since the theoretical models for a given radius assume absolute monodispersity of the shell properties such as thickness, viscosity and stiffness the response of two theoretical MBs with the same radius would be the same. On the evidence of the work of[34] the current assumptions may be modified to incorporate a realistic spread of the shell parameters for a given radius and may also be dependent on radius. This has been shown for hard-shelled agents, where shell stiffness increases at lower sizes[44] and the spread of stiffness values also changes with size. Defects that may relate to size[115] and the degree of crystallinity may be the reason for this. The initial shell displacement from equilibrium was assumed to be zero in the above simulations. However varying this parameter may have a great effect on the MB response since the residual stress and overpressure in the MB alter the dynamics. In the modelling of the contrast agent Sonovue^{TM} a model which accounts for the buckling and rupture of the lipid shell has been developed and agrees with several optically observed responses[78]. The effects of shell rupture and buckling may thus be important at higher driving amplitudes. The shell models used here to compare to the experimental responses from Definity® MBs do not account for this behaviour.

The response of the same MBs to multiple driving pulses has been tested optically and acoustically[78;132]. MBs have been observed to give different responses on subsequent insonations. Diffusion of the gas during the insonation and between the pulses may give rise to this change in response or the shell may be disrupted during the insonation or a combination of these effects may be responsible for the change in response. The change in the MB equilibrium state due to diffusion or shell disruption during insonation may give rise to disagreement of the experimental data with the theoretical models since the theoretical models used here to compare to the experimental data do not account for a change in MB equilibrium state during insonation.

5.6 Conclusion

Theoretical predictions of the response from Definity® MBs were compared rigorously to the experimentally measured response from single MBs. The shell parameters were estimated by comparing the theoretical models for a range of MI. The method of estimating the shell parameters of a MB from the acoustic response of single MBs is the first to the authors knowledge. The fundamental and second harmonic responses of MBs were compared to the theoretical prediction. The shell parameters that gave best statistical agreement were in close agreement with those measured previously from optical data. At higher driving amplitudes the theoretical models did not accurately predict the experimental response. While the theoretical models give good agreement at the lower driving amplitudes the models used here do not accurately model the contrast agent at higher driving amplitudes. The comparison of the acoustic response from single MBs to theoretical models could be further improved by measuring the radius of the MBs prior to insonation. This would allow direct comparison of theoretical and experimental MBs with the same radii. This technique is easily extended to comparing other time and frequency domain components of MBs that may refine the evaluation of theoretical models.

Chapter 6
Mechanisms of lipid-shelled microbubble decay: Diffusion vs Lipid shedding

6.1 Introduction

The lifetime of MBs is important in the clinical use of UCAs. From an imaging standpoint higher MI, that provides increased MB decay, is not favoured as live and continuous ultrasound imaging is not possible. However, the higher sensitivity that increased MI offers makes it attractive[129]. On the other hand, current imaging requires a sequence of pulses. Their design relies on the assumption of no-decay. Changes in the MB radius and shell overtime can greatly affect the scatter from the MB. An understanding of this process by means of mathematically formulated theory will facilitate pulse sequence design. It is known that fragmentation of a MB gives rise to rapid destruction of MBs and is dominant at high MI[5]. Molecular diffusion of the gas from a MB reduces the size and ultimately the scatter from a MB. In this chapter the experimentally measured multiple acoustic responses from single MBs are compared with the predictions of two theoretical models at low to medium MI, a molecular diffusion model and a new model to account for the loss of shell material.

6.2 Previous Work

Free gas MBs in saturated water will dissolve due to the pressure gradient caused by surface tension. The diffusion of gas in a static bubble due to surface tension was studied by Epstein and Plesset[35]. Numerical solutions for the diffusion of gas out of a bubble in an undersaturated solution and the growth of a bubble in an oversaturated solution were found. A model of the diffusion due to the radial motion of a bubble was derived by Eller and Flynn[30] using time averages from the RPNNP equation. This model was used by Church[20] to model the behaviour of micron sized bubbles at biomedical frequencies. The calculated growth rates compared well

to the experimentally measured growth rate for bubbles with radius less than 35 μm. The model developed by Fyrillas and Szeri[40] that couples the oscillation of the MB with the diffusion process was not necesscary since the timescale of the oscillation is over ten times less than the timescale of static diffusion.

The presence of the shell on a contrast agent reduces the rate of diffusion when compared to a free MB, which would dissolve in a degassed solution in under 1 s. Contrast MB agents will normally last for minutes if not hours[112]. The possible mechanisms responsible for the destruction of MBs have been investigated experimentally using a lipid shelled agent and a rigid shelled agent[18]. The decrease of diameter of the rigid shelled Albumin coated MBs and lipid shelled MBs was observed optically after the MBs were insonified by a single cycle 240 kPa pulse. The lipid shelled MBs were observed to experience little change in diameter between insonations but decreased in size after each driving pulse. The rigid shelled MBs were observed to decrease in diameter following insonation similar to a free MB dissolving. Using driving pulses of higher amplitude fragmentation of the lipid shelled agent was observed. Using the diffusion equation of Epstein and Plesset the response of lipid shelled MBs to low amplitude pulses following insonation by a high amplitude driving pulse was compared to theoretical predictions[5]. The theoretical predictions gave better agreement at higher driving amplitude provided fragmentation of the MB was included highlighting the need for including the effects of fragmentation at higher driving amplitudes.

The shell of an UCA slows down the diffusion of gas and a model to account for the effect of the shell on the diffusion of gas from a MB was developed by Borden and Longo[8]. Optical measurements on a lipid shelled agent confirmed as above that a single 10 μm bubble to reduce in radius. During the decrease in radius the shell was observed to become deformed and subsequently to return to its smooth spherical state. A mechanism responsible for the restoration of the shell to its spherical state called lipid shedding was proposed. The timescale for the diffusion of gas was much longer than the time required for the shell to return to its original smooth state. . Optical observations of the multiple responses from single Sonovue MBs have shown that the radius decreases with time and also that compression of the MB dominates as time increases[78]. A model to account for the buckling of the shell was developed. This model predicted the increase in the compression compared to the expansion as the MB equilibrium radius decreased to the buckling radius. The change in the shell properties contribute to the change in the response and not simply a change in the equilibrium radius of the MB.

An experimental data set of acoustic responses of single lipid-shelled Definity® MBs to multiple driving pulses is available. In this chapter a diffusion model, similar to that available in the literature,[30] and a newly developed model that accounts for the loss of shell material are used to create single MB acoustic response, which will be compared with the experiment . The new model was formulated on the experimental evidence that the change in MB equilibrium radius is greater after an insonation rather than between insonations[18] and that the shell can lose material[8].

6.3 Theory

Two theoretical models were used to model the time dependence of the MBs equilibrium state. The diffusion equation was used to model the molecular diffusion of gas out of the MB and a new model was proposed to account for lipid shedding. The new model was based on the previous experimental observations that the driving pulse has a greater effect on the change in MB equilibrium radius than the period of time between oscillations[18] and that the shell can lose material[8].

6.3.1 Diffusion

The Eller-Flynn Type equation is of the form

$$\dot{R} = \frac{DC_s}{\rho}\left(\frac{C_\infty}{C_s} - \frac{A}{B}\right)\left(A + R\left(\frac{B}{\pi D t}\right)^{\left(\frac{1}{2}\right)}\right), \tag{6.1}$$

where $\dot{R}$, D, C_s, C_∞, R and t are the MB wall velocity, the diffusion constant, the gas concentration in the liquid at the bubble wall, the gas concentration in the liquid at infinity, radius and time respectively. The constants A and B are constants found from the motion of the MB wall [30]. The duration of the motion of the MB is less than a tenth of the time between pulses where the MB is static so the motion of the MB is neglected and the constants A and B are set to 1. The liquid was assumed to be degassed so C_∞ was set to 0. The saturation concentration C_s is 0.024 Kg/m^3. This equation was used to simulate the diffusion of MBs.

6.3.2 Lipid shedding

Optical observations have shown that the shells of lipid shelled MBs can lose shell material[8]. This behaviour was observed when the gas dissolves out of the MB and the shell looses shell material to restore the shell to equilibrium. We propose that the loss of shell material from lipid shelled MBs may also be due to the acoustic oscillation. Two different assumptions on the shedding mechanism were considered: a. The amount shedding is such that the new shell equilibrium radius after the an insonation is linearly dependent on the minimum radius during the MB oscillation that precedes. b. The shell equilibrium radius is a constant distance from the post-insonation MB equilibrium radius and does not depend on the radius.

The lipid shedding is modelled by changing the equilibrium point of the shell while keeping the equilibrium point of the gas fixed. The coupled system of gas and shell that comprises the MB will then reach a new equilibrium where the pressures of the gas balance the pressures of the shell. The paramater that controls the change in the shell equilibrium, U (section 5.3.1), is varied to investigate the effect of shedding for the different shell models. The initial state of the MB before the first insonation by a driving pulse is assumed to be such that there is no residual stress on the shell of the MB i.e. the shell and gas equilibrium are equal. After the first insonation shedding is assumed to occur changing the shell equilibrium and introducing a non zero value of U into the equation of motion.

The shell equilibrium is included into the equations of motion of the Skalak and Mooney-Rivlin MBs in section 5.3.1. The loss of shell material is assumed to be proportional to the minimum radius such that the point at which there is no residual stress on the shell following an oscillation (the shell equilibrium), with minimum radius during the first oscillation R_{min}, is at $R_0 - \varepsilon(R_0 - R_{min})$, where $0 \leq \varepsilon \leq 1$ and R_0 are the lipid shedding parameter and the initial equilibrium radius of the bubble before insonation respectively. A value of 0 for ε, corresponds to no shedding and a value of 1 for ε corresponds to the shell having equilibrium at the minimum radius during the first driving pulse R_{min}. The shell equilibrium is not an equilibrium for the MB since the gas is compressed and exerts a greater pressure than the hydrostatic pressure. The equilibrium radius R_0' and initial displacement U' of the shell is found from the ideal gas law

$$PV = P'V', \tag{6.2}$$

where P is the pressure in the gas at equilibrium before the shedding occurs

$$P = \left(p_\infty + \frac{2\sigma}{R_0} + P_{SH}(R_0, U) \right), \tag{6.3}$$

V_0 is the initial volume of the MB at equilibrium, P_1 is the pressure in the gas at equilibrium after the shedding has occurred

$$P' = \left(p_\infty + \frac{2\sigma}{R_0'} + P_{SH}(R_0', U') \right) \tag{6.4}$$

and V_1 is the volume of the MB after the lipid shedding has occurred. The symbols p_∞, σ, R_0, R_0', $P_{SH}(R_0', U)$ and $P_{SH}(R_0', U')$ stand for the hydrostatic pressure, surface tension, equilibrium radius before shedding, equilibrium radius after shedding, pressure from the shell at equilibrium before shedding with shell deviation U and pressure from the shell at equilibrium after shedding with displacement U'. Before shedding the displacement U is assumed zero so there is no pressure due to the shell at equilibrium. After shedding the equilibrium radius and displacement change to restore the pressure balance. The new equilibrium radius and initial displacement are found numerically from equation 6.2.

6.4 Methodology

For each radius in the MB radius distribution the change in the equilibrium radius due to the molecular diffusion of gas out of the MB in between the ultrasound pulses was found using equation 6.1. The time between the insonations was 1 ms. The radius distribution after 1 ms was used to find the radial response. From the radial response the scattered pressure was found. The pressure waveform was then filtered to find the fundamental and harmonic response for a given radius. This was repeated over the radius distribution to give a distribution function for the fundamental RMS (root mean squared pressure) and harmonic RMS due to the insonation of a second pulse on the MBs.

The above process to calculate the change in MB distribution due to lipid shedding was implemented for each radius in the Definity® radius distribution to produce a new MB radius distribution and also a distribution of initial shell displacements due to the loss of shell given by equation 6.2. For each radius and initial displacement the numerical solution to 3.1 was found. From this the scattered pressure was found. This pressure waveform was then filtered

to find the fundamental and harmonic response for a given radius. This was repeated over the radius distribution to give a distribution function for the fundamental RMS (root mean squared pressure) and harmonic RMS due to the insonation of a second pulse on the MBs. In the previous chapter the shell stiffness and shell viscosities of the Skalak and Mooney-Rivlin models that gave best agreement were found to lie in the range of 0 MPa-5 MPa and 0.5 Pas-1 Pas respectively. Values of 0.5 MPa for the shell stiffness and 0.5 Pas for the shell viscosity were used in this chapter. As stated in the previous section two cases were considered for the shedding; a value dependent on the size of initial MB oscillation and a value independent of the size of initial MB oscillation. The lipid shedding parameter ε used was 1 or 0.5 and the constant shedding parameter was set at 0.1 μm and 0.2 μm.

Using the lipid shedding and the diffusion models the change in radius distribution of Definity® MBs was calculated 1 μs following the insonation to driving amplitudes of 160 kPa, 275 kPa, 375 kPa and 550 kPa with a centre frequency of 1.6 MHz. The post-insonation radius and shell deviation distribution was then used to calculate the distribution of fundamental and harmonic RMS to the second pulse of the same driving amplitude and centre frequency

The ratio of the fundamental or harmonic response from the second driving pulse to the fundamental or harmonic response from the first driving pulse of random samples of MBs from the theoretical distributions were found as described in section 4.2.3 and are plotted against the experimental responses from single MBs for each driving amplitude in figures 6.5-6.18.

6.5 Results

6.5.1 Effect of initial shell displacement on constitutive law

When the residual stress on the shell at equilibrium is nonzero (when U in equations 3.5,3.4) is nonzero) the radial response of the MB is altered. The fundamental, harmonic, subharmonic, ultraharmonic, expansion and compression are shown for Skalak and Mooney-Rivlin MBs with a shell stiffness of 0.5 MPa and a shell viscosity of 0.5 Pas for a range of Radii at a driving frequency of 1 MHz for MI of 0.025 to 0.2 in figures 6.2,6.1 respectively.

The resonance peak of the Mooney-Rivlin MBs with and without a shell displacement of one half the equilibrium radius are similar figure 6.1, while the Skalak MBs present differences figure 6.2. The resonance peaks, at the lowest driving amplitude, of the fundamental, harmonic,

expansion and compression are at 4 μm for the Mooney-Rivlin model with and without an initial shell displacement. For the Skalak model with an initial shell displacement the resonance peaks, at the lowest driving amplitude, of the fundamental, harmonic, expansion and compression are at 5 μm. From chapter 3 we know that the resonance radius increases as the shell stiffness increases. The shift in the resonance in figures 6.2(d), 6.2(e), 6.2(f) is due to an increased effective shell stiffness and also due to the increased residual stress. The effective shell stiffness G_{Seff} is found from the linearisation of equation 5.5 and equation 5.6 around the MB equilibrium radius

$$P_{Shell} = 12\frac{d_{Se}G_{Seff}}{R_0'}\epsilon + \eta_S 12\frac{d_{Se}}{R_0'}\dot{\epsilon} + P_{Residual}, \tag{6.5}$$

where $R = R_0'(1+\varepsilon)$ and the other variables are as in equation 3.7. This is the same form as equation 3.7 but with the residual stress $P_{Residual}$ added and the effective shell stiffness G_{Seff} instead of the shell stiffness G_S. Ignoring the viscosity we see that the residual stress is the pressure due to the shell at the MB equilibrium radius in figure 6.3. Differentiating equation 6.5 we find

$$\frac{DP_{Shell}}{D\epsilon} = 2\frac{d_{Se}G_{Seff}}{R}. \tag{6.6}$$

Hence the effective shell stiffness is directly proportional to the slope of the shell stiffness curves in figure 6.3. When the shell deviation is zero the effective shell stiffness G_{Seff} is equal to the shell stiffness G_S and is the same for the Skalak, Mooney-Rivlin, and Kelvin-Voigt models. When the shell deviation is one half the equilibrium radius the residual stress and the effective shell stiffness of the Skalak model are both much larger in the Mooney-Rivlin and Kelvin-Voigt models figure 6.3(b).

6.5.2 Experimental Comparison

Using the lipid shedding and the diffusion models the change in radius distribution of Definity® MBs was calculated 1 μs following the insonation to driving amplitudes of 160 kPa, 275 kPa, 375 kPa and 550 kPa with a centre frequency of 1.6 MHz. The post-insonation radius and shell deviation distribution was then used to calculate the distribution of fundamental and harmonic RMS for the second pulse of the same driving amplitude and centre frequency.

The shell stiffness and shell viscosities of the Skalak and Mooney-Rivlin models that gave best agreement in the previous chapter were found to lie in the range of 0 MPa-5 MPa and 0.5 Pas-1

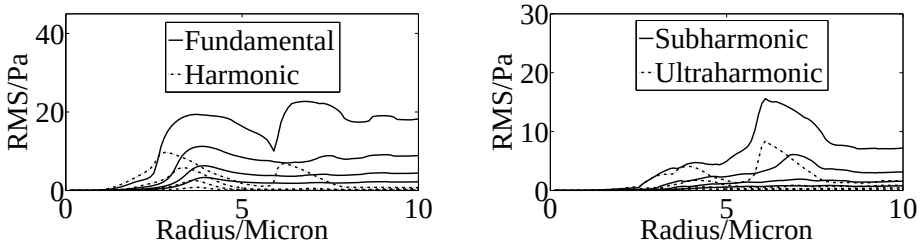

(a) Fundamental and Harmonic

(b) Subharmonic and Ultraharmonic

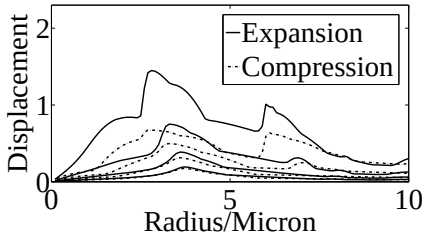

(c) Expansion and Compression

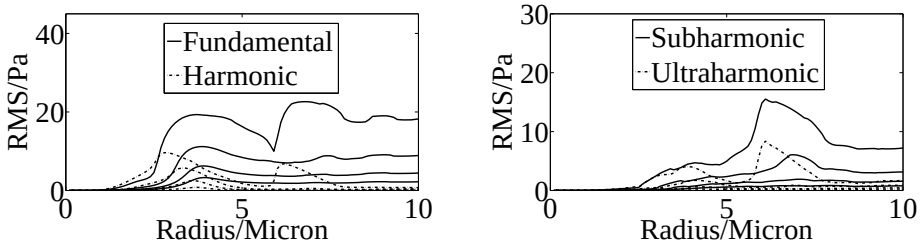

(d) Fundamental and Harmonic

(e) Subharmonic and Ultraharmonic

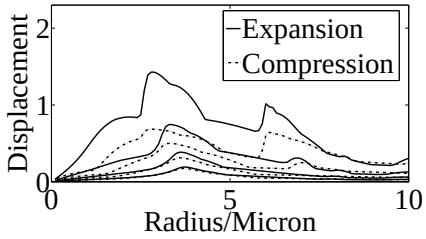

(f) Expansion and Compression

Figure 6.1: *The radius distribution and distribution of shell displacements of MBs when there is no initial shell displacement (figures 6.1(a),6.1(b),6.1(c)) and when the initial shell displacement is one half of the equilibrium radius (figures 6.1(d),6.1(e),6.1(f)) of the Mooney-Rivlin model. The shell stiffness was 0.5 MPa and the shell viscosity was 1 Pas. The resonance peaks are not greatly affected when an initial shell displacement of one half the equilibrium radius was introduced.*

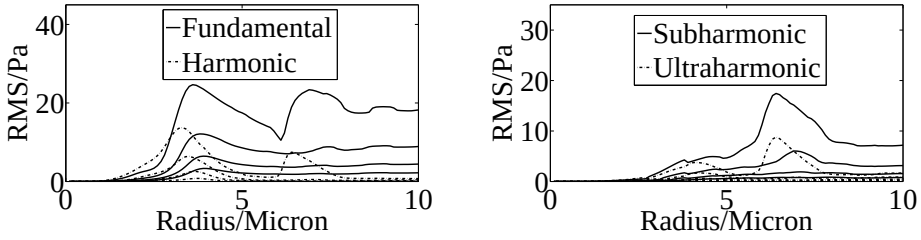

(a) Fundamental and Harmonic

(b) Subharmonic and Ultraharmonic

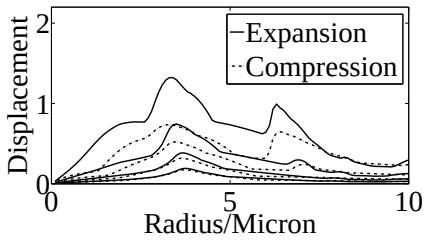

(c) Expansion and Compression

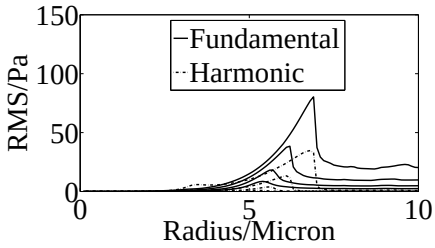

(d) Fundamental and Harmonic

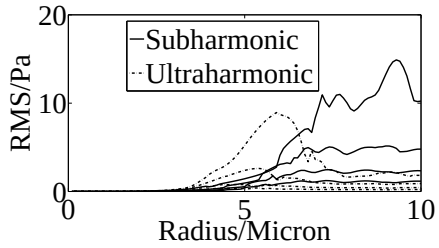

(e) Subharmonic and Ultraharmonic

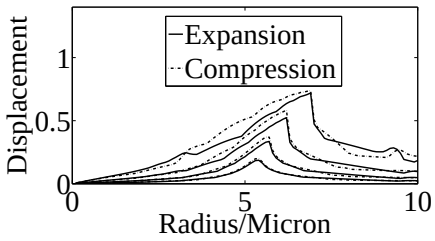

(f) Expansion and Compression

Figure 6.2: *The radius distribution and distribution of shell displacements of MBs when there is no initial shell displacement (figures 6.2(a),6.2(b),6.2(c)) and when the initial shell displacement is one half of the equilibrium radius (figures 6.2(d),6.2(e),6.2(f)) of the Skalak model. The shell stiffness was 0.5 MPa and the shell viscosity was 1 Pas. The resonance peaks are shifted to larger radii when an initial shell displacement of one half the equilibrium radius was introduced.*

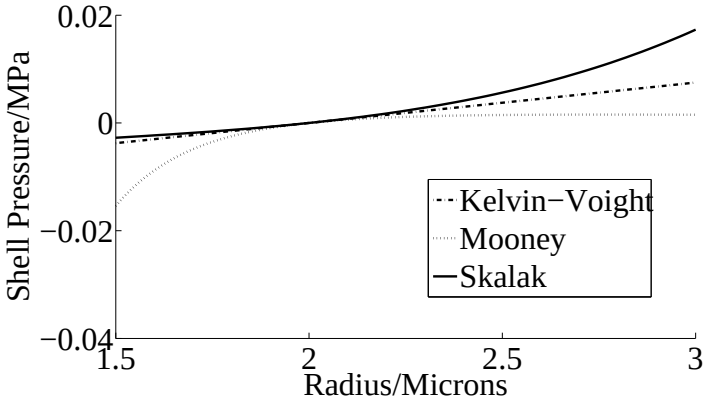

(a) Initial shell displacement is at 2μm

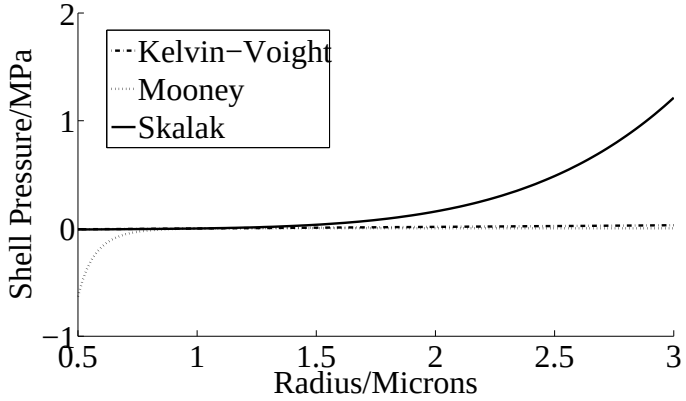

(b) Initial shell displacement is at 1μm

Figure 6.3: *The pressure due to the shell as a function of MB radius for the Skalak, Mooney-Rivlin, and Kelvin-Voigt models with shell equilibrium at 2 μm (figure. 6.4(a)) and with shell equilibrium at 1 μm (figure 6.4(b)) for MB with a 2 μm equilibrium radius. When the shell equilibrium is at 2 μm the Skalak, Mooney-Rivlin, and Kelvin-Voigt models are equivalent (figure 6.3(a)). When the shell equilibrium is at 1 μm the Skalak model has an increased effective shell stiffness while the Mooney-Rivlin model has a decreased effective shell stiffness (figure 6.3(b)).*

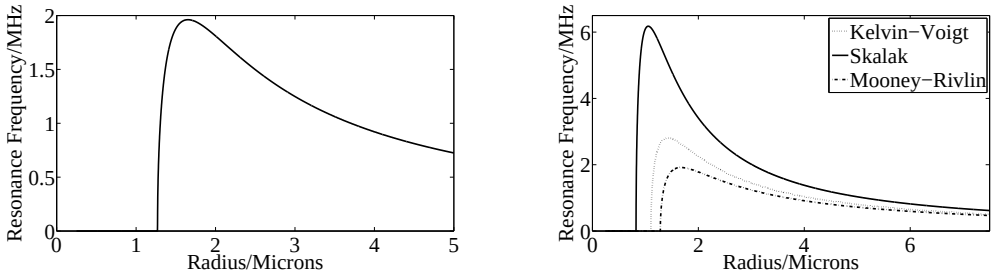

(a) Initial shell displacement is at 2μm

(b) Initial shell displacement is at 1μm

Figure 6.4: *The resonance curves of the Skalak, Mooney-Rivlin, and Kelvin-Voigt models with shell equilibrium at 2 μm (figure 6.4(a)) and with shell equilibrium at 1 μm (figure 6.4(b)) for a 2 μm MB. When the shell equilibrium is at 2 μm the Skalak, Mooney-Rivlin, and Kelvin-Voigt models are equivalent and so the resonance curve is equivalent (figure 6.4(a)). When the shell equilibrium is at 1 μm the Skalak models resonance frequency at a given radius is greater than the resonance frequency of the Kelvin-Voigt and Mooney-Rivlin models since the effective shell stiffness and residual shell stress is greater (figure 6.4(b)).*

Pas respectively. Values of 0.5 MPa for the shell stiffness and 0.5 Pas for the shell viscosity were used in this chapter. A value of 0 MPa for the shell stiffness was not used since in that case the shedding of lipid from the MB would have no affect on dynamics of the MB.

The lipid shedding parameter ε used was 1 or 0.5 and the constant shedding parameter was set at 0.1 μm and 0.2 μm. The ratio of the fundamental or harmonic response from the second driving pulse to the fundamental or harmonic response from the first driving pulse of random samples of MBs from the theoretical distributions were found as described in section 4.2.3 and are plotted against the experimental responses from single MBs for each driving amplitude in figures 6.5-6.18.

6.5.2.1 Diffusion

Using the radius distribution found from the equation 6.1 the ratio of the fundamental or harmonic response from the second driving pulse to the fundamental or harmonic response from the first driving pulse of random samples of MBs from the theoretical distributions of the Mooney-Rivlin and Skalak models are plotted with the experimental data in figure 6.5-6.8.

For driving amplitudes of 160 kPa and 275 kPa the ratio of the second fundamental or harmonic response to the first fundamental or harmonic response from the Mooney-Rivlin and

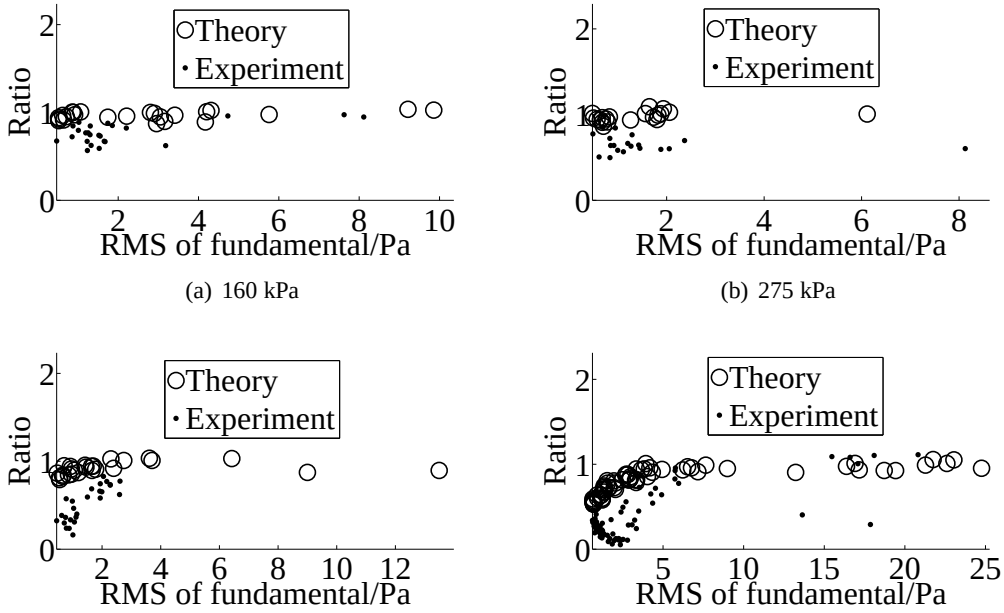

(a) 160 kPa

(b) 275 kPa

(c) 375 kPa

(d) 550 kPa

Figure 6.5: *The ratio of the second fundamental response to the first fundamental response against the first fundamental response of MBs chosen at random from the theoretical distribution of the Mooney-Rivlin MBs are plotted with the experimental response from single MBs for driving amplitudes of 160 kPa, 275 kPa, 375 kPa and 550 kPa. For the second insonation the radius distribution of MBs after molecular diffusion over a timescale of 1 μs occurred was used. The shell stiffness is 0.5 MPa and the shell viscosity is 0.5 Pas.*

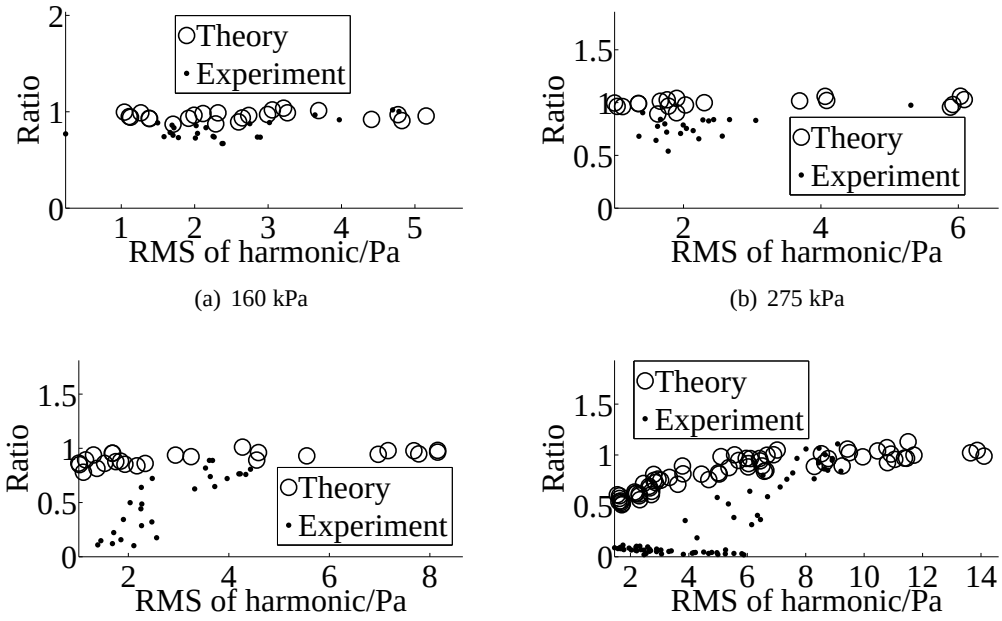

(a) 160 kPa

(b) 275 kPa

(c) 375 kPa

(d) 550 kPa

Figure 6.6: *The ratio of the second harmonic response to the first harmonic response against the first harmonic response of MBs chosen at random from the theoretical distribution of the Mooney-Rivlin MBs are plotted with the experimental response from single MBs for driving amplitudes of 160 kPa, 275 kPa, 375 kPa and 550 kPa. For the second insonation the radius distribution of MBs after molecular diffusion over 1 μs occurred was used. The shell stiffness is 0.5 MPa and the shell viscosity is 0.5 Pas.*

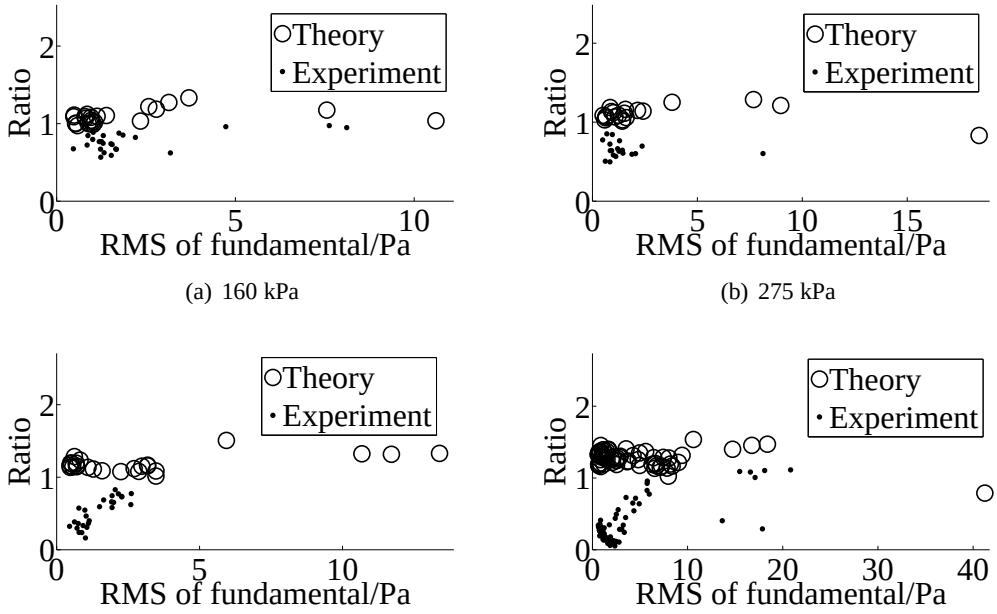

(a) 160 kPa

(b) 275 kPa

(c) 375 kPa

(d) 550 kPa

Figure 6.7: *The ratio of the second fundamental response to the first fundamental response against the first fundamental response of MBs chosen at random from the theoretical distribution of the Skalak MBs are plotted with the experimental response from single MBs for driving amplitudes of 160 kPa, 275 kPa, 375 kPa and 550 kPa. For the second insonation the radius distribution of MBs after molecular diffusion over 1 μs occurred was used. The shell stiffness is 0.5 MPa and the shell viscosity is 0.5 Pas.*

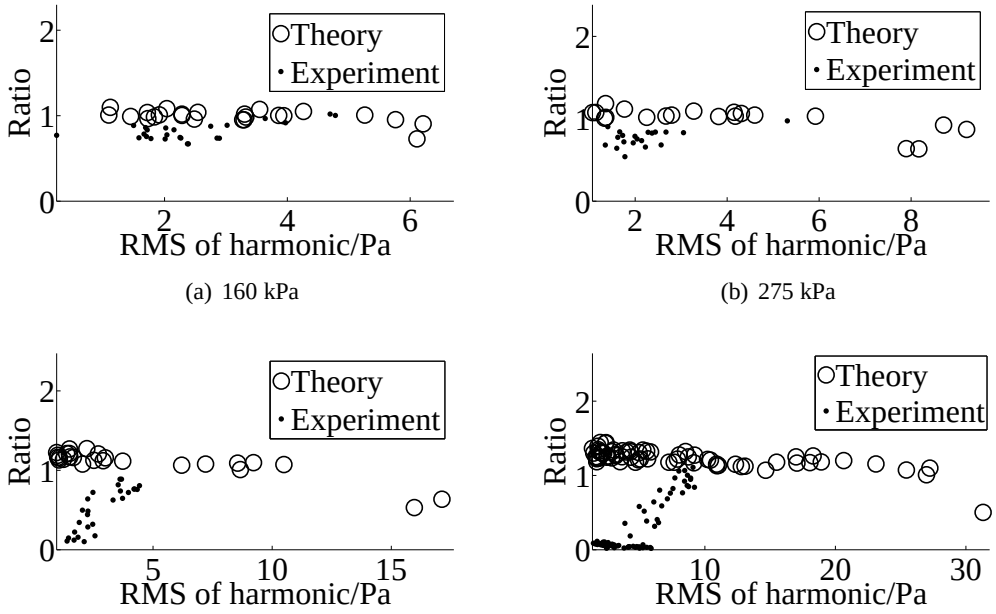

Figure 6.8: *The ratio of the second harmonic response to the first harmonic response against the first harmonic response of MBs chosen at random from the theoretical distribution of the Skalak MBs are plotted with the experimental response from single MBs for driving amplitudes of 160 kPa, 275 kPa, 375 kPa and 550 kPa. For the second insonation the radius distribution of MBs after molecular diffusion over 1 μs occurred was used. The shell stiffness is 0.5 MPa and the shell viscosity is 0.5 Pas.*

Skalak models using the diffusion model is not below 0.8 at each of these driving amplitudes (figures 6.5(a), 6.6(a), 6.5(b), 6.6(b), 6.7(a), 6.8(a), 6.7(b) and 6.8(b)). The ratio of the second fundamental or harmonic to the first fundamental or harmonic from Mooney-Rivlin and Skalak MBs using the diffusion model is not below 0.75 at a driving amplitude of 375 kPa (figures 6.5(c), 6.6(c), 6.7(c) and 6.8(c)). At a driving amplitude of 550 kPa the ratio of the second fundamental or harmonic to the first fundamental or harmonic from Mooney-Rivlin MBs has a minimum of 0.5 at the lowest first fundamental or harmonic response. This then increases to 1 as the first fundamental response increases (figures 6.5(d) and 6.6(d)). For all of the driving pulses the ratio of the second fundamental or harmonic to the first fundamental or harmonic from Skalak MBs using the diffusion model is greater than 1 for most of the MBs (figures 6.7 and 6.8). The diffusion model predicts a much lower decrease in acoustic response than has been measured experimentally.

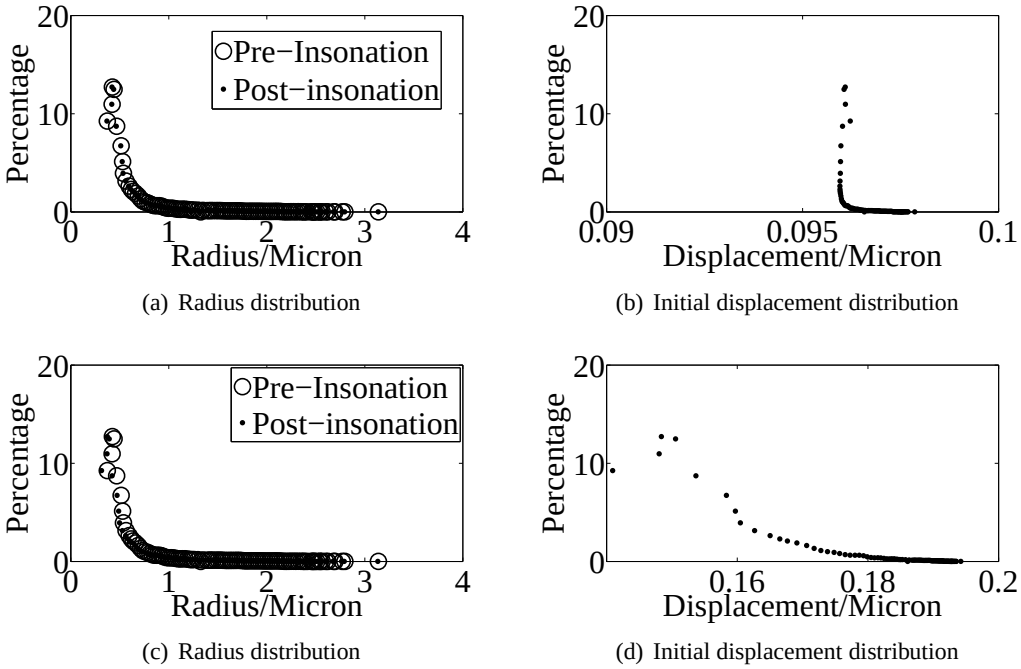

(a) Radius distribution

(b) Initial displacement distribution

(c) Radius distribution

(d) Initial displacement distribution

Figure 6.9: *The radial and shell displacement distributions of Definity® (Lantheus Medical Imaging,N Belarica, MA) MBs when lipid shedding reduces the shell equilibrium by 0.2 μm for the Skalak (figures a and b) and Mooney-Rivlin (figures c and d) models. The change in the radial distribution is greater for the Skalak model than the Mooney-Rivlin model.*

6.5.2.2 Shedding

An example of the radial distributions before and after shedding and the distribution of initial displacements is shown in figure 6.9. Using the radius distribution and the distribution of initial displacements found from the lipid shedding model with ε set to 1 the ratio of the fundamental or harmonic response from the second driving pulse to the fundamental or harmonic response from the first driving pulse of random samples of MBs from the theoretical distributions of the Mooney-Rivlin model with a shell stiffness of 0.5 MPa and a shell viscosity of 0.5 Pas are plotted with the experimental responses from single MBs for each driving amplitude in (figures 6.11-6.18).

The ratio of second fundamental or harmonic to first fundamental or harmonic from Mooney-Rivlin MBs using the lipid shedding model with ε set to 1 was not below 0.75 at all the driving amplitudes. Some Mooney-Rivlin MBs have a ratio of second fundamental or harmonic to first fundamental or harmonic greater than 1. Skalak MBs had a ratio of the second fundamental

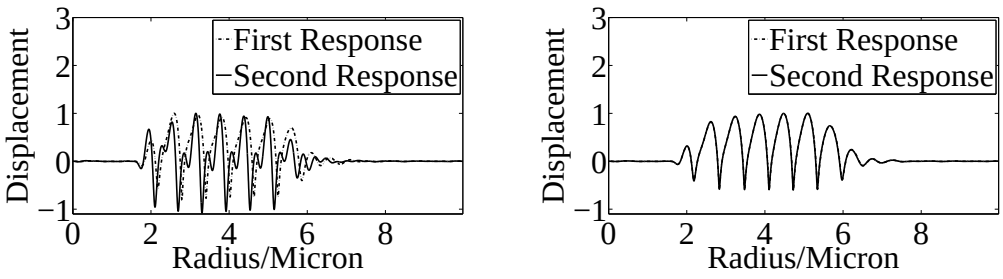

(a) Skalak (b) Mooney-Rivlin

Figure 6.10: *The first and second relative displacement of a 2.08 μm Skalak and Mooney-Rivlin MB due to a six cycle 160 kPa driving pulse. The Mooney-Rivlin MB is unchanged while the radial oscillation relative to the equilibrium radius is reduced in the Skalak model. The shell equilibrium is set at the minimum radius (ε is 0) during the first oscillation. The equilibrium radius of the Mooney-Rivlin MB is reduced to 2.07 μm after the first pulse and the equilibrium radius of the Skalak MB is reduced to 1.86 μm. The first and second pulse of the Mooney-Rivlin MB and the first pulse of the Skalak MB are expansion dominated while the second response from the Skalak MB is compression dominated.*

response to the first fundamental response of 0.5 at the lowest first fundamental response for all the driving pulses (figure 6.13). This decreased to close to zero at the highest first fundamental response (figure 6.13). At a driving amplitude of 160 kPa the ratio of the second harmonic response to the first harmonic response of below 0.75 for all values of first harmonic response. (figure 6.14). At driving amplitudes of 275 kPa, 375 kPa and 550 kPa Skalak MBs had a ratio of the second harmonic response to the first harmonic response of 0.5 at the lowest first harmonic response (figure 6.13). This decreased to close to zero at the highest first harmonic response unlike the experimental data (figure 6.13).

The radial response of a 2.08 μm Skalak and Mooney-Rivlin MB to two insonations from a 160 kPa driving pulse is shown in figure 6.10. The radial response of both MBs to the first pulse is expansion dominated . The radial response of the Mooney-Rivlin MB to the second pulse is almost identical but the radial response of the Skalak MB to the second response is reduced and is compression dominated.

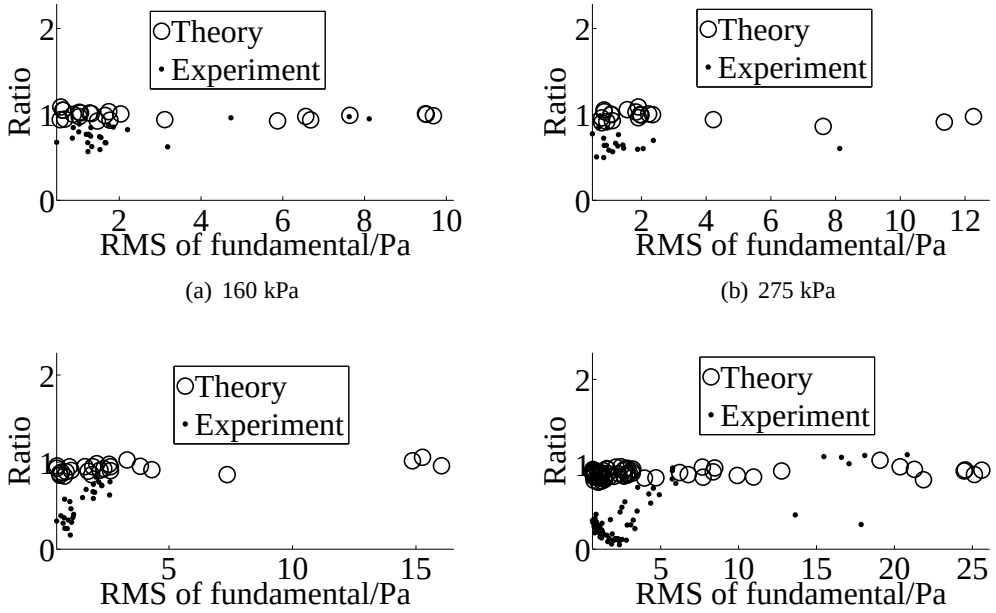

Figure 6.11: *The ratio of the second fundamental response to the first fundamental response against the first fundamental response of MBs chosen at random from the theoretical distribution of the Mooney-Rivlin MBs are plotted with the experimental response from single MBs for driving amplitudes of 160 kPa, 275 kPa, 375 kPa and 550 kPa. For the second insonation the radius distribution of MBs after lipid shedding occurred was used. A value for the lipid shedding factor ε of 1 was used. The shell stiffness is 0.5 MPa and the shell viscosity is 0.5 Pas.*

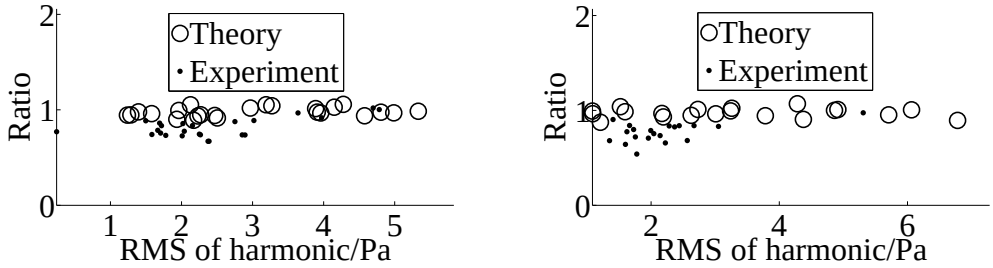

(a) 160 kPa

(b) 275 kPa

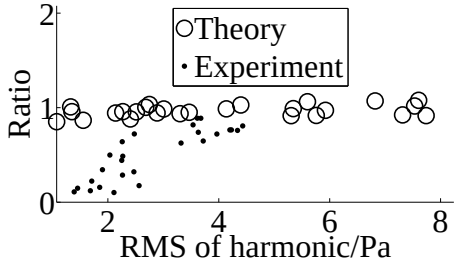

(c) 375 kPa

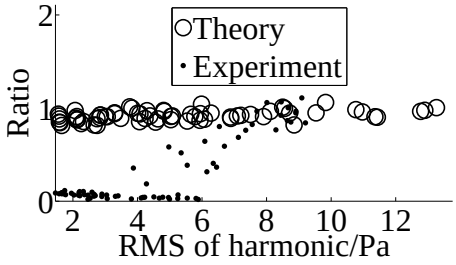

(d) 550 kPa

Figure 6.12: *The ratio of the second harmonic response to the first harmonic response against the first harmonic response of MBs chosen at random from the theoretical distribution of the Mooney-Rivlin MBs are plotted with the experimental response from single MBs for driving amplitudes of 160 kPa, 275 kPa, 375 kPa and 550 kPa. For the second insonation the radius distribution of MBs after lipid shedding occurred was used. A value for the lipid shedding factor ε of 1 was used. The shell stiffness is 0.5 MPa and the shell viscosity is 0.5 Pas.*

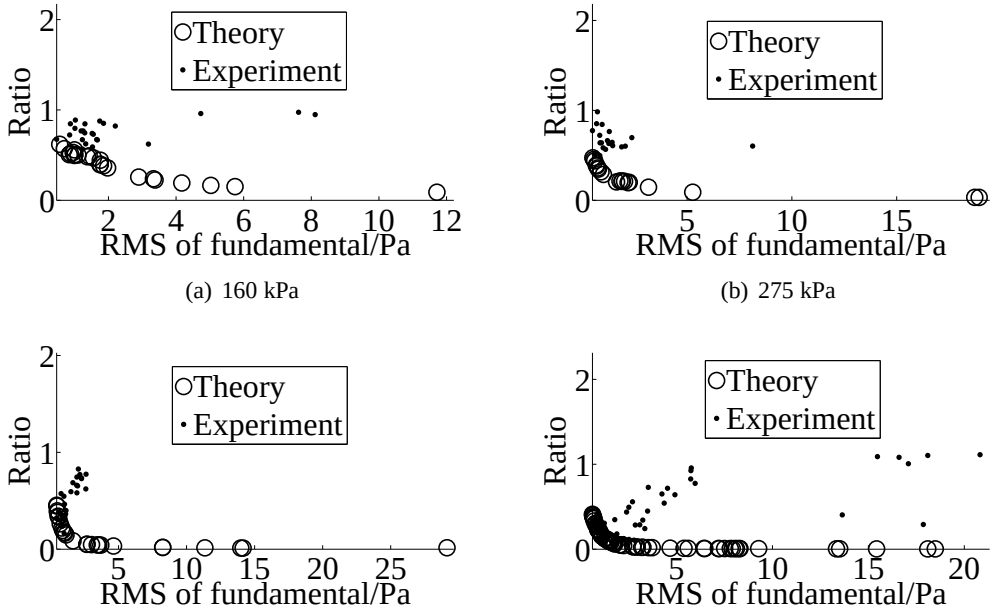

(a) 160 kPa

(b) 275 kPa

(c) 375 kPa

(d) 550 kPa

Figure 6.13: *The ratio of the second fundamental response to the first fundamental response against the first fundamental response of MBs chosen at random from the theoretical distribution of the Skalak MBs are plotted with the experimental response from single MBs for driving amplitudes of 160 kPa, 275 kPa, 375 kPa and 550 kPa. For the second insonation the radius distribution of MBs after lipid shedding occurred was used. A lipid shedding factor ε of 1 was used. The shell stiffness is 0.5 MPa and the shell viscosity is 0.5 Pas.*

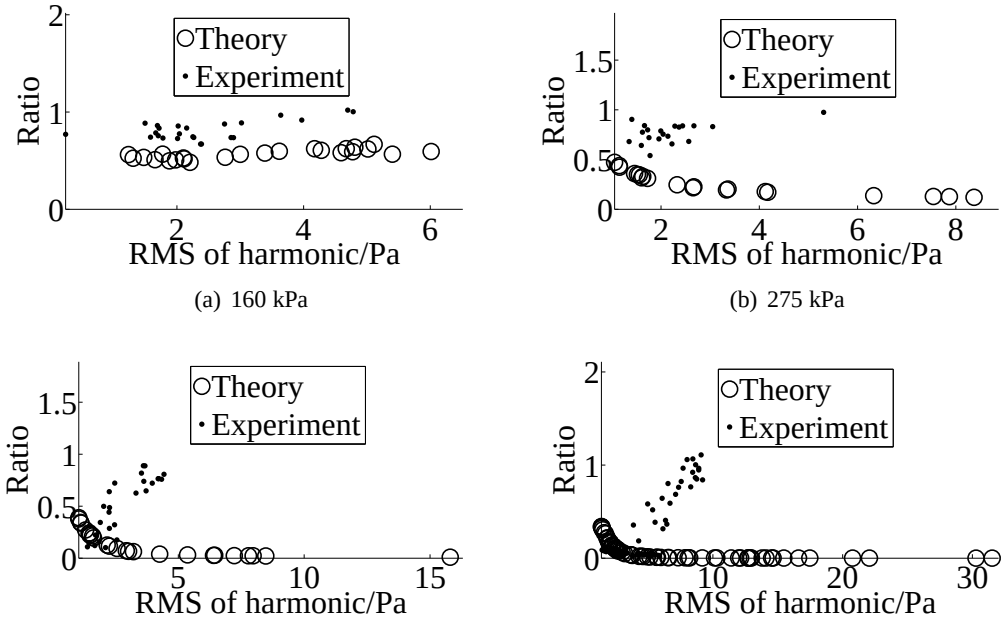

Figure 6.14: *The ratio of the second harmonic response to the first harmonic response against the first harmonic response of MBs chosen at random from the theoretical distribution of the Skalak MBs are plotted with the experimental response from single MBs for driving amplitudes of 160 kPa, 275 kPa, 375 kPa and 550 kPa. For the second insonation the radius distribution of MBs after lipid shedding occurred was used. A lipid shedding factor ε of 1 was used. The shell stiffness is 0.5 MPa and the shell viscosity is 0.5 Pas.*

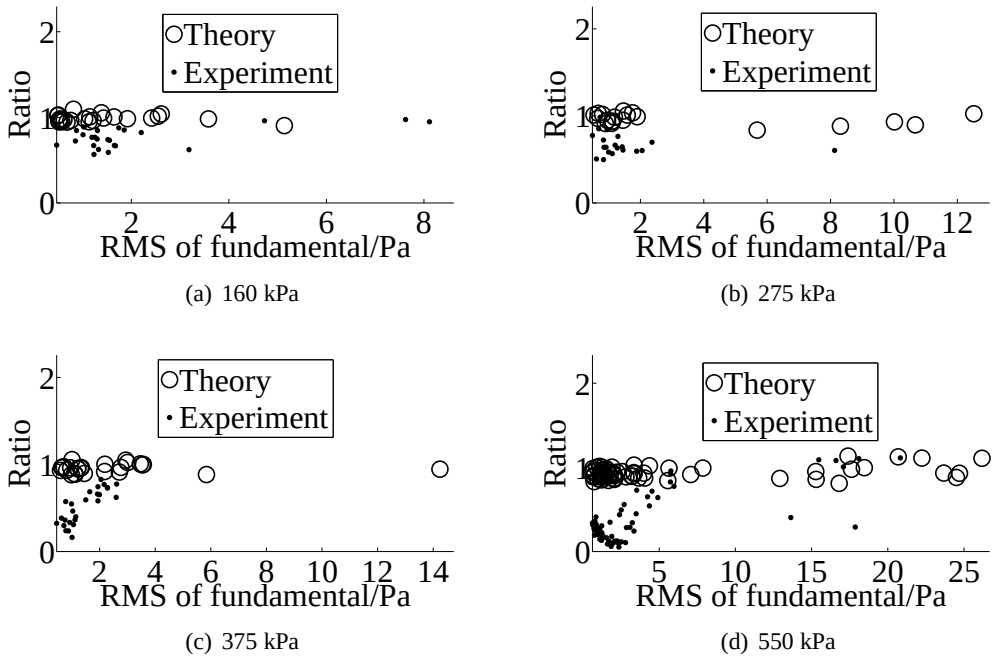

Figure 6.15: *The ratio of the second fundamental response to the first fundamental response against the first fundamental response of MBs chosen at random from the theoretical distribution of the Mooney-Rivlin MBs are plotted with the experimental response from single MBs for driving amplitudes of 160 kPa, 275 kPa, 375 kPa and 550 kPa. For the second insonation the radius distribution of MBs after lipid shedding occurred was used. A lipid shedding factor ε of 0.5 was used. The shell stiffness is 0.5 MPa and the shell viscosity is 0.5 Pas.*

Using the radius distribution and the distribution of initial displacements found from the lipid shedding model with ε set to 1 the ratio of the fundamental or harmonic response from the second driving pulse to the fundamental or harmonic response from the first driving pulse of random samples of MBs from the theoretical distributions of the Mooney-Rivlin model with a shell stiffness of 0.5 MPa and a shell viscosity of 0.5 Pas are plotted with the experimental responses from single MBs for each driving amplitude in (figures 6.11-6.18).

The ratio of second fundamental or harmonic to first fundamental or harmonic from Mooney-Rivlin MBs using the lipid shedding model with ε set to 1 not below 0.75 at all the driving amplitudes. Some Mooney-Rivlin MBs have a ratio of second fundamental or harmonic to first fundamental or harmonic greater than 1 which was above that found experimentally. Skalak MBs had a ratio of the second fundamental response to the first fundamental response of close to 1 at the lowest first fundamental response for all the driving pulses (figure 6.13). This decreased

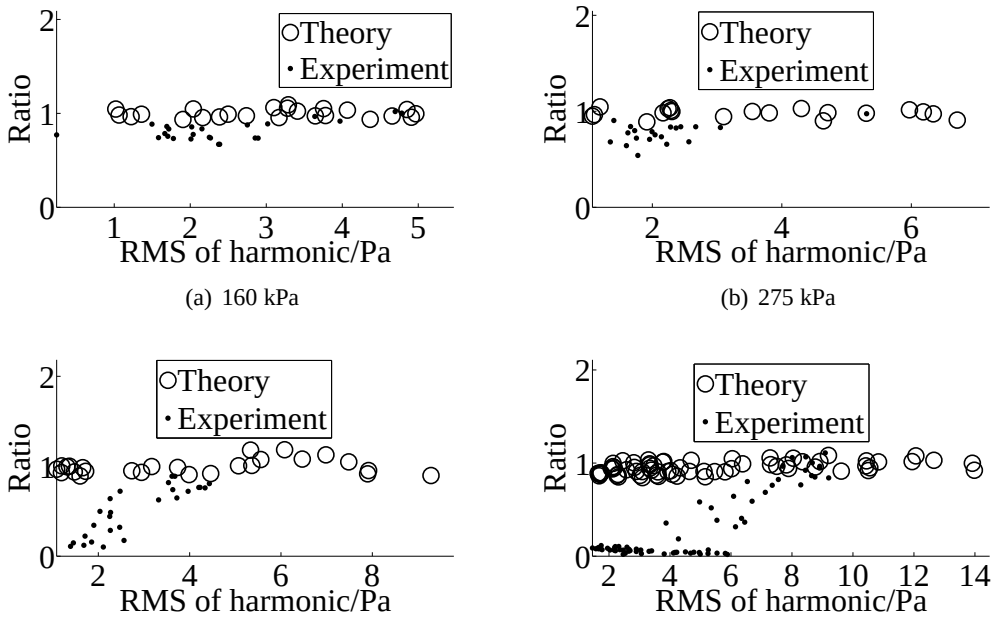

(a) 160 kPa

(b) 275 kPa

(c) 375 kPa

(d) 550 kPa

Figure 6.16: *The ratio of the second harmonic response to the first harmonic response against the first harmonic response of MBs chosen at random from the theoretical distribution of the Mooney-Rivlin MBs are plotted with the experimental response from single MBs for driving amplitudes of 160 kPa, 275 kPa, 375 kPa and 550 kPa. For the second insonation the radius distribution of MBs after lipid shedding occurred was used. A lipid shedding factor ε of 0.5 was used. The shell stiffness is 0.5 MPa and the shell viscosity is 0.5 Pas.*

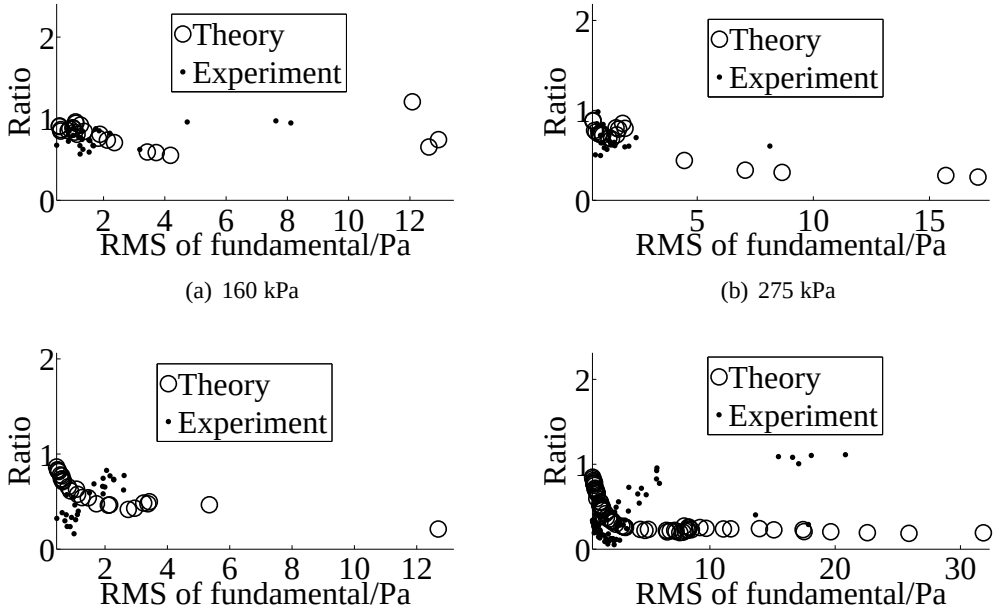

(a) 160 kPa

(b) 275 kPa

(c) 375 kPa

(d) 550 kPa

Figure 6.17: *The ratio of the second fundamental response to the first fundamental response against the first fundamental response of MBs chosen at random from the theoretical distribution of the Skalak MBs are plotted with the experimental response from single MBs for driving amplitudes of 160 kPa, 275 kPa, 375 kPa and 550 kPa. For the second insonation the radius distribution of MBs after lipid shedding occurred was used. A lipid shedding factor ε of 0.5 was used. The shell stiffness is 0.5 MPa and the shell viscosity is 0.5 Pas.*

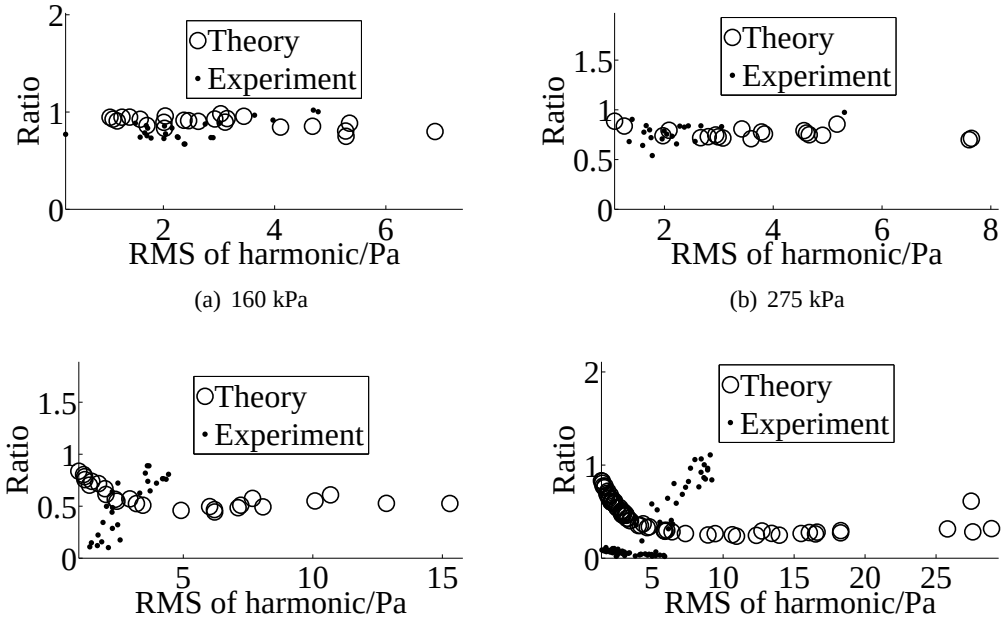

(a) 160 kPa

(b) 275 kPa

(c) 375 kPa

(d) 550 kPa

Figure 6.18: *The ratio of the second harmonic response to the first harmonic response against the first harmonic response of MBs chosen at random from the theoretical distribution of the Skalak MBs are plotted with the experimental response from single MBs for driving amplitudes of 160 kPa, 275 kPa, 375 kPa and 550 kPa. For the second insonation the radius distribution of MBs after lipid shedding occurred was used. A lipid shedding factor ε of 0.5 was used. The shell stiffness is 0.5 MPa and the shell viscosity is 0.5 Pas.*

to close to zero at the highest first fundamental response (figure 6.13). At driving amplitudes of 160 kPa and 275 kPa the ratio of the second harmonic response to the first harmonic response of below 0.75 for all values of first harmonic response (figure 6.14). At driving amplitudes of 375 kPa and 550 kPa Skalak MBs had a ratio of the second harmonic response to the first harmonic response of 0.5 at the lowest first harmonic response (figure 6.13). This decreased to close to below 0.5 at higher first harmonic responses (figure 6.13).

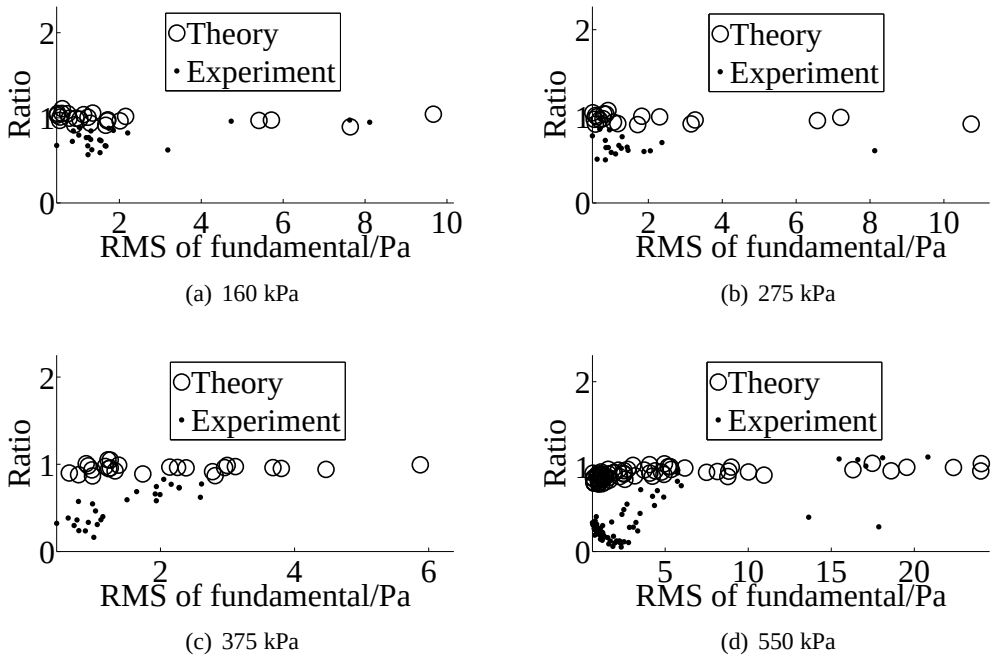

Figure 6.19: *The ratio of the second fundamental response to the first fundamental response against the first fundamental response of MBs chosen at random from the theoretical distribution of the Mooney-Rivlin MBs are plotted with the experimental response from single MBs for driving amplitudes of 160 kPa, 275 kPa, 375 kPa and 550 kPa. For the second insonation the radius distribution of MBs after lipid shedding occurred was used. The shell equilibrium was 0.1 μm from the initial equilibrium radius. The shell stiffness is 0.5 MPa and the shell viscosity is 0.5 Pas.*

Using the radius distribution found from the lipid shedding model with a shell equilibrium at a radius of $R_0 - 0.1\mu$m, where R_0 is the equilibrium radius of the MB before the first insonation the ratio of the fundamental or harmonic response from the second driving pulse to the fundamental or harmonic response from the first driving pulse of random samples of MBs from the theoretical distributions of the Mooney-Rivlin model with a shell stiffness of 0.5 MPa and a shell viscosity of 0.5 Pas are plotted with the experimental responses from single MBs for each driving amplitude in figures 6.11-6.18.

The ratio of second fundamental or harmonic to first fundamental or harmonic from Mooney-Rivlin MBs is not below 0.75 at all driving amplitudes (figures 6.19 and 6.20). Skalak MBs had a ratio of second fundamental or harmonic to first fundamental or harmonic that was not below 0.75 at all driving amplitudes unlike the experimental data.

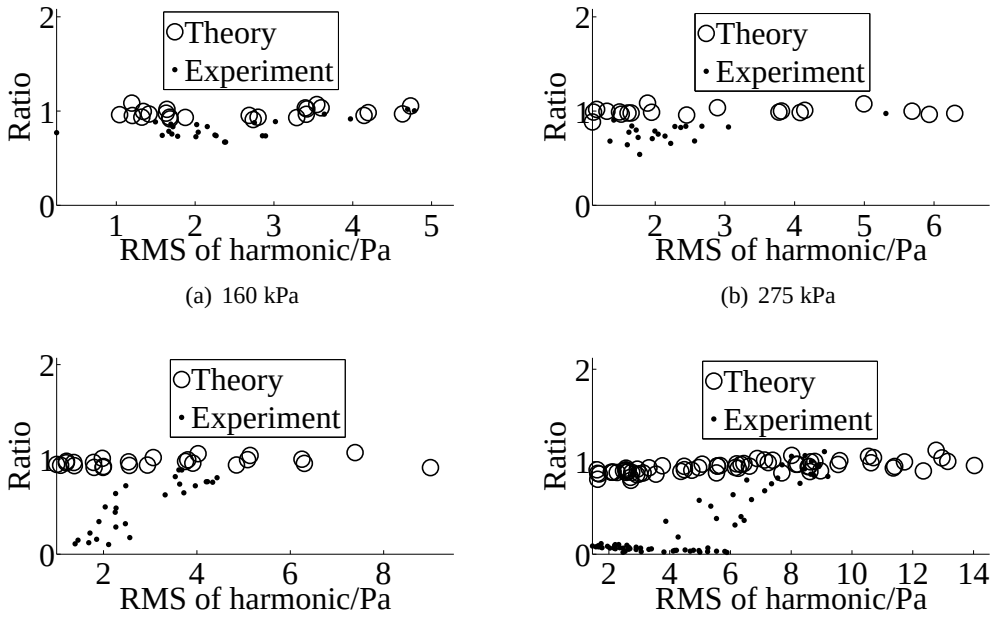

(a) 160 kPa

(b) 275 kPa

(c) 375 kPa

(d) 550 kPa

Figure 6.20: *The ratio of the second harmonic response to the first harmonic response against the first harmonic response of MBs chosen at random from the theoretical distribution of the Mooney-Rivlin MBs are plotted with the experimental response from single MBs for driving amplitudes of 160 kPa, 275 kPa, 375 kPa and 550 kPa. For the second insonation the radius distribution of MBs after lipid shedding occurred was used. The shell equilibrium was 0.1 μm from the initial equilibrium radius. The shell stiffness is 0.5 MPa and the shell viscosity is 0.5 Pas.*

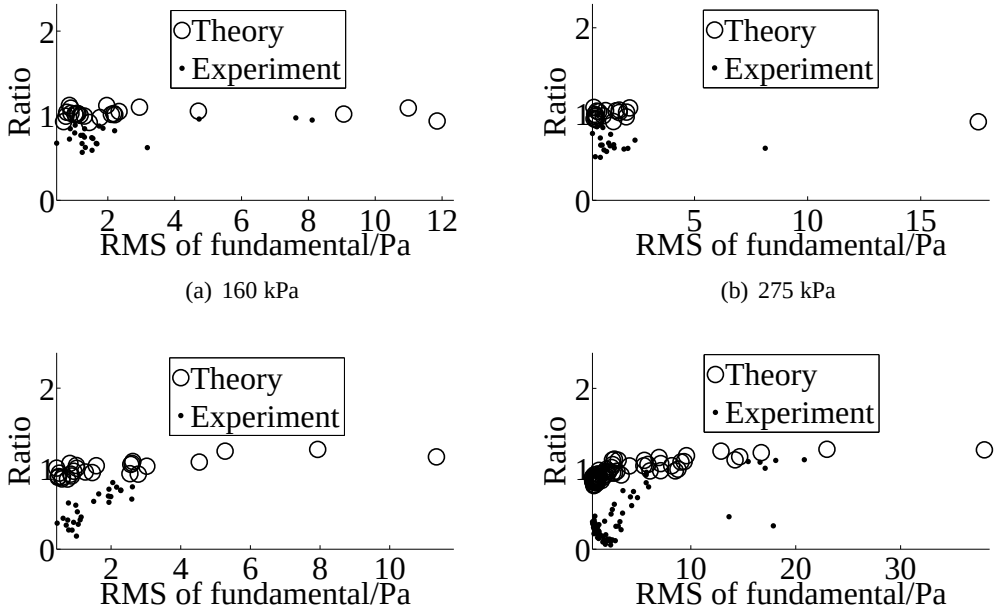

(a) 160 kPa

(b) 275 kPa

(c) 375 kPa

(d) 550 kPa

Figure 6.21: *The ratio of the second fundamental response to the first fundamental response against the first fundamental response of MBs chosen at random from the theoretical distribution of the Skalak MBs are plotted with the experimental response from single MBs for driving amplitudes of 160 kPa, 275 kPa, 375 kPa and 550 kPa. For the second insonation the radius distribution of MBs after lipid shedding occurred was used. The shell equilibrium was 0.1 μm from the initial equilibrium radius. The shell stiffness is 0.5 MPa and the shell viscosity is 0.5 Pas.*

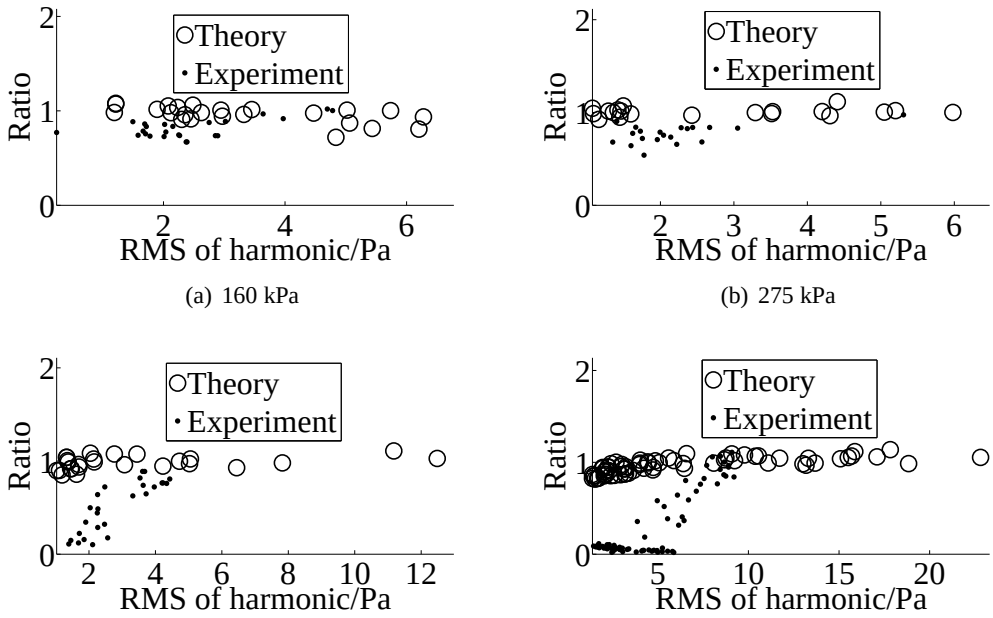

(a) 160 kPa

(b) 275 kPa

(c) 375 kPa

(d) 550 kPa

Figure 6.22: *The ratio of the second harmonic response to the first harmonic response against the first harmonic response of MBs chosen at random from the theoretical distribution of the Skalak MBs are plotted with the experimental response from single MBs for driving amplitudes of 160 kPa, 275 kPa, 375 kPa and 550 kPa. For the second insonation the radius distribution of MBs after lipid shedding occurred was used. The shell equilibrium was 0.1 μm from the initial equilibrium radius. The shell stiffness is 0.5 MPa and the shell viscosity is 0.5 Pas.*

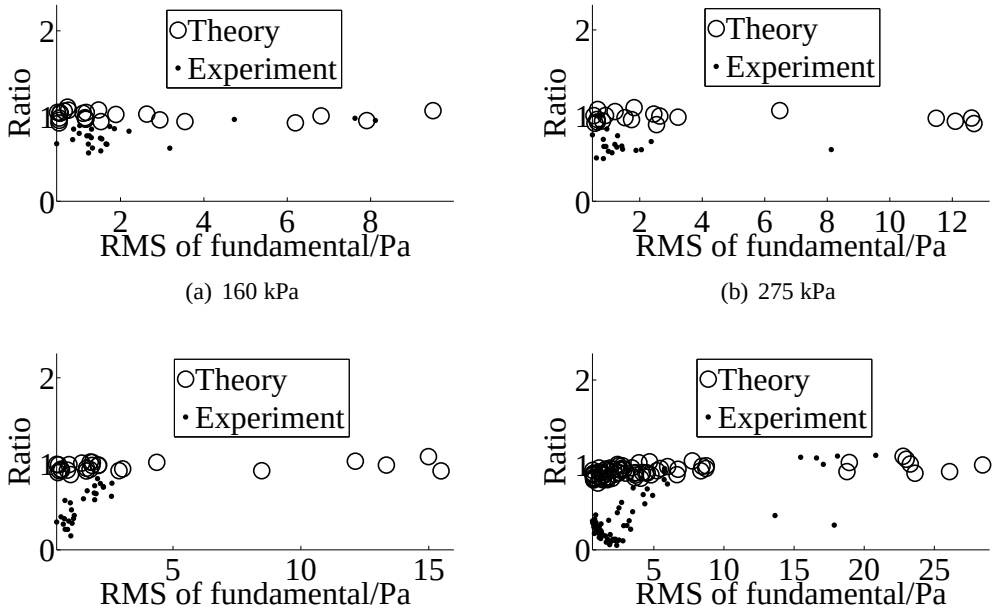

(a) 160 kPa

(b) 275 kPa

(c) 375 kPa

(d) 550 kPa

Figure 6.23: *The ratio of the second fundamental response to the first fundamental response against the first fundamental response of MBs chosen at random from the theoretical distribution of the Mooney-Rivlin MBs are plotted with the experimental response from single MBs for driving amplitudes of 160 kPa, 275 kPa, 375 kPa and 550 kPa. For the second insonation the radius distribution of MBs after lipid shedding occurred was used. The shell equilibrium was 0.2 μm from the initial equilibrium radius. The shell stiffness is 0.5 MPa and the shell viscosity is 0.5 Pas.*

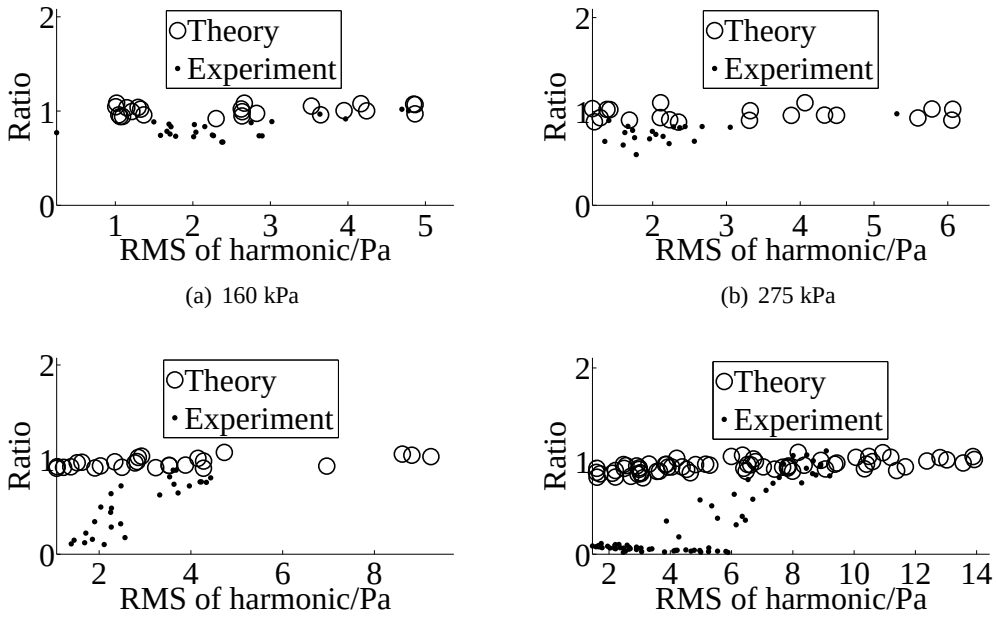

(a) 160 kPa

(b) 275 kPa

(c) 375 kPa

(d) 550 kPa

Figure 6.24: *The ratio of the second harmonic response to the first harmonic response against the first harmonic response of MBs chosen at random from the theoretical distribution of the Mooney-Rivlin MBs are plotted with the experimental response from single MBs for driving amplitudes of 160 kPa, 275 kPa, 375 kPa and 550 kPa. For the second insonation the radius distribution of MBs after lipid shedding occurred was used. The shell equilibrium was 0.2 μm from the initial equilibrium radius. The shell stiffness is 0.5 MPa and the shell viscosity is 0.5 Pas.*

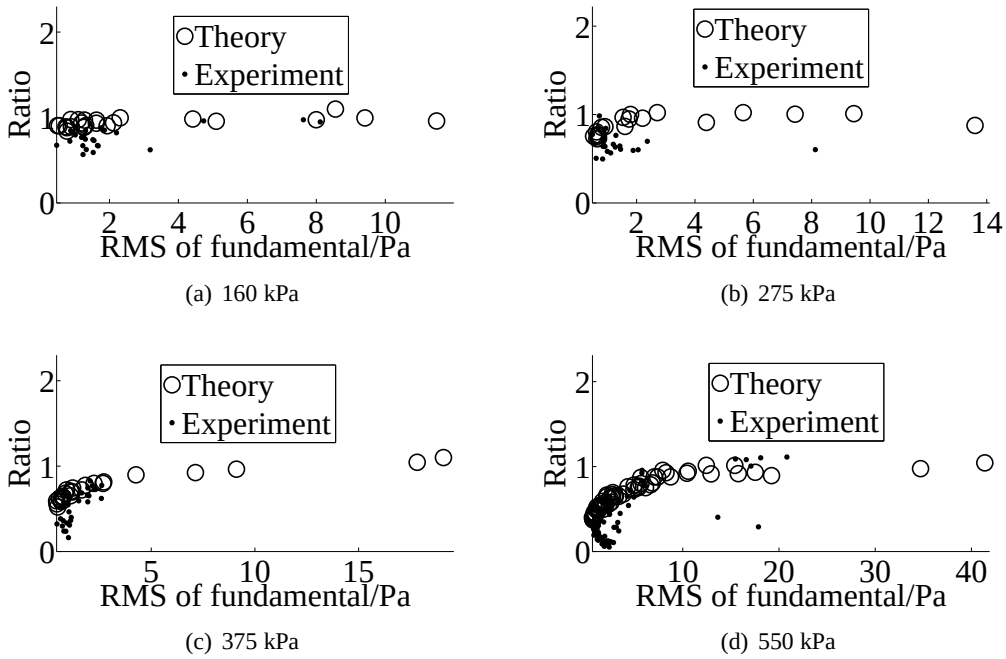

Figure 6.25: *The ratio of the second fundamental response to the first fundamental response against the first fundamental response of MBs chosen at random from the theoretical distribution of the Skalak MBs are plotted with the experimental response from single MBs for driving amplitudes of 160 kPa, 275 kPa, 375 kPa and 550 kPa. For the second insonation the radius distribution of MBs after lipid shedding occurred was used. The shell equilibrium was 0.2 μm from the initial equilibrium radius. The shell stiffness is 0.5 MPa and the shell viscosity is 0.5 Pas.*

Using the radius distribution found from the lipid shedding model with a shell equilibrium at a radius of $R_0 - 0.2\mu$m, where R_0 is the equilibrium radius of the MB before the first insonation the ratio of the fundamental or harmonic response from the second driving pulse to the fundamental or harmonic response from the first driving pulse of random samples of MBs from the theoretical distributions of the Mooney-Rivlin model with a shell stiffness of 0.5 MPa and a shell viscosity of 0.5 Pas are plotted with the experimental responses from single MBs for each driving amplitude in figure 6.11-6.18.

The ratio of second fundamental or harmonic to first fundamental or harmonic from Mooney-Rivlin MBs is not below 0.75 at all driving amplitudes (figures 6.19 and 6.20). For driving amplitudes of 160 kPa and 275 kPa Skalak MBs had a ratio of second fundamental or harmonic to first fundamental or harmonic that was not below 0.75. At driving amplitudes of 375 kPa and 550 kPa the ratio of second fundamental or harmonic to first fundamental or harmonic is

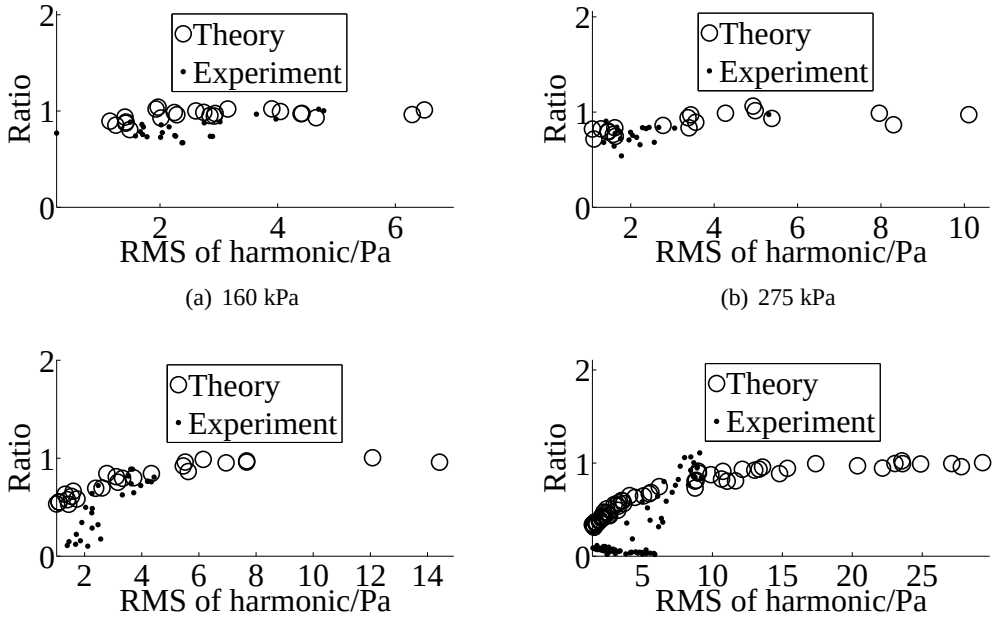

(a) 160 kPa

(b) 275 kPa

(c) 375 kPa

(d) 550 kPa

Figure 6.26: *The ratio of the second harmonic response to the first harmonic response against the first harmonic response of MBs chosen at random from the theoretical distribution of the Skalak MBs are plotted with the experimental response from single MBs for driving amplitudes of 160 kPa, 275 kPa, 375 kPa and 550 kPa. For the second insonation the radius distribution of MBs after lipid shedding occurred was used. The shell equilibrium was 0.2 μm from the initial equilibrium radius. The shell stiffness is 0.5 MPa and the shell viscosity is 0.5 Pas.*

0.5. At all driving amplitudes the ratio of second fundamental or harmonic to first fundamental or harmonic increases to 1 as the first fundamental or harmonic response increases for Skalak MBs similar to the experimental data.

6.6 Discussion

Possible mechanisms for reduced signal from MBs upon subsequent insonation other than the diffusion of the gas out of the MB or the disruption of the shell include the fragmentation of the MB and have been discsussed already in section 2.3. Optical interrogation of Definity® MBs has shown that at a MI of 160 kPa no fragmentation of the MB was observed[71]. At MI above 0.27 fragmentation of Definity® MBs was observed. These experimental observations suggest that the MBs at the lower driving amplitudes do not fragment and hence that the assumptions of the theoretical models used to calculate their acoustic response are valid at these driving amplitudes. The results of the previous chapter also show how the theoretical models gave good agreement at lower driving amplitudes but at higher driving amplitudes there was a greater discrepancy.

The constants used in equation 6.1 were set as those of a free MB, i.e maximum diffusion. The rate of diffusion of gas from a Definity® MB would be expected to be much lower than that of a free gas MB since the effect of shell on the diffusion of the gas from the MB was not taken into account and the gas used in Definity® MBs is a perfluorocarbon gas. The diffusivity of this gas is less a third of the diffusivity of air[107]. The resulting ratios of the second fundamental response to the first fundamental response were much higher than those measured experimentally, which strongly suggests that diffusion cannot be the sole mechanism for MB scatter decay. If molecular diffusion of gas is responsible for the changing size of lipid shelled MBs a continuous decrease of size of the MB between insonations would be expected. However, experimental work has shown that the decrease in diameter of a lipid shelled MB between insonations is small when compared to that occurring just after insonation of the MB[18]. The rates of diffusion considered for a free MB would not be sufficient to account for this decrease in radius just after the insonation suggesting that another mechanism is responsible for the drop in MB radius.

When the shedding of the MB is proportional to the minimum radial oscillation during the first oscillation the resulting ratios of the second to the first fundamental response predicted by the Mooney-Rivlin model were much higher than those measured experimentally. The resulting ratios of the second fundamental response to the first fundamental response predicted by the Skalak model were lower than those measured experimentally and decreased with increasing first fundamental or harmonic response unlike the experimental ratios which increased with first fundamental or harmonic response. The assumption of the proportional level of shedding

together with the Skalak shell model predicted a much great decrease in the acoustic response than that measured experimentally. Neither the diffusion model or the lipid shedding model with the Mooney-Rivlin shell model produced similar decreases in the acoustic response.

When the shedding of the MB is a constant distance of 0.1 μm or 0.2 μm from the initial equilibrium radius the resulting ratios of the second to the first fundamental response predicted by the Mooney-Rivlin model were much higher than those measured experimentally. The resulting ratios of the second to the first fundamental response predicted by the Skalak model were slightly higher than those measured experimentally and increased with increasing first fundamental or harmonic response similar to the experimental ratios which increased with first fundamental or harmonic response. The shedding model together with the Skalak strain hardening gave a much better agreement with the experimental decrease in acoustic response.

Using the Skalak model with lipid shedding predicts a much greater decrease in the scatter since the effective shell stiffness and the residual pressure in the MB increases much faster than the Mooney-Rivlin model figure 6.3. As the effective shell stiffness increases the Skalak model becomes increasingly compression dominated (chapter(3)) (figure 6.10). Previous optical measurements on the contrast agent Sonovue have shown that on subsequent insonations the radial response of a single MB becomes increasingly compression dominated[78].

6.7 Conclusion

The acoustic response of MBs due to a first and second driving pulses was compared to two theoretical models for the change in MB equilibrium state and also for two shell models for a range of MI. The diffusion model and the lipid shedding model with the Mooney-Rivlin shell model underestimated the decrease in response at all MI while the lipid shedding model where the shedding was proportional to the initial minimum radius with the Skalak shell model overestimated the decrease in the response. Experimental MBs with a low fundamental or harmonic response generally experienced a greater relative decrease in scatter than MBs with higher fundamental or harmonic responses. The lipid shedding model with the Skalak shell model predicted an increase in the compression dominated responses on subsequent insonations resulting from the loss of the shell material.

Chapter 7
Conclusions

7.1 Introduction

The goal of the thesis was to increase the understanding of Ultrasound Contrast Agents. Improved understanding of the behaviour of Ultrasound Contrast Agents could give improved detection of disease. Theoretical models of MBs were developed and were compared to the acoustic response from single MBs.

7.2 Summary

The results of this thesis improved the understanding of UCAs by comparing theoretical models to the response of single MBs. Three cases of interest were considered. The first was rigid shelled MBs, the second was soft shelled MBs and the third was the multiple responses from soft shelled MBs.

While theoretical models have been compared to the acoustic response of clouds of MBs and also to the optical response of MBs they have never been compared to the acoustic response from single MBs. This method of comparison has the benefit that the MBs are not constrained as they are in the optical experiments and also that the response is from single MBs and hence interaction of MBs can be neglected. The comparison of the acoustic response from single MBs to theoretical models is complicated by the fact that UCAs have a distribution of radii and hence a distribution of acoustic responses. A statistical approach was developed in this thesis to allow the comparison of the distributions.

Three theoretical models were introduced in the first technical chapter. The linearisation of these models was discussed. The phase response as a function of radius was found for a range of shell parameters and radii. The dependence of these models on the shell parameters and driving parameters was examined at higher MI where nonlinear behaviour is present. The linear model gave a good prediction of the resonance response at the lowest driving amplitude.

Shifts in the resonance were observed at higher MI. Subharmonic responses were also present at twice the resonance radius.

No theoretical model adequately describes the response of rigid shelled MBs at higher MI. In this thesis a model was developed based on previous optical observations to model the behaviour of rigid shelled MBs. Using the statistical method to compare the new theoretical model (the GL model) to the experimental response from single MBs the GL model was found to give better agreement at intermediate MI than two previously established models.

Theoretical models were then compared to the response of soft shelled MBs. Two shell models were used, the Skalak strain hardening and the Mooney-Rivlin strain softening. By varying the shell parameters the theoretically expected distribution of responses could be determined. For each set of parameters the theoretical distribution was compared to the experimental distributions for a range of driving amplitudes. In this way the shell parameters that gave agreement with the experimental data were established. Both the Skalak and Mooney-Rivlin models gave statistical agreement at the lower driving amplitudes for a similar range of shell parameters but at the higher very few shell parameters gave agreement.

The final chapter looked at the multiple responses of single MBs to subsequent insonation. Theoretical models that consider the destruction of MBs have focused on the fragmentation and dissolution of the gas from the MB as the mechanisms responsible for the destruction. The dissolution was considered and the dissolution of the MB was estimated neglecting the effects of the shell, hence, overestimating the decrease in radius of the MB. The change in response was less than that measured experimentally suggesting that the effects of dissolution of the gas alone did not adequately predict the change in response of a MB over time. A new model was developed to account for the loss of shell material from the shell. Again both the Skalak and Mooney-Rivlin models were used. In this case the Skalak and Mooney-Rivlin model gave very different results. Due to the loss of shell material the Skalak model had an increased effective shell stiffness while the Mooney-Rivlin did not. As a result the responses from the Skalak model experienced a much greater decrease in magnitude on subsequent insonations than similar response from the Mooney-Rivlin model. The visual comparison of the Skalak model with the experimental data gave qualitative agreement.

7.3 Further work

The comparison of the theoretical models in this thesis has compared the distribution of responses as a result of the distribution of radii of the MBs to the distribution of experimentally measured acoustic responses. If the radius of the MB was known prior to the insonation the experimental acoustic MB response could be compared directly to the theoretical prediction allowing. This would allow the shell parameters to be established to a better accuracy and for better comparison of theoretical models to the experimental data. Due to the bandwidth of the transducer the comparison of the theoretical models to the experimental data has focused on the use of the fundamental and harmonic component. Accurate measurement of other frequency components such as subharmonic responses would allow further comparison of the theoretical models with the experimental data.

The theoretical model of the rigid shelled contrast agents could be improved further by including the effect of the nature of the defect that allows the gas to leak from the MB. Better modelling may predict the experimentally observed features that include the jetting of gas from the MB and the strong dependence of response. of the MBs on driving amplitude. The shell behaviour is also not well understood for the soft shelled MBs studied in this thesis. Present models do give agreement at low driving amplitudes. At higher driving amplitudes the models used in this thesis did not give agreement. Different models for the shell elasticity and viscosity may give better agreement with the experimental response. However, the response of the MB to multiple driving pulses shows that present models for the long term behaviour of MBs are not adequate. Again better modelling of the behaviour of the shell of soft shelled contrast agents would give better agreement with the experimental data. The modelling of the MB depends on modelling the long term behaviour of the shell in response to ultrasound. As has been shown the loss of shell material can predict some of the features that have been observed of soft shelled MBs in response to multiple pulses. A dynamic model that included the evolution of the shell would be an improvement on the model proposed in this thesis which assumes the shell is unchanged during the MB oscillation.

MB research has now moved on to consider the behaviour of MBs in confined media. Theoretical models have already been developed for MBs in confined media. The comparison of the acoustic responses of single MBs in confined media to the experimentally measured acoustic responses would allow the validation of these theoretical models. These models can be developed further to model the behaviour of MBs in compliant vessels. The improved understanding

of MBs in constrained media may help the imaging of small blood vessels where the vessel diameter is not much greater than the MB diameter.

7.4 Final remarks

A novel technique for the comparison of the experimentally measured acoustic response of single MBs to theoretical models has been developed. This technique was used to compare a newly developed model for the behaviour of rigid shelled MBs to the response of a rigid shelled UCA. This technique of comparison was also used to determine the shell parameters of a soft shelled UCA. A new model was also developed to study the effect of multiple responses of MBs. This work has furthered the knowledge of MBs and it is hoped that the results of this thesis can be used to further improve our understanding of MBs and improve disease treatment and diagnosis.

Appendix A
Figures and tables of chapter 5

MPa / Pas	0.5		5		15		25		50		100	
	F	H	F	H	F	H	F	H	F	H	F	H
160	0	1	0	0	0	0	0	0	0	0	0	1
275	1	1	1	0	1	1	1	1	1	1	1	1
375	0	1	0	0	1	1	1	1	1	0	0	0
550	1	0	1	1	1	1	1	0	0	0	0	0

Table A.1: *The results of the KS statistic for the Skalak model for driving amplitudes of 160 kPa to 550 kPa at driving frequency of 1.6 MHz with radially dependent shell viscosity. 1 denotes not significantly different and 0 denotes significantly different.*

MPa / Pas	0.5		5		15		25		50		100	
	F	H	F	H	F	H	F	H	F	H	F	H
160	0	1	0	0	0	0	0	0	0	0	0	1
275	1	1	1	1	1	0	1	0	1	1	1	1
375	1	1	1	1	1	1	1	0	1	1	0	1
550	0	0	0	0	1	1	0	1	1	1	0	1

Table A.2: *The results of the KS statistic for the Mooney-Rivlin model for driving amplitudes of 160 kPa to 550 kPa at driving frequency of 1.6 MHz with radially dependent shell viscosity. 1 denotes not significantly different and 0 denotes significantly different.*

MPa / Pas	0.5		5		15		25		50		100	
	F	H	F	H	F	H	F	H	F	H	F	H
0	0	0	0	0	0	0	0	0	0	1	0	1
0.5	1	1	1	1	0	1	0	1	0	1	0	1
1	1	1	0	1	0	1	0	1	0	1	0	1
2	1	1	0	1	0	0	0	0	0	0	0	0
6	0	0	0	0	0	0	0	0	0	0	0	0

Table A.3: *The results of the KS statistic for the Skalak model at a driving amplitude of 160 kPa and driving frequency of 1.6 MHz. 1 denotes not significantly different and 0 denotes significantly different.*

MPa / Pas	0.5		5		15		25		50		100	
	F	H	F	H	F	H	F	H	F	H	F	H
0	1	0	1	0	1	1	1	1	1	1	0	0
0.5	1	0	1	1	1	1	1	1	1	1	0	1
1	0	0	1	1	1	1	1	1	1	1	1	1
2	0	0	1	1	1	1	1	1	1	1	1	1
6	1	0	1	0	1	0	1	0	1	0	1	0

Table A.4: *The results of the KS statistic for the Skalak model at a driving amplitude of 275 kPa and driving frequency of 1.6 MHz. 1 denotes not significantly different and 0 denotes significantly different.*

MPa / Pas	0.5		5		15		25		50		100	
	F	H	F	H	F	H	F	H	F	H	F	H
0	1	1	1	1	1	1	1	1	1	0	0	0
0.5	0	0	1	1	1	1	1	1	1	1	0	0
1	0	0	0	1	1	1	1	1	1	0	0	0
2	0	0	1	1	1	1	1	0	1	0	1	0
6	1	0	1	0	1	0	1	0	1	0	0	0

Table A.5: *The results of the KS statistic for the Skalak model at a driving amplitude of 375 kPa and driving frequency of 1.6 MHz. 1 denotes not significantly different and 0 denotes significantly different.*

MPa / Pas	0.5		5		15		25		50		100	
	F	H	F	H	F	H	F	H	F	H	F	H
0	1	0	1	1	1	1	1	0	0	0	0	0
0.5	1	0	1	1	1	1	1	0	0	0	0	0
1	0	0	1	1	1	1	1	0	0	0	0	0
2	1	1	1	1	1	0	1	0	0	0	0	0
6	1	0	1	0	0	0	0	0	0	0	0	0

Table A.6: *The results of the KS statistic for the Skalak model at a driving amplitude of 550 kPa and driving frequency of 1.6 MHz. 1 denotes not significantly different and 0 denotes significantly different.*

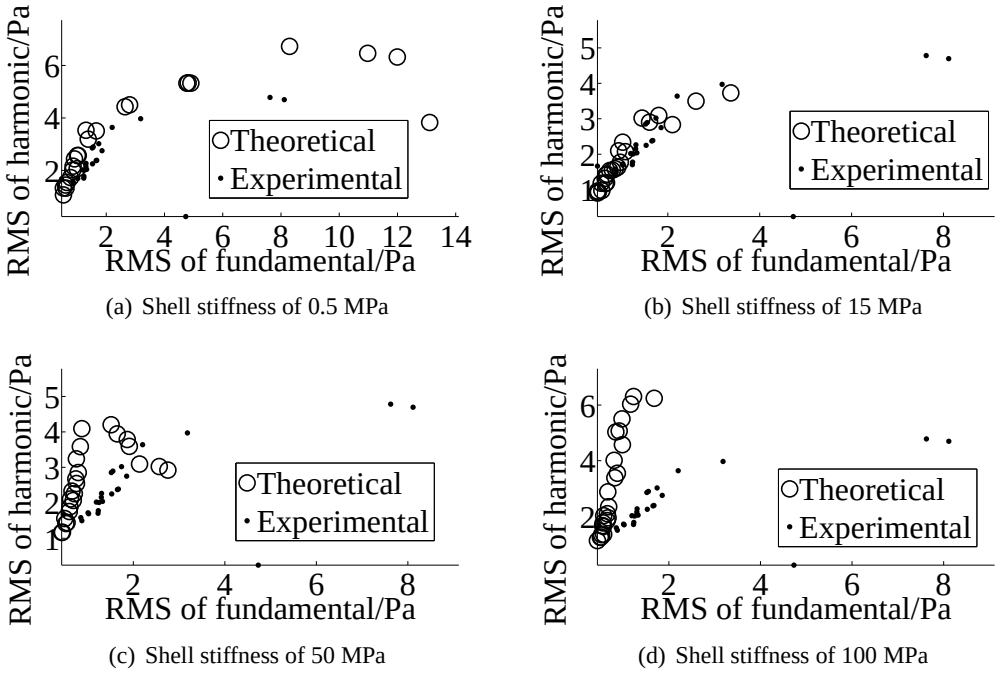

(a) Shell stiffness of 0.5 MPa

(b) Shell stiffness of 15 MPa

(c) Shell stiffness of 50 MPa

(d) Shell stiffness of 100 MPa

Figure A.1: *MBs chosen at random from the theoretical distribution of the Skalak MBs with a shell viscosity of 0.5 Pas are plotted with the experimental response from single MBs for shell stiffnesses of 0.5 MPa, 15 MPa, 50 MPa and 100 MPa at a driving amplitude of 160 kPa. Either the fundamental or harmonic theoretical distribution is significantly different to the experimental response for all of the shell stiffnesses except 0.5 MPa.*

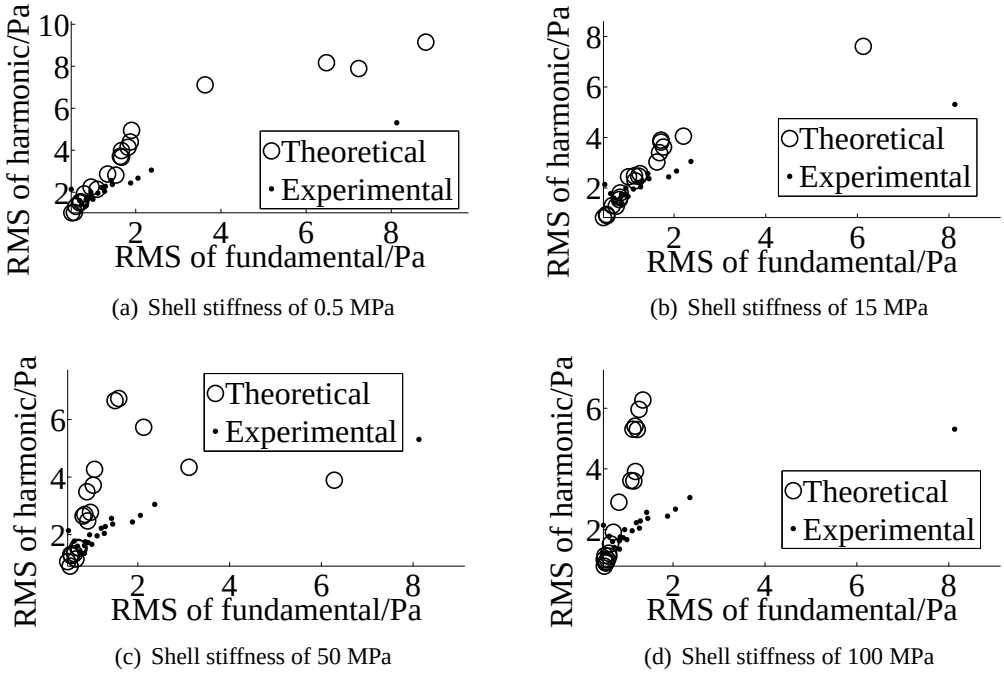

(a) Shell stiffness of 0.5 MPa

(b) Shell stiffness of 15 MPa

(c) Shell stiffness of 50 MPa

(d) Shell stiffness of 100 MPa

Figure A.2: *MBs chosen at random from the theoretical distribution of the Skalak MBs with a shell viscosity of 0.5 Pas are plotted with the experimental response from single MBs for shell stiffnesses of 0.5 MPa, 15 MPa, 50 MPa and 100 MPa at a driving amplitude of 275 kPa. Either the fundamental or harmonic theoretical distribution is not significantly different to the experimental response for all of the shell stiffnesses except 100 MPa.*

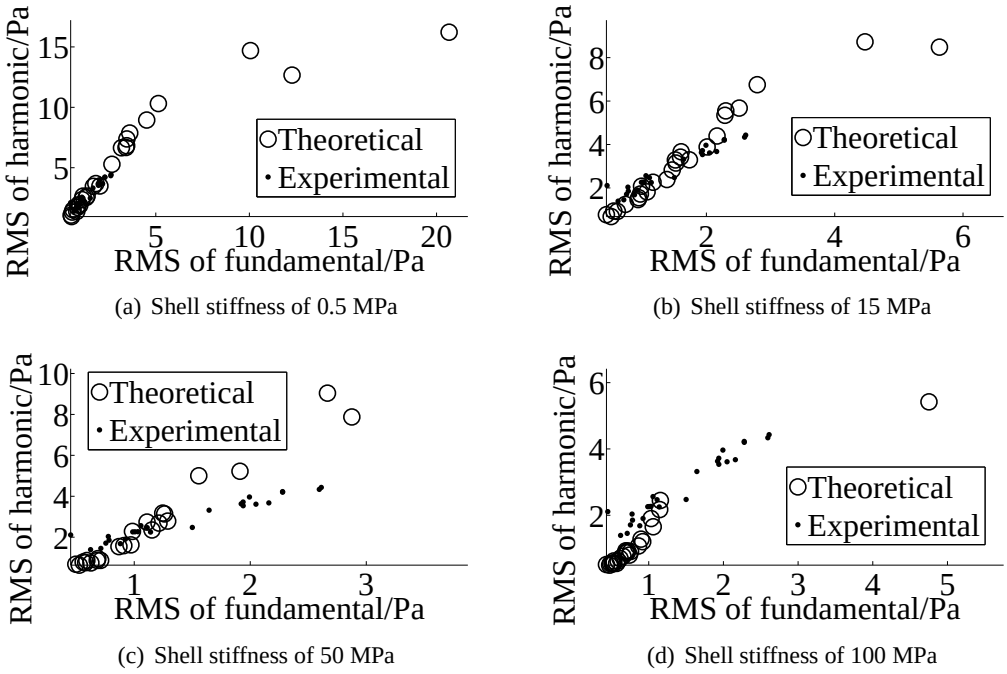

(a) Shell stiffness of 0.5 MPa

(b) Shell stiffness of 15 MPa

(c) Shell stiffness of 50 MPa

(d) Shell stiffness of 100 MPa

Figure A.3: *MBs chosen at random from the theoretical distribution of the Skalak MBs with a shell viscosity of 0.5 Pas are plotted with the experimental response from single MBs for shell stiffnesses of 0.5 MPa, 15 MPa, 50 MPa and 100 MPa at a driving amplitude of 375 kPa. Either the fundamental or harmonic theoretical distribution is not significantly different to the experimental response for all of the shell stiffnesses except 100 MPa.*

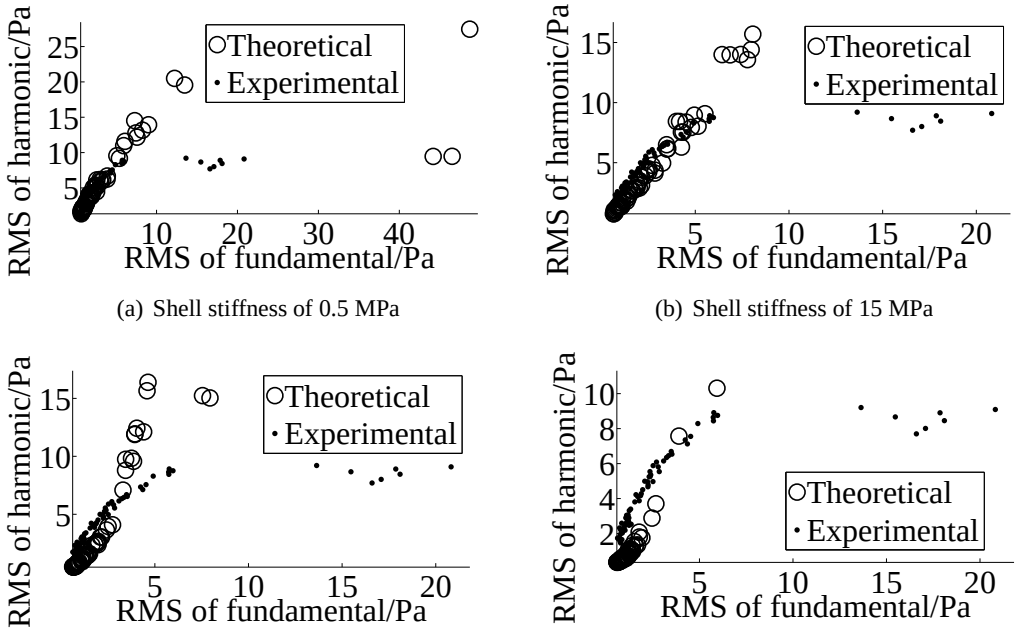

(a) Shell stiffness of 0.5 MPa

(b) Shell stiffness of 15 MPa

(c) Shell stiffness of 50 MPa

(d) Shell stiffness of 100 MPa

Figure A.4: *MBs chosen at random from the theoretical distribution of the Skalak MBs with a shell viscosity of 0.5 Pas are plotted with the experimental response from single MBs for shell stiffnesses of 0.5 MPa, 15 MPa, 50 MPa and 100 MPa at a driving amplitude of 550 kPa. Either the fundamental or harmonic theoretical distribution is significantly different to the experimental response for all of the shell stiffnesses except 15 MPa.*

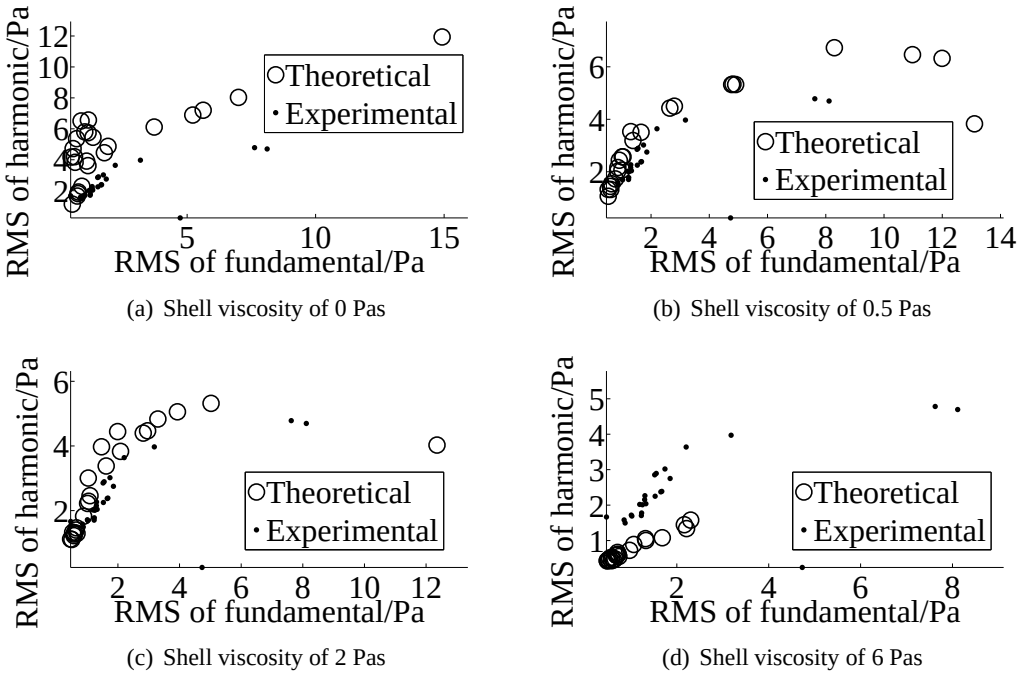

(a) Shell viscosity of 0 Pas

(b) Shell viscosity of 0.5 Pas

(c) Shell viscosity of 2 Pas

(d) Shell viscosity of 6 Pas

Figure A.5: *MBs chosen at random from the theoretical distribution of the Skalak MBs with a shell stiffness of 0.5 MPa are plotted with the experimental response from single MBs for shell viscosities of 0 Pas, 0.5 Pas, 2 Pas and 6 Pas at a driving amplitude of 160 kPa. Either the fundamental or harmonic theoretical distribution is not significantly different to the experimental response for all of the shell viscosities except 0.5 Pas.*

MPa / Pas	0.5		5		15		25		50		100	
	F	H	F	H	F	H	F	H	F	H	F	H
0	0	1	1	1	0	1	0	1	0	0	0	0
0.5	1	1	0	1	0	1	0	1	0	0	0	0
1	1	1	1	1	0	1	0	1	0	1	0	0
2	1	0	0	0	0	0	0	0	0	1	0	0
6	0	0	0	0	0	0	0	0	0	0	0	0

Table A.7: *The results of the KS statistic for the Mooney-Rivlin model at a driving amplitude of 160 kPa and driving frequency of 1.6 MHz. 1 denotes not significantly different and 0 denotes significantly different.*

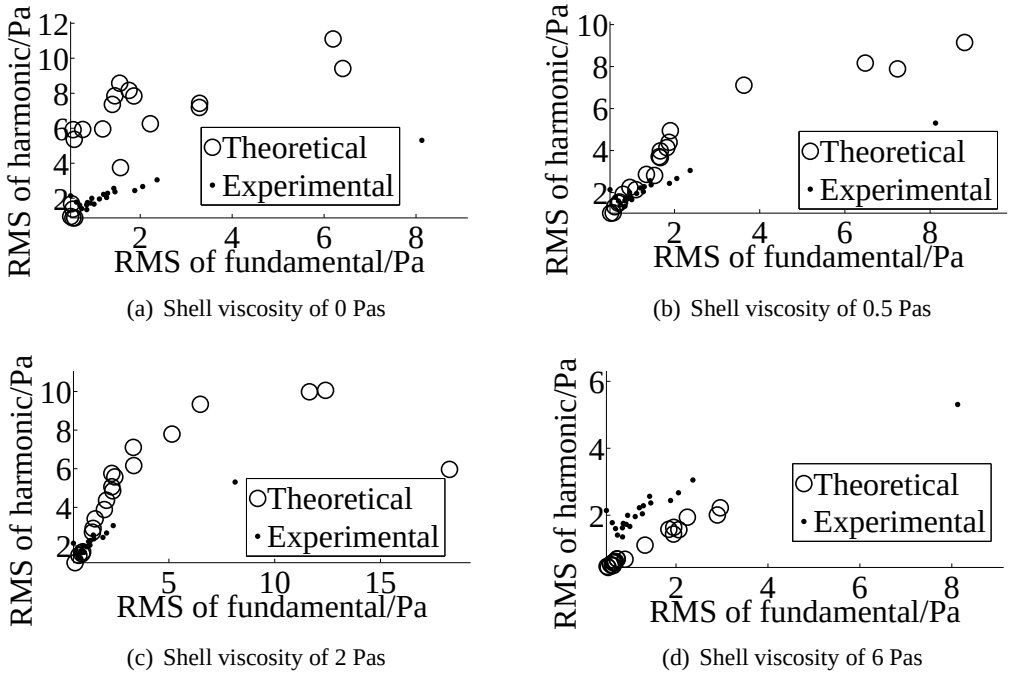

(a) Shell viscosity of 0 Pas

(b) Shell viscosity of 0.5 Pas

(c) Shell viscosity of 2 Pas

(d) Shell viscosity of 6 Pas

Figure A.6: *MBs chosen at random from the theoretical distribution of the Skalak MBs with a shell stiffness of 0.5 MPa are plotted with the experimental response from single MBs for shell viscosities of 0 Pas, 0.5 Pas, 2 Pas and 6 Pas at a driving amplitude of 275 kPa. Either the fundamental or harmonic theoretical distribution is not significantly different to the experimental response for all of the shell viscosities except 0.5 Pas and 2 Pas.*

MPa / Pas	0.5		5		15		25		50		100	
	F	H	F	H	F	H	F	H	F	H	F	H
0	1	1	0	0	1	0	1	1	1	1	0	0
0.5	1	1	0	0	1	1	1	1	1	1	1	0
1	0	1	1	0	1	0	1	1	1	1	1	0
2	1	1	1	1	1	1	1	1	1	1	1	0
6	1	0	1	0	1	0	1	0	1	0	0	0

Table A.8: *The results of the KS statistic for the Mooney-Rivlin model at a driving amplitude of 275 kPa and driving frequency of 1.6 MHz. 1 denotes not significantly different and 0 denotes significantly different.*

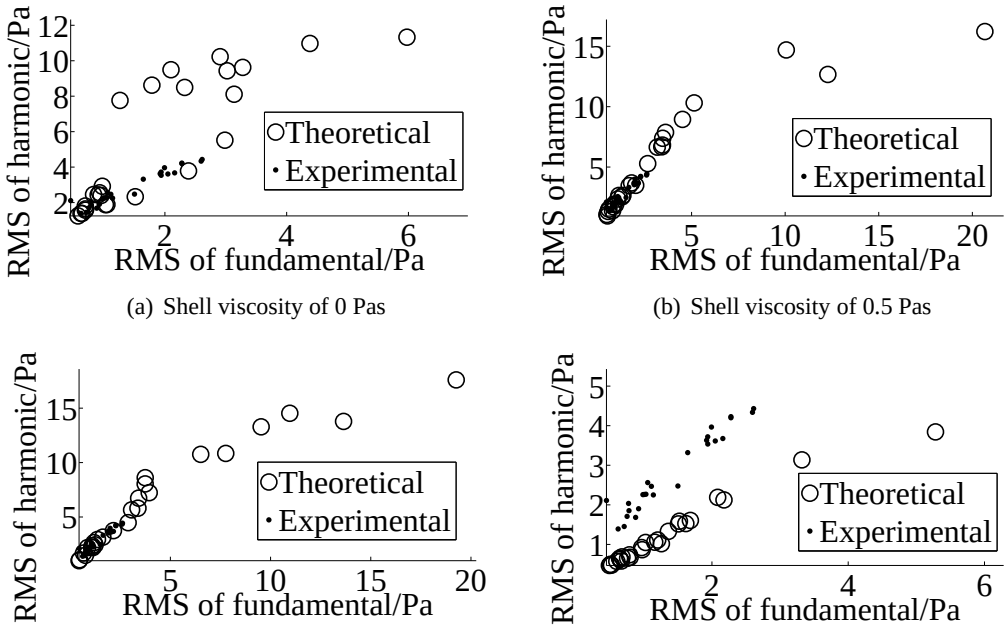

(a) Shell viscosity of 0 Pas

(b) Shell viscosity of 0.5 Pas

(c) Shell viscosity of 2 Pas

(d) Shell viscosity of 6 Pas

Figure A.7: *MBs chosen at random from the theoretical distribution of the Skalak MBs with a shell stiffness of 0.5 MPa are plotted with the experimental response from single MBs for shell viscosities of 0 Pas, 0.5 Pas, 2 Pas and 6 Pas at a driving amplitude of 375 kPa. Either the fundamental or harmonic theoretical distribution is not significantly different to the experimental response for all of the shell viscosities except 0 Pas, 0.5 Pas and 2 Pas.*

MPa / Pas	0.5		5		15		25		50		100	
	F	H	F	H	F	H	F	H	F	H	F	H
0	1	1	1	1	0	0	0	0	1	0	0	0
0.5	0	1	0	1	0	0	0	0	1	1	0	0
1	0	1	0	1	0	0	0	0	1	1	0	0
2	0	1	0	1	0	1	1	1	1	1	0	0
6	1	0	1	0	1	0	1	0	1	0	0	0

Table A.9: *The results of the KS statistic for the Mooney-Rivlin model at a driving amplitude of 375 kPa and driving frequency of 1.6 MHz. 1 denotes not significantly different and 0 denotes significantly different.*

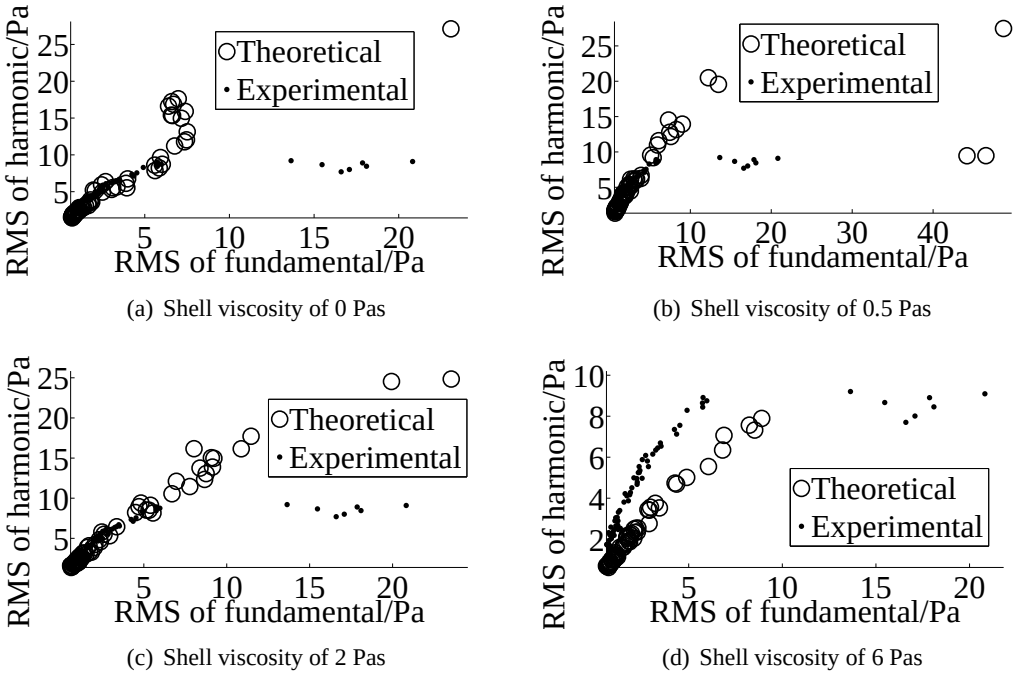

(a) Shell viscosity of 0 Pas

(b) Shell viscosity of 0.5 Pas

(c) Shell viscosity of 2 Pas

(d) Shell viscosity of 6 Pas

Figure A.8: *MBs chosen at random from the theoretical distribution of the Skalak MBs with a shell stiffness of 0.5 MPa are plotted with the experimental response from single MBs for shell viscosities of 0 Pas, 0.5 Pas, 2 Pas and 6 Pas at a driving amplitude of 550 kPa. The fundamental and harmonic theoretical distributions are not significantly different to the experimental response for all of the shell viscosities except 0 Pas, 0.5 Pas and 2 Pas.*

Pas \ MPa	0.5		5		15		25		50		100	
	F	H	F	H	F	H	F	H	F	H	F	H
0	0	0	0	0	0	0	0	1	0	0	0	0
0.5	1	1	1	1	0	1	0	0	0	0	0	0
1	0	1	0	1	0	1	0	1	0	0	0	0
2	0	1	0	1	0	1	0	1	1	1	0	0
6	1	0	1	0	1	0	1	0	1	0	0	0

Table A.10: *The results of the KS statistic for the Mooney-Rivlin model at a driving amplitude of 550 kPa and driving frequency of 1.6 MHz. 1 denotes not significantly different and 0 denotes significantly different.*

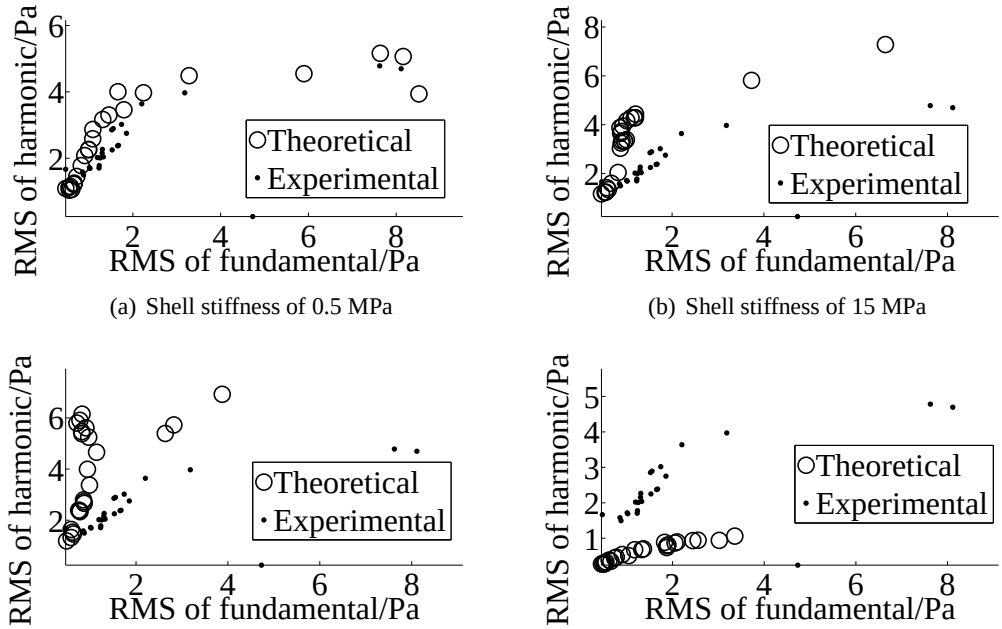

(a) Shell stiffness of 0.5 MPa

(b) Shell stiffness of 15 MPa

(c) Shell stiffness of 50 MPa

(d) Shell stiffness of 100 MPa

Figure A.9: *MBs chosen at random from the theoretical distribution of the Mooney-Rivlin MBs with a shell viscosity of 0.5 Pas are plotted with the experimental response from single MBs for shell stiffnesses of 0.5 MPa, 15 MPa, 50 MPa and 100 MPa at a driving amplitude of 160 kPa. Either the fundamental or harmonic theoretical distribution is significantly different to the experimental response for all of the shell stiffnesses except 0.5 MPa.*

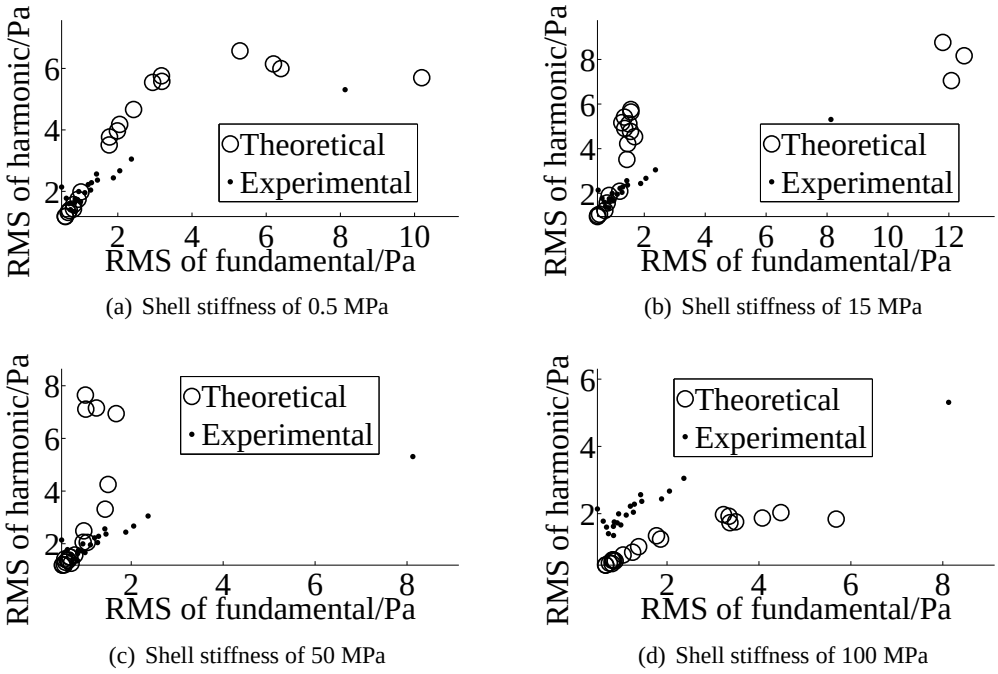

Figure A.10: *MBs chosen at random from the theoretical distribution of the Mooney-Rivlin MBs with a shell viscosity of 0.5 Pas are plotted with the experimental response from single MBs for shell stiffnesses of 0.5 MPa, 15 MPa, 50 MPa and 100 MPa at a driving amplitude of 275 kPa. The fundamental and harmonic theoretical distributions are not significantly different to the experimental response for all of the shell stiffnesses except 100 MPa.*

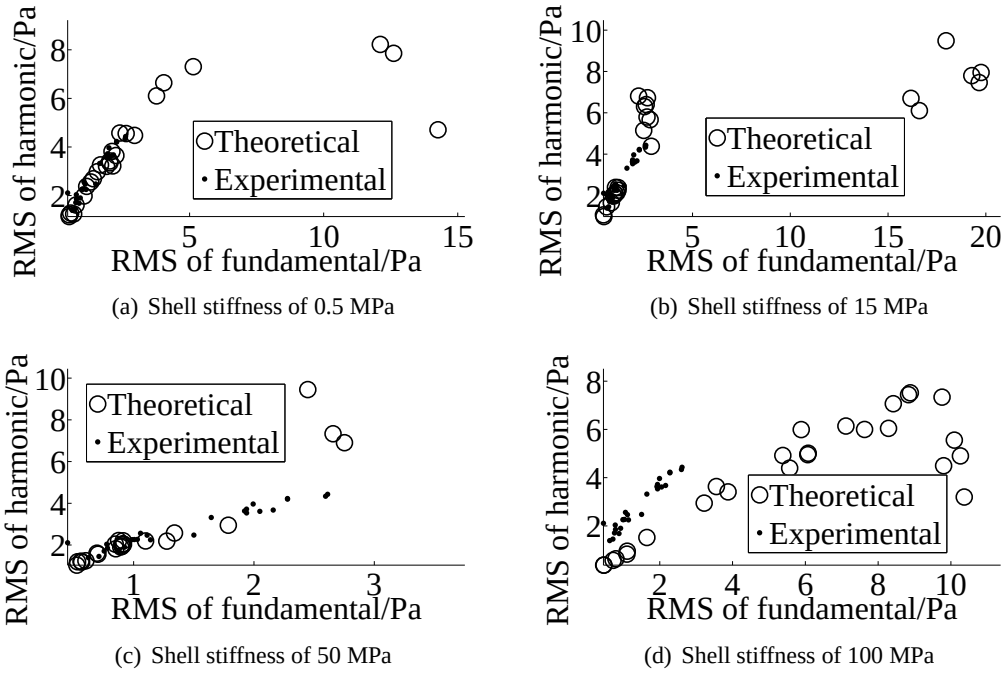

Figure A.11: *MBs chosen at random from the theoretical distribution of the Mooney-Rivlin MBs with a shell viscosity of 0.5 Pas are plotted with the experimental response from single MBs for shell stiffnesses of 0.5 MPa, 15 MPa, 50 MPa and 100 MPa at a driving amplitude of 375 kPa. Either the fundamental or harmonic theoretical distributions are significantly different to the experimental response for all of the shell stiffnesses except 100 MPa.*

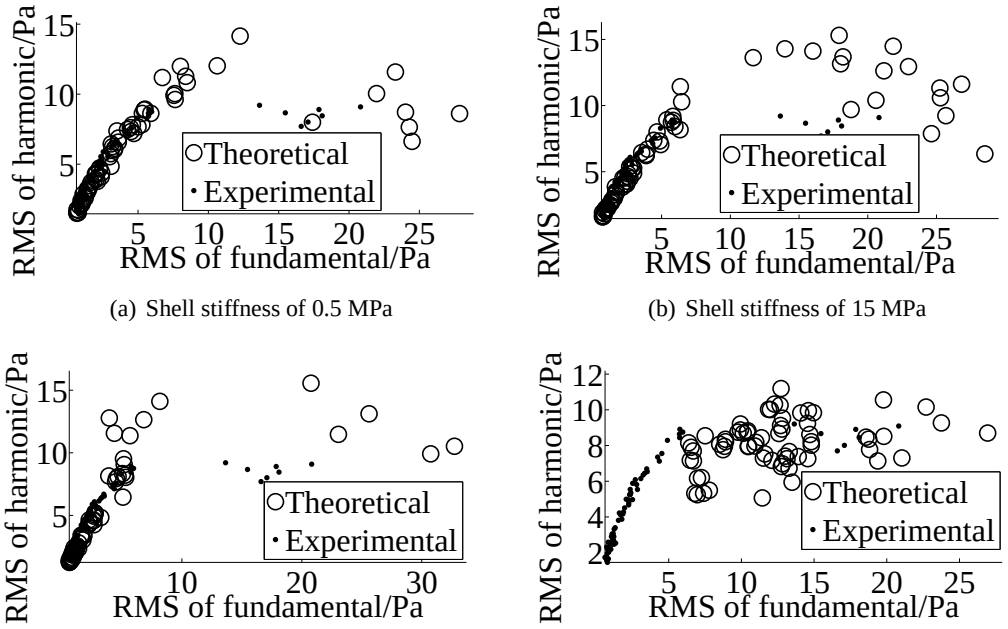

(a) Shell stiffness of 0.5 MPa

(b) Shell stiffness of 15 MPa

(c) Shell stiffness of 50 MPa

(d) Shell stiffness of 100 MPa

Figure A.12: *MBs chosen at random from the theoretical distribution of the Mooney-Rivlin MBs with a shell viscosity of 0.5 Pas are plotted with the experimental response from single MBs for shell stiffnesses of 0.5 MPa, 15 MPa, 50 MPa and 100 MPa at a driving amplitude of 550 kPa. The fundamental and harmonic theoretical distributions are not significantly different to the experimental response for all of the shell stiffnesses except 0.5 MPa.*

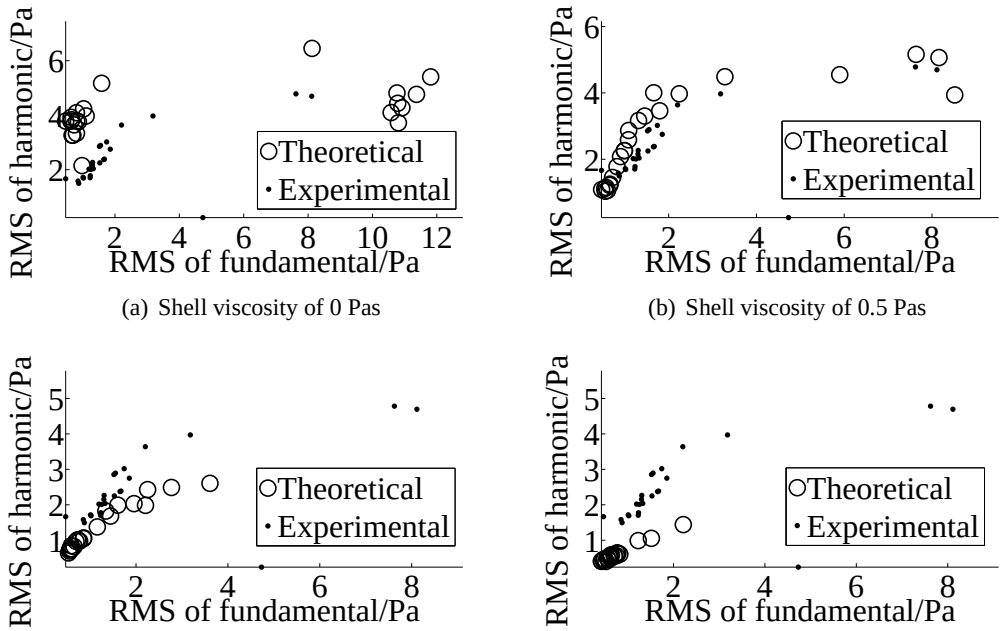

(a) Shell viscosity of 0 Pas

(b) Shell viscosity of 0.5 Pas

(c) Shell viscosity of 2 Pas

(d) Shell viscosity of 6 Pas

Figure A.13: *MBs chosen at random from the theoretical distribution of the Mooney-Rivlin MBs with a shell stiffness of 0.5 MPa are plotted with the experimental response from single MBs for shell viscosities of 0 Pas, 0.5 Pas, 2 Pas and 6 Pas at a driving amplitude of 160 kPa. Both the fundamental and harmonic theoretical distributions are not significantly different to the experimental response for all of the shell viscosities except 0 Pas and 1 Pas.*

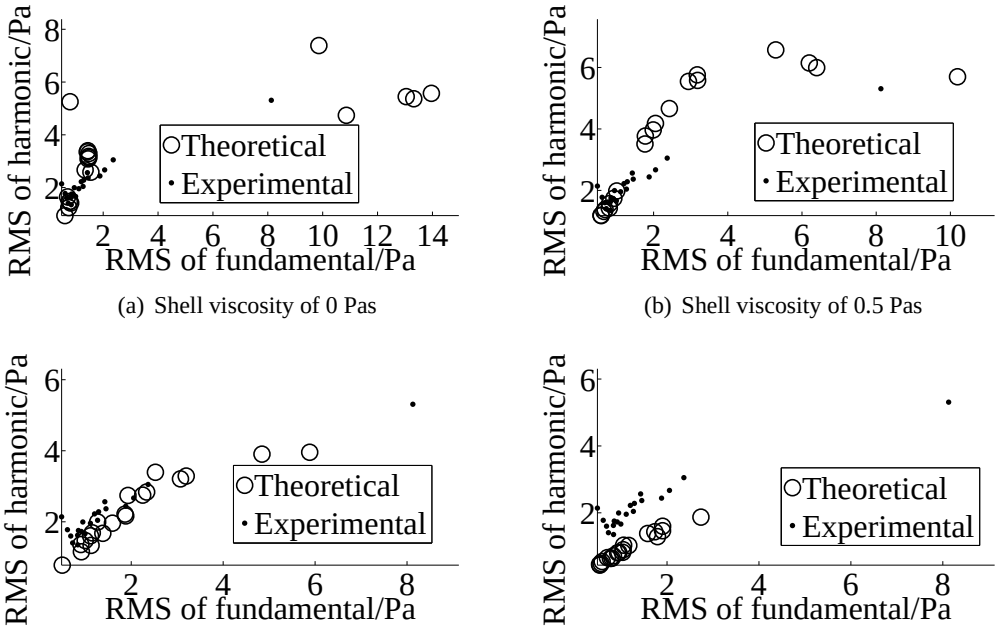

(a) Shell viscosity of 0 Pas

(b) Shell viscosity of 0.5 Pas

(c) Shell viscosity of 2 Pas

(d) Shell viscosity of 6 Pas

Figure A.14: *MBs chosen at random from the theoretical distribution of the Mooney-Rivlin MBs with a shell stiffness of 0.5 MPa are plotted with the experimental response from single MBs for shell viscosities of 0 Pas, 0.5 Pas, 2 Pas and 6 Pas at a driving amplitude of 275 kPa. Both the fundamental and harmonic theoretical distributions are not significantly different to the experimental response for shell viscosities of 0 Pas and 1 Pas.*

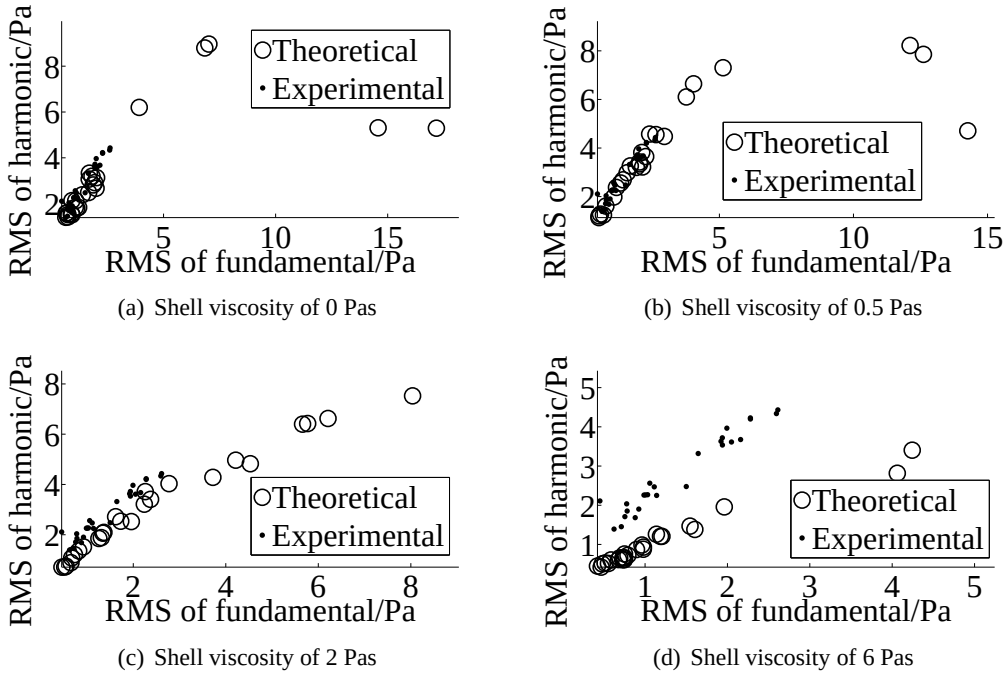

(a) Shell viscosity of 0 Pas

(b) Shell viscosity of 0.5 Pas

(c) Shell viscosity of 2 Pas

(d) Shell viscosity of 6 Pas

Figure A.15: *MBs chosen at random from the theoretical distribution of the Mooney-Rivlin MBs with a shell stiffness of 0.5 MPa are plotted with the experimental response from single MBs for shell viscosities of 0 Pas, 0.5 Pas, 2 Pas and 6 Pas at a driving amplitude of 375 kPa. Both the fundamental and harmonic theoretical distributions are not significantly different to the experimental response for all of the shell viscosities except 0 Pas.*

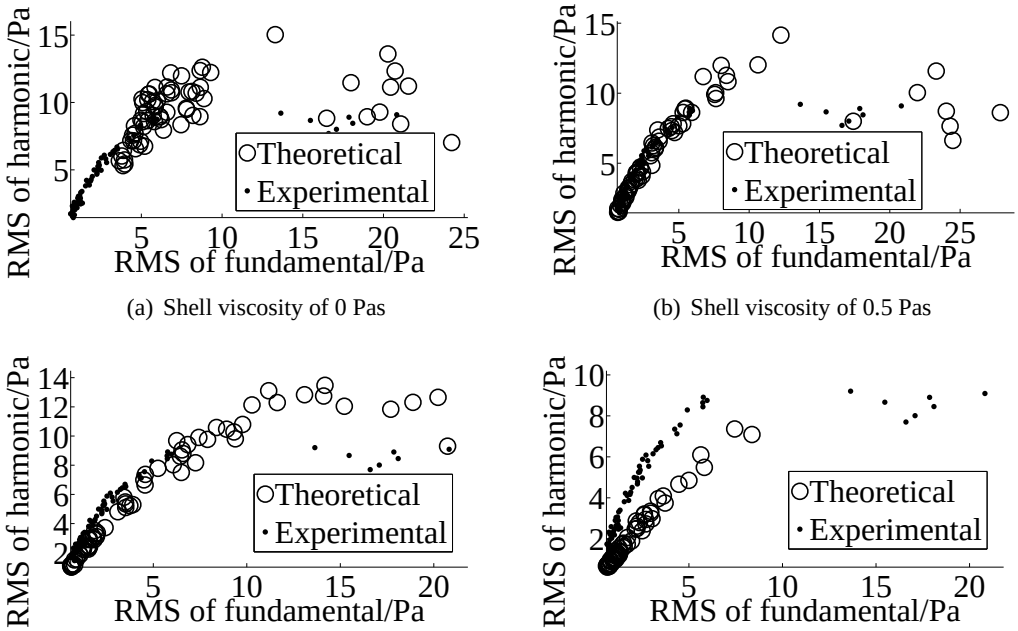

(a) Shell viscosity of 0 Pas

(b) Shell viscosity of 0.5 Pas

(c) Shell viscosity of 2 Pas

(d) Shell viscosity of 6 Pas

Figure A.16: *MBs chosen at random from the theoretical distribution of the Mooney-Rivlin MBs with a shell stiffness of 0.5 MPa are plotted with the experimental response from single MBs for shell viscosities of 0 Pas, 0.5 Pas, 2 Pas and 6 Pas at a driving amplitude of 550 kPa. Both the fundamental and harmonic theoretical distributions are not significantly different to the experimental response for all of the shell viscosities except 0.5 Pas.*

Appendix B
Publications

Conference publications

P. Looney, D. Thomas, R Steel, T. Anderson, N. Pelekasis1, V. Sboros. A new theoretical model for cracked microbubbles. In Proceedings of IEEE sysmposium on Ultrasonics, Rome, September 2009.

D.H. Thomas, **P. Looney**, T. Anderson, N. Pelekasis,W.N.McDicken, V. Sboros. Acoustic detection of microbubble resonance. In Proceedings of 14th European Symposium on Ultrasound Contrast Imaging, Rotterdam, poster presentation, January 2009.

P. Looney, D Thomas, R Steel, T Anderson, N Pelekasis1, V Sboros. A realistic model for ultrasound contrast microbubbles: Initial results. In Proceedings of Warwick Innovative Manufacturing Research Centre 3rd International Cavitation Forum, July 2008.

Journal publications

D.H. Thomas, **P. Looney**, R. Steel, N. Pelekasis, W.N. McDicken, T. Anderson, V. Sboros. Acoustic detection of a microbubble resonance. Applied Physics Letters, 94(23) June 2009.

Appendix C
Matlab Code

Statistics code

Code to find the cumulative distribution

```
%%CUMulative distribution function

cd dist1; \\
cd input; \\
[names,TIMESTEP,VALUE,GAMA,PINFDIM,CL,PL,ML,SRB,RB,GSDIM,THICKNESS,YLIKO,B,URDIM,MSK,FREQ,SD,CONST,DISTANCE]...\\
=textread('Input_CONTRAST1D.txt','\%s\%f%f%f%f%f%f%f%f%f%f%f%f%f%f%f%f%f%f%f%f%f','headerlines',2);\\
cd ..;\\

%[ainm,EXP,NUM,VOL]=textread('Definitydist1.txt','%s%f%f%f');\\

[XFREQ JFREQ]=unique(FREQ);\\
names5={'fhdstnum_' 'emitfhdstnum_' 'shellfhdstnum_'};\\
cd ..;\\
noise1=cutofffun;\\
\\%%%LOAD 2DDIST FILES\\
for EXPERNUM=5%[1 3 4 5 6 8 ]%\\
    cd dist1/AVG;
EXPERNUM
%cd AVG
%cd AVG2
FILE1= load(strcat(char(names5(EXPERNUM1)),char(PAMP)));%%NULL
cd ../..;

%cd AVG1;
cd dist2/AVG;
FILE2= load(strcat(char(names5(EXPERNUM1)),char(PAMP)));%%EXP
cd ../..;
%cd ..;
%FILE3= load('funnoise.txt');
%FILE4= load('harnoise.txt');
fileainm=fopen(strcat('Dfun',char(names5(EXPERNUM1)),char(PAMP)),'w+');
%cd ..;
%%%END LOAD 2DIST FILES
X1=FILE1(:,2);
PRO1=FILE1(:,4);

%Y1=FILE1(:,3);
%PRO=FILE1(:,4);
X2=FILE2(:,2);
PRO2=FILE2(:,4);

%%%%Implement noise cutoff

IND=find(X1>noise1);
X11=X1(IND);
PRO11=PRO1(IND);
```

```
PRO11=PRO11/sum(PRO11);
%PRO1=PRO(IND);

IND=find(X2>noise1);
X21=X2(IND);
PRO21=PRO2(IND);
PRO21=PRO21/sum(PRO21);
%%%%%

%%%Find cumulative distribution 1 fundamental
X11;
[X111,IND1]=(sort(X11));
PRO111=PRO11(IND1);
PRO111=PRO111/sum(PRO111);

QUAD1=0;
for I=1:(length(X111))
QUAD1=sum(PRO111(1:I));
CUMPRO1(I)=QUAD1;
end
%%%


%%%Find cumulative distribution 2 fundamental
X21;
[X211,IND2]=(sort(X21));
PRO211=PRO21(IND2);
PRO211=PRO211/sum(PRO211);


QUAD2=0;
for I=1:(length(X211))
QUAD2=sum(PRO211(1:I));
CUMPRO2(I)=QUAD2;
end
%%%


figure;
plot(X111(1:(length(X11))),CUMPRO1,'.');
hold on;
plot(X211(1:(length(X21))),CUMPRO2,'o');

%%%Find max difference

for I=1:(length(X211))
%A(I)=  spline(XhAon,CUMPROhAon,X2(I))
if X211(I)<X111(1)
DI(I)=(abs(0-CUMPRO2(I)));
end
if X211(I)>X111(end)
DI(I)=(abs(1-CUMPRO2(I)));
end
if X211(I)>X111(1) && X211(I)<X111(end)
DI(I)=(abs(interp1(X111,CUMPRO1,X211(I))-CUMPRO2(I)));
I;
end
end
%keyboard
X21(find(max(DI)));
max(DI)
%X2
%%%%

fprintf(fileainm,'%d\n',max(DI));
```

```
fclose(fileainm);
clear X2 CUMPRO2 CUMPROhAon DI PROAS1  X11 X1 XONE CUMPRO1 IND X2 J K PRO1 PRO XTWO;
end
```

Code to solve Keller Miksis

```
clear
%%%%%%%%%%%%%%%%%%%%%%%%%%%%%%%%%%%%INPUT DATA%%%%%%%%%%%%%%%%%%%%%%%%%%%%%%%%%%%%
cd input;
[names,TIMESTEP,VALUE,GAMA,PINFDIM,CL,PL,ML,SRB,RB,GSDIM,THICKNESS,YLIKO,B,URDIM,MSK,FREQ,SD,CONST,DISTANCE]...
=textread('Input_CONTRAST1D.txt','%s%f%f%f%f%f%f%f%f%f%f%f%f%f%f%f%f%f%f%f%f','headerlines',2);
cd ..;

[ainm,EXP,NUM,VOL]=textread('Definitydist7.txt','%s%f%f%f');
RADI=resample(((10^(-6))/2)*EXP,100,length(ainm));
PRO = resample(NUM/100,100,length(ainm));
names2={'185.txt' '275.txt' '335.txt' '550.txt' '750.txt' '1110.txt' '1500.txt'};
B
GSDIM
MSK

%interpcons=[0.8556 0.7818 0.9636 0.8933 0.9091 1.00364 0.9467 1.1333 0.9275];
%%%%%%%%%%%%%%%%%%%%%%%%%%%%%%%%%%%%INPUT DATA%%%%%%%%%%%%%%%%%%%%%%%%%%%%%%%%%%%%
%%%%%%%%%%%%%%%%%%%%%%%%%%READ EXPERIMENTAL DATA FROM FILE%%%%%%%%%%%%%%%%%%
for EXPERNUM=1:length(names)
    cd lipshed;
A=load(strcat('RUFIN',char(names2(EXPERNUM))));
BB=load(strcat('R_',char(names2(EXPERNUM))));
BBB=BB(:,1);
%RADI=A(:,1).*RADI;

cd ..;
warning off;
%PA=100000;
%TEXP=[0:0.0000002:0.0002];
%FREQ(EXPERNUM)=25000;
%PA=PA*(1+75*TEXP);
%PEXP=PA.*sin(2.0D0*pi*FREQ(EXPERNUM)*TEXP);
%LEXP=length(TEXP);
cd input;
EXPERIMENT=load(char(names(EXPERNUM)));
LEXP=size(EXPERIMENT,1);
TEXP=EXPERIMENT(:,1);
PEXP=EXPERIMENT(:,2);

VALUE(EXPERNUM)=1;
cd ..;
%%%%%%%%%%%%%%%%%%%%%%%%%%READ EXPERIMENTAL DATA FROM FILE%%%%%%%%%%%%%%%%%%
%%%%%%%%%%%%%%%%%%%%%%%%%%OPEN RESULT FILES%%%%%%%%%%%%%%%%%%%%%%%%%%%%%%%%%%%%

%%%%%%%%%%%%%%%%%%%%%%%%%%OPEN RESULT FILES%%%%%%%%%%%%%%%%%%%%%%%%%%%%%%%%%%%%
%%%%%%%%%%%%%%%%%%%%%%%%%%%%%%%%%%DIMENSIONLESS%%%%%%%%%%%%%%%%%%%%%%%%%%%%%%%%
for UIMHIR=1:length(PRO)
    names(EXPERNUM)
    UIMHIR
cd (strcat(char(num2str(UIMHIR))));
file2=fopen(strcat('SecT_R_DRDT_D2RDT_PRESSCATTER_',char(names2(EXPERNUM))),'w+');
cd ..;
%URDIM(EXPERNUM)=-(RADI(UIMHIR)-BBB(UIMHIR));
```

```
RB(EXPERNUM)=RADI(UIMHIR);
MS=3*MSK(EXPERNUM)*THICKNESS(EXPERNUM);
OMEGA=2.0D0*pi*FREQ(EXPERNUM);
REL=PL(EXPERNUM)*OMEGA*RB(EXPERNUM)^2.0D0/ML(EXPERNUM);
RES=PL(EXPERNUM)*OMEGA*RB(EXPERNUM)^3.0D0/MS;
MACH=OMEGA*RB(EXPERNUM)/CL(EXPERNUM);
GS=GSDIM(EXPERNUM)*THICKNESS(EXPERNUM)/(PL(EXPERNUM)*RB(EXPERNUM)^3.0D0*OMEGA^2.0D0);
%GS=0;
%MS=0;
WEBSRB=(PL(EXPERNUM)*RB(EXPERNUM)^3.0D0*OMEGA^2.0D0)/SRB(EXPERNUM);
PINF=PINFDIM(EXPERNUM)/(PL(EXPERNUM)*RB(EXPERNUM)^2.0D0*OMEGA^2.0D0);
U=URDIM(EXPERNUM)/RB(EXPERNUM)
R=RB(EXPERNUM)/RB(EXPERNUM);
Z=DISTANCE(EXPERNUM)/RB(EXPERNUM);
TEXPU=TEXP*OMEGA;
PEXPU=PEXP/(PL(EXPERNUM)*RB(EXPERNUM)^2.0D0*OMEGA^2.0D0);
%%%%%%%%%%%%%%%%%%%%%%%%%%%%%%%%DIMENSIONLESS%%%%%%%%%%%%%%%%%%%%%%%%%%%%%%%%
%%%%%%%%%%%%%%%%%%%%%%%%%%INITIAL VALUES%%%%%%%%%%%%%%%%%%%%%%%%%%%%%%%%%%%%
TSTEPEXPU=TEXPU(2)-TEXPU(1);
STARTTIMEXPU=TEXPU(1);
ENDTIMEXPU=TEXPU(end);
DPEXPUDT(1)=(-PEXPU(3)+4*PEXPU(2)-3*PEXPU(1))/2/TSTEPEXPU;
for IEXP=2:LEXP-1
DPEXPUDT(IEXP)=(PEXPU(IEXP+1)-PEXPU(IEXP-1))/2/TSTEPEXPU;
end
DPEXPUDT(LEXP)=(PEXPU(LEXP-2)-4*PEXPU(LEXP-1)+3*PEXPU(LEXP))/2/TSTEPEXPU;
ENDTIME=ENDTIMEXPU;
STARTTIME=STARTTIMEXPU;
TIME=STARTTIME;
NUMSTEP=(ENDTIME-STARTTIME)/TIMESTEP(EXPERNUM);
TSTEP=TIMESTEP(EXPERNUM);
DRDT=0.0D0;
RDRDT=0.0D0;
D2RDT=0.0d0;
METR=1;
J=1;
TSTEP=0.000001;

%ode45 integrator
   options = odeset('InitialStep',TSTEP,'RelTol',1e-3,'AbsTol',1e-6);%integrator options
   [T,Y] = ode23s('FUND2RDT_variable_step_RS',[STARTTIME:TIMESTEP:ENDTIME],[DRDT,R]',options,WEBSRB,PINF,MACH,...
   GAMA(EXPERNUM),REL,RES,GS,B(EXPERNUM),U,YLIKO(EXPERNUM),TEXPU,PEXPU,DPEXPUDT); %Matlab 5 syntax
   RAD=Y(:,2);
   %add code that Kostas uses to get PScattervector - ode45 can be set up to call a
   %function after each step to do this
   VELOCITY= Y(:,1);
   RADIUS= Y(:,2);
   for I=1:length(T)
       x = T(I);
       R = RADIUS(I);
       DRDT = VELOCITY(I);
       RRADIUS=R;
       RDRDT=DRDT;
       PSPLINE=spline(TEXPU,PEXPU,TIME);
       DPDTSPLINE=spline(TEXPU,DPEXPUDT,TIME);
       D2RDT=FUND2RDT(TIME,RRADIUS,RDRDT,WEBSRB,PINF,PSPLINE,DPDTSPLINE,MACH,GAMA(EXPERNUM),REL...
       ,RES,GS,B(EXPERNUM),U,YLIKO(EXPERNUM));
       PSCATTERVECTOR(I)=FUNPSCATTER(TIME,R,DRDT,D2RDT,WEBSRB,PINF,PSPLINE,GAMA(EXPERNUM),REL,RES....
       ,GS,B(EXPERNUM)...
       ,U,YLIKO(EXPERNUM),CONST(EXPERNUM),Z);
       TIME=x;
   fprintf(file2,'%E\t%E\t%E\t%E\t%E\n',TIME/OMEGA,R*RB(EXPERNUM),DRDT*RB(EXPERNUM)*OMEGA,....
   D2RDT*RB(EXPERNUM)*OMEGA^2,....
   PSCATTERVECTOR(I)*PL(EXPERNUM)*RB(EXPERNUM)^2.0D0*OMEGA^2.0D0);
   end
```

```
   fclose(file2);




end

end
%%%%%%%%%%%%%%%%%%%%%%%%%%%%FFT%%%%%%%%%%%%%%%%%%%%%%%%%%%%%%%%%%%%%%%%%%%%%%%%

function D2RDTF=FUND2RDT(TIME,R,DRDT,WEBSRB,PINF,PSPLINE,DPDTSPLINE,MACH,GAMA,REL,RES,GS,B,U,YLIKO)
%%%%%%%%%%%%%%%%%%%%%%%%%%%%%%%%%%%%%%%%%%%%%%%%%%%%%%%%%%%%%%%%%%%%%%%%%%%%%%%
if YLIKO==1
clear PIBA PIBB OROS1 OROS2 ARITH PARON ARITH1 ARITH2 D2RDTF;
OROS1=1.0D0+DRDT*MACH;
OROS2=R*MACH;
PIBA=(1.0D0-(1.0D0-U)^6.0D0)*(1.0D0+B*(-1.0D0+(1.0D0/(1.0D0-U))^2.0D0));
PIBB=(1.0D0-((1.0D0-U)/R)^6.0D0)*(1.0D0+B*(-1.0D0+(R/(1.0D0-U))^2.0D0));
ARITH1=(1.0D0/R)^(3.0D0*GAMA)*(PINF+2.0D0/WEBSRB+2.0D0*GS*PIBA);
ARITH1=ARITH1-2.0D0/(WEBSRB*R)-4.0D0*DRDT/(REL*R)-2.0D0*GS*PIBB/R-4.0D0*DRDT/(RES*R^2.0D0)-PINF-PSPLINE;
ARITH2=-3.0D0*GAMA*DRDT*R^(-3.0D0*GAMA-1.0D0)*(PINF+2.0D0/WEBSRB+2.0D0*GS*PIBA);
ARITH2=ARITH2+2.0D0*DRDT/(WEBSRB*R^2.0D0)+2.0D0*GS*DRDT/(R^2.0D0);
ARITH2=ARITH2-2.0D0*GS*B*DRDT/((1.0D0-U)^2.0D0)-2.0D0*GS*B*DRDT/(R^2.0D0);
ARITH2=ARITH2-14.0D0*GS*DRDT*((1.0D0-U)^6.0D0)/(R^8.0D0);
ARITH2=ARITH2-10.0D0*GS*B*DRDT*((1.0D0-U)^4.0D0)/(R^6.0D0)+14.0D0*GS*B*DRDT*((1.0D0-U)^6.0D0)/(R^8.0D0)-DPDTSPLINE;
ARITH=OROS1*ARITH1+OROS2*ARITH2-(3.0D0/2.0D0-DRDT*MACH/2.0D0)*(DRDT^2.0D0)+4.0D0*MACH*(DRDT^2.0D0)/(REL*R);
ARITH=ARITH+8.0D0*MACH*(DRDT^2.0D0)/(RES*R^2.0D0);
PARON=(1.0D0-DRDT*MACH)*R+4.0D0*MACH/(REL)+4.0D0*MACH/(RES*R);
D2RDTF=ARITH/PARON;
clear PIBA PIBB OROS1 OROS2 ARITH PARON ARITH1 ARITH2
end
%%%%%%%%%%%%%%%%%%%%%%%%%%%%%%%%%%%%%%%%%%%%%%%%%%%%%%%%%%%%%%%%%%%%%%%%%%%%%%%
%%%%%%%%%%%%%%%%%%%%%%%%%%%%%%%%%%%%%%%%%%%%%%%%%%%%%%%%%%%%%%%%%%%%%%%%%%%%%%%
if YLIKO==2
clear PIBA PIBB PIBR OROS1 OROS2 ARITH PARON ARITH1 ARITH2 D2RDTF
OROS1=1.0D0+DRDT*MACH;
OROS2=R*MACH;
PIBA=(1.0D0-B)*(1.0D0/(1.0D0-U))^(2.0D0)+B*(1.0D0/(1.0D0-U))^(6.0D0)-1.0D0;
PIBR=(1.0D0-B)*(R/(1.0D0-U))^(2.0D0)+B*(R/(1.0D0-U))^(6.0D0)-1.0D0;
PIBB=2.0D0*(1.0D0-B)*R*DRDT/((1.0D0-U)^(2.0D0))+6.0D0*B*DRDT*(R^5.0D0)/((1.0D0-U)^(6.0D0));
ARITH1=(1.0D0/R)^(3.0D0*GAMA)*(PINF+2.0D0/WEBSRB+2.0D0*GS*PIBA);
ARITH1=ARITH1-2.0D0/(WEBSRB*R)-4.0D0*DRDT/(REL*R)-2.0D0*GS*PIBR/R-4.0D0*DRDT/(RES*R^2.0D0)-PINF-PSPLINE;
ARITH2=-3.0D0*GAMA*DRDT*R^(-3.0D0*GAMA-1.0D0)*(PINF+2.0D0/WEBSRB+2.0D0*GS*PIBA);
ARITH2=ARITH2+2.0D0*DRDT/(WEBSRB*R^2.0D0)+4.0D0*(DRDT^2.0D0)/(REL*R^2.0D0);
ARITH2=ARITH2-2.0D0*GS*PIBB/R+8.0D0*(DRDT^2.0D0)/(RES*R^3.0D0);
ARITH2=ARITH2-DPDTSPLINE;
ARITH=OROS1*ARITH1+OROS2*ARITH2-(3.0D0/2.0D0-DRDT*MACH/2.0D0)*(DRDT^2.0D0);
PARON=(1.0D0-DRDT*MACH)*R+4.0D0*MACH/(REL)+4.0D0*MACH/(RES*R);
D2RDTF=ARITH/PARON;
clear PIBA PIBB PIBR OROS1 OROS2 ARITH PARON ARITH1 ARITH2
end
if YLIKO==3
clear PIBA PIBB PIBR OROS1 OROS2 ARITH PARON ARITH1 ARITH2 D2RDTF
OROS1=1.0D0+DRDT*MACH;
OROS2=R*MACH;
PIBA=1-exp(-8*(U));
PIBB=exp(-4*(U));
PIBAR=1-exp(-8*(R-1));
PIBBR=exp(-4*(R-1));
RESS=(1/RES)*4;
GSS=(3/2)*GS;
ARITH1=(1.0D0/R)^(3.0D0*GAMA)*(PINF+2.0D0/WEBSRB+GSS*PIBA);
```

```
ARITH1=ARITH1-2.0D0/(WEBSRB*R)-GSS*PIBAR-RESS*PIBBR*DRDT-4.0D0*DRDT/(REL*R)-PINF-PSPLINE;
ARITH2=-3.0D0*GAMA*DRDT*R^(-3.0D0*GAMA-1.0D0)*(PINF+2.0D0/WEBSRB+2.0D0*GS*PIBA);
ARITH2=ARITH2+2.0D0*DRDT/(WEBSRB*R^2.0D0)+8*DRDT*GSS*exp(-8*(R-1))-4*RESS*PIBBR*DRDT;
ARITH2=ARITH2-DPDTSPLINE;
ARITH=OROS1*ARITH1+OROS2*ARITH2-(3.0D0/2.0D0-DRDT*MACH/2.0D0)*(DRDT^2.0D0)+4.0D0*MACH*(DRDT^2.0D0)/(REL*R);
PARON=(1.0D0-DRDT*MACH)*R+4.0D0*MACH/(REL)+RESS;
D2RDTF=ARITH/PARON;
clear PIBA PIBB OROS1 OROS2 ARITH PARON ARITH1 ARITH2 PIBBR PIBAR
end
%%%%%%%%%%%%%%%%%%%%%%%%%%%%%%%%%%%%%%%%SKALAK%%%%STRAIN-HARDENING%%%%%%%%%%%%%%%%%%%%%%%%%%%%%%%%
```

Code to calculate the diffusion from a MB

```
clear
%%%%%%%%%%%%%%%%%%%%%%%%%%%%%%%%%%INPUT DATA%%%%%%%%%%%%%%%%%%%%%%%%%%%%%%%%%%

cd inputII;
[names,TIMESTEP,VALUE,GAMA,PINFDIM,CL,PL,ML,SRB,RB,GSDIM,THICKNESS,YLIKO,B,URDIM,MSK,FREQ,SD,CONST,DISTANCE]...
=textread('Input_CONTRAST1D.txt','%s%f%f%f%f%f%f%f%f%f%f%f%f%f%f%f%f%f%f%f%f','headerlines',2);
cd ..;

%%%%%%%%%%%%%%%%%%%%%%%%%%%%%%%%%%INPUT DATA%%%%%%%%%%%%%%%%%%%%%%%%%%%%%%%%%%

%%%%%%%%%%%%%%%%%%%%%%%%%%READ EXPERIMENTAL DATA FROM FILE%%%%%%%%%%%%%%%%%%
for EXPERNUM=1
%VALUE(EXPERNUM)=1;

cd inputII;
warning off;
EXPERIMENT=load(char(names(EXPERNUM)));
LEXP=size(EXPERIMENT,1);
PEXP=EXPERIMENT(:,2);
cd ..;

%%%%%%%%%%%%%%%%%%%%%%%%%%READ EXPERIMENTAL DATA FROM FILE%%%%%%%%%%%%%%%%%%

%%%%%%%%%%%%%%%%%%%%%%%%%%%%%%%%OPEN RESULT FILES%%%%%%%%%%%%%%%%%%%%%%%%%%%%%%%%
%fil=load(strcat('T_R_DRDT_D2RDT_PRESSCATTER_',char(names(EXPERNUM))),'w+');
TEXP=[1:1:200000]*10^(-8);%fil(:,1);
%Rt=fil(:,2);
RAD=10*10^(-6);
Rt=1;%Rt/Rt(1);
RFOUR=Rt.*Rt.*Rt.*Rt;
PERIOD=1/FREQ(EXPERNUM);
DENS=PL(EXPERNUM);
%%%%%%%%%%%%%%%%%%%%%%%%%%%%%%%%OPEN RESULT FILES%%%%%%%%%%%%%%%%%%%%%%%%%%%%%%%%

%%%%%%%%%%%%%%%%%%%%%%%%%%%%%%%%%%%%%%%%DIMENSIONLESS%%%%%%%%%%%%%%%%%%%%%%%%%%%%%%%%%%%%
%RAD=10*10^(-6);

%%%%%%%%%%%%%%%%%%%%%%%%%%%%%%%%%%%%%%%%DIMENSIONLESS%%%%%%%%%%%%%%%%%%%%%%%%%%%%%%%%%%%%



%%%%%%%%%%%%%%%%%%%%%%%%%%%%%%%%%%%%%%%%INITIAL VALUES%%%%%%%%%%%%%%%%%%%%%%%%%%%%%%%%%%%%
TSTEP=TIMESTEP(1);
%%%%%%%%%%%%%%%%%%%%%%%%%%%%%%%%%%%%%%%%INITIAL VALUES%%%%%%%%%%%%%%%%%%%%%%%%%%%%%%%%%%%%

At = 1; % (1/PERIOD)*trapz(T,Rt)/6
Bt = 1; % (1/PERIOD)*trapz(T,RFOUR)/6
```

```
options = odeset('InitialStep',TSTEP,'RelTol',1e-15,'AbsTol',1e-29);
[SEC,Y] = ode45('FUNDIFF',[STARTTIME,ENDTIME],[R]',options,WEBSRB,PINF,DENS,RAD,GS,B(EXPERNUM),U,At,Bt);

RO=Y(:,1);
figure;
plot(SEC,RO);
end

function g=FUNDIFF(x,R,flg,WEBSRB,PINF,DENSGAS,RAD,GS,At,Bt,Co,Ci)
%Kostas' function adapted to Matlab5 format.
%%%%%%%%%%%%%%%%%%%%%%%%%%%%%%%%%%%%%%%%%%%%MOONEY-RIVLIN%%%%STRAIN-SOFTENING%%%%
%%%%%%%%%%%%%%%%%%%%%%%%%%%%%%%%%%%%%%%%%%%%%%%%%%%%%%%%%%%%%%%%%%%%%%%%%%%%%%%

PIBA=0;
%PO=(PINF+2.0D0/WEBSRB+2.0D0*GS*PIBA)*(DENS*RADˆ2.0D0*OMEGAˆ2.0D0);
%At=1;
%Bt=1;
clear ARITH DRODT Csn PO
PO=(PINF+2/(WEBSRB*RAD*R)+2.0D0*GS*PIBA);
Csn=Co*(PO/PINF);
ARITH=((At+(R/x)*sqrt(0/pi))*Csn*((Ci/Csn)-(At/Bt))*2*x)/(DENSGAS*R);
DRDT=ARITH;
g=[DRDT];
clear ARITH Csn PO
```

Code to calculate the change in MB radius due to shell loss

```
%%%%Lipid Shedding
clear
%%%%%%%%%%%%%%%%%%%%%%%%%%%%%%%%%%%%%%%%%%%%%%%%%%%%%%%%%%%%%%%%%%%%%%%%%%%%%%%
cd ..;


cd input;
[names,TIMESTEP,VALUE,GAMA,PINFDIM,CL,PL,ML,SRB,RB,GSDIM,THICKNESS,YLIKO,B,URDIM,MSK,FREQ,SD,CONST,DISTANCE]...
=textread('Input_CONTRAST1D.txt','%s%f%f%f%f%f%f%f%f%f%f%f%f%f%f%f%f%f%f%f%f%f','headerlines',2);
cd ..;


[ainm,EXP,NUM,VOL]=textread('Definitydist1.txt','%s%f%f%f');
RADI=resample(((10ˆ(-6))/2)*EXP,100,length(ainm));
PRO = resample(NUM/100,100,length(ainm));
names2={'185.txt' '275.txt' '335.txt' '550.txt' '750.txt' '1110.txt' '1500.txt'};
cd lipshed;


for EXPERNUM=1:length(names2)


filename=strcat('R_',char(names2(EXPERNUM)));
FIN=load(filename);

RADI=FIN(:,3);
%IND=find(RADI)>0.1*10ˆ(-6);
RMIN=RADI-0.4*10ˆ(-6);
%PINFDIM(EXPERNUM)/(PL(EXPERNUM)*RADI(X)ˆ2.0D0*OMEGAˆ2.0D0);
%PINF=PINFDIM(EXPERNUM);
U=0;
```

```
for X=1:length(RADI)
cd(num2str(X));
file3=fopen(strcat('equilplt',char(names2(EXPERNUM))),'w+');
cd ..;
for R=0.5:0.01:1
U0=(R-(1+1*(RMIN(X)/RADI(X)-1)));
if YLIKO==1
clear PIBA PIBB OROS1 OROS2 ARITH PARON ARITH1 ARITH2 D2RDTF;
%OROS1=1.0D0+DRDT*MACH;
%OROS2=R*MACH;
PIBA=(1.0D0-(1.0D0-U)^6.0D0)*(1.0D0+B(EXPERNUM)*(-1.0D0+(1.0D0/(1.0D0-U))^2.0D0));
PIBA0=(1.0D0-(1.0D0-U0)^6.0D0)*(1.0D0+B(EXPERNUM)*(-1.0D0+(1.0D0/(1.0D0-U0))^2.0D0));
PIBB=(1.0D0-((1.0D0-U)/R)^6.0D0)*(1.0D0+B*(-1.0D0+(R/(1.0D0-U))^2.0D0));
ARITH1=((1.0D0/R)^(3.0D0*1))*(PINFDIM(EXPERNUM)+2.0D0*SRB(EXPERNUM)/RADI(X)+...
2.0D0*GSDIM(EXPERNUM)*PIBA)/(PINFDIM(EXPERNUM)+2.0D0*SRB(EXPERNUM)/(R*RADI(X))+...
2.0D0*GSDIM(EXPERNUM)*PIBA0*(THICKNESS(EXPERNUM)/(R*RADI(X))));
clear PIBA PIBB OROS1 OROS2 ARITH PARON
end
%%%%%%%%%%%%%%%%%%%%%%%%%%%%%%%%%%%%%%%%%%%%MOONEY-RIVLIN%%%%STRAIN-SOFTENING%%%%%%%%%%%%%%%%%%%%%%%%%%%%
%%%%%%%%%%%%%%%%%%%%%%%%%%%%%%%%%%%%%%%%%%%%SKALAK%%%%STRAIN-HARDENING%%%%%%%%%%%%%%%%%%%%%%%%%%%%%%%%%%%%
if YLIKO==2
clear PIBA PIBB PIBR OROS1 OROS2 ARITH PARON ARITH1 ARITH2 D2RDTF
%OROS1=1.0D0+DRDT*MACH;
%OROS2=R*MACH;
PIBA=(1.0D0-B(EXPERNUM))*(1.0D0/(1.0D0-U))^(2.0D0)+B(EXPERNUM)*(1.0D0/(1.0D0-U))^(6.0D0)-1.0D0;
PIBA0=(1.0D0-B(EXPERNUM))*(1.0D0/(1.0D0-U0))^(2.0D0)+B(EXPERNUM)*(1.0D0/(1.0D0-U0))^(6.0D0)-1.0D0;
PIBR=(1.0D0-B(EXPERNUM))*(R/(1.0D0-U))^(2.0D0)+B(EXPERNUM)*(R/(1.0D0-U))^(6.0D0)-1.0D0;
%PIBB=2.0D0*(1.0D0-B)*R*DRDT/((1.0D0-U)^(2.0D0))+6.0D0*B*DRDT*(R^5.0D0)/((1.0D0-U)^(6.0D0));
ARITH1=((1.0D0/R)^(3.0D0*1))*(PINFDIM(EXPERNUM)+2.0D0*SRB(EXPERNUM)/RADI(X)+.....
2.0D0*GSDIM(EXPERNUM)*PIBA*(THICKNESS(EXPERNUM)/(R*RADI(X))))/(PINFDIM(EXPERNUM)+....
2.0D0*SRB(EXPERNUM)/(R*RADI(X))+2.0D0*GSDIM(EXPERNUM)*(THICKNESS(EXPERNUM)/(R*RADI(X)))*PIBA0);
clear PIBA PIBB PIBR OROS1 OROS2 ARITH PARON  ARITH2
end
%%%%%%%%%%%%%%%%%%%%%%%%%%%%%%%%%%%%%%%%%%%%SKALAK%%%%STRAIN-HARDENING%%%%%%%%%%%%%%%%%%%%%%%%%%%%%%%%%%%%
%%%%%%%%%%%%%%%%%%%%%%%%%%%%%%%%%%%%%%%%%%%%HOFF MODEL%%%%%%%%%%%%%%%%%%%%%%%%%%%%%%%%%%%%%%%%%%%%%%%%%%%%
if YLIKO==3
clear PIBA PIBB PIBR OROS1 OROS2 ARITH PARON ARITH1 ARITH2 D2RDTF
OROS1=1.0D0+DRDT*MACH;
OROS2=R*MACH;
PIBA=1-exp(8*(U));
PIBB=-exp(4*(U));
PIBAR=1-exp(8*(R-1));
PIBBR=-exp(4*(R-1));
RESS=(1/RES)*4*PIBAR;
GSS=(3/2)*GS;
ARITH1=(1.0D0/R)^(3.0D0*GAMA(EXPERNUM))*(PINF+2.0D0/WEBSRB+2.0D0*GS*PIBA);
clear PIBA PIBB OROS1 OROS2 ARITH PARON ARITH2 PIBBR PIBAR
end
%%%%%%%%%%%%%%%%%%%%%%%%%%%%%%%%%%%%%%%%%%%%HOFF MODEL%%%%%%%%%%%%%%%%%%%%%%%%%%%%%%%%%%%%%%%%%%%%%%%%%%%%
fprintf(file3,'%E\t%E\t%E\n',ARITH1,R,U0);
end

fclose(file3);
end

end
```

Appendix D
Experimental Methodology

The methodology used by David Thomas[131] to measure the acoustic responses from MBs encompassed the calibration of the ultrasound system and optimisation of the environment that the MBs are in relative to the ultrasound system. The design of the system can be found Sboros et al.; Sboros et al.[117;114].

Calibration of the ultrasound system

A modified version of a Philips Sonos 5500 (Philips Medical Systems, Andover, MA) imaging system was used to insonify the MBs. The modifications allowed a RF (radio frequency) signal to be captured from the machine. The ultrasound beam from this scanner was measured across a range of driving frequencis and pressures. The ultrasound received and transmited signal were calibrated so that the absolute magnitude of the transmitted pulse and received pulse were known.

Calibration of the transmitted signal

A membrane hydrophone was used to calibrate the transmitted signal. The membrane hydrophone was supplied with a National Physics Laboratory calibration certificate. The ultrasound transducer was clamped at the top of a 20 litre cylindrical tank and the hydrophone was positioned such that it gave the maximum output voltage. Six cycle pulses were used in the alignment and also in the experiments since they allow the non transient behaviour of the MBs to be observed and to detect the response of single MBs. The parameters of the ultrasound scanner were set to clinical settings. The focus of the ultrasound scanner was set at 6 cm. The region of interest for the received signals was set at 7.5 cm to allow the transmitted wave to be close to a plane wave. The beam plots found using the hydrophone verified this location as optimal. The transmit pulses were sampled with a sampling rate of 19.63 MHz and stored electronically so they could be easily used in further analysis and theoretical simualtions.

Calibration of the received signal

To convert the received signal into an absolute pressure and allow quantitative analysis the signals received by the transducer were also calibrated. Using copper spheres attached to a thin membrane the echoes of copper spheres with radii less than 150 μm were measured at the optimal location found when calibrating the transmitted signal. The membrane was thin enough so that the echo from the membrane could be neglected. Since the theoretical response of copper spheres is known the received signal can be calibrated for each frequency component allowing an absolute value of fundamental, second harmonic and third harmonic to be determined.

MB environment

By establishing a flow of water in the tube and injecting a dilute concentration of MBs into the flow a stream of single MBs can be directed towards the trandsucer in the centre of the ultrasonic beam. By controlling the dilution of the MBs injected one can ensure that a single MB will be contained in the region of interest in every third frame. This decreases the chance of multiple MB interactions. A sum of the squares technique was used to find frames in which MBs echoes were present. Using the calibrated transmit pulses echoes of single MBs were measured over a range of driving parameters and could be calibrated and compared to theoretical simulations.

Appendix E
List of symbols

Mathematical sysmbols

ρ	density of water
R	bubble radius
$\dot{R}$	bubble wall velocity
$\ddot{R}$	bubble wall acceleration
R_0	equilibrium radius
R_c	radius of leaked MB
c	velocity of sound in the fluid
P_∞	hydrostatic pressure
P	pressure on bubblewall
P_{Sh}	pressure due to shell
P_{Sc}	pressure at distance r from MB
σ	surface tension
γ	ratio of specific heats
G_S	shell stiffness
η_S	shell viscosity
d_{Se}	shell thickness
r	distance to MB
C_S	gas saturation concentration
C_∞	gas concentration at infinity
D	diffusion constant of the gas
U	shell displacement from equilibrium

Table E.1: *Table of parameters used throughout the thesis.*

Accronyms

MRI	magnetic resonance imaging
CT	computed tomography
MB	microbubble
UCA	ultrasound contrast agents
RPNNP	Rayleigh, Plesset, Noltingk, Neppiras and Poritsky
MI	mechanical index
RMS	root mean squared
GL	gas leaking
KS	Komolgorov-Smirnov

Table E.2: *Table of parameters used throughout the thesis.*

References

[1] J. S. Allen, D. E. Kruse, P. A. Dayton, and K. W. Ferrara. Effect of coupled oscillations on microbubble behavior. *The Journal of the Acoustical Society of America*, 114(3): 1678–1690, 2003.

[2] B. Angelsen, T. Johansen, and L. Hoff. Simulation of gas bubble scattering for large mach-numbers. *Ultrasonics Symposium, 1999. Proceedings. 1999 IEEE*, 1:505–508 vol.1, 1999.

[3] R. Basude and M. A. Wheatley. Generation of ultraharmonics in surfactant based ultrasound contrast agents: use and advantages. *Ultrasonics*, 39(6):437–444, 2001.

[4] T. B. Benjamin and A. T. Ellis. The Collapse of Cavitation Bubbles and the Pressures thereby Produced against Solid Boundaries. *Royal Society of London Philosophical Transactions Series A*, 260:221–240, 1966.

[5] P. D. Bevan, R. Karshafian, and P. N. Burns. The influence of fragmentation on the acoustic response from shrinking bubbles. *Ultrasound in Medicine & Biology*, 34:1–11, 2008.

[6] E. Biagi, L. Breschi, E. Vannacci, and L. Masotti. Stable and transient subharmonic emissions from isolated contrast agent microbubbles. *Ultrasonics, Ferroelectrics and Frequency Control, IEEE Transactions on*, 54:480–497, 2007.

[7] S. H. Bloch, M. Wan, P. A. Dayton, and K. W. Ferrara. Optical observation of lipid- and polymer-shelled ultrasound microbubble contrast agents. *Applied Physics Letters*, 84(631):631–+, 2004.

[8] M. A. Borden and M. L. Longo. Dissolution behavior of lipid mono-layer-coated, air-filled microbubbles: Effect of lipid hydrophobic chain length. *Langmuir*, 18:9225–9233, 2002.

[9] A. Bouakaz and K. Shung. Selective destruction of contrast agent microspheres [drug delivery application]. *Ultrasonics Symposium, 1999. Proceedings. 1999 IEEE*, 2:1693–1696 vol.2, 1999.

[10] A. Bouakaz, M. Versluis, and N. de Jong. High-speed optical observations of contrast agent destruction. *Ultrasound in Medicine & Biology*, 31:391–399, 2005.

[11] C. E. Brennen. Fission of collapsing cavitation bubbles. *Journal of Fluid Mechanics*, 472:153–166, 2002.

[12] M. P. Brenner, D. Lohse, and T. F. Dupont. Bubble shape oscillations and the onset of sonoluminescence. *Phys. Rev. Lett.*, 75(5):954–957, 1995.

[13] M. B. Butler, D. H. Thomas, S. D. Pye, C. M. Moran, W. N. McDicken, and V. Sboros. The acoustic response from individual attached and unattached rigid shelled microbubbles. *Applied Physics Letters*, 93(22):223906–+, 2008.

[14] C. F. Caskey, D. E. Kruse, P. A. Dayton, T. K. Kitano, and K. W. Ferrara. Microbubble oscillation in tubes with diameters of 12, 25, and 195 microns. *Applied Physics Letters*, 88(3):033902–+, Jan. 2006. doi: 10.1063/1.2164392.

[15] I. M. Chakravarti, R. G. Laha, and J. Roy. *Handbook of Methods of Applied Statistics*, volume 1. John Wiley and Sons, 1967.

[16] D. Chatterjee and K. Sarkar. A newtonian rheological model for the interface of microbubble contrast agents. *Ultrasound in Medicine & Biology*, 29(12):1749–1757, 2005.

[17] C. T. Chin and P. N. Burns. Predicting the acoustic response of a microbubble population for contrast imaging in medical ultrasound. *Ultrasound in Medicine & Biology*, 26(8): 1293 – 1300, 2000.

[18] J. E. Chomas, P. Dayton, D. May, and K. W. Ferrara. Mechanisms of contrast agent destruction. *Ultrasonics, Ferroelectrics and Frequency Control, IEEE Transactions on*, 48(1):232–248, 2001.

[19] J. E. Chomas, P. A. Dayton, D. J. May, and K. W. Ferrara. Threshold of fragmentation for ultrasonic contrast agents. *Journal of Biomedical Optics*, 6:141–150, 2001.

[20] C. C. Church. Prediction of rectified diffusion during nonlinear bubble pulsations at biomedical frequencies. *The Journal of the Acoustical Society of America*, 83(6):2210–2217, 1988.

[21] C. C. Church. The effects of an elastic solid surface layer on the radial pulsations of gas bubbles. *The Journal of the Acoustical Society of America*, 97(3):1510–1521, 1995.

[22] L. A. Crum. Measurements of the growth of air bubbles by rectified diffusion. *The Journal of the Acoustical Society of America*, 68(1):203–211, 1980.

[23] P. Dayton, K. Morgan, A. Klibanov, G. Brandenburger, and K. Ferrara. Optical and acoustical observations of the effects of ultrasound on contrast agents. *Ultrasonics, Ferroelectrics and Frequency Control, IEEE Transactions on*, 46(1):220–232, 1999.

[24] N. de Jong and L. Hoff. Ultrasound scattering properties of Albunex microsperes. *Ultrasonics*, 31:175–181, 1993.

[25] N. de Jong, L. Hoff, T. Skotland, and N. Bom. Absoprtion and scatter of encapsulated gas filled microspheres: theoretical considerations and some measurements. *Ultrasonics*, 30:95–103, 1992.

[26] N. de Jong, R. Cornet, and C. T. Lance. Higher harmonics of vibrating gas-filled microspheres.Part One:simulations. *Ultrasonics*, 32:447–453, 1994.

[27] N. de Jong, R. Cornet, and C. T. Lance. "Compression-only" behaviour of phospholipid-coated contrast bubbles. *Ultrasound in Medicine & Biology*, 33:653–656, 2007.

[28] A. A. Doinikov and P. A. Dayton. Maxwell rheological model for lipid-shelled ultrasound microbubble contrast agents. *The Journal of the Acoustical Society of America*, 121(6):3331–3340, 2007.

[29] B. Dollet, S. M. van der Meer, V. Garbin, N. de Jong, D. Lohse, and M. Versluis. Nonspherical oscillations of ultrasound contrast agent microbubbles. *Ultrasound in Medicine & Biology*, 34, 2008.

[30] A. Eller and H. G. Flynn. Rectified diffusion during nonlinear pulsations of cavitation bubbles. *The Journal of the Acoustical Society of America*, 37(3):493–503, 1965.

[31] A. Eller and H. G. Flynn. Generation of subharmonics of order one-half by bubbles in a sound field. *The Journal of the Acoustical Society of America*, 46(3B):722–727, 1969.

[32] A. I. Eller. Growth of bubbles by rectified diffusion. *The Journal of the Acoustical Society of America*, 46(5B):1246–1250, 1969.

[33] A. I. Eller and L. A. Crum. Instability of the motion of a pulsating bubble in a sound field. *The Journal of the Acoustical Society of America*, 47(3B):762–767, 1970.

[34] M. Emmer, A. van Wamel, D. E. Goertz, and N. de Jong. The onset of microbubble vibration. *Ultrasound in Medicine & Biology*, 33:941–949, 2007.

[35] P. S. Epstein and M. S. Plesset. On the Stability of Gas Bubbles in Liquid-Gas Solutions. *jcp*, 18:1505–1509, 1950.

[36] F. Forsberg, W. T. Shi, and B. B. Goldberg. Subharmonic imaging of contrast agents. *Ultrasonics*, 38:93–98, 2000.

[37] P. J. A. Frinking and N. de Jong. Acoustic modeling of shell-encapsulated gas bubbles. *Ultrasound in Medicine & Biology*, 24(4):523–533, 1998.

[38] P. J. A. Frinking, N. de Jong, and E. I. Céspedes. Scattering properties of encapsulated gas bubbles at high ultrasound pressures. *The Journal of the Acoustical Society of America*, 105(3):1989–1996, 1999.

[39] S. Fujikawa and T. Akamatsu. Effects of the non-equilibrium condensation of vapour on the pressure wave produced by the collapse of a bubble in a liquid. *Journal of Fluid Mechanics*, 97:481–512, 1980.

[40] M. M. Fyrillas and A. J. Szeri. Dissolution or growth of soluble spherical oscillating bubbles. *Journal of Fluid Mechanics*, 277:381–407, 1994.

[41] Y. Ganor, D. Adam, and E. Kimmel. Time and pressure dependence of acoustic signals radiated from microbubbles. *Ultrasound in Medicine & Biology*, 31:1367–1374, 2005.

[42] P. Germonpre, P. Dendale, P. Unger, and C. Balestra. Patent foramen ovale and decompression sickness in sports divers. *J Appl Physiol*, 84(5):1622–1626, 1998.

[43] F. R. Gilmore. The growth or collapse of a spherical bubble in a viscous compressible liquid. Technical Report 3B, California Institute of Technology, Pasadena, CA, 1952.

[44] E. Glynos, K. V., W. McDicken, C. Moran, S. Pye, J. Ross, and V. Sboros. Nanomechanics of biocompatible hollow thin-shell polymer microspheres. *Langmuir*, 25:7514–7522, 2009.

[45] H. G. Goldstein, C. P. Poole, and J. Safko. *Classical Mechanics*. Addison Wesley, 2002.

[46] J.-M. Gorce, M. Arditi, and M. Schneider. Influence of bubble size distribution on the echogenicity of ultrasound contrast agents. *Investigative Radiology*, 35(11):661–671, 2000.

[47] R. K. Gould. Rectified diffusion in the presence of, and absence of, acoustic streaming. *The Journal of the Acoustical Society of America*, 56(6):1740–1746, 1974.

[48] R. Gramiak and P. Shah. Echocardiography of the aortic root. *Invest. Radiol.*, 3:356–366, 1968.

[49] S. Grossmann, S. Hilgenfeldt, D. Lohse, and M. Zomack. Sound radiation of 3-mhz driven gas bubbles. *The Journal of the Acoustical Society of America*, 102(2):1223–1230, 1997.

[50] P. Hall and G. Seminara. Nonlinear oscillations of non-spherical cavitation bubbles in acoustic fields. *Journal of Fluid Mechanics*, 101:423–444, 1980.

[51] J. Hancock, H. Dittrich, D. E. Jewitt, and M. J. Monaghan. Evaluation of myocardial, hepatic, and renal perfusion in a variety of clinical conditions using an intravenous ultrasound contrast agent (Optison) and second harmonic imaging. *Heart*, 81(6):636–641, 1999.

[52] C. J. Harvey, M. J. Blomley, R. J. Eckersley, R. A. Heckemann, J. Butler-Barnes, and D. O. Cosgrove. Pulse-inversion mode imaging of liver specific microbubbles: improved detection of subcentimetre metastases. *The Lancet*, 355(9206):807 – 808, 2000.

[53] C. Herring. Osrd report no 236. *NDRC C 4-sr 10-010*, 1941.

[54] D. M. Heyes. Non-newtonian behaviour of simple liquids. *Journal of Non-Newtonian Fluid Mechanics*, 21(2):137 – 155, 1986.

[55] S. Hilgenfeldt and D. Lohse. The acoustics of diagnostic microbubbles: dissipative effects and heat deposition. *Ultrasonics*, 38:99–104, 2000.

[56] S. Hilgenfeldt, D. Lohse, and M. Zomack. Sound scattering and localized heat deposition of pulse-driven microbubbles. *The Journal of the Acoustical Society of America*, 107(6): 3530–3539, 2000.

[57] L. Hoff. *Acoustic Characterization of Contrast Agents for Medical Ultrasound Imaging*. Kluwer Academic Publishers, 2001.

[58] L. Hoff. Nonlinear response of sonazoid. numerical simulations of pulse-inversion and subharmonics. *Ultrasonics Symposium, 2000 IEEE*, 2:1885–1888 vol.2, Oct 2000.

[59] L. Hoff and T. Johansen. Nonlinear scatter from sonazoid. In *Ultrasonics Symposium, 1999. Proceedings. 1999 IEEE*, volume 2, pages 1681–1684 vol.2, 1999.

[60] L. Hoff, P. C. Sontum, and J. M. Hovem. Oscillations of polymeric microbubbles: Effect of the encapsulating shell. *The Journal of the Acoustical Society of America*, 107(4): 2272–2280, 2000.

[61] Y. Hu, S. Qin, T. Hu, K. W. Ferrara, and Q. Jiang. Asymmetric oscillation of cavitation bubbles in a microvessel and its implications upon mechanisms of clinical vessel injury in shock-wave lithotripsy. *International Journal of Non-Linear Mechanics*, 40:341–350, 2005.

[62] V. Kamath and A. Prosperetti. Numerical integration methods in gas-bubble dynamics. *The Journal of the Acoustical Society of America*, 85(4):1538–1548, 1989.

[63] J. B. Keller and M. Miksis. Bubble oscillations of large amplitude . *Acoustical Society of America Journal*, 68:628–633, 1980.

[64] D. B. Khismatullin. Resonance frequency of microbubbles: Effect of viscosity. *Acoustical Society of America Journal*, 116:1463–1473, 2004.

[65] D. B. Khismatullin and I. S. Akhatov. Sound–ultrasound interaction in bubbly fluids: Theory and possible applications. *Physics of Fluids*, 13(12):3582–3598, 2001.

[66] D. B. Khismatullin and A. Nadim. Radial oscillations of encapsulated microbubbles in viscoelastic liquids. *Physics of Fluids*, 14(10):3534–3557, 2002.

[67] A. L. Klibanov, P. T. Rasche, M. S. Hughes, J. K. Wojdyla, K. P. Galen, J. H. Wible, Jr, and G. H. Brandenburger. Detection of individual microbubbles of an ultrasound contrast agent: Fundamental and pulse inversion imaging. *Academic Radiology*, 9(2, Supplement 1):S279 – S281, 2002.

[68] J. Kolb and W. L. Nyborg. Small-scale acoustic streaming in liquids. *The Journal of the Acoustical Society of America*, 28(6):1237–1242, 1956.

[69] B. Krasovitski and E. Kimmel. Gas bubble pulsation in a semiconfined space subjected to ultrasound. *The Journal of the Acoustical Society of America*, 109(3):891–898, 2001.

[70] B. Krasovitski and E. Kimmel. Stability of an encapsulated bubble shell. *Ultrasonics*, 44:216–220, 2006.

[71] N. Kudo and K. Yamamoto. Physical properties of ultrasound contrast agents. *Ultrasonics in Medicine. Proceedings of the 7th Congress of the Asian Federation of Ultrasound in Medicine and Biology*, 1274:49–52, 2004.

[72] W. Lauterborn and U. Parlitz. Methods of chaos physics and their application to acoustics. *The Journal of the Acoustical Society of America*, 84(6):1975–1993, 1988.

[73] P. Lechat, J. Mas, G. Lascault, P. Loron, M. Theard, M. Klimczac, G. Drobinski, D. Thomas, and Y. Grosgogeat. Prevalence of patent foramen ovale in patients with stroke. *N Engl J Med*, 318(18):1148–1152, 1988.

[74] T. G. Leighton. *The acoustic bubble*. Academic Press, 1997.

[75] A. Lezzi and A. Prosperetti. Bubble dynamics in a compressible liquid. Part 2. Second-order theory. *Journal of Fluid Mechanics*, 185:289–321, 1987.

[76] O. Lotsberg, J. M. Hovem, and B. Aksum. Experimental observation of subharmonic oscillations in infoson bubbles. *The Journal of the Acoustical Society of America*, 99(3): 1366–1369, 1996.

[77] C. A. Macdonald and J. Gomatam. Chaotic dynamics of microbubbles in ultrasonic fields. *J.Mechanical Engineering Science*, 220(2):333–343, 2005.

[78] P. Marmottant, S. van der Meer, M. Emmer, M. Versluis, N. de Jong, S. Hilgenfeldt, and D. Lohse. A model for large amplitude oscillations of coated bubbles accounting for buckling and rupture. *The Journal of the Acoustical Society of America*, 118(6): 3499–3505, 2005.

[79] R. N. Meidani and M. Hasan. Mathematical and physical modelling of bubble growth due to ultrasound. *Applied Mathematical Modelling*, 28:333–351, 2004.

[80] A. B. Michiel Postema and N. de Jong. Noninvasive microbubble-based pressure measurements: a simulation study. *Ultrasonics*, 42:759–762, 2004.

[81] M. Mooney. A theory of large elastic deformation. *Journal of Applied Physics*, 11(9): 582–592, 1940.

[82] K. Morgan, J. Allen, P. Dayton, J. Chomas, A. Klibaov, and K. Ferrara. Experimental and theoretical evaluation of microbubble behavior: effect of transmitted phase and bubble size. *Ultrasonics, Ferroelectrics and Frequency Control, IEEE Transactions on*, 47(6): 1494–1509, 2000.

[83] K. E. Morgan, J. S. Allen, J. E.Chomas, P. A.Dayton, and K. W.Ferrara. Experimental and theoretical analysis of individual contrast agent behaviour. *IEEE Ultrasonics symposium*, pages 1685–1688, 1999.

[84] E. A. Neppiras. Subharmonic and other low-frequency signals from sound-irradiated liquids. *Journal of Sound Vibration*, 10:176–176, 1969.

[85] E. A. Neppiras and B. E. Noltingk. Cavitation Produced by Ultrasonics: Theoretical Conditions for the Onset of Cavitation . *Proceedings of the Physical Society B*, 64: 1032–1038, 1951.

[86] B. E. Noltingk and E. A. Neppiras. Cavitation produced by Ultrasonics . *Proceedings of the Physical Society B*, 63:674–685, 1950.

[87] W. L. Nyborg. Acoustic streaming near a boundary. *The Journal of the Acoustical Society of America*, 30(4):329–339, 1958.

[88] H. N. Oguz and A. Prosperetti. The natural frequency of oscillation of gas bubbles in tubes. *The Journal of the Acoustical Society of America*, 103(6):3301–3308, 1998.

[89] U. Parlitz, V. Englisch, C. Scheffczyk, and W. Lauterborn. Bifurcation structure of bubble oscillators. *The Journal of the Acoustical Society of America*, 88(2):1061–1077, 1990.

[90] M. S. Plesset. The dynamics of cavitation bubbles. *Journal of Applied Mechanics*, 16: 277–282, 1949.

[91] M. S. Plesset and A. Prosperetti. Bubble dynamics and cavitation. *Annual Review of Fluid Mechanics*, 9:145–185, 1977.

[92] H. Poritsky. The collapse or growth of a spherical cavity in a viscous fluid. *Proceedings of the first U.S. National Congress on Applied Mechanics*, pages 813–821, 1952.

[93] M. Postema and G. Schmitz. Ultrasonic bubbles in medicine: Influence of shell. *The Journal of the Acoustical Society of America*, 106(2):674–681, 1999.

[94] M. Postema, A. van Wamel, C. T. Lance, and N. de Jong. Ultrasound-induced encapsulated microbubble phenomena. *Ultrasound in Medicine & Biology*, 30(6):827 – 840, 2004.

[95] M. Postema, A. Bouakaz, M. Versluis, and N. de Jong. Ultrasound-induced gas release from contrast agent microbubbles. *Ultrasonics, Ferroelectrics and Frequency Control, IEEE Transactions on*, 52(6):1035–1041, 2005.

[96] M. Postema, N. de Jong, and G. Schmitz. Shell rupture threshold, fragmentation threshold, blake threshold. *Ultrasonics Symposium, 2005 IEEE*, 3:1708–1711, 2005.

[97] R. J. Price, D. M. Skyba, S. Kaul, and T. C. Skalak. Delivery of Colloidal Particles and Red Blood Cells to Tissue Through Microvessel Ruptures Created by Targeted Microbubble Destruction With Ultrasound. *Circulation*, 98(13):1264–1267, 1998.

[98] A. Prosperetti. Nonlinear oscillations of gas bubbles in liquids: steady-state solutions. *The Journal of the Acoustical Society of America*, 56(3):878–885, 1974.

[99] A. Prosperetti. Nonlinear oscillations of gas bubbles in liquids. transient solutions and the connection between subharmonic signal and cavitation. *The Journal of the Acoustical Society of America*, 57(4):810–821, 1975.

[100] A. Prosperetti. Bubble dynamics: a review and some recent results. *Applied Scientific Research*, 38:145–164, 1982. ISSN 0003-6994. URL `http://dx.doi.org/10.1007/BF00385945`. 10.1007/BF00385945.

[101] A. Prosperetti and A. Lezzi. Bubble dynamics in a compressible liquid. Part 1. First-order theory. *Journal of Fluid Mechanics*, 168:457–478, 1986.

[102] S. Qin and K. W. Ferrara. Acoustic response of compliable microvessels containing ultrasound contrast agents. *Physics in Medicine and Biology*, 51:5065–5088, 2006.

[103] J. W. Rayleigh. On the pressure in a liquid during the collapse of a spherical cavity. *Philos. Mag.*, 34:94, 1917.

[104] R. S. Rivlin. Large Elastic Deformations of Isotropic Materials. III. Some Simple Problems in Cylindrical Polar Co-Ordinates. *Royal Society of London Philosophical Transactions Series A*, 240:509–525, 1948.

[105] M. H. Safar. RESEARCH NOTES: The exploitation of the subharmonic pressure waves from pulsating gas bubbles in an acoustic field in liquids. *Journal of Physics D Applied Physics*, 3:635–636, 1970.

[106] K. Sarkar, W. T. Shi, D. Chatterjee, and F. Forsberg. Characterization of ultrasound contrast microbubbles using in vitro experiments and viscous and viscoelastic interface models for encapsulation. *The Journal of the Acoustical Society of America*, 118(1): 539–550, 2005.

[107] K. Sarkar, A. Katiyar, and P. Jain. Growth and dissolution of an encapsulated contrast microbubble: effects of encapsulation permeability. *Ultrasound in Medicine & Biology*, 35:1385–1396, 2009.

[108] E. Sassaroli and K. Hynynen. Forced linear oscillations of microbubbles in blood capillaries. *The Journal of the Acoustical Society of America*, 115(6):3235–3243, 2004.

[109] E. Sassaroli and K. Hynynen. Resonance frequency of microbubbles in small blood vessels: a numerical study. *Physics in Medicine and Biology*, 50:5293–5305, 2005.

[110] K. Sato, Y. Tomita, and A. Shima. Numerical analysis of a gas bubble near a rigid boundary in an oscillatory pressure field. *The Journal of the Acoustical Society of America*, 95 (5):2416–2424, 1994.

[111] V. Sboros. Response of contrast agents to ultrasound. *Advanced drug delivery*, 60: 1117–1136, 2008.

[112] V. Sboros, C. M. Moran, T. Anderson, L. Gatzoulis, A. Criton, M. Averkiou, S. D. Pye, and W. N. McDicken. An in vitro system for the study of ultrasound contrast agents using a commercial imaging system. *Physics in Medicine and Biology*, 46:3301–3321, 2001.

[113] V. Sboros, C. M. Moran, S. D. Pye, and W. N. McDicken. The behaviour of individual contrast agent microbubbles. *Ultrasound in Medicine & Biology*, 29(5):687–694, 2003.

[114] V. Sboros, S. D. Pye, C. A. MacDonald, J. Gomatam, C. M. Moran, and W. N. McDicken. Absolute measurement of ultrasonic backscatter from single microbubbles. *Ultrasound in Medicine & Biology*, 31(8):1063 – 1072, 2005.

[115] V. Sboros, E. Glynos, S. Pye, C. Moran, M. Butler, J. Ross, R. Short, W. McDicken, and V. Koutsos. Nano-interrogation of ultrasonic contrast agent microbubbles using atomic force microscopy. *Ultrasound in Medicine & Biology*, 32:579–585, 2006.

[116] V. Sboros, E. Glynos, S. Pye, C. Moran, M. Butler, J. Ross, W. McDicken, and V. Koutsos. Nanomechanical probing of microbubbles using the atomic force microscope. *Ultrasonics*, 46(4):349 – 354, 2007.

[117] V. Sboros, S. D. Pye, T. A. Anderson, C. M. Moran, and W. N. McDicken. Acoustic Rayleigh scattering at individual micron-sized bubbles. *Applied Physics Letters*, 90(12): 123902–+, 2007.

[118] P. M. Shankar, P. D. Krishna, and V. L. Newhouse. Subharmonic backscattering from ultrasound contrast agents. *The Journal of the Acoustical Society of America*, 106(4): 2104–2110, 1999.

[119] W. T. Shi and F. Forsberg. Ultrasonic characterization of the nonlinear properties of contrast microbubbles. *Ultrasound in Medicine & Biology*, 26(1):93 – 104, 2000.

[120] W. T. Shi, F. Forsberg, A. Tornes, J. Ostensen, and B. B. Goldberg. Destruction of contrast microbubbles and the association with inertial cavitation. *Ultrasound in Medicine & Biology*, 26:1009–1019, 2000.

[121] R. Skalak, A. Tozeren, R. P. Zarda, and S. Chien. Strain Energy Function of Red Blood Cell Membranes. *Biophys. J.*, 13(3):245–264, 1973.

[122] L. A. Skinner. Acoustically induced gas bubble growth. *The Journal of the Acoustical Society of America*, 51(1B):378–382, 1972.

[123] M. Strasberg. Excitation of Oscillations in the Shape of Pulsating Gas Bubbles; Experimental Work. *Acoustical Society of America Journal*, 30:697–+, 1958.

[124] E. Stride and N. Saffari. On the destruction of microbubble ultrasound contrast agents. *Ultrasound in Medicine & Biology*, 29:563–573, 2002.

[125] E. Stride and N. Saffari. Microbubble ultrasound contrast agents: a review. *Proceedings of the Institution of Mechanical Engineers, Part H: Journal of Engineering in Medicine*, 217:429–447, 2003.

[126] H. Takahira, S. Yamane, and T. Akamatsu. Nonlinear oscillations of a cluster of bubbles in a sound field : Bifurcation structure. *JSME international journal. Ser. B, Fluids and thermal engineering*, 38(3):432–439, 19950815. ISSN 13408054.

[127] H. Takahira, E. Okura, and T. Nagata. Influence of gas diffusion on the stability and merger of microbubbles. *Fifth international symposium on Cavitation(CAV2003)*, pages 1–7, 2003.

[128] M.-X. Tang and R. Eckersley. Nonlinear propagation of ultrasound through microbubble contrast agents and implications for imaging. *Ultrasonics, Ferroelectrics and Frequency Control, IEEE Transactions on*, 53(12):2406–2415, 2006.

[129] V. S. . M.-X. Tang. The assessment of microvascular flow and tissue perfusion using ultrasound imaging. *Proceedings of the Institution of Mechanical Engineers, Part H: Journal of Engineering in Medicine*, 224:273–290, 2010.

[130] G. Taylor. The Instability of Liquid Surfaces when Accelerated in a Direction Perpendicular to their Planes. I. *Royal Society of London Proceedings Series A*, 201:192–196, Mar. 1950.

[131] D. Thomas, M. Butler, A. Dermitzakis, T. Anderson, N. McDicken, and V. Sboros. The acoustic scatter from single bisphere^{TM} microbubbles. Submitted to Ultrasound in Medicine & Biology, 2010.

[132] D. H. Thomas. *An acoustic investigation of microbubble response to medical imaging ultrasound pulses*. PhD thesis, University of Edinburgh, 2009.

[133] Y. Tomita and A. Shima. On the behavior of a spherical bubble and the impulse pressure in a viscous compressible liquid. *JSME Bulletin*, 20:1453–1460, 1977.

[134] B. Tran, J. Seo, T. Hall, J. Fowlkes, and C. Cain. Effects of contrast agent infusion rates on thresholds for tissue damage produced by single exposures of high-intensity ultrasound. *Ultrasonics, Ferroelectrics and Frequency Control, IEEE Transactions on*, 52:11211130, 2005.

[135] F. Tranquart, N. Grenier, V. Eder, and L. Pourcelot. Clinical use of ultrasound tissue harmonic imaging. *Ultrasound in Medicine & Biology*, 25(6):889 – 894, 1999.

[136] L. Trilling. The collapse and rebound of a gas bubble. *Journal of Applied Physics*, 23 (1):14–17, 1952.

[137] K. Tsiglifis and N. A. Pelekasis. Nonlinear radial oscillations of encapsulated microbubbles subject to ultrasound: The effect of membrane constitutive law. *The Journal of the Acoustical Society of America*, 123(6):4059–4070, 2008.

[138] K. A. Tsilglifis. *Numerical simulation of bubble dynamics in response to acoustic disturbances*. PhD thesis, University of Thessaly, 2007.

[139] V. Uhlendorf. Physics of ultrasound contrast imaging: scattering in the linear range. *Ultrasonics, Ferroelectrics and Frequency Control, IEEE Transactions on*, 41(1):70–79, Jan 1994.

[140] S. M. van der Meer, B. Dollet, M. M. Voormolen, C. T. Chin, A. Bouakaz, N. de Jong, M. Versluis, and D. Lohse. Microbubble spectroscopy of ultrasound contrast agents. *The Journal of the Acoustical Society of America*, 121(1):648–656, 2007.

[141] M. Versluis, P. Palanchon, D. Goertz, S. van der Meer, I. Heitman, B. Dollet, N. de Jong, and D. Lohse. Surface modes of bubbles in an acoustic field. *APS Meeting Abstracts*, pages G3+, 2006.

[142] K. Vokurka. On Rayleigh's model of a freely oscillating bubble. I. Basic relations. *Czechoslovak Journal of Physics*, 35:28–40, 1985.

[143] K. Vokurka. Comparison of Rayleigh's, Herring's and Gilmore's models of gas bubbles. *Acustica*, 59:214–219, 1986.

[144] N. J. Weissman, M. C. Cohen, T. C. Hack, L. D. Gillam, J. L. Cohen, and D. W. Kitzman. Infusion versus bolus contrast echocardiography: A multicenter, open-label, crossover trial. *American Heart Journal*, 139(3):399 – 404, 2000.

[145] J. K. Willmann, R. Paulmurugan, K. Chen, O. Gheysens, M. Rodriguez-Porcel, A. M. Lutz, I. Y. Chen, X. Chen, and S. S. Gambhir. US Imaging of Tumor Angiogenesis with Microbubbles Targeted to Vascular Endothelial Growth Factor Receptor Type 2 in Mice. *Radiology*, 246(2):508–518, 2008.

[146] S. Yang, D. Kruse, P. Dayton, and K. Ferrara. High-frequency dynamics of ultrasound contrast agents. *Ultrasonics, Ferroelectrics and Frequency Control, IEEE Transactions on*, 52(11):1981–1991, 2005.

[147] S. Zhao, D. E. Kruse, K. W. Ferrara, and P. A. Dayton. Acoustic response from adherent targeted contrast agents. *The Journal of the Acoustical Society of America*, 120(6):EL63–EL69, 2006.

[148] H. Zheng, O. Mukdadi, and R. Shandas. Theoretical predictions of harmonic generation from submicron ultrasound contrast agents for nonlinear biomedical ultrasound imaging. *Physics in Medicine and Biology*, 51:557–573, 2006.

[149] P. Zhong, Y. Zhou, and S. Zhu. Dynamics of bubble oscillation in constrained media and mechanisms of vessel rupture in swl. *Ultrasound in Medicine & Biology*, 27(1): 119–134, 2001.